THE UNIVERSITY OF QUEENSLAND

AUSTRALIA

Dirty Water: Remote Sensing of Water Quality in Tropical and Sub-tropical Freshwater Impoundments

Glenn Campbell

A thesis submitted for the degree of Doctor of Philosophy at

The University of Queensland in August 2010

School of Geography, Planning and Environmental Management

Declaration by Author

This thesis is composed of my original work, and contains no material previously published or written by another person except where due reference has been made in the text. I have clearly stated the contribution by others to jointly-authored works that I have included in my thesis.

I have clearly stated the contribution of others to my thesis as a whole, including statistical assistance, survey design, data analysis, significant technical procedures, professional editorial advice, and any other original research work used or reported in my thesis. The content of my thesis is the result of work I have carried out since the commencement of my research higher degree candidature and does not include a substantial part of work that has been submitted to qualify for the award of any other degree or diploma in any university or other tertiary institution. I have clearly stated which parts of my thesis, if any, have been submitted to qualify for another award.

I acknowledge that an electronic copy of my thesis must be lodged with the University Library and, subject to the General Award Rules of The University of Queensland, immediately made available for research and study in accordance with the *Copyright Act 1968*.

I acknowledge that copyright of all material contained in my thesis resides with the copyright holder(s) of that material.

Contributions to Jointly Authored Works Contained in the Thesis

Peer-reviewed journal publications

Campbell, G., and S. R. Phinn. 2010. An assessment of the accuracy and precision of water quality parameters retrieved with the Matrix Inversion Method. *Limnology and Oceanography Methods.* **8**, 16-29.

Campbell, G., S. R. Phinn and P. Daniel. The Specific Inherent Optical Properties of Three Sub-tropical and Tropical Water Reservoirs in Queensland, Australia. *Hydrobiologia* (accepted)

Conference Proceedings

Campbell, G., and S. R. Phinn. 2008. The efficacy of band weighting schemes for improving the accuracy and precision of water quality parameters estimated from MERIS and MODIS image data. *In Proceedings of 14th Australasian Remote Sensing & Photogrammetry Conference.* Spatial Sciences Institute. pp. 12.

Campbell, G., and S. R. Phinn, 2009, Accuracy and precisions of water quality parameters retrieved from particle swarm optimisation in a sub-tropical lake, *Proceedings of Remote Sensing of the Ocean, Sea Ice, and Large Water Regions 2009,* 7473, Berlin, Germany. pp.12.

The responsibilities for these publications are allocated in the table below.

Manuscript	Author	%	Task Performed
Campbell & Phinn (2008)	G. Campbell	90%	Field campaign, data collection, computer code development, processing, manuscript
	S.R. Phinn	10%	Manuscript review and editing
Campbell & Phinn (2009)	G. Campbell	90%	Computer code development, processing, manuscript
	S.R. Phinn	10%	Manuscript review and editing
Campbell & Phinn (2010)	G. Campbell	90%	Computer code development, processing, manuscript
	S.R. Phinn	10%	Manuscript review and editing
Campbell et al (accepted)	G. Campbell	85%	Field campaigns, data collection, processing, manuscript
	S.R. Phinn	10%	Manuscript review and editing
	P. Daniel	5%	Field campaigns, data collection,

Contributions by Others to the Thesis as a Whole

Chapter 1. Prof. Stuart Phinn and Dr Vittorio Brando were responsible for reviewing and editing.

Chapter 2. Mr Paul Daniel was responsible for calibration of the field instruments prior to the fieldwork and assisted in the field data collection. Ms Leslie Clementson was responsible for the laboratory absorption and water quality concentration measurements. Dr Vittorio Brando supplied initial IDL code used for correction of the *Hydroscat-6* scattering measurements. Prof. Stuart Phinn, Prof. Arnold Dekker and Dr Vittorio Brando were responsible for reviewing and editing.

Chapter 3. Mr Paul Daniel was responsible for calibration of the field instruments prior to the fieldwork and assisted in the field data collection. Dr Vittorio Brando supplied the c-WOMBAT-c atmospheric correction code. Dr Thomas Schroeder and Dr Vittorio Brando were responsible for reviewing and editing part of the chapter. Prof. Stuart Phinn was responsible for reviewing and editing.

Chapter 4. Prof. Stuart Phinn was responsible for reviewing and editing.

Chapter 5. Citiwater**,** Townsville was responsible for the total suspended sediment concentration measurement and Ms Michele Skuza was responsible for the chlorophyll *a* concentration measurement. Prof. Stuart Phinn and Prof. Arnold Dekker were responsible for reviewing and editing.

Chapter 6. Citiwater**,** Townsville was responsible for the total suspended sediment concentration measurement and Ms Michele Skuza was responsible for the chlorophyll *a* concentration measurement. Prof. Stuart Phinn and Prof. Arnold Dekker were responsible for reviewing and editing.

Chapter 7 Prof. Stuart Phinn, Prof. Arnold Dekker and Dr Vittorio Brando were responsible for reviewing and editing.

Statement of Parts of the Thesis Submitted to Qualify for the Award of Another Degree

None.

Acknowledgements

No man is an island and neither is any PhD. I would like to thank my advisors, Prof. Stuart Phinn, Prof. Arnold Dekker and Dr Vittorio Brando for their guidance and their genuine interest in my work and the development of my research skills. I would like to express my gratitude to Assoc. Prof. Armando Apan for encouraging my nascent interest in remote sensing and for recommending and introducing me to Prof. Phinn.

The Surveying and Spatial Science Institute's Bicentennial Education Fund provided seed funding for the project and generous in-kind support was provided by Sunwater, SEQWater, CSIRO Land and Water and the DTS Group. The European Space Agency provided the MERIS images under the AO 595 agreement. I would like to thank James Udy from SEQWater and Matthew Barrett form Sunwater for championing this work in their respective organisations. The generosity shown by Britta Schaffelke and Michele Skuza of the Australian Institute of Marine Science in Townsville was all the more important because it arrived when it was most needed.

My gratitude goes to other people who took time out of their busy work schedules to help me on my way. Jürgen Overheu from UQ went out of his way to help negotiate the intersection of two university computer systems which was result of me working off campus. Suzi Johnson of SEQWater, Glenn McGregor of the Department of Environment and Resource Management and Briony Pomplun of Sunwater all allowed me to ask them stupid questions about how water bodies are monitored and managed. Sam Gillingham spent time instructing me in the dark arts of FORTRAN compilation. From CSIRO, Paul Daniel's optimistic bent and easy humour was invaluable in keeping the fieldwork relaxed and calm and Lesley Clementson was patient with my laboratory methods questions. Thomas Schroeder was able to give me some valuable advice on atmospheric correction, for which I thank him, and for introducing me to the Berliner weisse for which I am not quite sure thanks is the right sentiment.

For those that helped me with my spirit rather than my mind, those other sailors on the good ship UQ PhD, Tony Gill, Julie Scopélitis, Ian Leiper, Mitch Lyons, Michael Hewson and David Blondeau- Patissier, I hope those who haven't found shore yet do it with a minimum of scurvy. My brother-in-law Anthony Carrigan and his wife Emily let me live in their cellar for a semester.

That was well beyond the call of family duty so I sincerely thank them for that. I'd also like to thank Prof. Rod Smith, Assoc. Prof. Kevin McDougall, Joseph Foley and Assoc. Prof. Jim Ball for their advice on the 'soft skills' of academia.

Lastly, I would like to direct my inadequate gratitude towards my children Georgia, Dominic, Genevieve and Phoebe for doing without Sundays and living with a bear with a bad head at times. As always, I would like express my love for Diana, who has now done more reading about remote sensing than a man could reasonably expect from a wife.

Abstract

Tropical and sub-tropical lakes and reservoirs not only provide drinking water and locations for recreation, fisheries and aquaculture but they have also been shown recently to have a disproportionate effect on the on the global carbon cycle. The purpose of this study was to investigate how techniques developed for the remote sensing of water quality parameters (chlorophyll *a*, tripton and coloured dissolved organic matter (CDOM)) in inland waters in temperate northern hemisphere environments could be adapted or improved to allow them to be applied to tropical and sub-tropical water bodies. This aim was achieved by adapting existing image based atmospheric correction techniques, by measuring and modelling the specific inherent optical properties of water quality parameters in a selection of the Northern Australian water bodies and by modifying existing inversion algorithms. The final algorithms were applied to a tropical water body using the MERIS sensor to determine the monitoring accuracy and precision that could be expected for each water quality parameter.

The water quality parameter specific inherent optical properties (SIOPs) were measured in three large water storages in north-eastern Australia, Wivenhoe Dam (27° 21´ S, 152° 36´ E), Fairbairn Dam (23° 42´ S, 148° 02´ E) and Burdekin Falls Dam (20° 37´ S, 147° 0´ E). Three existing MERIS atmospheric correction methods were applied and found to be unsuitable because they use inappropriate water leaving radiance assumptions. A site specific atmospheric correction method was developed that utilised the 6S atmospheric model and the reflectance of the dense dark vegetation that surrounded the study sites. The study used two inversion methods, the direct, Matrix Inversion Method (MIM) and the stochastic, Particle Swarm Optimisation (PSO). Both methods were implemented on an over-determined system of reflectance equations with semi-analytic models of the anisotropy of the in-water light field. The MIM used differential weighting for each sensor band and the PSO used four different reflectance matching criteria. The SIOPs, the typical water quality constituent concentrations and the *Hydrolight*® radiative transfer model were used to simulate reflectance spectra that could be employed to parameterise the reflectance models and investigate how the inversion methods performed in the presence of noise. The methods were applied to two images of Burdekin Falls Dam and the results were validated against *in situ* measurements.

The results of the application of the MIM algorithm showed that the best weighting scheme had a mean chlorophyll *a* retrieval error of 1.0 μgl^{-1}, the conventional three band scheme had a mean error of 4.2 μgl^{-1} and the unweighted scheme had a mean error of 5.5 μgl^{-1}. For tripton, the best performed weighting scheme had a mean error of 1.2 mgl^{-1}, the three band scheme had a mean error of 3.4 mgl^{-1} and the unweighted scheme had a mean error of 1.8 mgl^{-1}. For the CDOM retrieval, the mean error was found to be 0.12 m^{-1} for the best performed weighting scheme, 0.25 m^{-1} for the three band scheme and 0.52 m^{-1} for the unweighted scheme. In the case of the PSO the mean retrieval error of the best performed similarity measure was 2.0 μgl^{-1}, 2.45 mgl^{-1} and 0.3 m^{-1} for chlorophyll *a*, tripton and CDOM respectively.

The study concluded that the atmospheric correction methods for MERIS images of Northern Australian inland waters cannot rely on site independent *a priori* knowledge of the water leaving radiance that has been developed from other environments and that instead, images of inland water bodies can be corrected by taking advantage of dense dark vegetation surrounding the impoundment. It also concluded that there was sufficient intra-impoundment variation in the specific absorption and specific scattering of phytoplankton and tripton to require a well distributed network of measurement stations when characterising a new water body and that some inland water bodies may need more than one SIOP set to characterise the optical domains present. Significant improvements in the accuracy and precision of retrieved water quality parameter values can be obtained by using semi-analytically estimated values for the anisotropy factor and that over-determined systems of equations can be used to mitigate the effect of unknown and inherent sources of error in the remote sensing system. After application of the modified retrieval algorithms it was found that optical closure can be used to identify the most appropriate SIOP set in water bodies that have multiple SIOP domains, the over-determined weighted MIM algorithm can be more accurate and precise than the conventional three band or unweighted approach and the PSO does not offer improvements in accuracy and precision sufficient enough to justify the increased computational overhead in the inversion.

Keywords

Remote sensing, inland water, absorption, backscattering, Matrix Inversion Method, Particle Swarm Optimisation, atmospheric correction, phytoplankton, tripton, coloured dissolved organic matter

Australian and New Zealand Standard Research Classifications (ANZSRC)

090905 Photogrammetry and Remote Sensing 70%, 050206 Environmental Monitoring 20%, 060204 Freshwater Ecology 10%

Table of Contents

List of Figures

List of Tables

List of Abbreviations and Symbols

Abbreviations

AIMS	Australian Institute of Marine Science	NIR	Near infrared
AOP	Apparent optical property	NN	Neural network
AOT	Aerosol optical thickness	PSO	Particle swarm optimisation
ARVI	Atmospherically resistant vegetation index	PSU	Practical salinity units
BRDF	Bi-directional reflectance distribution function	SAM	Spectral angle mapper
CDOM	Coloured dissolved organic matter	SCM	Spectral correlation mapper
CHL	Chlorophyll *a*	SID	Spectral information divergence
CTD	Conductivity-Temperature-Depth	SIOP	Specific inherent optical property
DDV	Dense dark vegetation	SPM	Suspended particulate matter
FWHM	Full width half maximum	TOA	Top of atmosphere
IOP	Inherent optical property	TR	Tripton
LUT	Look up table	TSM	Total suspended material
MIM	Matrix inversion method	VSF	Volume Scattering Function

Symbols

a	spectral absorption coefficient (m^{-1})
a_0	peak amplitude for a Gaussian band
a_w	spectral absorption by water (m^{-1})
A_{CDOM}	spectral absorbance of CDOM (-)
a_ϕ, a_{TR}, a_{CDOM}	spectral absorption by phytoplankton, tripton and coloured dissolved organic matter (m^{-1})
a^*_i	the specific absorption coefficient for constituent *i* (m^2 μg^{-1})
b	the spectral scattering coefficient (m^{-1})
b_b	the spectral backscattering coefficient (from 90° to 180°)(m^{-1})
$\widetilde{b_b}$	back scattering probability (-)
b^*_{bi}	the specific backscattering coefficient for constituent i (m^2 μg^{-1})
b_{bu}	uncorrected backscattering measured by the *Hydroscat-6* (m^{-1})
C_i	the concentration of a constituent ($\mu g\ l^{-1}$ or $mg\ l^{-1}$ or $g\ m^{-3}$)
c	the spectral attenuation co-efficient (m^{-1})
$_d$	subscript denoting a downwelling property
E	irradiance ($Wm^{-2}nm^{-1}$)
E_{ad}	total surface irradiance ($Wm^{-2}nm^{-1}$)
f	anisotropy factor
f_Q	anisotropy factor normalised by Q
l	cell path length (m)
L	the spectral radiance ($Wm^{-2}sr^{-1}nm^{-1}$)
L_b	the spectral radiance of the background ($Wm^{-2}sr^{-1}nm^{-1}$)

L_t	the spectral radiance of the target ($Wm^{-2}sr^{-1}nm^{-1}$)
L_{pa}	the spectral atmospheric path radiance ($Wm^{-2}sr^{-1}nm^{-1}$)
L_{pb}	the spectral background path radiance ($Wm^{-2}sr^{-1}nm^{-1}$)
$NE\Delta R_E$	environmental noise-equivalent delta reflectance
n_w	relative refractive index for air/water
Q	radiance to irradiance conversion factor
$r(\theta)$	Fresnel reflectance
$R(0^-)$	the subsurface irradiance reflectance
R_{app}	remote sensing reflectance above the water surface
s^*	spherical reflectance for illumination from below
S	spectral slope for absorption
t	transmission from air to water
t^*	transmission from water to air
t_d	diffuse atmospheric transmittance
$_u$	subscript denoting a upwelling property
β	volume scattering function
γ	spectral slope for backscattering
θ_s	sun angle
θ_v	view angle
λ	wavelength
$\Delta\lambda_{½}$	FWHM of a Gaussian band
μ	cosine of the zenith angle
μ_0	cosine of the sun zenith angle
μ_w	cosine of the in-water sun angle
ρ	reflectance
ρ_t	top of atmosphere reflectance
$\rho_a, \rho_r, \rho_{ra}, \rho_g, \rho_w$	reflectance due to aerosol scattering, Rayleigh scattering, Rayleigh scattering and aerosols scattering, sun glint, water
ϕ_s	sun azimuth
ϕ_v	view azimuth
τ	optical depth
χ	PSO constriction factor
ω_0	single scattering albedo (b/c)
ω_b	backscatting albedo ($\frac{b_b}{a+b_b}$)
ω_w	backscatting albedo due to water
ω_p	backscatting albedo due to particles

1. Introduction and Background

Water resource managers have the responsibility to deliver water of sufficient quality to urban, agricultural and industrial users as well as maintaining the recreational and ecological amenity of the inland water bodies under their control. To deliver these objectives it is critical that they monitor and maintain the quality of the water in their storage reservoirs. Two of the important qualities of water that are relevant for the managers' objectives are the turbidity of the water body and the level of algal activity within it. The turbidity, or clarity of the water, which is a major influence on the ecology of aquatic systems, is determined by the absorption and scattering processes that take place within the water column. Three water quality parameters; algal cells, tripton (the non-algal particles of the suspended particulate matter), and coloured dissolved organic matter (CDOM) represent the major absorption and scattering agents within the water.

Algal blooms, especially cyanobacterial (blue-green algae) blooms, in water can cause adverse health effects in humans and animals ranging from skin irritations to permanent organ damage and death (Australian State of the Environment Committee 2001; Chorus et al. 2003). Almost all water bodies in the state of Queensland, Australia, including those used for human consumption, feature cyanobacteria blooms at some time (Garnett et al. 2003) and approximately 80% of the water used in Australia is extracted from surface waters (Australian State of the Environment Committee 2001). In Queensland it is predicted by global climate change models that average daily minimum temperatures will rise more quickly than maximum temperatures. The increased growth rate of cyanobacteria that results from higher night time temperatures will allow hazardous blooms to develop faster (Garnett et al. 2003). The problem of algal blooms in water supply is serious, ubiquitous and has the potential to get worse. Hence, the monitoring of water quality parameters is critical to maintain usable water resources.

1.1 Remote Sensing as a Monitoring Tool

The current state mandated monitoring regime in Queensland classifies storage bodies on a scale from A1 through to C with each classification providing for a different level of sampling and

analytical precision and hence cost (Queensland Department of Natural Resources and Mines 2005). The monitoring standard recommends that in high priority cases water samples are to be taken from open water in the vicinity of each recreational area and at the water supply off-take tower. Single point sampling may be of limited utility because the horizontal spatial distribution of suspended sediment and phytoplankton concentrations in water bodies is highly variable (Hotzel & Croome 1999; Jupp et al. 1994; Kutser 2004; Vos et al. 2003). The variability of the phytoplankton concentration can be addressed by a more intensive point sampling routine, but the taking of water samples is labour intensive so the cost per sample point is a limit. In practice, the number of sampling sites and samples taken is a function of the aims of the monitoring, the morphology of the water body and the financial resources available (Hotzel & Croome 1999). Satellite remote sensing has been used for simultaneous measurement of water quality parameters in each pixel of an image, meaning that the marginal cost for each measurement is small. However, it is not possible to make a generic assessment of remote sensing's cost effectiveness as each application will have its own trade-offs between the expediency of point sampling and the usefulness of a synoptic view and each algorithm will require different amounts of field work and laboratory processing to deliver a water quality parameter map. The area monitored by a point sample will change depending on the spatial variability of the physical quantity being measured. It is perhaps useful to compare the alternatives using a "cost per monitored area" measure (Bukata 2005). For example if, for a large lake, one sample per 5000 ha was adequate to describe the spatial variability then the cost of remote sensing would not be justified, however if one sample per 10 ha was required then it most probably would. Nevertheless it is unlikely that remote sensing will ever evolve to stage where it can measure, at the same levels of accuracy and precision, all the quality parameters that *in situ* sampling can.

When optical remote sensing has been used to retrieve water quality parameters the primary focus of work to date has been on oceanic and coastal waters. Morel & Prieur (1977) classified water into two types; case-I where the optical properties are only determined by phytoplankton and the water itself and case-II where contributions to the optical properties are made by CDOM and suspended inorganic particles as well. With case-II waters, researchers have been interested in understanding the dynamics of water bodies so there has been a focus on high spatial

resolution at the expense of short production time-scales. It is recognised that moving to an analytical solution will allow for multi-temporal series to be developed without repeated *in situ* measurements.

1.1.1. The Problem of Abstraction

Any process that turns data into information requires a level of abstraction and synthesis. In the case of spatial data it is necessary to take the physical world and change it into an image or a map. The remote sensing system is like a transducer that takes the physical world in at one end and produces the image or map out the other. At the next level within the transducer are all the steps involved in sensor calibration, image correction and image inversion. These steps can be further broken down into processes that involve simplifying assumptions and approximations, each with their associated errors. Due to interactions between the errors, the error of the whole system is not simply the linear sum of the individual errors.

The reflectance spectrum measured by optical sensors is a result of the cumulative interactions of light with the water itself, the water quality parameters, the atmosphere, the sensor's optics and the detector. To retrieve the water quality parameter concentrations it is necessary to invert the processes that produce the reflectance spectrum. The water quality parameter concentrations and the reflectance spectrum are linked by the inherent optical properties (IOPs) of the water. The IOPs have magnitudes that are independent of the geometric structure of the light field. Properties that are dependent on the geometric structure of the light field are referred to as Apparent Optical Properties (AOPs). The absorption coefficient a describes the chances of a photon being absorbed, the scattering coefficient b describes the chances of a photon being scattered and the volume scattering function (VSF) β describes the probability of a scattered photon being scattered in a particular direction. Any successful semi-analytic inversion approach needs to relate the reflectance to the IOPs and then the IOPs to the water quality parameter concentrations.

Any attempt at inversion to estimate water quality parameters must come to terms with atmospheric effects, the amount of diffusion in the illuminating light field, the illumination geometry and the change in the light field at the air-water interface. An attempt at inversion must

be able to model how the total absorption and scattering spectrum of the water and its constituents changes with the concentration of water quality parameters, as well as how this total spectrum modifies the light field. If the water is optically shallow, where the light reflects off the bottom and returns to the water's surface, or quasi-optically shallow, where the angular distribution of light has not taken on a fixed form (the asymptotic radiance distribution) (Kirk 1981), the inversion must be able to remove the influence of the lake bottom. It must be able to represent how the physical characteristics of the sensor will add random and perhaps systematic error to the reflectance signal and finally it must use some form of mathematical method to invert the reflectance signal and retrieve the IOPs or concentrations. Each of the assumptions, approximations and field measurements required will have an error associated with it. How these errors interact and propagate through the algorithm will affect the accuracy of the remote sensing system. The approximations and assumptions that contribute the largest amount of the error are those that warrant the closest scrutiny.

1.2 Remote Sensing of Water Bodies

The body of knowledge that now exists on the interaction between light and water has evolved from work initially concerned with radiation in foggy atmospheres (Schuster 1905), then colour matching of plastics (Duntley 1942) and finally to light in water (Preisendorfer 1959).

1.2.1. Using Remote Sensing to Retrieve Biophysical Properties of Water

There exist two dominant approaches to the optical remote sensing of water quality. Firstly there is the empirical approach which seeks to find correlations between the desired water quality parameter and the reflectance value of specific bands or band ratios. One of the influential drivers of this type of algorithm development has been the wish to develop a method that has the desirable traits of being mathematically simple and requiring unsophisticated processing. In contrast, the semi-analytical approach relies on modelling the interaction of the light field with the optical properties of the water. The approach is not totally analytical as it uses empiricism to parameterise several of the terms in the model (O'Reilly et al. 1998; Rijkeboer et al. 1997).

The physics based semi-analytical approach has the advantage of requiring less field data and allowing greater scope for multi-temporal series to be developed without repeated *in situ* measurements. For these reasons the following discussion focuses on the semi-analytical approach.

Semi-Analytical Applications and Case Studies

The studies that apply semi-analytical algorithms vary with the environment they are assessing, the water quality parameter they are targeting, the reflectance, absorption and scattering models they use as well as the techniques used to measure model parameters. Furthermore, there is a variation in the imagery and observations that are used and the techniques involved in inverting the observations. To investigate the knowledge gaps in this area it is perhaps more instructive to consider the outcomes and conclusions of these studies rather than the minutiae of the techniques.

The effect of errors and variation of SIOPs has been identified by a number of studies (Hakvoort et al. 2002; Hoge & Lyon 1996; Hoogenboom et al. 1998b; Pasterkamp et al. 1999; Vos et al. 2003). Even within one inland lake the variability of SIOPs must be taken into account (Hoogenboom et al. 1998b) but the spatial variation is greater than the temporal variation (Vos et al. 2003) and the effect of measurement error in the SIOPs has a minor effect on the derived concentrations when compared to errors in the measurement of the sub-surface irradiance reflectance ($R(0^-)$) (Hakvoort et al. 2002). Nevertheless, quantifying the variation in the SIOPs is a prerequisite for a realistic error analysis of the retrieved concentrations (Hoogenboom et al. 1998b).

While there is a multitude of individual approaches to model inversion, the majority fall within four general types: the look up table (LUT) approach which matches measured spectra to large number of previously calculated spectra (Keller 2001a; Matarrese et al. 2004; Mobley et al. 2005); the neural network (NN) approach which uses a large set of training data to relate the measured spectra to the parameters used to create the training set (Baruah et al. 2001; Doerffer & Schiller 2007; Schaale et al. 1998; Su et al. 2006); and the inversion and optimisation approaches. The two former approaches have value and continue to be developed, however, it is

necessary to limit the scale of this project and so they are considered as outside the scope of this work.

In the inversion and optimisation approaches a forward model is used to simulate the spectra from a number of parameters and the set of parameters that minimises a selected cost function is selected as the solution. If the forward model is linear and the cost function is the sum of the squares of the residuals then this reduces to the matrix inversion method (MIM).

The MIM models the measured reflectance as a function of the absorption and backscattering coefficients in each band and then solves the resultant system of linear equations. With the increase in the number of bands in more recent instruments there have been moves from using exact (same number of bands as unknowns) systems (Brando & Dekker 2003; Giardino et al. 2007; Hoge & Lyon 1996; Hoge et al. 1999; Hoogenboom et al. 1998b; Lyon & Hoge 2006) to over-determined (more bands than unknowns) systems (Boss & Roesler 2006; Hakvoort et al. 2002; Vos et al. 2003).

Once the system is over-determined, the solution cannot be exact because of errors in the measurement and model, so the MIM method uses a measure of consistency and then finds the solution that minimises this error. As well as the constituent concentrations, the use of the MIM on an over-determined system will return the residuals. A *prima facie* case can be made that the relative and absolute size of the residuals will contain information on the consistency and reliability of the results but no literature that explored this idea was found. Perhaps the residuals can be used in some form to weight the individual bands in a subsidiary inversion as it has been asserted, but not demonstrated, that that application of the weighted least-squares method significantly improves the accuracy of the results (Hakvoort et al. 2002). If an iterative approach is taken then it is possible to extend weighted least squares to cover non-linear problems where it has been shown that the residuals are smaller for the non-linear model than for a comparable linear model (Vos et al. 2003). Like some of the spectral matching techniques there is the risk that the MIM will find a local minimum dependant on the starting point rather than the absolute minimum (Keller 2001a). There has been little work done on the effects of over-determined systems except a finding that the MIM method was less accurate when using 15 or more bands

(Vos et al. 2003) and that the need to convolve the IOPs with the response function of the sensor leads to a biased error especially for broad bands (Keller 2001a). Furthermore, work by Lee and Carder (2002) showed that for deep water there was no difference in the performance of 5 nm, 10 nm, 20 nm contiguous bands and the MERIS band set. They found a difference between the contiguous bands and MERIS for shallow waters. Although they were using inversion optimisation it is likely that a similar result will be obtained with MIM.

Other optimisation techniques use iterative rather than direct solutions. The traditional methods (Lee & Carder 2002; Odermatt et al. 2008a; Pozdnyakov et al. 2002; van der Woerd & Pasterkamp 2008; Wettle & Brando 2006) start with an estimate of the solution and then use characteristics of the search space, such as the gradient at that point, to calculate a new estimate. However, if the search space is non-convex, discontinuous, multi-modal, or is not easily differentiable traditional methods may return local rather than global minima (Slade et al. 2004). Stochastic methods such as simulated annealing (Maritorena et al. 2002), the genetic algorithm (Zhan et al. 2003) and particle swarm intelligence (Slade et al. 2004) use multiple initial approximations selected by stochastic sampling to make allowance for difficult search spaces.

There has been very little work done on comparing the performance of inversion methods. One result found that the standard deviation of the results of MIM was lower than the curve fitting result, but the result was closer and more consistent for chlorophyll *a* with curve fitting (Keller 2001a). Another report (IOCCG 2006) compared the performance of eight algorithms designed to retrieve the IOPs rather than the water quality parameter concentrations. Each algorithm was applied to large synthetic and *in situ* data sets. There was a greater variation in performance across the synthetic data set but this may only reflect the deviation of the bio-optical model behind each algorithm from that of the bio-optical model used to prepare the synthetic data set. There was little variation in the performance of the algorithms on the *in situ* data set. Notably one of the spectral optimisation techniques (Devred et al. 2006) failed to converge in 25% of cases while the over constrained MIM algorithm (Boss & Roesler 2006) calculated but rejected 23% of its solutions. While it is a substantial body of work, the report itself recommends that a better quantification of uncertainties in derived products through an in-depth analysis of error sources and their propagation is required (IOCCG 2006, p. 110).

To date, the preponderance of inland water remote sensing studies described in literature have focused on temperate northern hemisphere environments. Environmental zones differ in temperature, rainfall intensity and seasonal distribution, algal species, soils and geology. All these factors have an influence on the optical properties of the water quality parameters, so it is unlikely that the parameterisations developed for temperate regions can applied to tropical regions without modification.

1.3 Study Approach

The research problem was summarised as follows:

The parameterisations developed for the remote sensing of inland waters in temperate northern hemisphere environments must be adapted or improved before they can be applied to tropical and sub-tropical water bodies.

The above problem was addressed through the following objectives:

1. Adapt existing atmospheric correction techniques to create an image based correction approach that allows images of inland water bodies to be corrected in the absence of *in situ* data.

2. Measure and model the specific inherent optical properties in a selection of Northern Australian water bodies.

3. Parameterise and modify existing algorithms to retrieve water quality parameter concentrations and map water quality parameters from optically deep inland waters so they can be applied to Northern Australian water bodies and available data.

4. Apply and validate the algorithms for Northern Australian water bodies and determine the monitoring accuracy and precision that could be expected for each water quality parameter concentration in each study site.

1.3.1. Thesis Structure

The work performed to address the objectives listed above is reported in the following six chapters that are inter-related in the way shown in Figure 1-1.

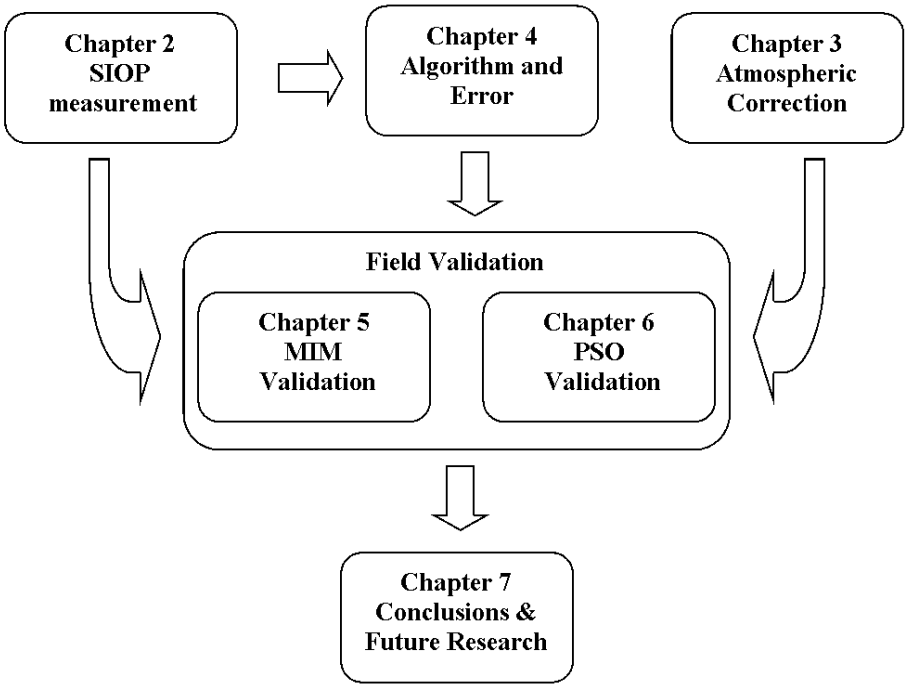

Figure 1-1 A representation of the inter-relationship of the material contained in the thesis chapters.

Chapter 2 Specific Inherent Optical Property Measurement

This chapter details the work associated with the measurement of the SIOPs in three inland water bodies. The SIOPs are required to complete objective 2 as well as being essential input data in the completion of objectives 3 and 4. The chapter describes the results of field campaigns conducted in July 2007 and October 2008.

Chapter 3 Atmospheric Correction of MERIS Images Over Inland Water Bodies

This chapter details the work associated with the adaptation of existing atmospheric correction techniques to create an image based correction approach that satisfies objective 1. The chapter shows that the MERIS standard product, the BEAM MERIS Case-2 Waters Eutrophic Lakes Processor (MC2WEUL) Plug-in (Doerffer & Schiller 2008) and the *c-WOMBAT-c* (coastal Waters and Ocean MODTRAN-4 Based Atmospheric correction) software (Brando & Dekker

2003) are inappropriate for images of the studied water bodies. The chapter details how the *c-WOMBAT-c* approach was modified to utilise the 6S atmospheric model and the dense dark vegetation (DDV) surrounding the study sites.

Chapter 4 Algorithms and Errors for Retrieving Water Quality Parameters

This chapter details the work associated with the parameterisation and modification of existing semi-analytic algorithms required to complete objective 3. The chapter shows that for the MIM, overdetermined differentially weighted systems can be used to mitigate the effect of unknown and inherent sources of error in the remote sensing system. It shows that significant improvements in the accuracy and precision of retrieved water quality constituent values can be obtained by accounting for the spatial non-uniformity of the light field by using semi-analytically estimated values for the anisotropy factor that are calculated for each band separately.

The chapter also examines the performance of four similarity measures that can be used in conjunction with the Particle Swarm Optimisation (PSO) when it is applied to the problem of inland water remote sensing.

Chapter 5 Field Validation of the MIM Algorithm at Wivenhoe and Burdekin Falls Dam, Queensland, Australia

This chapter details the work associated with completing objective 4 for the MIM algorithm. *In situ* observations of water quality parameters taken from field campaigns at Burdekin Falls Dam in October 2008 and August 2009 are compared to the water quality parameters retrieved from MERIS images of the water body. The chapter looks at the relative performance of many weighting schemes and draws conclusions and explains which ones are the most appropriate for this water body. The chapter shows how the optical closure of each water pixel can be used to select the most appropriate SIOP set to be applied in the inversion.

Chapter 6 Field Validation of the PSO Algorithm at Burdekin Falls Dam, Queensland, Australia

This chapter details the work associated with completing objective 4 for the PSO algorithm. Using the same *in situ* data sets from Chapter 5 the chapter compares the performance of four

similarity measures and draws conclusions and explains which ones are the most appropriate for this water body.

Chapter 7 Conclusions and Future Research

This chapter synthesises the results of the preceding five chapters and outline directions for future research.

1.4 Background to Methods and Data Used

1.4.1. *Hydrolight*®

Water reflectances can be modelled with *Hydrolight 4.2*®, a numerical model which solves the radiative transfer equation to produce radiance distributions and derived quantities for natural waters (Mobley & Sundman 2001). Users have the ability to specify horizontally homogeneous but vertically varying IOPs of the water, sun and observer positions, the condition of the water surface, the sky spectral radiance distribution and the depth and reflectance of a bottom boundary. Users can calculate the resultant irradiance and radiances and the AOPs. The flexibility of *Hydrolight*® makes it the ideal tool to investigate the effect of errors on the retrieval of water quality parameters as the solution can be directly compared to the input values.

Radiative Transfer Equation

The radiative transfer equation describes how the radiance (L) varies along a given path and at a specified point as a result of the optical properties of the water. For a horizontally stratified water body, with a constant input of mono-chromatic unpolarised light and no inelastic scattering, it is possible to describe the change in the light as it travels through an absorbing and scattering medium as

$$\frac{dL(z,\theta,\phi)}{dr} = -c(z)\,L(z,\theta,\phi) + L^{*}(z,\theta,\phi)\,. \qquad (1\text{-}1)$$

Where *r* is distance along the path of the light, *c* is the attenuation and the angles are as shown in Figure 1-2. Typically, researchers are interested in the variation with depth rather than path length so the substitution $dr = \frac{\cos\theta}{dz}$ is made.

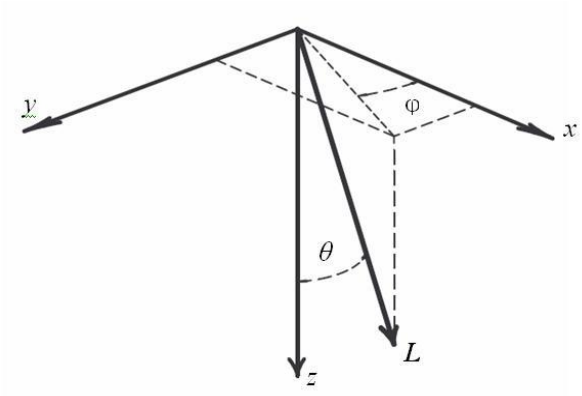

Figure 1-2 Definition of the geometry for the radiative transfer equation

The first part of the right hand side describes the attenuation of the light and the second part is the gain from light that has been scattered from other directions. This second part is defined as

$$L^*(z,\theta,\phi) = \int_{2\pi} \beta(z,\theta,\phi,\theta',\phi')\, L\ (z,\theta',\phi')\, d\omega(\theta',\phi') \qquad (1\text{-}2)$$

Where β is the volume scattering function between the pre-scattered (θ',ϕ') and post scattered (θ,ϕ) directions and $d\omega(\theta',\phi')$ is an infinitesimal cone in the direction (θ,ϕ). The scattering coefficient *b* is the proportion of all incident flux which is scattered, which is the integral over all directions of the volume scattering function.

$$b = 2\pi\int_0^{\pi} \beta(\alpha)\sin\alpha\, d\alpha = \int_{4\pi} \beta(\alpha) d\omega \qquad (1\text{-}3)$$

We can get b_f (forward) and b_b (backward) scattering by integrating from 0 to $\pi/2$ and $\pi/2$ to π respectively. Similarly, upward scattering refers to light that travels with decreasing *z* after scattering and downward scattering refers to light that travels with increasing *z* after scattering.

Although this is an exact description, the complexity of the volume scattering function means that it cannot be directly solved. As a result all practical models of the underwater light field resort to some form of approximation.

1.4.2. MEdium Resolution Imaging Spectrometer (MERIS)

The MERIS imaging spectrometer is deployed on the European Space Agency's ENVISAT polar orbiting platform which was launched in March 2002. It is a pushbroom sensor with a 68.5° field of view which at an altitude of 799 km equates to a swath on ground of approximately 1150 km. This means that it has three day global coverage and a 35 day repeat coverage (Curran & Steele 2005). The nominal pixel size at nadir is 290 m along track and 260 m across track for the full resolution mode. It has 15 programmable spectral bands restricted to the visible near-infrared part of the spectrum (390-1040 nm). The default band settings are listed in Table 1-1 and the spectral response curves are shown in Figure 1-3.

Table 1-1 MERIS band location, width and primary applications. (ESA 2006)

Band index	Band centre (nm)	Band width (nm)	Application(s)
1	412.5	10	Yellow substance and detrital pigments
2	442.5	10	Chlorophyll absorption maximum
3	490	10	Chlorophyll and other pigments
4	510	10	Suspended sediment, red tides
5	560	10	Chlorophyll absorption minimum
6	620	10	Suspended sediment
7	665	10	Chlorophyll absorption & fluorescence\ reference
8	681.25	7.5	Chlorophyll peak
9	708.75	10	Fluorescence reference, atmosphere corrections
10	753.75	7.5	Vegetation, cloud
11	760.625	3.75	O_2 R- branch absorption band
12	778.75	15	Atmosphere corrections
13	865	20	Vegetation, water vapour reference
14	885	10	Atmosphere corrections
15	900	10	Water vapour, land

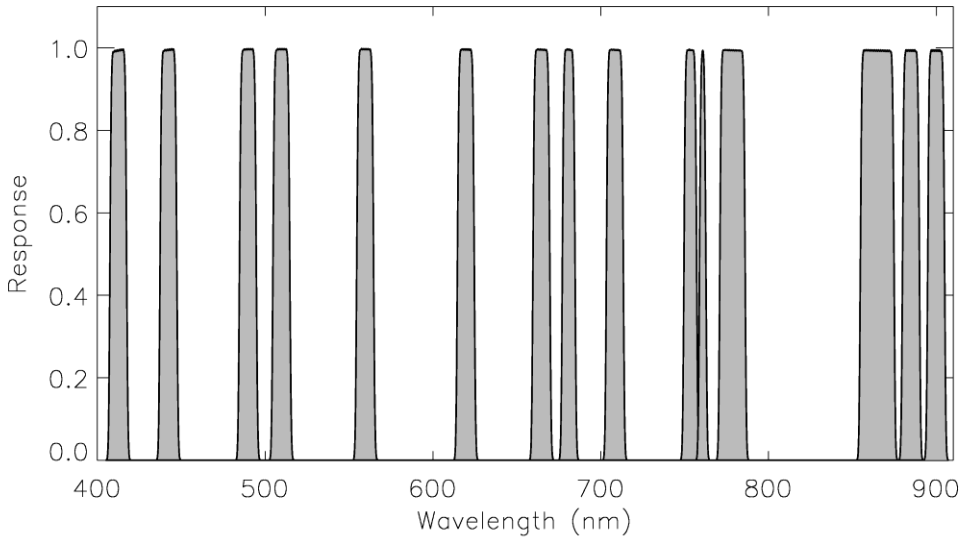

Figure 1-3 The spectral response functions for the MERIS sensor (Bourg 2004).

1.5 Study Sites

Three water storages in north-eastern Australia, Wivenhoe Dam (Lake Wivenhoe, 27° 21´ S, 152° 36´ E), Fairbairn Dam (Lake Maraboon, 23° 42´ S, 148° 02´ E) and Burdekin Falls Dam (Lake Dalrymple, 20° 37´ S, 147° 0´ E) were used for the studies that form this thesis. The major geographic parameters of the three sites are shown in Table 1-2.

Table 1-2 The key geographic parameters of the three study sites.

Study site	Storage Capacity (ML)	Maximum Depth	Feeding River(s)	Inundated Area at Full Supply Level (Ha)	Mean Rainfall (mm/yr)	Evaporation (mm/yr)
Wivenhoe Dam *	1,165,000	44.0	Brisbane R	10,940	1000	1600
Fairbairn Dam†	1,300,000	31.7	Nogoa R	15,000	600	2000
Burdekin Falls Dam†	1,860,000	40.0	Burdekin R Cape R Belyando/Suttor R	22,000	600	2400

*(South East Queensland Water Corporation Ltd 2005), † (Sunwater 2005)

Wivenhoe Dam (Lake Wivenhoe)

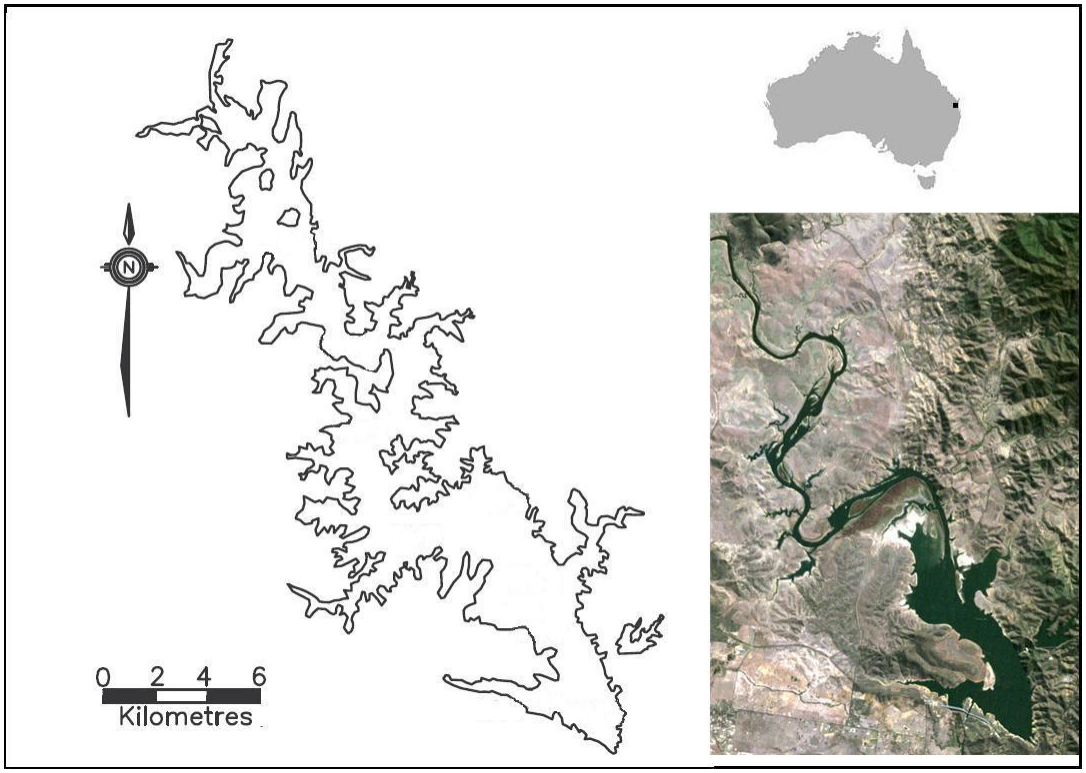

Figure 1-4 Wivenhoe Dam, Australia. The left hand image shows the calculated full supply level and the right hand side shows a true colour Landsat 5 Thematic Mapper (TM) image, at the same scale, captured on 16th July 2007. Note the reduced water extent at the time of the fieldwork activities which were performed in July 2007.

Wivenhoe Dam (Figure 1-4) is the principal source of drinking water for the city of Brisbane in South East Queensland. It receives inflows from the Upper Brisbane River as well as controlled releases from Somerset Dam which controls the Stanley River. It has a catchment of 7020 km^2 that is dominated by grazing (>50%) and natural vegetation (20%) (Burford & O'Donohue 2006). A recent study on the in-dam sediment showed that fine sediment is dominated by the Esk Formations that lie under the path of the Upper Brisbane River (Douglas et al. 2007). The catchment receives rainfall of approximately 1000 mm/yr, mainly falling over the summer months. Water released from the dam enters the Brisbane River and discharges into Moreton Bay approximately 150 km downstream.

Fairbairn Dam (Lake Maraboon)

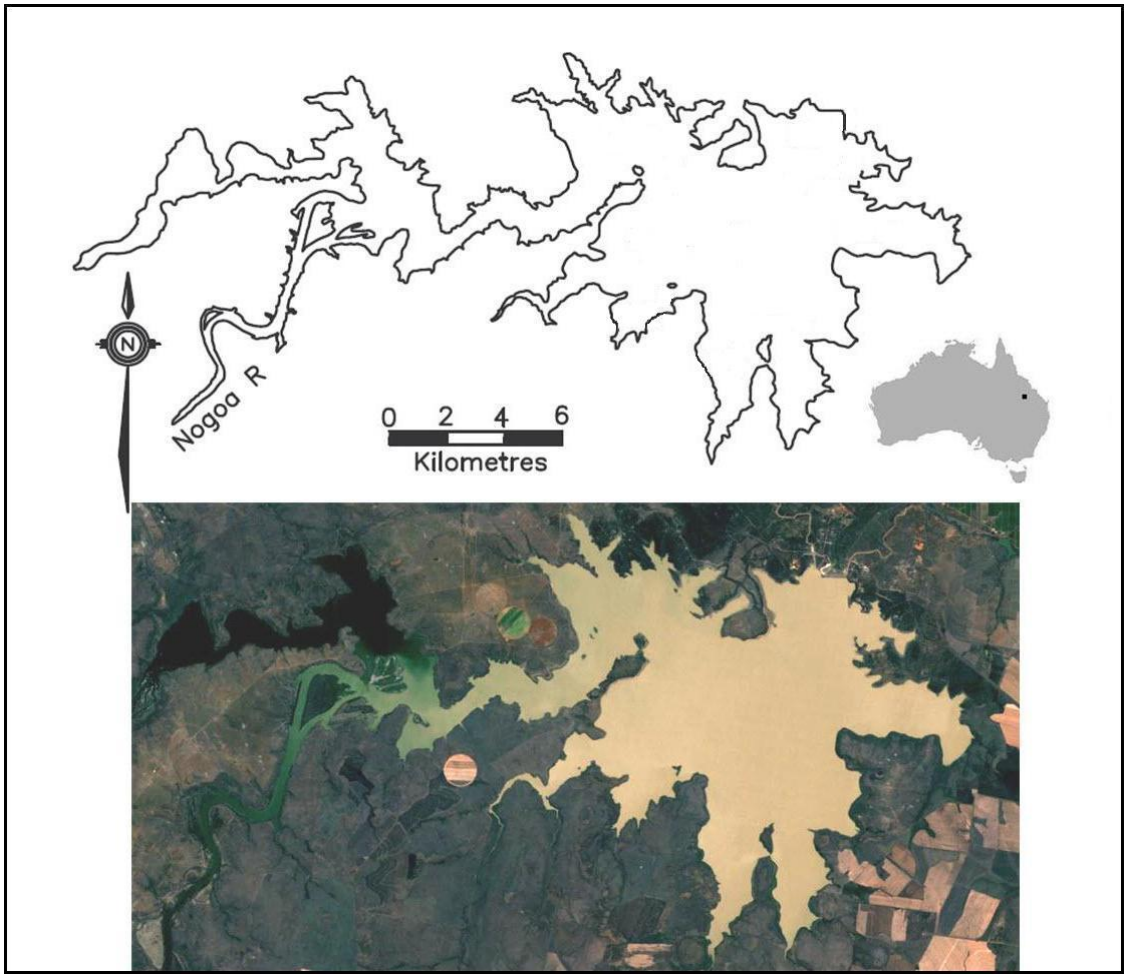

Figure 1-5 Fairbairn Dam, Australia. The top image shows the calculated full supply level and the bottom image shows a Landsat 5 TM true colour image at the same scale as the map, captured on 3rd November 2008.

The Nogoa River has a catchment of 27,130 km^2 and before being blocked by Fairbairn Dam (Figure 1-5) it had a mean annual sediment load of 1.23 Mt. It forms one of the four major tributaries to the Fitzroy River and it carries the highest sediment load of all the tributaries (Joo et al. 2005). The predominant land use in the catchment is grazing with small portions of dryland and irrigated cropping. The catchment receives rainfall of approximately 600 mm/yr mainly falling over the summer months. Water released from the dam eventually enters the Fitzroy River and discharges into the Great Barrier Reef lagoon approximately 600 km downstream.

Burdekin Falls Dam (Lake Dalrymple)

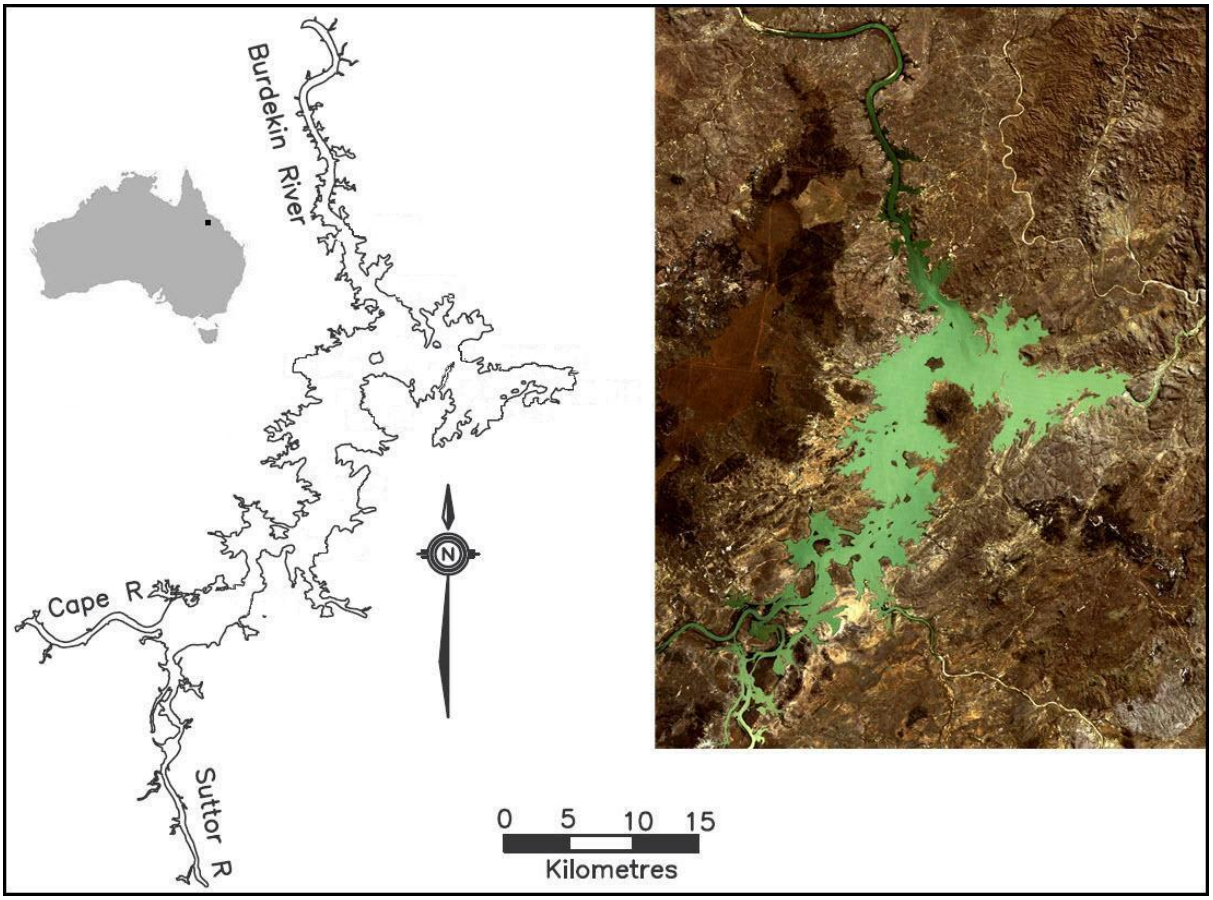

Figure 1-6 Burdekin Falls Dam, Australia. The left hand image shows the calculated full supply level and the right hand image shows a Landsat 5 TM true colour image at the same scale as the map, captured on 22nd August 2008.

The Burdekin Falls Dam (Figure 1-6) receives inputs from four major sub-catchments that cover a total area of 114,000 km^2. From the north the Burdekin River has its origin in tropical rainforest but primarily flows through tropical savannah. From the west the lake is fed from the Cape River which rises in reasonably steep sedimentary country and then flows through flat less erodible areas. The Belyando and Suttor Rivers meet just beyond the inundated area and feed the lake from the south. The Belyando River and Suttor River suffer from persistent turbidity as they flow slowly over clay soils (O'Reagain et al. 2005). During full flow conditions the former river takes on a grey colour and the latter red. The highly variable particle size distributions which have been measured over single flow events in all tributaries (Lewis et al. 2009) suggest that the optical properties of the suspended sediment may be complex. It is estimated that the

dam traps 88% of the sediment that flows in from the tributaries during flow events with the bulk of sediment being transported by the Burdekin River (Bainbridge et al. 2006a; Bainbridge et al. 2006b). However the majority of the turbidity in the water during no flow conditions is associated with the fine clays that are transported from the south (O'Reagain et al. 2005). The impoundment is split into an upper and lower basin by a narrow neck of land. Water released from the dam enters the Burdekin River and discharges into the Great Barrier Reef lagoon approximately 200 km downstream.

1.6 Conclusion

Lakes and reservoirs provide sources of freshwater for urban, agricultural and industrial users as well as providing the means for recreational activities, fisheries and aquaculture. The responsibility to deliver water of sufficient quality for these users as well as maintaining the ecological amenity of the inland water bodies is given to water resource managers. To deliver these objectives it is critical that they monitor and maintain the quality of the water in their storage reservoirs.

Remote sensing is an essential tool to understand the spatial distribution of the factors involved in the ecology of aquatic systems but its application to tropical and sub-tropical inland impoundments, like those found in Northern Australia, has been limited. Before remote sensing can be used on Australian inland waters it is necessary to establish the validity, or otherwise, of the implicit assumptions and approximations usually used in inland water remote sensing. This was goal of this thesis. It was done by firstly, selecting three representative water bodies and measuring the optical properties of the water quality parameters. Secondly, by adapting existing atmospheric correction techniques to create an image based correction. Thirdly, by parameterising and modifying existing semi-analytic algorithms and finally, by applying and validating the algorithms for Northern Australian water bodies.

The results contained in this thesis will show that the environmental factors are sufficiently different in Northern Australia that remote sensing techniques for inland waters need to be adapted to a regional, rather than a global approach.

2. Specific Inherent Optical Properties Measurement

Key Points

- *Measured backscattering ratios deviated from the conventional Petzold turbid water ratio, with Burdekin Falls Dam being substantially higher and Wivenhoe Dam being marginally lower.*
- *There was sufficient intra-impoundment variation in the specific absorption and specific scattering of phytoplankton and tripton to require a well distributed network of measurement stations to fully characterise the SIOPs of the optical water quality parameters.*
- *Burdekin Falls Dam required more than one SIOP set to characterise the optical domains present.*

This chapter details the work associated with the measurement of the SIOPs in three inland water bodies. The SIOPs are necessary to simulate the reflectance spectra required to complete objective 2 as well as being essential input data in the completion of objectives 3 and 4.

The chapter shows that it is not possible to characterise the SIOPs for an Australian inland water body without using a well distributed network of measurement stations. Significant variation in the phytoplankton and tripton SIOPs were found for Burdekin Falls Dam and the SIOPs were allocated into domains using a hierarchical clustering algorithm (ITT Visual Information Solutions). After being allocated to domains the Burdekin Falls Dam SIOPs were combined by averaging to allow for the natural variation associated with biological and environmental parameters and the inherent measurement errors associated with each of the field and laboratory procedures. The chapter describes how the concentration of suspended material in the Fairbairn Dam water limited the applicability of preferred laboratory and *in situ* measurement methods. An alternative method used by Ma et al. (2009) for the retrieval of the particulate scattering from the *in situ* measured reflectance was applied after first being validated for the Burdekin Falls Dam water samples. The validation found that the ill-posed or ambiguous nature of the IOP -

reflectance relationship meant that the results of the Ma approach needed to be treated with caution (Defoin-Platel & Chami 2007).

2.1 Field Measurements

The field data were collected in the Australian winter of 2007 (July) and the spring of 2008 (October), which represent the beginning and end of a mid-year dry season for each catchment. None of the water bodies exhibited small scale patchiness in water colour. For the three years prior to the fieldwork Fairbairn Dam and Burdekin Falls Dam catchments had received their expected rainfall, but the Wivenhoe Dam catchment had received only 64% of its expected rainfall (Commonwealth Bureau of Meteorology 2009). The data obtained is summarised in Table 2-1.

Table 2-1 The *in situ* data measured at the three study sites.

Study site	Fieldwork dates	Measurement Stations	Water Quality Parameter Concentrations	SIOP Measurements	Spectroradiometric Observations
Wivenhoe Dam	3-4 July 2007	9	Yes	Yes	No
Fairbairn Dam	8-10 Oct 2008	10	Yes	Partial	Partial
Burdekin Falls Dam	13-15 Oct 2008	11	Yes	Yes	Yes

The following absorption properties were measured using the *WET Labs* absorption and attenuation meter (*ac-9*) (WET Labs Inc 2005), a Conductivity-Temperature-Depth (CTD) sensor and the laboratory analysis described below.

- total absorption coefficient a
- the absorption by CDOM a_{CDOM}
- the absorption by tripton a_{TR}
- the absorption by the phytoplankton a_{φ}
- the backscattering by the particulate matter b_{bp}

The *ac-9* is a dual beam spectrophotometer consists of two flow tubes to measure the attenuation and the absorption of the water.

The backscattering properties were measured using a *Hydroscat-6* backscattering sensor which emits light at six wavelengths and then measures the amount of light that is returned at a backscatter angle of 140° (Maffione & Dana 1997). Secchi depths (Kirk 1994) were recorded at each station.

Water samples were taken from approximately 0.3 m below the surface and kept cool for later laboratory measurement of tripton (the non-algal particles of the suspended particulate matter), chlorophyll *a* (CHL) concentration and coloured dissolved organic matter (CDOM) concentration. Due to the restricted craft size available for the field work it was not always practical to deploy the CTD, *ac-9* and *Hydroscat-6* instruments simultaneously within the water column. When the sampling craft was on station a small electric bilge pump was used to continuously sample the water from 0.5 m below the surface into a de-bubbling chamber. From there, it was gravity fed successively through a CTD sensor, *ac-9* and into a black PVC container (Figure 2-1). The *ac-9* measured at nine wavelengths (412, 440, 488, 510, 532, 555, 650, 676 and 715 nm). During the July 2007 fieldwork an *ac-9* with a 10 cm flow tube was used. Unfortunately this instrument was not available for the October 2008 field campaign and it was replaced for that fieldtrip with an *ac-9* with a 25 cm flow tube. The effect of this is discussed in §2.5.3. The *Hydroscat-6* was suspended in the black PVC container at Wivenhoe Dam and deployed directly into the lake at the other sites (Figure 2-2). For the Wivenhoe Dam measurements the *Hydroscat-6* measured at wavelengths of 420, 442, 488, 550, 676 and 700 nm. For the other water bodies the 700 nm wavelength was replaced with a wavelength of 852 nm. A separate measurement of the backscattering due to phytoplankton cells was not feasible. It was necessary to make an assumption about the ratio of the concentration of chlorophyll *a* to the dry weight of phytoplankton. A value of 1 $\mu g l^{-1}$ of chlorophyll *a* being approximately equal to 0.07 $mg l^{-1}$ total suspended material (TSM) was measured for Dutch lakes (Buiteveld 1995). The backscattering was apportioned using this same assumption. The validity of this assumption is discussed in §2.6.

Figure 2-1 The de-bubbler (left), the conductivity-temperature sensor (right) and the *WET Labs* absorption and attenuation meter (*ac-9*) (centre) being deployed.

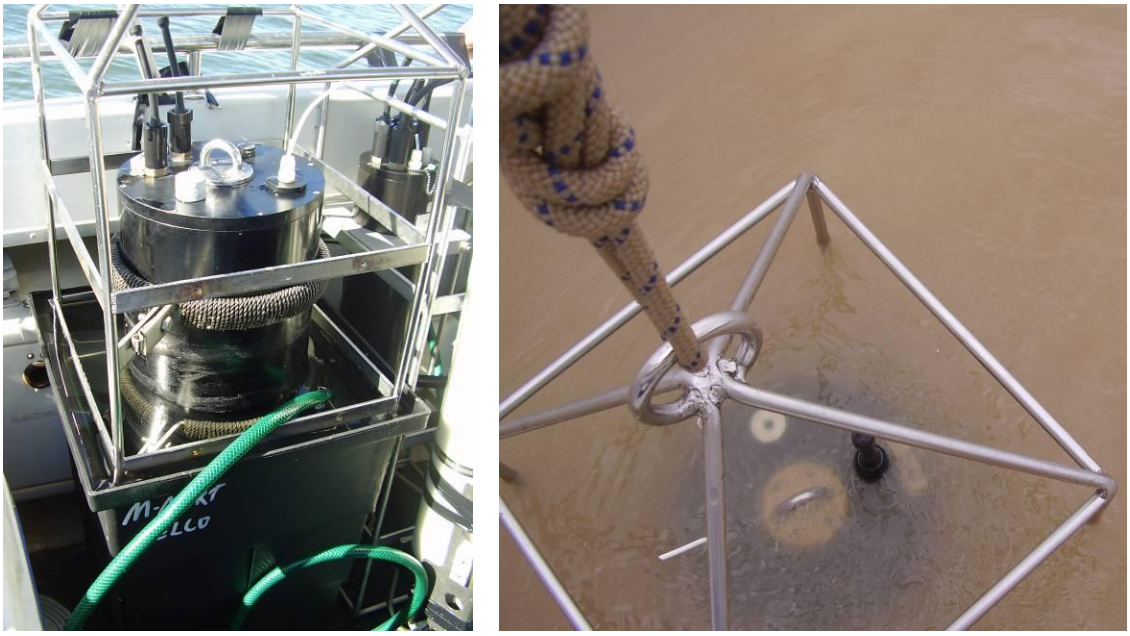

Figure 2-2 The *Hydroscat-6* being deployed while suspended in the black PVC container at Wivenhoe Dam (left) and being deployed directly into the lake at the other sites (right).

2.2 Laboratory Analysis

Ten litre water samples taken at each station were kept cool in opaque storage containers and were filtered on the day of collection. Prior to filtering the samples were agitated to ensure they were well mixed. The laboratory analysis was carried out by L. Clementson at CSIRO Marine and Atmospheric Research Laboratory in Hobart.

2.2.1. Phytoplankton Pigments

Water samples were filtered through a 25 mm diameter GF/F glass-fibre filter (Whatman, nominal pore size; 0.7 μm) until sufficient material was seen on the filter and the filter was then stored in liquid nitrogen. For Wivenhoe Dam the filtered volume ranged between 500 ml and 600 ml, for Burdekin Falls Dam the filtered volumes ranged between 250 ml and 400 ml and for Fairbairn Dam 100 ml was filtered.

Samples were extracted over 15-18 hours in an acetone solution before analysis by HPLC using a C_8 column and binary gradient system with an elevated column temperature following a modified version of the Van Heukelem and Thomas (2001) method. Pigments were identified by retention time and absorption spectrum from a photo-diode array detector and concentrations of pigments were determined from commercial and international standards (Sigma; DHI, Denmark).

2.2.2. Total Suspended Matter

Water samples were filtered through 47 mm diameter pre-weighed Whatman GF/F filters that had been prepared according to the MERIS calibration protocols (Tilstone et al. 2002) until sufficient material was seen on the filter. For Wivenhoe Dam the filtered volume ranged between 800 ml and 1200 ml, for Burdekin Falls Dam the filtered volume ranged between 700 ml and 1000 ml and for Fairbairn Dam between 200 ml and 250 ml was filtered. After the sample had been filtered, the filter paper was stored flat in a petri slide (Millipore). After collection, the filter papers were oven-dried at 60ºC until they achieved a constant weight and then weighed.

2.2.3. Particulate (Algal and Nonalgal) Absorption

Water samples were filtered through a 25 mm diameter GF/F glass-fibre filter (Whatman, with a pore size of 0.7 μm) until sufficient material was seen on the filter which was then stored flat in liquid nitrogen until analysis. For Wivenhoe Dam the filtered volume ranged between 500 ml and 600 ml, for Burdekin Falls Dam the filtered volumes ranged between 250 ml and 400 ml and for Fairbairn Dam 100 ml was filtered.

The optical density spectrum was measured over the 200–900 nm spectral range in 1.3 nm increments, using a GBC 916 UV/VIS dual beam spectrophotometer equipped with an integrating sphere. The pigmented material on the sample filter was then extracted using the Kishino et al. (1985) method and then the filter was remeasured to determine the optical density of the non-algal particles. The optical density due to phytoplankton was obtained by the difference between the optical density of the total particulate and non-algal fractions. The path length amplification effect due to the filter (so-called ‘‘β-factor’’) was corrected using the algorithm of Mitchell (1990). A more detailed description of the method is given by Clementson et al. (2001).

2.2.4. CDOM Absorption

Water samples were collected in glass bottles and filtered through a 0.22 μm polycarbonate filter (Millipore) using an all glass filtering unit. The filtrate was transferred to a clean glass bottle, preserved with sodium azide (0.5 ml of 10 g l^{-1} NaN_3 per 100 ml of sample) and kept cool and dark until analysis. Samples were allowed to equilibrate to room temperature before absorbance was measured from 200 to 900 nm using a 10-cm path length quartz cell in a GBC 916 UV/VIS spectro-photometer, with Milli-Q water (Millipore) as a reference. The CDOM absorption coefficients (m^{-1}) were calculated using the equation

$$a_{CDOM} = 2.3\frac{A_{CDOM}(l)}{l} \qquad (2\text{-}1)$$

where $A_{CDOM}\ (l)$ is the absorbance normalized to zero at 680 nm and l is the cell path length in metres. Spectral slopes are sensitive to the spectral range they are determined over, as subtle differences in the shape of spectra can be overlooked if a broad wavelength interval is used

(Helms et al. 2008). As the focus for this work was to characterise the CDOM absorption over the visible spectrum rather than provide compositional insights, the spectra were then fitted with a single exponential function over the range 350–680 nm.

2.3 Backscattering Corrections

Simultaneous measurement of the absorption and attenuation of the water was required, as the raw *Hydroscat-6* backscatter observations contain systematic errors associated with the water and water quality parameter absorption. Similarly, because the absorption of water is affected by the salinity and temperature of water (Pegau & Zaneveld 1993) corrections must be made to the *ac-9* absorption measurements before they can be used to correct backscatter observation.

2.3.1. Temperature and Salinity Correction

The effect of temperature and salinity on the absorption of water is linear, but wavelength dependent. The absorption co-efficient measured by the *ac-9* was characterised by Pegau et al.(1997) as:

$$a_m^{TS}(\lambda,T,S) = a_m(\lambda,T_r,0) + \psi_T(T-T_r) + \psi_S S \quad (2\text{-}2)$$

where T is the temperature, T_r is a reference temperature and S is the salinity in Practical Salinity Units (PSU). The PSU of a sample of water is defined in terms of the ratio of electrical conductivity of the sample to that of a potassium chloride (KCl) solution. The ψ values are linear temperature (T) and salinity (S) slopes. As the three study sites are freshwater impoundments the effect of salinity was negligible and a correction was not applied. The values for the temperature slope were taken to be those reported by Pegau et al. (1997). The temperature effect is negligible except at the red and NIR wavelengths but as these values are used to correct scattering at all wavelengths (see §2.3.2) there is an indirect effect on all wavelengths.

As the scattering coefficient is only affected by temperature or salinity in the ultraviolet wavelengths the effect on the attenuation coefficient in the visible and NIR regions is the same as the absorption coefficient (WET Labs Inc 2005).

2.3.2. Scattering Correction

The dual beam spectrophotometer consists of two flow tubes to measure the attenuation and the absorption. In the non-reflecting attenuation flow tube, all photons that are scattered are absorbed by the sides of the tube, whereas the absorption tube is highly reflective so that those photons are reflected back into the detector at the end of the tube. This means that photons are only removed from the stream by absorption by the medium. In practice photons that are scattered backwards do not reach the detector. There are however, some losses due to the imperfect reflection of the flow tube and some photons reach the end of the tube but evade the detector (Kirk 1992; Mueller et al. 2003).

Zaneveld et al. (1994) suggested three scattering correction methods. The first assumes that the absorption in the near infrared (NIR) (*a(715)*) for the water quality parameters is negligible and the absorption is entirely due to pure water. The second approach assumes that the scattering error is a wavelength independent fraction (ε) of the measured scattering coefficient and so calculates the value for the NIR and applies this value to all wavelengths. There is some confusion in the literature as to accepted values. Sources recommend that a value of $\varepsilon \approx 0.14$ be used for predominantly biological particles and $\varepsilon \approx 0.18$ for waters dominated by suspended sediments (Mueller et al. 2003; WET Labs Inc 2005) citing work by Kirk (1992). However, Kirk's paper reports values for a tube reflectance of 94% and an acceptance angle for the detector of 180° of $\varepsilon \approx 0.160$ be used for predominantly biological particles and $\varepsilon \approx 0.121$ for waters dominated by suspended sediments. The values will vary with the design of the flow tube but since ε is dependent on the scattering phase function of the medium it is unlikely that the relative proportions should change. The third method negates the need to assume an *a priori* scattering error and calculates the proportional error in the NIR and applies that to all wavelengths. The correction becomes:

$$a(\lambda) - a_w(\lambda) = a_m^{TS}(\lambda) - \left[\frac{a_m^{TS}(\lambda_{NIR})}{c_m^{TS}(\lambda_{NIR}) - a_m^{TS}(\lambda_{NIR})}\right]\left[c_m^{TS}(\lambda) - a_m^{TS}(\lambda)\right] \quad (2\text{-}3)$$

This method still assumes that the absorption in the NIR (*a(715)*) for the water quality parameters is negligible but allows for the scattering correction to change with wavelength and

the material present. Figure 2-6 shows that the NIR absorption assumption may not be true for all the sample stations. The first method is attractive due to its simplicity but the third method, while requiring simultaneous measurement of absorption and attenuation, should be the most accurate. Both first and third methods were applied and their effect on the final backscatter results was compared.

2.3.3. Correction for Raw *Hydroscat-6* Data

In high light-attenuating waters the measured backscatter can be appreciably lower than the true backscatter. This effect can be corrected by:

$$b_b(\lambda) = \sigma(K_{bb}) b_{bu}(\lambda) \qquad \text{(Dana \& Maffione 2002)} \tag{2-4}$$

where b_b and b_{bu} are the corrected and uncorrected backscatter respectively.

The factor σ is calculated by:

$$\sigma(K_{bb}) = k_1 \exp(k_{\exp} K_{bb}) \tag{2-5}$$

where $K_{bb} = a + 0.4b$ and with k_1 set by calibration so the value $\sigma(K_{bbw}) = 1$ where K_{bbw} is the attenuation, excluding that of pure water, of the water in which the instrument was calibrated (HOBILabs Inc 2008).

2.4 Calculation of SIOPs

The chlorophyll *a* specific absorption co-efficient (a^*_{φ}) was obtained by normalising the absorption due to phytoplankton by the chlorophyll *a* concentration. Similarly, the tripton mass specific absorption co-efficient (a^*_{TR}) was obtained by normalising the absorption due to non-algal particles by the weight of the TSM less the weight of the phytoplankton. The phytoplankton dry weight was estimated using the assumption that 1 μgl^{-1} of chlorophyll *a* was approximately equal to 0.07 mgl^{-1} TSM (Buiteveld 1995).

The specific absorption spectra for CDOM were fitted to the model

$$a^*_{CDOM} = a^*_{CDOM}(\lambda_0) \exp(-S(\lambda - \lambda_0)) \tag{2-6}$$

were λ_0 = 440nm and $a^*_{CDOM}(\lambda_0)$ = 1 by definition and *S* is the spectral slope.

The specific absorption spectra for tripton were fitted to the model

$$a^*_{TR} = a^*_{TR}(\lambda_0)\exp(-S(\lambda - \lambda_0)) \quad (2\text{-}7)$$

with λ_0 = 550nm.

The specific backscattering spectra were calculated by normalising the apportioned tripton and phytoplankton fractions by their respective dry weights. The specific backscattering of tripton and phytoplankton were fitted to the standard model (Morel & Prieur 1977):

$$b^*_b(\lambda) = b^*_b(\lambda_0)\left(\frac{\lambda}{\lambda_0}\right)^{\gamma}, \quad \lambda_0 = 542\text{nm} \quad (2\text{-}8)$$

2.5 Results

2.5.1. Wivenhoe Dam

The SIOPs were sampled at the stations shown in Figure 2-3.

Water Quality Parameter Concentrations

SEQWater supplied monitoring data for the 5 years previous to the June 2007 fieldwork. At each station an extra water sample was taken and processed by SEQWater in their standard fashion to derive estimates of chlorophyll *a* and tripton. SEQWater does not measure CDOM absorption. The range of the measured chlorophyll *a* values was 5.0 – 42.7 μgl^{-1} for CSIRO and 5 – 60 μgl^{-1} for SEQWater. The range of the measured tripton was 0.9 – 11.2 mgl^{-1} for CSIRO and 2 - 11 mgl^{-1} for SEQWater. The measured CDOM range was 0.36 – 0.65 m^{-1} and the Secchi depth range was 0.9 – 2.5 m. A table showing the individual measurements is in Appendix A.

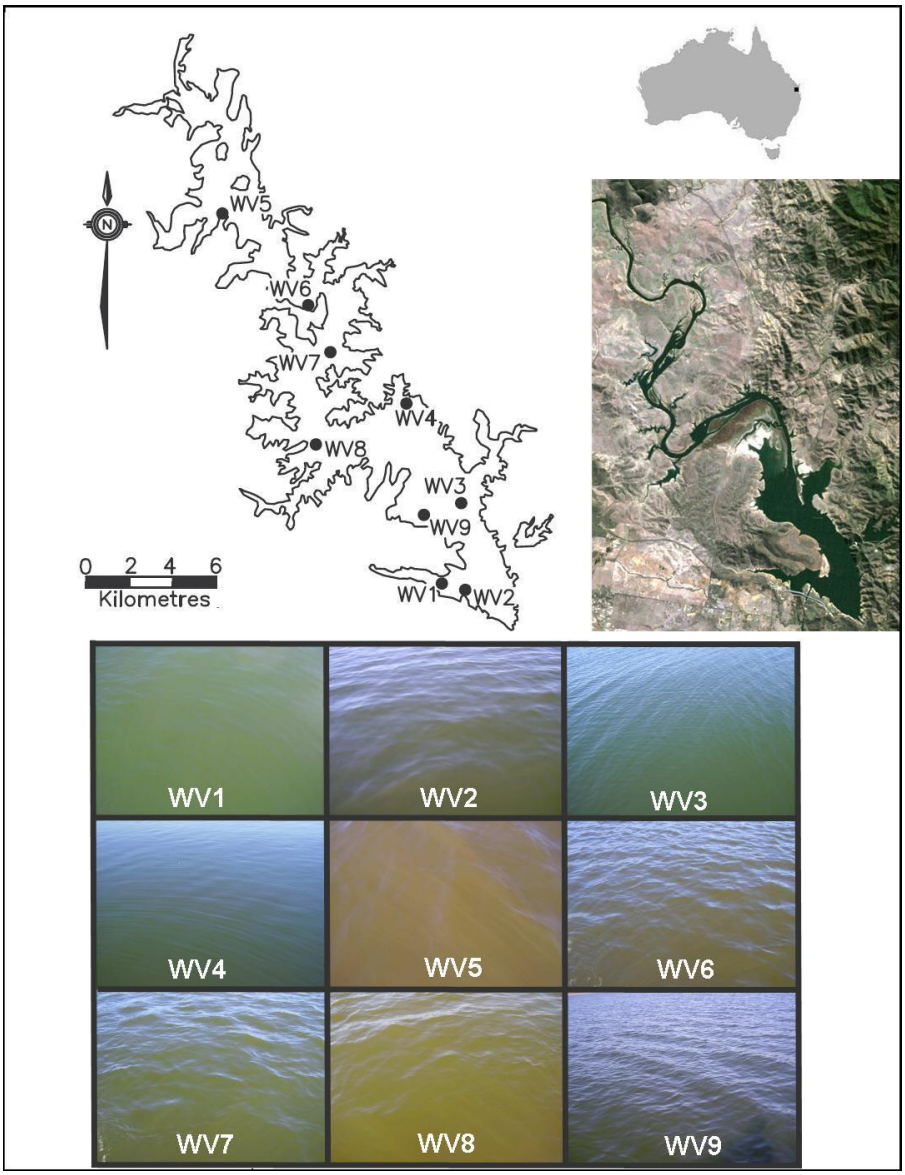

Figure 2-3 Location of the SIOP sample sites for the July 2007 fieldwork activities on Wivenhoe Dam, Australia. The upper left hand image shows the calculated full supply level and the upper right hand side shows a true colour Landsat 5 Thematic Mapper (TM) image, at the same scale captured on 16th July 2007. Note the reduced water extent at the time of the fieldwork activities. The lower section of the figure shows photographs of the sample sites taken at the time of sampling.

Phytoplankton Absorption

The laboratory measured absorption spectra for phytoplankton are shown in Appendix A and the corresponding specific absorption spectra shown in Figure 2-4 below.

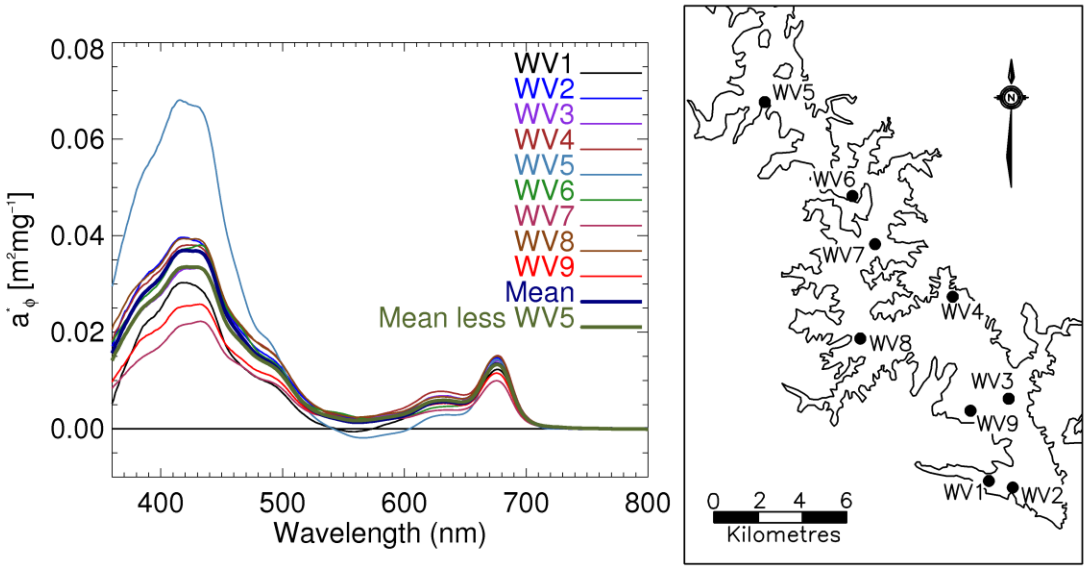

Figure 2-4 Plot of specific absorption for phytoplankton for the Wivenhoe Dam stations. Two mean spectra are shown. The first is the mean of all stations and the second is the mean excluding the anomalous station WV5 result. Station WV5 may represent a local, atypical phytoplankton assemblage that does not warrant inclusion as an IOP set in its own right.

CDOM Absorption

The laboratory measured absorption spectra for CDOM are shown in Appendix A and the corresponding specific absorption spectra shown in Figure 2-5.

There is very little variation in the CDOM absorption for the Wivenhoe Dam sample stations and hence one model of CDOM absorption should be sufficient to cover the entire storage.

There was very little variation between stations with the spectral slopes being in the range of 0.0173 – 0.0190 nm^{-1} with a mean spectrum slope of 0.0185 nm^{-1}. This is marginally outside the range of 0.012-0.018 nm^{-1} for a variety of Australian inland waters reported by Kirk (1994). The wavelength range over which these slopes were calculated was not described. The full list of spectral slopes is shown in Table 2-2.

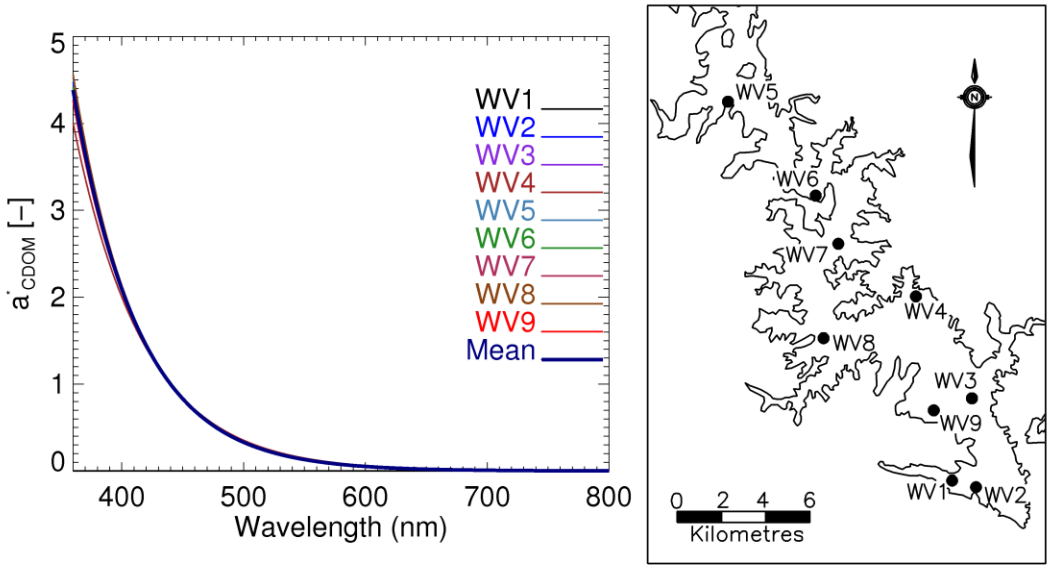

Figure 2-5 The specific absorption for CDOM for the Wivenhoe Dam stations. The mean spectrum is the mean of all stations.

Tripton Absorption

The laboratory measured absorption spectra for tripton are shown in Appendix A and the corresponding specific absorption spectra shown in Figure 2-6.

The spectral slopes ranged from 0.0080 – 0.0088 nm^{-1} with a mean spectrum slope of 0.0085 nm^{-1} and $a^*_{TR}(550)$ ranged from of 0.035 – 0.145 m^2g^{-1}. The full list of parameters is shown in Table 2-2. There is very little variation present in the slope of the absorption curves but WV1 has a substantially larger $a^*_{TR}(\lambda_0)$ value. This difference may be an artefact of the very low tripton measurement for this station as small measurement errors will have a large effect on the specific absorption when the tripton concentration is very low. The mean slope and $a^*_{TR}(\lambda_0)$ for the whole group and the group excluding WV1 is listed in Table 2-3.

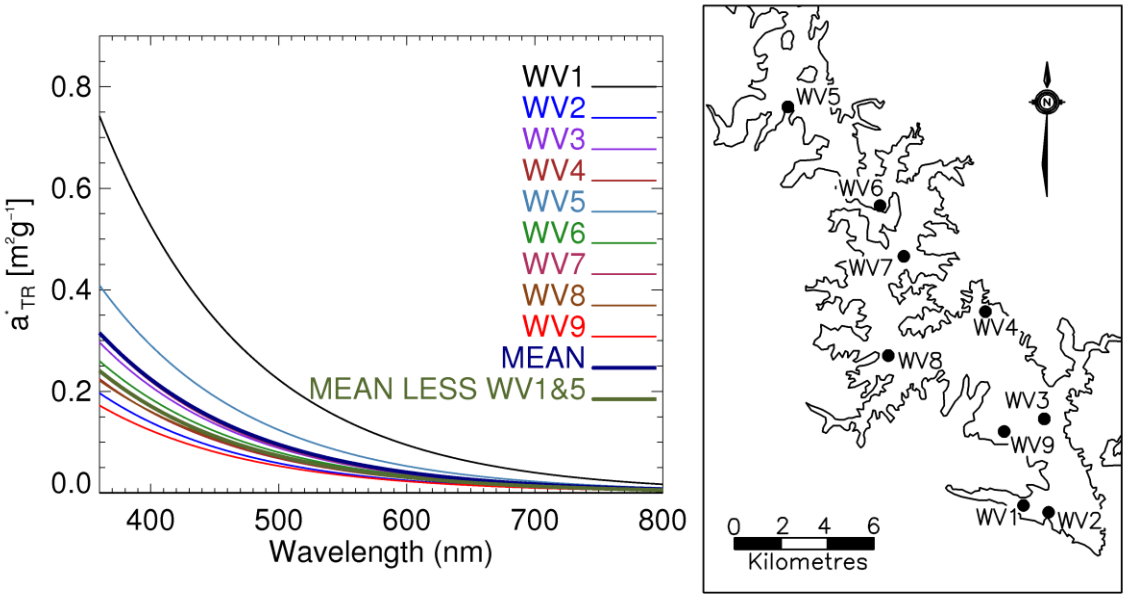

Figure 2-6 The specific absorption for tripton for the Wivenhoe Dam stations. Two mean spectra are shown. The first is the mean of all stations and the second is the mean excluding the anomalous stations WV1 and WV5. The anomalous spectra represent either valid measurements of a minor sediment sources or corrupted measurement of the dominant sediment source. In either case it they do not warrant inclusion as an IOP set in their own right.

Table 2-2 The mean fitted parameters for the tripton and CDOM absorption for the Wivenhoe Dam observation stations.

Station Name	CDOM slope (S) (nm^{-1})	$a^*_{TR}(\lambda_0)$ (m^2g^{-1})	Tripton slope (S) (nm^{-1})
WV1	0.0185	0.145	0.0086
WV2	0.0187	0.038	0.0087
WV3	0.0189	0.057	0.0086
WV4	0.0173	0.044	0.0085
WV5	0.0189	0.081	0.0085
WV6	0.0186	0.052	0.0084
WV7	0.0181	0.059	0.0088
WV8	0.0190	0.048	0.0080
WV9	0.0181	0.035	0.0084

Table 2-3 The mean fitted parameters for the tripton absorption for the Wivenhoe Dam observation stations.

Specimen Group	$a^*_{TR}(\lambda_0)$ (m^2g^{-1})	Slope (S) (nm^{-1})
Mean	0.062	0.0085
Mean less WV1 & WV5	0.048	0.0085

Specific Backscattering Spectra

The *Hydroscat-6* measurements were reduced using the corrections described in §2.3.1-2.3.3. The measured parameters for tripton are given in Table 2-4 and phytoplankton in Table 2-5. A second calculation of the backscattering parameters, in the manner of Oubelkheir et al. (2006), was made after discarding the values at 440 and 676 nm because of the anomalous effects of absorption by chlorophyll *a* at these wavelengths. The four wavelength fitting parameters are shown for reference only, the six wavelength fit were used in the SIOP sets.

Table 2-4 The parameters associated with the tripton backscattering in Wivenhoe Dam. The data has been processed using all six *Hydroscat-6* wavelengths and then the four wavelengths used by Oubelkheir et al. (2006).

Station	All Wavelengths				Four wavelengths			
	γ	$b^*_{bTR}(\lambda_0)$	Mean $b_{bp}:b_p$	R^2	γ	$b^*_{bTR}(\lambda_0)$	Mean $b_{bp}:b_p$	R^2
WV1	-0.91	0.021	0.014	0.97	-0.84	0.021	0.014	0.97
WV2	-1.00	0.008	0.014	0.87	-0.73	0.008	0.015	0.99
WV3	-0.92	0.014	0.014	0.99	-0.89	0.014	0.014	1.00
WV4	-0.88	0.013	0.013	0.99	-0.88	0.013	0.013	0.98
WV5	-0.49	0.009	0.013	0.74	-0.36	0.009	0.013	0.57
WV6	-0.76	0.008	0.013	0.94	-0.67	0.008	0.013	0.93
WV7	-0.86	0.008	0.013	0.92	-0.72	0.008	0.013	0.91
WV8	-0.93	0.010	0.014	0.99	-0.87	0.009	0.013	0.99
WV9	-0.93	0.007	0.013	0.98	-0.93	0.007	0.013	0.98

Table 2-5 The parameters associated with the phytoplankton backscattering in Wivenhoe Dam. The data has been processed using all six *Hydroscat-6* wavelengths and then the four wavelengths used by Oubelkheir et al. (2006).

Station	All Wavelengths			Four wavelengths		
	γ	$b^*_{b\varphi}(\lambda_0)$	R^2	γ	$b^*_{b\varphi}(\lambda_0)$	R^2
WV1	-0.91	0.002	0.97	-0.84	0.002	0.97
WV2	-1.00	0.001	0.87	-0.73	0.001	0.99
WV3	-0.92	0.001	0.99	-0.89	0.001	1.00
WV4	-0.88	0.001	0.99	-0.88	0.001	0.98
WV5	-0.49	0.001	0.74	-0.36	0.001	0.57
WV6	-0.76	0.001	0.94	-0.67	0.001	0.93
WV7	-0.86	0.001	0.92	-0.72	0.001	0.91
WV8	-0.93	0.001	0.99	-0.87	0.001	0.99
WV9	-0.93	0.001	0.98	-0.93	0.001	0.98

Once again the high value for $b^*_{bTR}(\lambda_0)$ for WV1 is more likely due to measurement error than any significant difference in the tripton itself. As with the phytoplankton and tripton absorption the values for WV5 are the exception. Previous isotopic and statistical analysis of the Wivenhoe Dam sediments showed that the area around WV5 was dominated by sediment produced from the igneous Neara Volcanic rocks, whereas the rest of the basin is dominated by sediment produced from the Esk Formation sandstones and shales (Douglas et al. 2007). Therefore it is not unreasonable to suspect that the IOPs of the suspended material may be different for WV5. Alternatively it could be argued that the high chlorophyll *a* concentration indicates a greater proportion of larger particles associated with phytoplankton which leads to a flattening of the backscattering spectra. This argument is undermined by the similar water quality parameter concentrations at WV6 showing a less anomalous result. Nevertheless, the relatively poor correlation coefficient of the fit suggests that there is a greater uncertainty in this measured value than the others. Notwithstanding whether it is a valid measurement of a minor sediment source or a corrupted measurement of the dominant sediment source the WV5 SIOP measurement does not warrant inclusion as an IOP set in its own right.

IOP Set

The accuracy of semi-analytic remote sensing algorithms relies on their correct parameterisation with SIOP sets that are appropriate for the water pixel being inverted. As horizontal gradients in SIOPs within a water body can exist in some cases, the fit between the measured spectrum and the forward model spectrum is used to select the most appropriate SIOP set from a reference group (Dekker et al. 2004; Wettle & Brando 2006). If this approach is to be used then it is first necessary to allocate *in situ* measured SIOP spectra into domains based on whether the spectra are likely to be different SIOP populations or are samples from the same SIOP population. There is natural within-population variation associated with biological and environmental parameters and inherent measurement errors associated with each of the field and laboratory procedures. Once the SIOP spectra are allocated into domains, the spectra were combined by averaging to rationalise the number of SIOP sets.

Once suspected unreliable measurements such as WV1 and WV5 were omitted, the water of Wivenhoe Dam could be characterised by the single SIOP set that is shown in Figure 2-7. This set was used in simulations and algorithm testing described in Chapter 4.

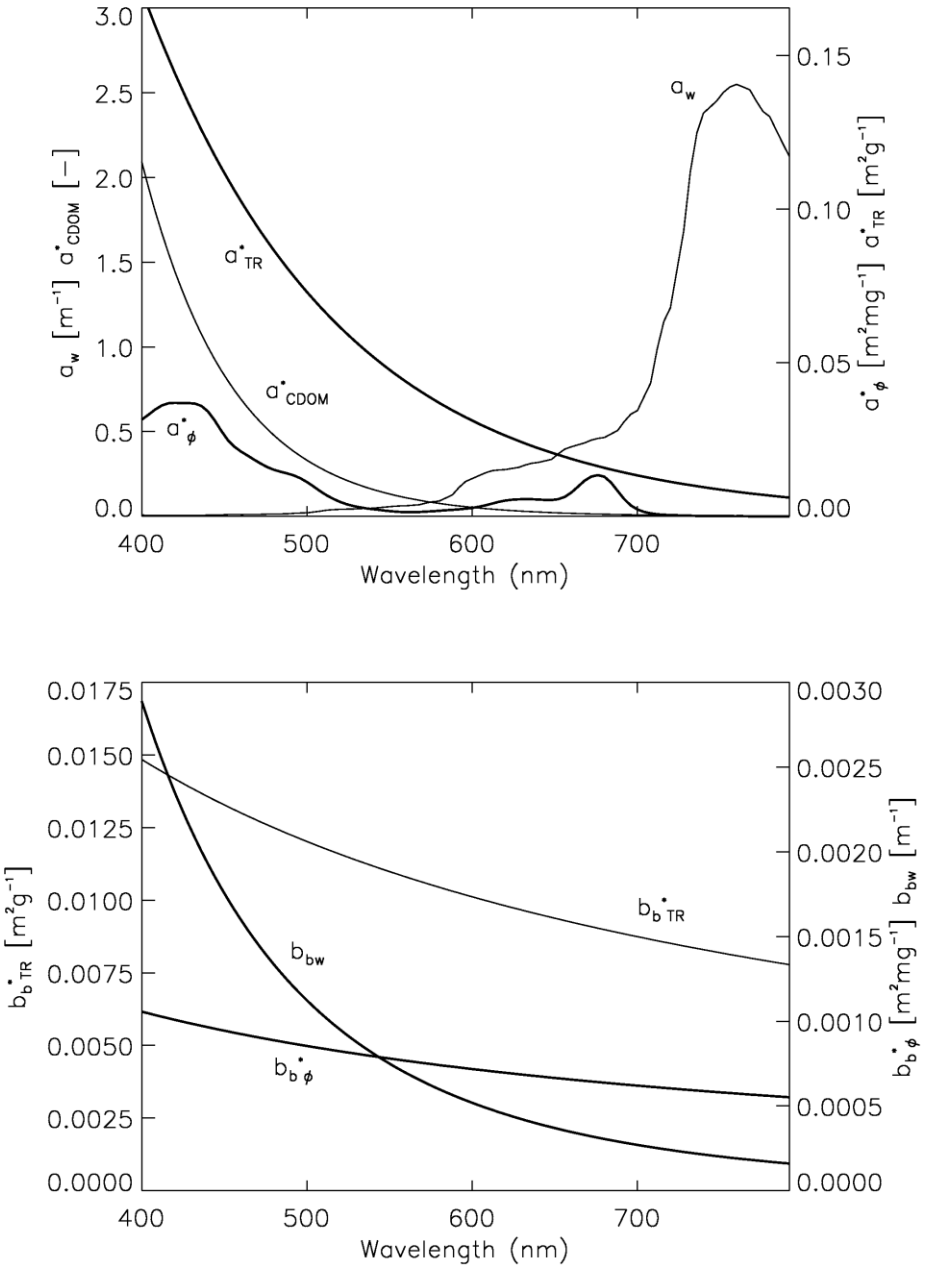

Figure 2-7 Average SIOPs for Wivenhoe Dam: The upper graph shows the spectral absorption of water (*w*) and the chlorophyll *a* specific absorption spectra of phytoplankton (ϕ), tripton (*TR*) and coloured dissolved organic matter (*CDOM*). The lower shows the spectral backscattering of water (*w*) and the specific backscattering spectra of chlorophyll *a*(ϕ) and tripton (TR).

Representation of Phytoplankton Absorption

The direct comparison of phytoplankton absorption spectra is limited by the predominance of reporting just the spectral graphs without including the underlying numerical spectral data values. The other SIOPs for an optical domain can be described analytically making it easier for other researchers to use the SIOP set for comparison. The phytoplankton specific absorption curves are too complex to describe analytically and so many researchers either plot or refer to the size of prominent absorption features. The exception is those who adopt the Bricaud et al. (1995) approach. Perhaps an impediment to the wider adoption of this approach has been the large number of parameters (152) required to describe a spectrum. Alternatively, it has been shown that the phytoplankton specific absorption spectra can be modelled as the sum of 10-13 Gaussian curves (Hoepffner & Sathyendranath 1991; Lohrenz et al. 2003). Such an approach has been used in the past by researchers who have been interested in the connection between these curve amplitudes, full width half maximums (FWHMs) and centres and their relationship to auxiliary pigments and species. Notwithstanding these possibilities, on a more prosaic level a list of those three factors will allow any reported phytoplankton specific absorption spectra to be recreated accurately without resorting to scaling from spectral figures or a very large table of parameters.

Each of the final phytoplankton specific absorption spectra were decomposed into thirteen Gaussian bands of the following form:

$$f(\lambda) = a_0 \exp\left[-\ln 2\left(\frac{2(\lambda-\lambda_0)}{\Delta\lambda_{1/2}}\right)\right]^2 \qquad (2\text{-}9)$$

where a_0 is the peak amplitude, λ_0 is the band centre and $\Delta\lambda_{½}$ is the FWHM. The band centres were held constant to the initial values of Lohrenz et al. (2003) and the other two parameters were varied to obtain the optimal fit using the least squares criterion. The results are shown in Table 2-6 and Figure 2-8.

Table 2-6 The optimal modelled parameters describing the phytoplankton specific absorption spectra for Wivenhoe Dam.

λ_0 (nm)	a_0 (m^2mg^{-1})	FWHM (nm)	λ_0 (nm)	a_0 (m^2mg^{-1})	FWHM (nm)
376	0.05132	30.5	586	0.00212	38.5
409	0.02310	27.6	622	0.00487	34.3
435	0.03038	35.1	642	0.00306	24.8
461	0.00025	8.7	652	0.00083	16.0
464	0.00889	28.3	675	0.01315	29.2
490	0.01220	44.8	701	0.00058	53.1
539	0.00214	41.5			

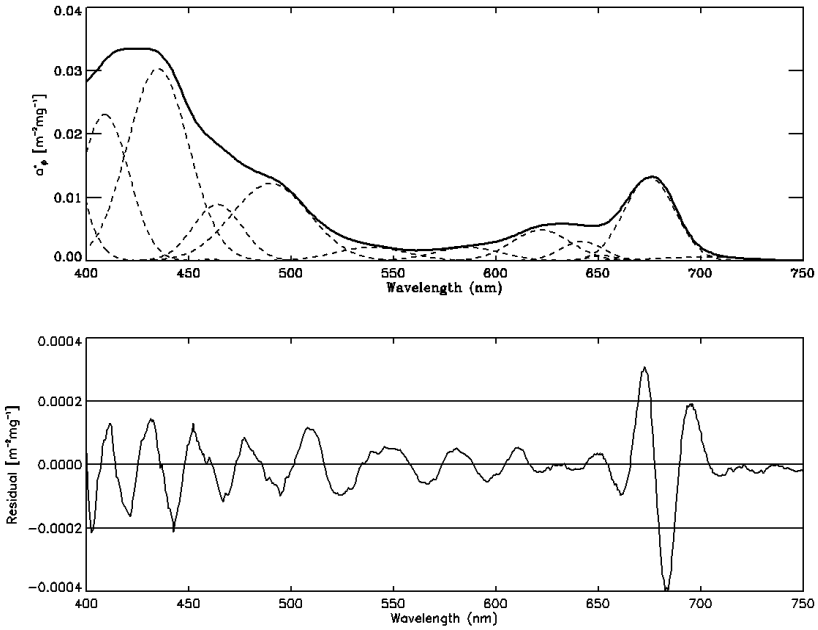

Figure 2-8 The decomposed Wivenhoe Dam specific phytoplankton absorption spectrum. The upper plot shows the Wivenhoe Dam specific phytoplankton absorption spectrum (bold) and the thirteen Gaussian bands into which it was decomposed (dashed). The lower plot shows the difference between the reconstructed and original spectrum.

2.5.2. Burdekin Falls Dam

The SIOPs were sampled at the stations shown in Figure 2-9.

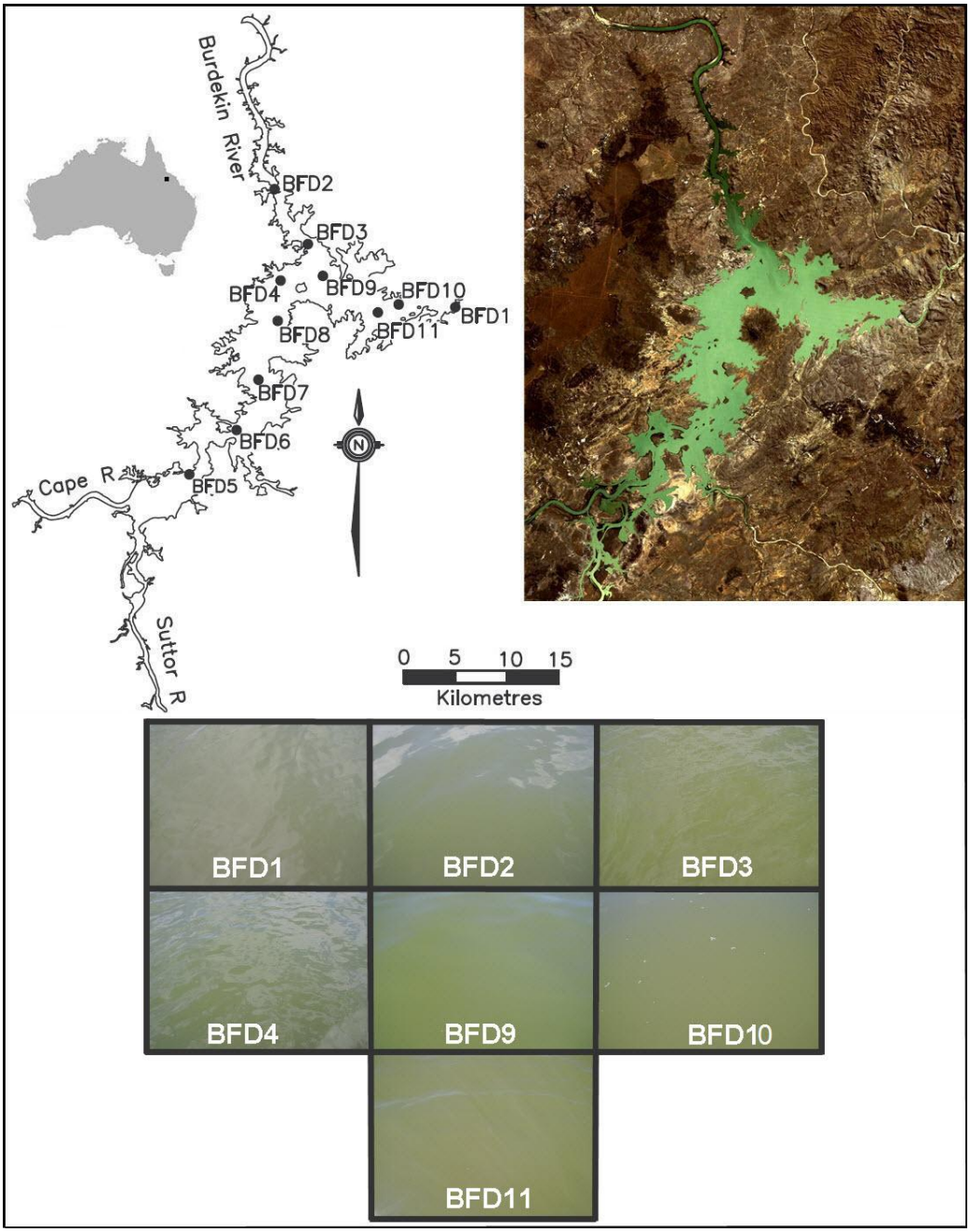

Figure 2-9 Location of the SIOP sample sites for the October 2008 fieldwork activities on Burdekin Falls Dam, Australia. The upper left hand image shows the calculated full supply level and the upper right hand image shows a Landsat 5 TM true colour image at the same scale as the map, captured on 22nd August 2008. The lower section of the figure shows photographs of the sample sites taken at the time of sampling. No photographs were taken of Stations 5-8 due to a camera malfunction.

Water Quality Parameter Concentrations

The range of the measured chlorophyll *a* values was 2.8 – 7.7 μgl^{-1}, the range of the measured tripton was 5.6 – 10.3 mgl^{-1}, the measured CDOM range was 0.88 – 1.21 m^{-1} and the Secchi depth range was 0.9 – 1.3 m. A table showing the individual measurements is shown in Appendix A.

Phytoplankton Absorption

The laboratory measured absorption spectra for phytoplankton in Burdekin Falls Dam are shown in Appendix A with the corresponding specific absorption spectra shown in Figure 2-10.

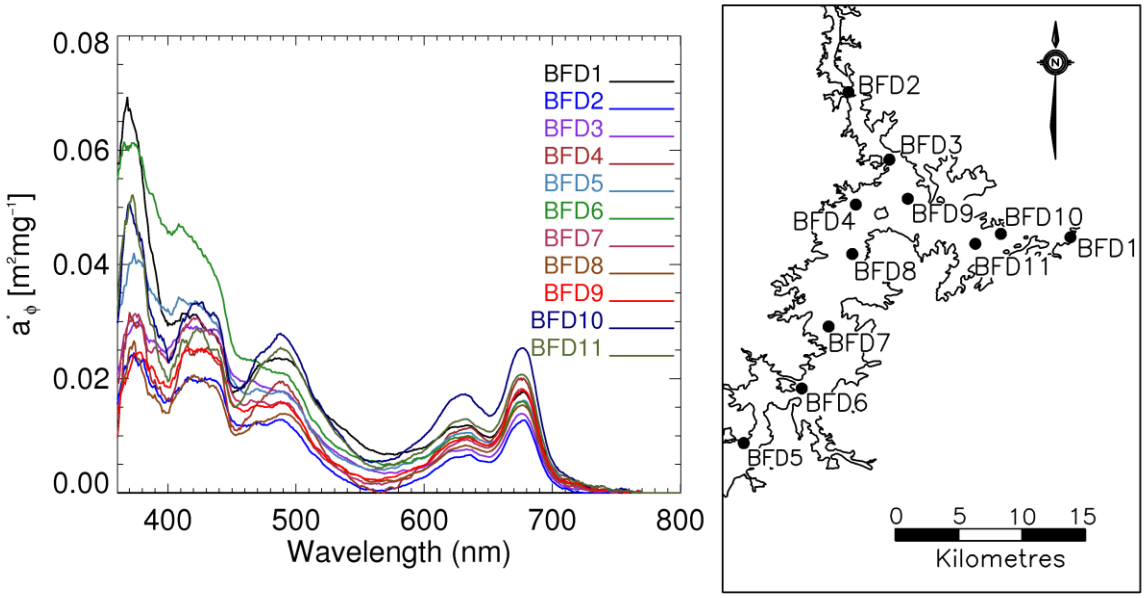

Figure 2-10 The specific absorption for phytoplankton for the Burdekin Falls Dam stations.

Different algal groups, and also different physiological states of the same alga, differ quantitatively and qualitatively in pigment composition and hence the specific absorption varies widely between and within organisms (Davies-Colley et al. 1986; Sathyendranath et al. 1987). It is clear from Figure 2-10 that there are differences in the phytoplankton assemblages within the water body. The absorption maxima observed (ca. 630nm) indicate that the phytoplankton assemblages were dominated by cyanobacteria (Richardson 1996). Although cyanobacteria are capable of regulating their buoyancy, studies have shown that the dynamics of the mixed layer is the dominant factor in the phytoplankton vertical distribution (Ibelings et al. 1991; Mitrovic et al.

2001). As the water samples were taken in the same time period on each day and the prevailing weather conditions were similar it seems unlikely that this is the cause of the variation. The spectral angle mapper algorithm (SAM) was used to calculate the similarity between eleven measured spectra over the 200–900 nm spectral range in 1.3 nm increments. The SAM angle was then used as the parameter in the IDL hierarchical clustering algorithm (ITT Visual Information Solutions) using a weighted pair wise average. The clusters are shown in Figure 2-11.

The phytoplankton absorption spectra clustered into three groups which broadly represent the Suttor River basin (Stn 5, 6 and 1), the lower basin (Stn 10 and 11) and the Burdekin River Basin (Stns 2, 3, 4, 7, 8 and 9). If the spectra were grouped strictly on location, BFD1 would be grouped with the other lower basin sites.

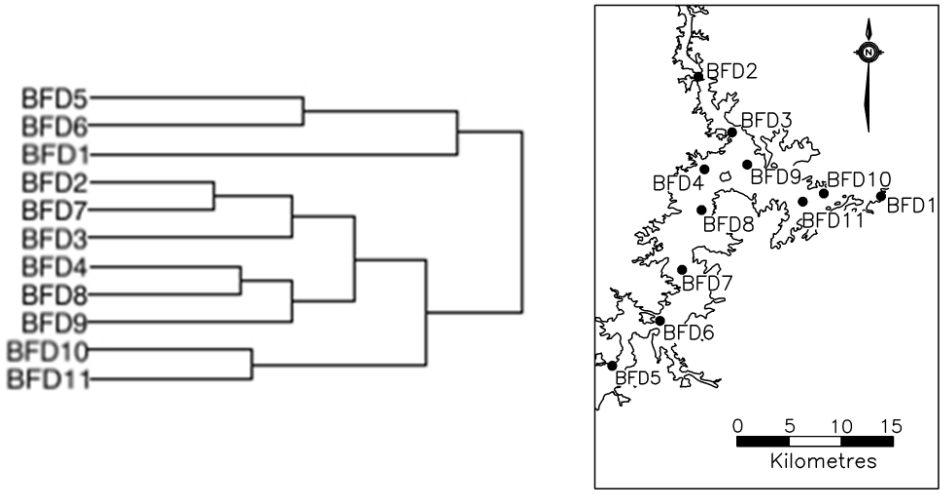

Figure 2-11 The dendrogram produced by the hierarchical clustering algorithm using a weighted pair wise average and the full resolution phytoplankton absorption spectra for the eleven Burdekin Falls Dam stations.

Figure 2-12 shows that a number of the significant differences between the groups occur in parts of the light spectrum that are outside of the MERIS bands. The same analysis was run using spectra that had been convolved with the MERIS bands. The result of that cluster analysis is shown in Figure 2-13. In this case the spectra resolve into two groups with less geographic bias.

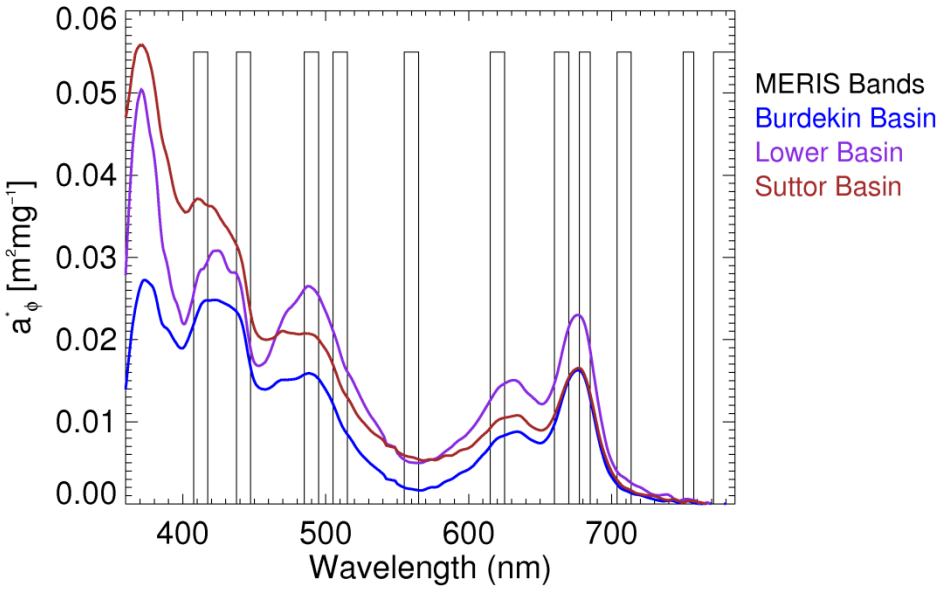

Figure 2-12 The specific absorption for phytoplankton groups for the Burdekin Falls Dam stations.

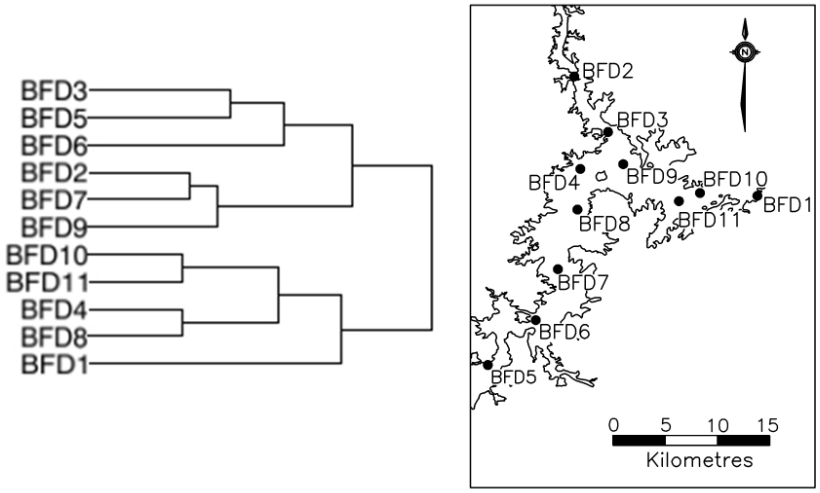

Figure 2-13 The dendrogram produced by the hierarchical clustering algorithm using a weighted pair wise average and the MERIS band convolved phytoplankton absorption spectra for the eleven Burdekin Falls Dam stations.

Mean spectra for the two groups are shown in Figure 2-14.

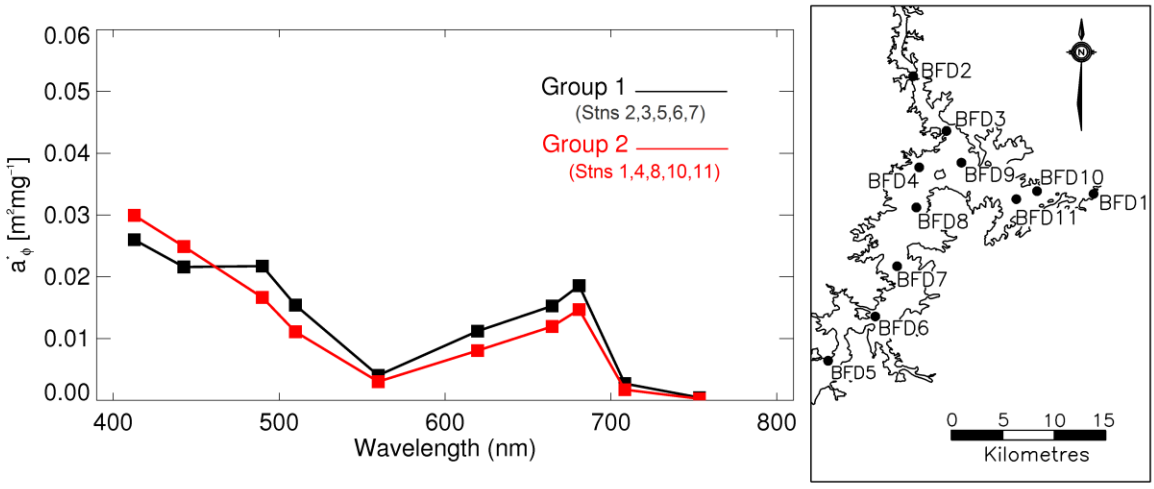

Figure 2-14 The specific absorption for phytoplankton groups for the Burdekin Falls Dam stations when the clustering is done using spectra that have been convolved to the MERIS band widths and positions. Group 1 is the average of Stations 2, 3, 5, 6, 7 and 9 and Group 2 is the average of Stations 1, 4, 8, 10 and 11.

CDOM Absorption

The results of the laboratory measurement of the CDOM absorption for the Burdekin Falls Dam stations are shown in Appendix A and those measurements converted to specific absorption spectra are shown in Figure 2-15.

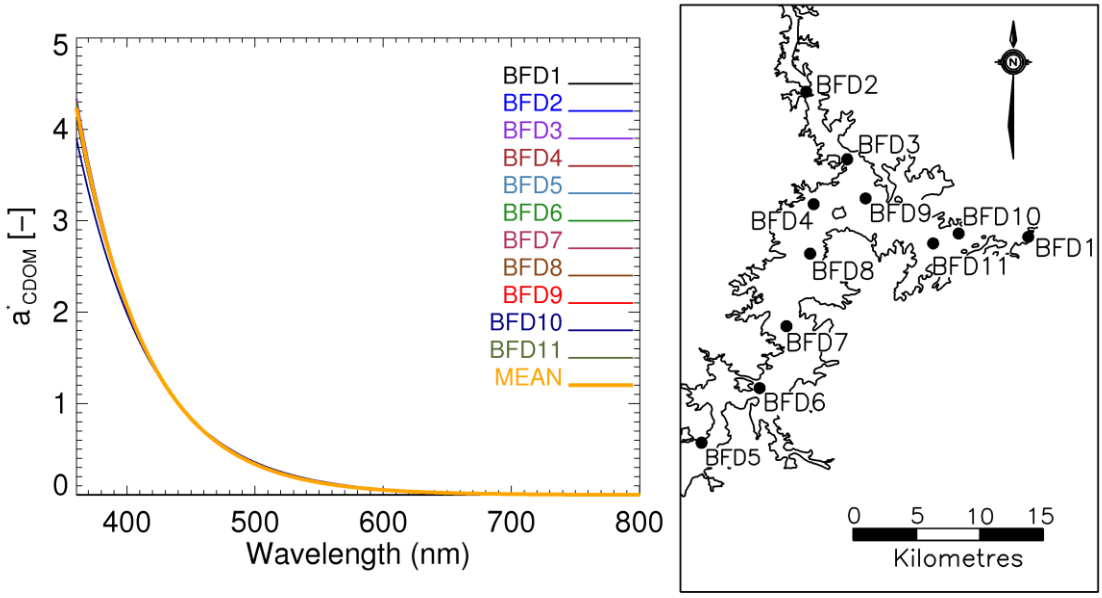

Figure 2-15 The specific absorption for CDOM for the Burdekin Falls Dam stations. The mean spectrum is the mean of all stations.

It is clear that there is very little variation in the CDOM absorption for the Burdekin Falls sample stations and hence one model of CDOM absorption should be sufficient to cover the entire storage. The spectral slopes ranged from 0.0171 – 0.0185 nm^{-1} with a mean spectrum slope of 0.0182 nm^{-1}. The full list of spectral slopes is shown in Table 2-7.

Tripton Absorption

The results of the laboratory measurement of the tripton absorption for the Burdekin Falls stations are shown in Appendix A and those measurements converted to specific absorption spectra are shown in Figure 2-17.

The spectral slopes for the specific tripton absorption ranged from 0.0123 - 0.0153 nm^{-1} with a mean spectrum slope of 0.0136 nm^{-1} and $a^*_{TR}(550)$ ranged from 0.014 – 0.022 m^2g^{-1} with a mean value of 0.019 m^2g^{-1}. The full list of parameters is shown in Table 2-7.

Table 2-7 The mean fitted parameters for the tripton and CDOM absorption for the Burdekin Falls Dam observation stations.

Station Name	CDOM slope (S) (nm^{-1})	$a^*_{TR}(\lambda_0)$ (m^2g^{-1})	Tripton slope (S) (nm^{-1})
BFD1	0.0179	0.014	0.0153
BFD2	0.0185	0.020	0.0137
BFD3	0.0184	0.021	0.0127
BFD4	0.0183	0.020	0.0127
BFD5	0.0184	0.020	0.0129
BFD6	0.0183	0.020	0.0135
BFD7	0.0182	0.020	0.0129
BFD8	0.0181	0.018	0.0150
BFD9	0.0184	0.016	0.0152
BFD10	0.0171	0.021	0.0123
BFD11	0.0184	0.019	0.0131

The modelled slope (S) and $a^*_{TR}(\lambda_0)$ were used as dimensions in a clustering process. This split the measurements into two groups representing the upper and lower basin. The result of the clustering is shown in Figure 2-16.

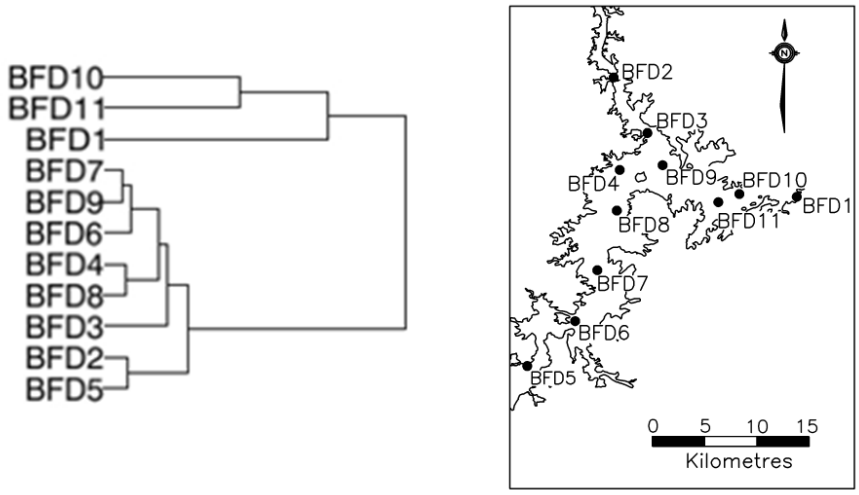

Figure 2-16 The dendrogram produced by the hierarchical clustering algorithm using a weighted pair wise average and the tripton absorption spectra slope and $a^*_{TR}(\lambda_0)$ values for the eleven Burdekin Falls Dam stations.

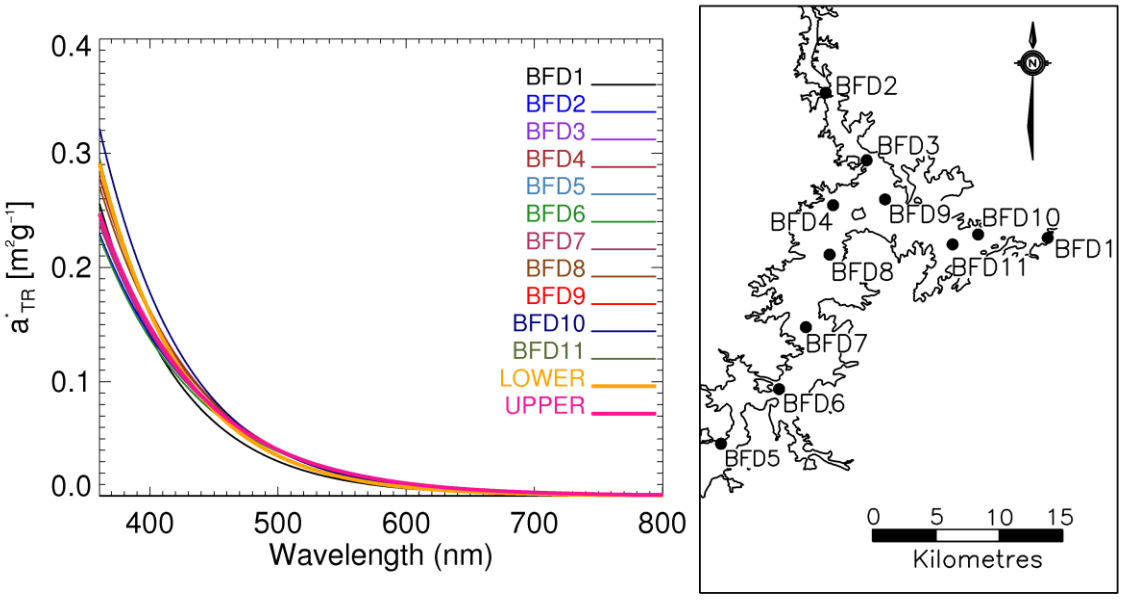

Figure 2-17 The specific absorption for tripton for the Burdekin Falls Dam stations. Two mean spectra are shown. The first is the mean of all stations in the lower basin (Stns 1, 10 and 11) and the second is the mean of all the stations in the upper basin.

The mean slope and $a^*_{TR}(\lambda_0)$ for the two basins are shown in Table 2-8.

Table 2-8 The mean fitted parameters for the tripton absorption for the Burdekin Falls Dam observation stations.

Specimen Group	$a^*_{TR}(\lambda_0)$	*slope (S)*
Upper Basin	0.021	0.0130
Lower Basin	0.016	0.0153

Specific Backscattering Spectra

The *Hydroscat-6* measurements were reduced using the corrections described in §2.3.1-2.3.3. The specific backscattering of tripton and phytoplankton were fitted to the standard model and the measured parameters for tripton are shown tabulated in Table 2-9 and phytoplankton in Table 2-10.

Table 2-9 The parameters associated with the tripton backscattering in Burdekin Falls Dam. The data has been processed using all six *Hydroscat-6* wavelengths and then the four wavelengths used by Oubelkheir et al. (2006).

Station	All Wavelengths				Four wavelengths			
	γ	$b^*_{bTR}(\lambda_0)$	Mean $b_{bp}:b_p$	R^2	γ	$b^*_{bTR}(\lambda_0)$	Mean $b_{bp}:b_p$	R^2
BFD1	-1.54	0.049	0.093	0.95	-1.31	0.049	0.090	0.99
BFD2	-1.27	0.029	0.039	0.93	-1.11	0.029	0.041	0.98
BFD3	-1.31	0.031	0.042	0.93	-1.13	0.032	0.044	0.99
BFD4	-1.57	0.038	0.041	0.96	-1.42	0.039	0.046	0.99
BFD5	-1.14	0.035	0.043	0.92	-0.98	0.036	0.045	0.98
BFD6	-1.32	0.037	0.041	0.94	-1.16	0.037	0.044	0.98
BFD7	-1.41	0.035	0.045	0.95	-1.26	0.035	0.048	0.98
BFD8	-1.45	0.039	0.048	0.95	-1.29	0.039	0.052	0.98
BFD9	-1.47	0.036	0.049	0.95	-1.31	0.036	0.052	0.98
BFD10	-1.54	0.061	0.074	0.95	-1.38	0.062	0.077	0.99
BFD11	-1.57	0.056	0.076	0.96	-1.42	0.057	0.079	0.99

Table 2-10 The parameters associated with the phytoplankton backscattering in Burdekin Falls Dam. The data has been processed using all six *Hydroscat-6* wavelengths and then the four wavelengths used by Oubelkheir et al. (2006).

Station	All Wavelengths			Four wavelengths		
	γ	$b^*_{b\varphi}(\lambda_0)$	R^2	γ	$b^*_{b\varphi}(\lambda_0)$	R^2
BFD1	-1.54	0.004	0.95	-1.31	0.004	0.99
BFD2	-1.27	0.002	0.93	-1.11	0.002	0.98
BFD3	-1.31	0.002	0.93	-1.13	0.002	0.99
BFD4	-1.57	0.003	0.96	-1.42	0.003	0.99
BFD5	-1.14	0.003	0.92	-0.98	0.003	0.98
BFD6	-1.32	0.003	0.94	-1.16	0.003	0.98
BFD7	-1.41	0.003	0.95	-1.26	0.003	0.98
BFD8	-1.45	0.003	0.95	-1.29	0.003	0.98
BFD9	-1.47	0.003	0.95	-1.31	0.003	0.98
BFD10	-1.54	0.004	0.95	-1.38	0.004	0.99
BFD11	-1.57	0.004	0.96	-1.42	0.004	0.99

Significant spatial variation in the tripton backscattering spectral slope, $b^*_{bp}(\lambda_0)$ and the backscattering ratio values was observed between the eleven stations. The lower end of the backscattering ratio values are comparable to values measured in another Queensland tropical freshwater system, the Fitzroy River (Oubelkheir et al. 2006) and the Great Barrier Reef lagoon (Blondeau-Patissier et al. 2009) but the values measured in the lower basin are approximately double the magnitude. This backscatter ratio is dependent on the real part of the refractive index (Twardowski et al. 2001). The particle size distribution is often approximated with a hyperbolic (Junge-type) distribution but some authors have concluded that this function over-estimates the number of small particles and under-estimates the number of large particles (Risovic 1993). Depending on which distribution model is chosen, theoretical studies have shown that the particle size distribution is a significant factor in determining the backscattering ratio (Ulloa et al. 1994) or only in some ranges of the real part of the refractive index (Twardowski et al. 2001). Notwithstanding this, both models show an increase in the backscattering ratio when particle size distributions are dominated by smaller particles. In general terms terrigeneous particles are smaller than biogenic particles (Risovic 1993), so it is not unreasonable to expect that the backscattering ratio from the Burdekin Falls Dam stations, where tripton dominates, should be larger than those measured at the Wivenhoe Dam sites, where biogenic particles dominate.

Previous studies have measured backscattering ratios for riverine water of 0.025-0.07 (Whitlock et al. 1981) and a freshwater lake of 0.041 with a standard deviation of 0.03 (Ma et al. 2009). Observations of the Oslo Fjord returned a mean value of 0.02, approximately 5% of the 630 observations were greater than 0.04 and the largest observations were of the order of 0.12 (Aas et al. 2005). In the latter study there was sufficient evidence for the authors to conclude that the deviations from the typical Petzold (1972) turbid water backscattering ratio were too numerous to ignore and were most likely to be caused by a predominance of small particles. The values observed at Burdekin Falls Dam were at the high end of the modelled ranges and there is a possibility that this is because of errors or incorrect assumptions in the *Hydroscat-6* correction procedure. The most obvious candidate would be the σ correction for the *Hydroscat-6* measurements. As this is an empirically derived relationship fitted to an exponential function there is a possibility that the highly scattering water being measured is outside the bounds of the empirical fit. Notwithstanding this possibility, a conservative estimate of the accuracy of this backscattering ratio measurement method was put at 20% (Whitmire et al. 2007).

The modelled tripton backscattering spectra slope, $b^*_{bTR}(\lambda_0)$ and mean $b_{bp}:b_p$ values were used as dimensions in a clustering process. This split the measurements into two groups representing the upper (Stations 2-9) and lower (Stations 1, 10 and 11) basin of the impoundment. The result of the clustering is shown in Figure 2-18 and their parameters are detailed in Table 2-11.

Table 2-11 The mean fitted parameters for the tripton backscattering for the Burdekin Falls Dam observation stations.

Specimen Group	$b^*_{bTR}(\lambda_0)$	γ
Upper Basin	0.035	-1.37
Lower Basin	0.055	-1.48

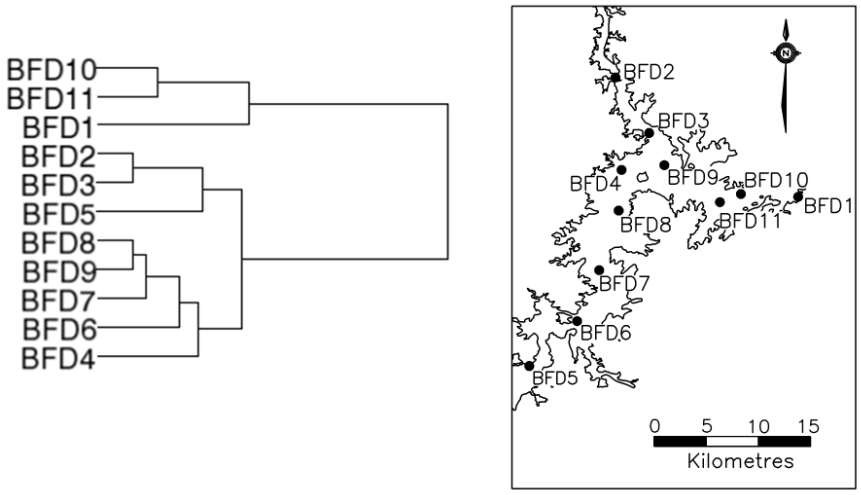

Figure 2-18 The dendrogram produced by the hierarchical clustering algorithm using a weighted pair wise average and the tripton backscattering spectra slope, $b^{*}_{bTR}(\lambda_0)$ and mean $b_{bp}:b_p$ values for the eleven Burdekin Falls Dam stations.

The phytoplankton scattering spectra were combined in the same groups.

Alternative Scattering Calculation

Given that there were suggestions in the previous section that the highly scattering water being measured is outside the bounds of the empirical fit of σ correction, an alternative method for the retrieval of the particulate scattering was attempted (Ma et al. 2009).

The Gordon et al. (1975) reflectance model related the IOPs to the subsurface reflectance, which is related to the above-surface remote sensing reflectance by:

$$R_{rs}(\lambda) = \frac{R(0^-,\lambda)}{Q} = \frac{f_1}{Q}\frac{b_b}{a+b_b} + \frac{f_2}{Q}\left(\frac{b_b}{a+b_b}\right)^2 = f_{1Q}\frac{b_b}{a+b_b} + f_{2Q}\left(\frac{b_b}{a+b_b}\right)^2 \quad (2\text{-}10)$$

where $R(0^-)$ is the sub-surface irradiance reflectance (the ratio of the upwelling to downwelling irradiance in the water), Q is the ratio of upwelling irradiance to upwelling radiance and the f's are the anisotropy factors. Further detailed explanation of the model is provided in §4.2.1. The conversion factor from radiance to irradiance changes in a reasonably parallel manner to changes in f so that the f_Q factors can be treated as spectrally invariant (Morel & Gentili 1993). Since reflectance is affected by the angular structure of the light within the water then the values should be affected by the solar altitude, the scattering phase function and proportion of diffuse

light (Kirk 1984). There is no guarantee that the f_Q factors will be constant within the same waterbody and under differing illumination conditions, so ideally they should be allowed to vary in the particle backscatter retrieval. If the particulate backscattering model and the measured absorption are substituted into this expression the remote sensing reflectance becomes a function of four unknowns.

$$R_{app}(\lambda) = f_{1Q}\frac{b_{bpo}\left(\frac{\lambda}{\lambda_0}\right)^{\gamma} + b_{bw}}{a + b_{bpo}\left(\frac{\lambda}{\lambda_0}\right)^{\gamma} + b_{bw}} + f_{2Q}\left(\frac{b_{bpo}\left(\frac{\lambda}{\lambda_0}\right)^{\gamma} + b_{bw}}{a + b_{bpo}\left(\frac{\lambda}{\lambda_0}\right)^{\gamma} + b_{bw}}\right)^2 \tag{2-11}$$

For each station with spectroradiometric observations, simultaneous measurements of downwelling irradiance (E_d) and upwelling radiance (L_u) were combined to calculate the above surface reflectance (R_{app}). A more detailed description of the spectroradiometric field observations is given in §3.2. These observations were convolved with the Gaussian bands with a FWHM of 10 nm (WET Labs Inc 2006) centred on the *ac-9* wavelengths to create a set of over-determined simultaneous equations. These non-linear equations can be solved iteratively using non-linear least squares fitting. Using initial estimates of the unknown parameters the system of equations are manipulated to form the matrix equation:

$$\mathbf{A}\partial p = \partial\beta \tag{2-12}$$

where

$$\mathbf{A} = \begin{bmatrix} \frac{\partial R_{app}}{\partial f_{1Q}}(\lambda_1) & \frac{\partial R_{app}}{\partial f_{2Q}}(\lambda_1) & \frac{\partial R_{app}}{\partial b_{bp0}}(\lambda_1) & \frac{\partial R_{app}}{\partial \gamma}(\lambda_1) \\ \vdots & \vdots & \vdots & \vdots \\ \frac{\partial R_{app}}{\partial f_{1Q}}(\lambda_9) & \frac{\partial R_{app}}{\partial f_{2Q}}(\lambda_9) & \frac{\partial R_{app}}{\partial b_{bp0}}(\lambda_9) & \frac{\partial R_{app}}{\partial \gamma}(\lambda_9) \end{bmatrix} \tag{2-13}$$

is a matrix of partial derivatives

$$\partial p = \begin{bmatrix} \partial f_{1Q} \\ \partial f_{2Q} \\ \partial b_{bp0} \\ \partial \gamma \end{bmatrix} \tag{2-14}$$

is a matrix of the desired corrections to the parameter estimates and

$$\partial \beta = \begin{bmatrix} R_{meas}(\lambda_1) - R(f_Q, \partial b_{bp0}, \partial \gamma, a(\lambda_1), \lambda_1) \\ . \\ . \\ . \\ . \\ R_{meas}(\lambda_9) - R(f_Q, \partial b_{bp0}, \partial \gamma, (\lambda_9), \lambda_9) \end{bmatrix} \tag{2-15}$$

is a matrix of the difference between the measured and forward estimated reflectances.

The standard solution of this expression is

$$\partial p = \left[\mathbf{A}^{\mathbf{T}}\mathbf{A}\right]^{-1}\mathbf{A}^{\mathbf{T}}\partial\beta \tag{2-16}$$

It is possible to differentially weight the importance of each band to give greater influence to those bands which are deemed to be more reliable. In this case the weight matrix is a square (9x9) diagonal matrix (W) where W_{ii}= signal to noise ratio of band *i*.

The solution then becomes

$$\partial p = \left[\mathbf{A}^{\mathbf{T}}\mathbf{W}\mathbf{A}\right]^{-1}\mathbf{A}^{\mathbf{T}}\mathbf{W}\partial\beta \tag{2-17}$$

The method was applied to the mean spectra measured at each of the stations with the bands being weighted in inverse proportion to the standard deviation of that measurement. When this iterative approach is used to extend weighted least squares to cover non-linear problems there is the risk that the non-linear MIM will find a local minimum dependent on the starting point, rather than the absolute minimum (Keller 2001a). Since the results in this case were highly dependent on the starting condition it would appear that this was occurring. In an attempt to circumvent this ill-posed problem an optimisation approach that used a forward model to calculate a reflectance spectrum from water quality constituent values and then used a similarity

measure to match it to the measured reflectance spectrum was employed. The Particle Swarm Optimisation (PSO) is a stochastic search technique which includes a random element in the search approach that was first applied to ocean colour by Slade et al. (2004). The algorithm represents the solution as an *n*-dimensional vector in an *n*-dimensional solution space. It then mimics the action of a swarm by generating a number of potential solutions or 'particles' and after each iteration having them react to the closest match in its local area as well as the best match from all the particles. The best match can be defined by any appropriate cost function or similarity measure. Further detailed explanation of the PSO is provided in §4.3.2.

The PSO was applied with 64 particles to the reflectance spectra allowing the four unknowns to vary and using the minimum Euclidian distance as the similarity measure. The solutions for the two anisotropy factors were limited to physically meaningful positive numbers. Once again the calculation did not supply a unique solution. It has been shown previously that the inverse problem of ocean colour using the case-I water simplification is ill-posed or ambiguous in that many disparate combinations of IOPs can produce the same reflectance spectrum (Defoin-Platel & Chami 2007). Furthermore it was shown that the ambiguity error on the total backscattering co-efficient was higher in turbid scattering waters. To see whether this was true in this case the PSO was run 20 times on the same spectrum. The results for b_{bp0} and γ are plotted in Figure 2-19 and the residuals between the forward modelled and measured spectra were plotted in Figure 2-20.

It is clear from Figure 2-19 and Figure 2-20 that very similar reflectance spectra can be produced even though there are large differences in the value of b_{bp0}. This happens because the values for the anisotropy factors are allowed to vary independently to b_{bp0} and γ. When the factors are allowed to vary independently the values in the best fit solution are clearly correlated as seen in Figure 2-21.

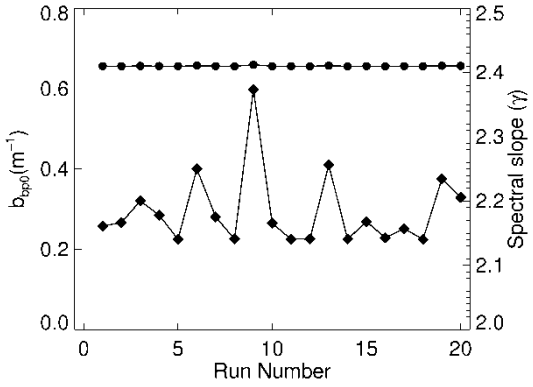

Figure 2-19 The magnitude of the retrieved b_{bp0} (diamonds) and spectral slope (γ) (circles) values for the 20 runs.

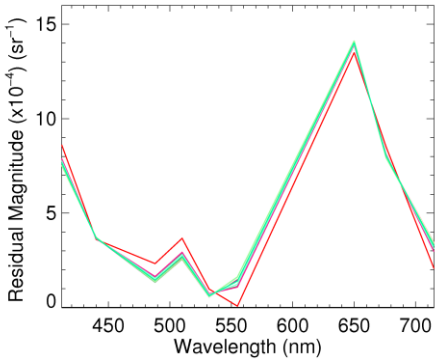

Figure 2-20 The magnitude of the residuals between the forward modelled best solution and the measured reflectance for a selection of the 20 runs. Note the similarity between the values for the solutions.

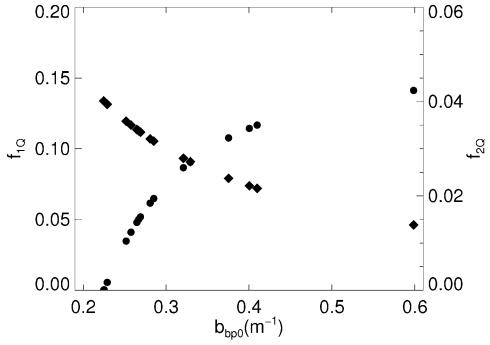

Figure 2-21 The correlation between the retrieved values of values b_{bp0}, f_{1Q} (diamonds) and f_{2Q} (circles) for the 20 runs.

Notwithstanding the previous discussion as to the variability of the f_Q factors, to resolve the ambiguity it was necessary to fix the values of the anisotropy factors. Lee et al. (1999) assert that

for case-II coastal water values $f_{1Q} = 0.084$ and $f_{2Q} = 0.17$ can be used. The resulting b_{bp0} and γ values are plotted against the same values measured using the more typical *Hydroscat-6* approach in Figure 2-22 and Figure 2-23. The reflectance method underestimates by approximately 50% in the case of b_{bp0} and in the case of γ it has an appreciable bias and overestimates by about 40%. The apparent linear trend in both plots suggests that better *a priori* values for the f_Q factors would lead to more consistent results, however since this requires better information on the scattering phase function the problem becomes a case of *petitio principii*. For this reason the method was not pursued.

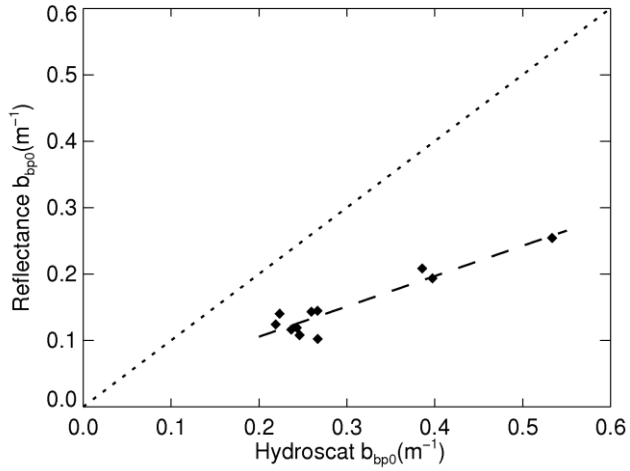

Figure 2-22 The *Hydroscat-6* derived b_{bp0} vs Reflectance derived bb_{p0} for the Burdekin Falls Dam stations. The dashed line shows a line of best fit for the data and the dotted line is a 1:1 correspondence line.

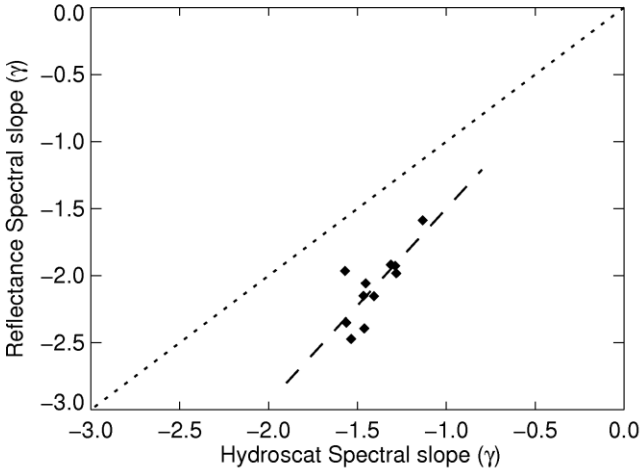

Figure 2-23 The *Hydroscat-6* derived γ vs. Reflectance derived γ for the Burdekin Falls Dam stations. The dashed line shows a line of best fit for the data and the dotted line is a 1:1 correspondence line.

IOP Sets

The clustering procedures based on the separate SIOPs did not result in entirely consistent groups, but there was sufficient similarity to conclude that the water in Burdekin Falls Dam could be characterised by two IOP sets, the upper basin and the lower basin that are shown in Figure 2-24. These sets were used in simulations to parameterise the retrieval algorithm described in §4.3.

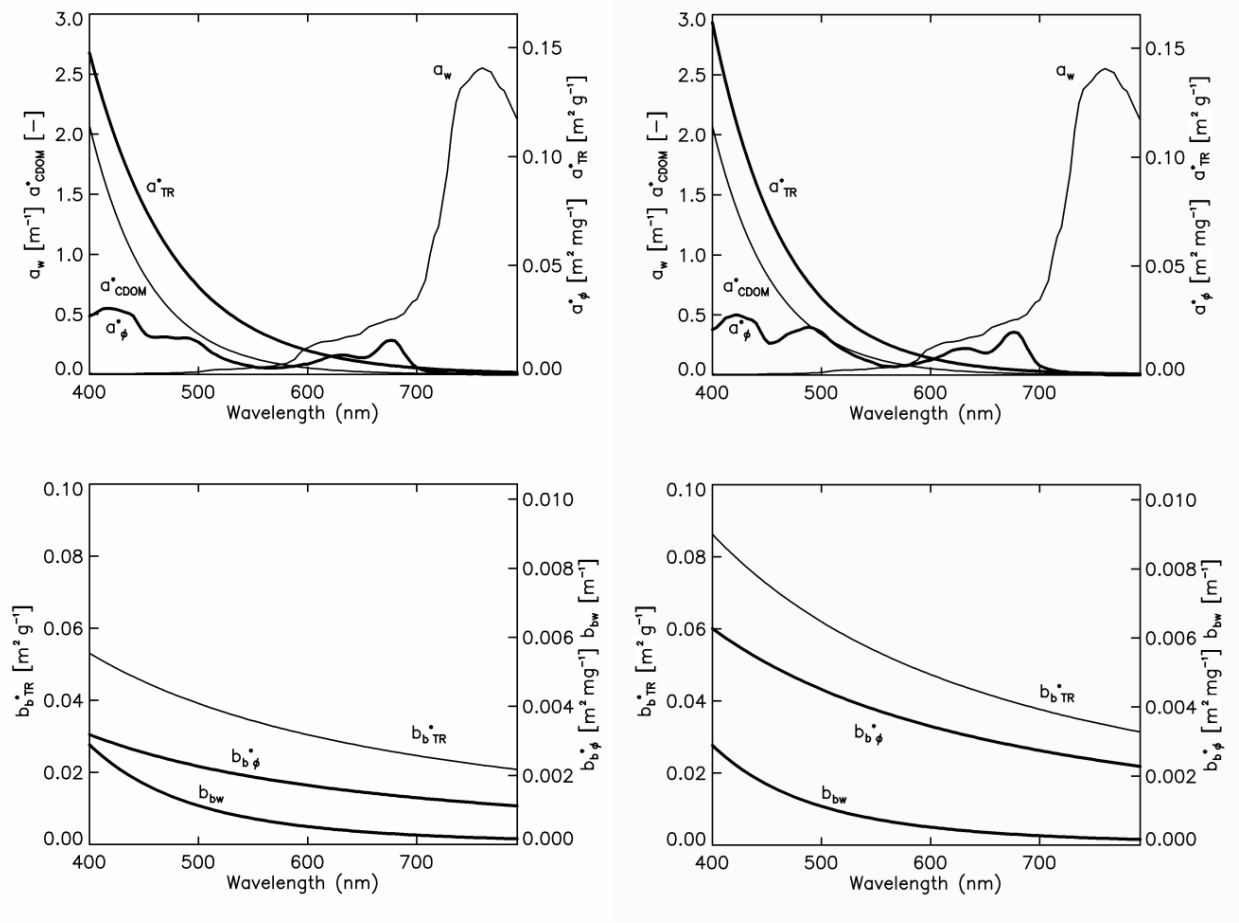

Figure 2-24 Average SIOPs for Burdekin Falls Dam (left: Upper basin, right: lower basin): The upper graph shows the spectral absorption of water (*w*) and the chlorophyll *a* specific absorption spectra of phytoplankton (ϕ), tripton (*TR*) and coloured dissolved organic matter (*CDOM*). The lower shows the spectral backscattering of water (*w*) and the specific backscattering spectra of chlorophyll *a*(ϕ) and tripton (TR).

Again the phytoplankton specific absorption spectra were decomposed into thirteen Gaussian bands. The band centres were held fixed on the initial values of Lohrenz (2003) and the other two parameters were varied to obtain the optimal fit. In each case some bands were found to be redundant. The results are shown in Table 2-12, Figure 2-25 and Figure 2-26.

Table 2-12 The optimal modelled parameters describing the phytoplankton specific absorption spectra for Wivenhoe Dam and Burdekin Falls Dam.

	Wivenhoe Dam		Burdekin Falls Upper		Burdekin Falls Lower	
λ_0 (nm)	a_0 (m^2mg^{-1})	FWHM (nm)	a_0 (m^2mg^{-1})	FWHM (nm)	a_0 (m^2mg^{-1})	FWHM (nm)
376	0.05132	30.5	0.01557	159.5		
409	0.02310	27.6	0.01379	28.7	0.02295	33.5
435	0.03038	35.1	0.01611	30.0	0.02054	28.7
461	0.00025	8.7				
464	0.00889	28.3	0.00344	17.8	0.00507	22.4
490	0.01220	44.8	0.01291	49.1	0.02155	51.8
539	0.00214	41.5	0.00303	41.0	0.00537	40.1
586	0.00212	38.5	0.00308	40.3	0.00435	38.4
622	0.00487	34.3	0.00707	36.2	0.00989	37.4
642	0.00306	24.8	0.00444	26.2	0.00570	27.1
652	0.00083	16.0	0.00057	12.3	0.00089	15.4
675	0.01315	29.2	0.01521	29.7	0.01876	29.3
701	0.00058	53.1	0.00122	56.3	0.00210	59.0

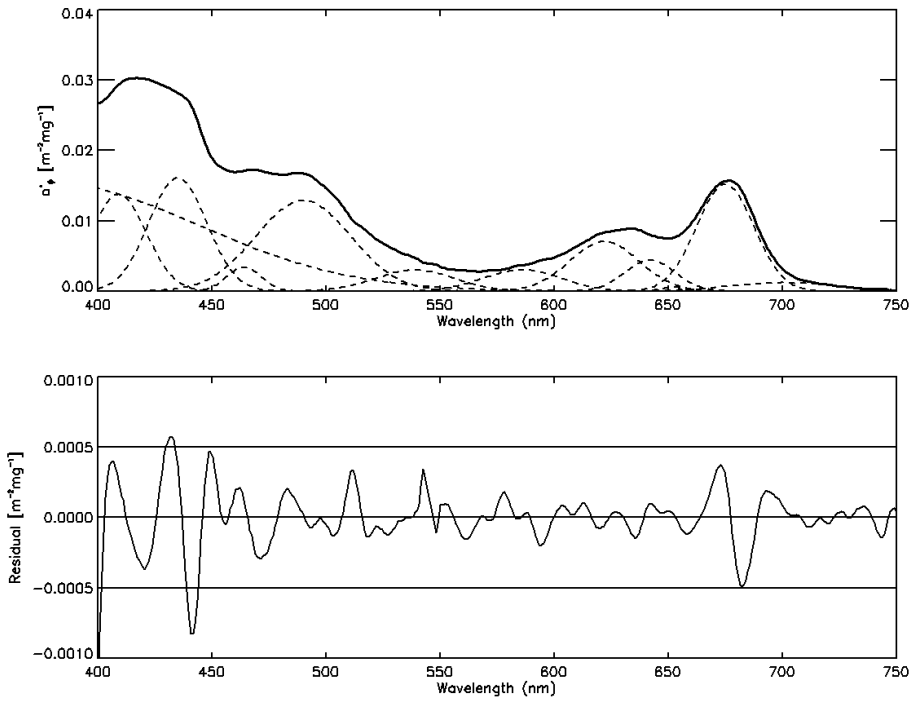

Figure 2-25 The decomposed Burdekin Falls Dam Upper Basin specific phytoplankton absorption spectrum. The upper plot shows the Burdekin Falls Dam Upper Basin specific phytoplankton absorption spectrum (bold) and the thirteen Gaussian bands into which it was decomposed (dashed). The lower plot shows the difference between the reconstructed and original spectrum.

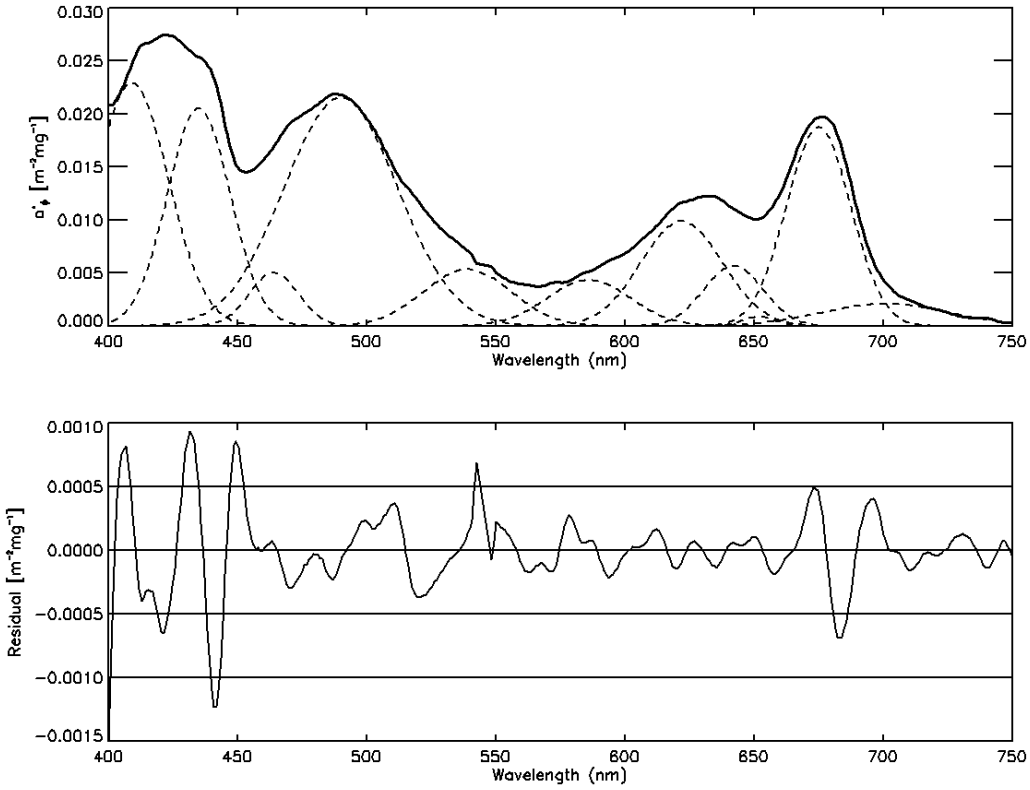

Figure 2-26 The decomposed Burdekin Falls Dam Lower Basin specific phytoplankton absorption spectrum. The upper plot shows the Burdekin Falls Dam Lower Basin specific phytoplankton absorption spectrum (bold) and the thirteen Gaussian bands into which it was decomposed (dashed). The lower plot shows the difference between the reconstructed and original spectrum.

2.5.3. Fairbairn Dam

The SIOPs were sampled at the stations shown in Figure 2-27.

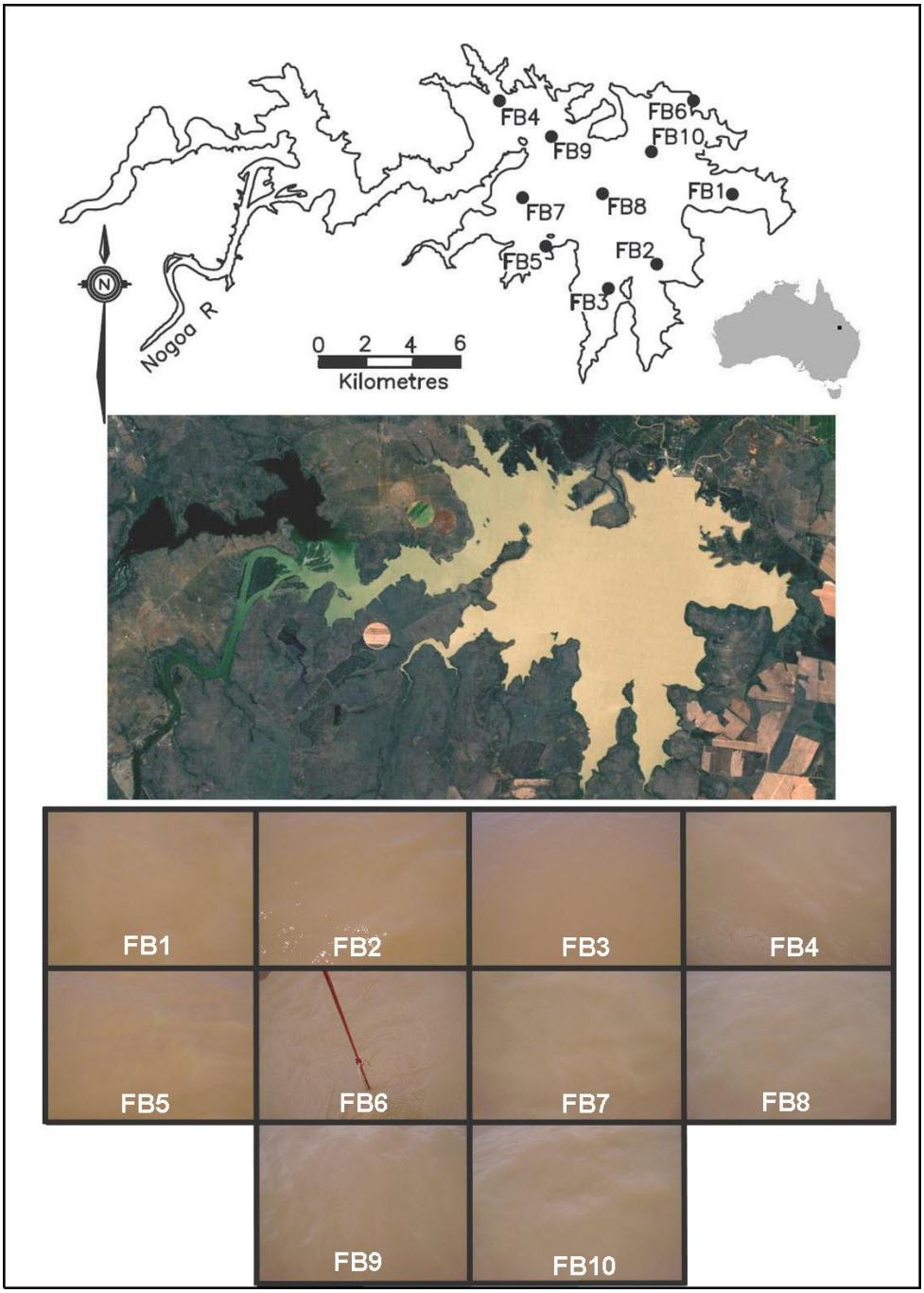

Figure 2-27 Location of the SIOP sample sites for the October 2008 fieldwork activities on Fairbairn Dam, Australia. The top image shows the calculated full supply level and the middle image shows a Landsat 5 TM true colour image at the same scale as the map, captured on 3rd November 2008. The lower section of the figure shows photographs of the sample sites taken at the time of sampling.

Water Quality Parameter Concentrations

The range of the measured chlorophyll *a* values was 0.9 – 2.9 μgl^{-1}, the range of the measured tripton was 149.0 – 170.4 mgl^{-1}, the measured CDOM range was 1.16 - 1.59 m^{-1} and the Secchi depth range was 0.15 – 0.2 m. Due to the very heavy tripton levels a CDOM sample was not filtered at every station. A table showing the individual measurements is shown in Appendix A.

Phytoplankton Absorption

The amount of suspended material in the Fairbairn Dam samples that was extracted from the water onto a filter was too great to allow measurement of the phytoplankton absorption at all ten sites.

CDOM Absorption

The laboratory measured absorption spectra for CDOM were taken at seven of the ten sampling stations and are shown in Appendix A with the corresponding specific absorption spectra shown in Figure 2-28.

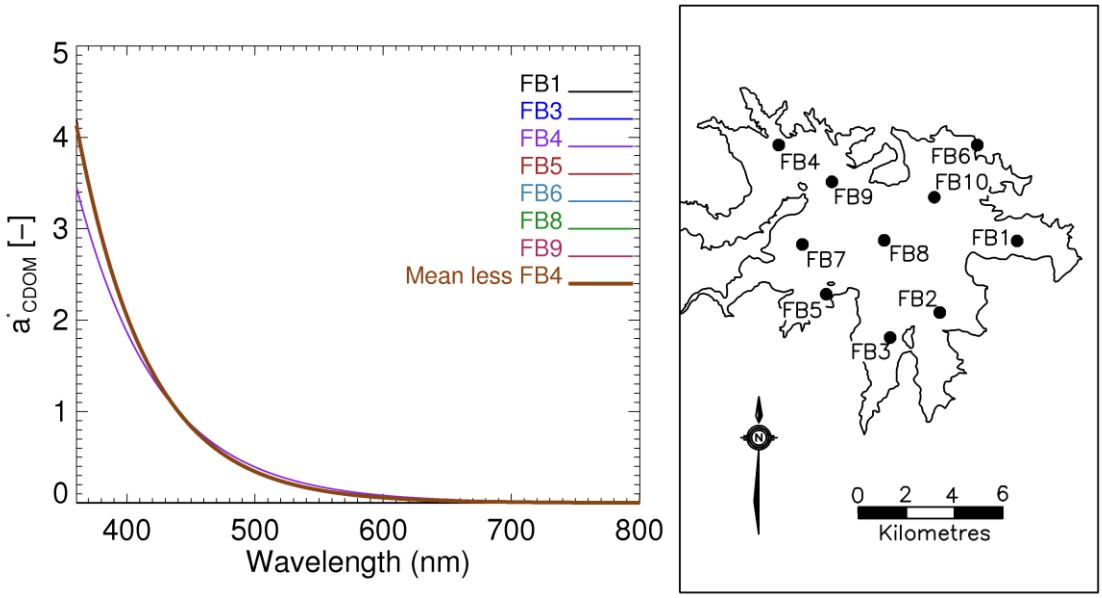

Figure 2-28 The specific absorption for CDOM for the Burdekin Falls Dam stations. The mean spectrum is the mean of all stations with the exception of FB4.

The spectral slopes for CDOM ranged from 0.0156 – 0.0181 nm^{-1} with a mean spectrum slope of 0.0175 nm^{-1}. There is very little variation in the CDOM absorption for the Fairbairn Dam sample stations with the exception of station FB4. The slope of the CDOM absorption curve has been shown to be inversely proportional to the molecular weight of fulvic acids (Carder et al. 1989; Hayase & Tsubota 1985) and is affected by the photodegradation (Morris & Hargreaves 1997). Loiselle et al. (2009a) found an increase in the CDOM spectral slope with distance from the main inlet for a subtropical lake. FB4 was exceptional in that it was in an area of the water body that was heavily dominated by dead standing timber as shown in Figure 2-29. It is therefore not unreasonable to expect a difference in spectral slope with respect to the rest of the water body, but it is not possible to conclude whether different molecular qualities or a lack of photodegradation is responsible for the difference.

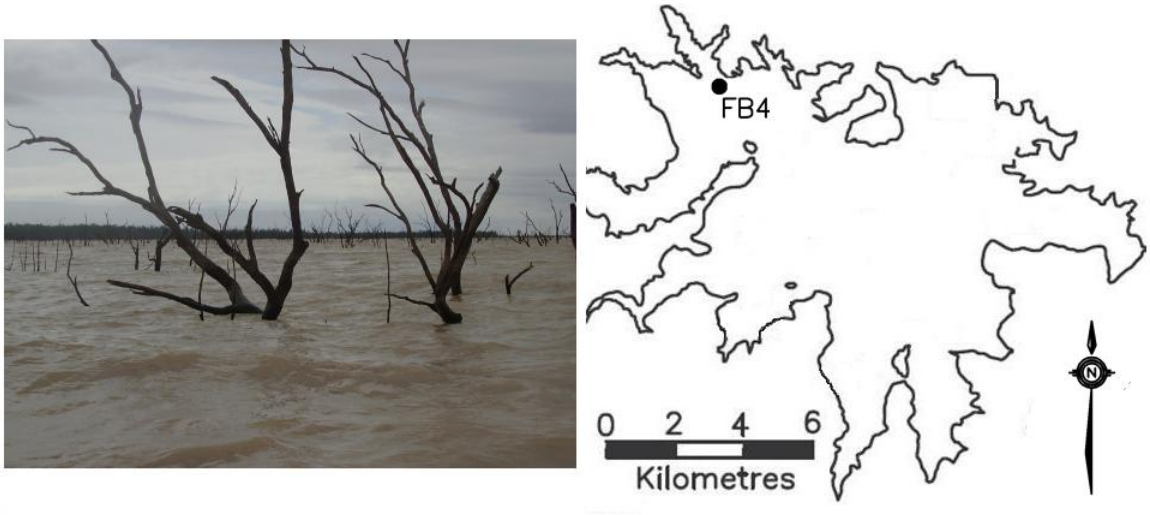

Figure 2-29 The dead standing timber that dominated the area surrounding FB4 on Fairbairn Dam.

The mean spectrum of the stations excluding FB4 has a slope of 0.0179 nm^{-1} and the FB4 sample has a slope of 0.0156 nm^{-1}.

Tripton Absorption

The amount of suspended material in the Fairbairn Dam samples that was extracted from the water onto the filter was too great to allow the laboratory measurement of the tripton absorption. At each station, however, the attenuation and absorption information was logged at nine

wavelengths using the *ac-9*. A 25 cm path length *ac-9* was used for the Fairbairn Dam field operation as the 10 cm path length *ac-9* was unavailable. The very high turbidity of the Fairbairn Dam water meant that the dynamic range of the instrument was exceeded. The quoted RMS noise is less than 1 mV out of 5 volts, the resolution is considered to be one bit on a twelve bit analog to digital converter. The resolutions are the difference between the attenuation coefficients at the signal level plus and minus a half bit (Welt Labs Inc, pers. comm.). Figure 2-30 shows a graph of the predicted resolution against the beam attenuation for the two path lengths.

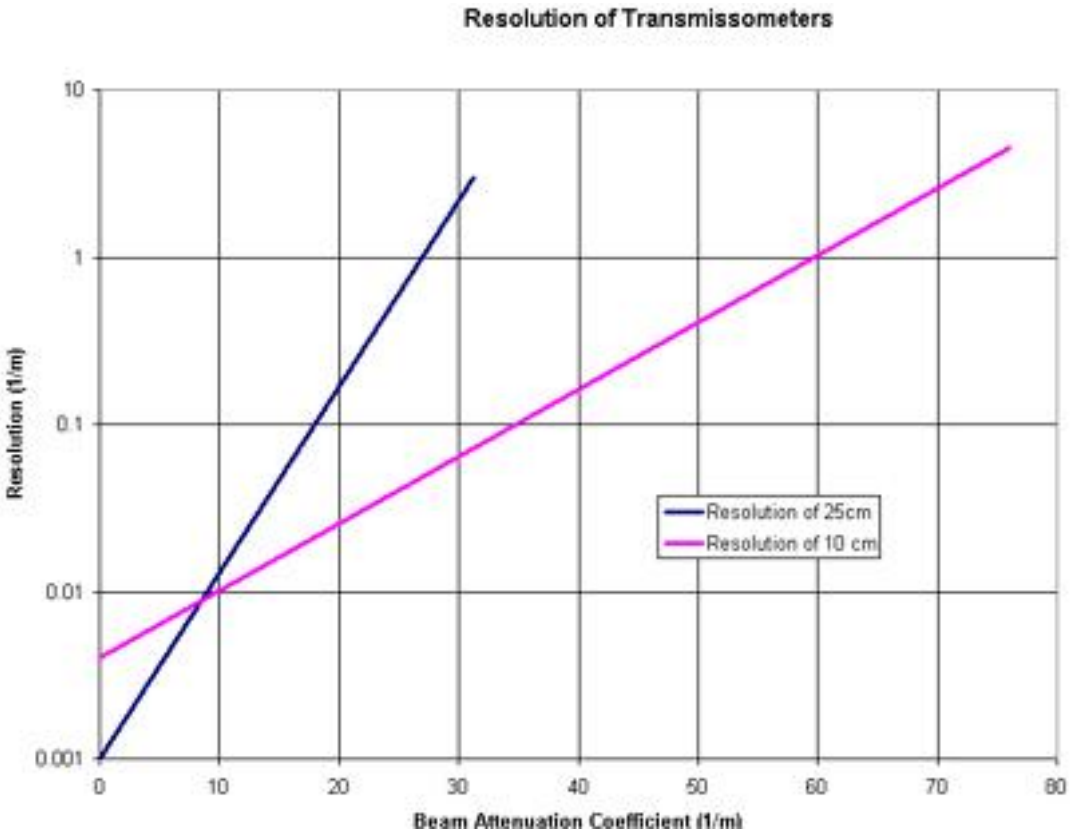

Figure 2-30 The resolution vs. beam attenuation co-efficient for the two types of Wet labs *ac-9* meters (Wet Labs Inc, pers. comm.).

It is clear that the 25 cm path length *ac-9* becomes increasingly unreliable for attenuation values above 30 m^{-1}. The raw measurements of attenuation reach a maximum of 60 m^{-1} so the results could not be used. In contrast the absorption values measured were always below 20 m^{-1} but due

to that lack of scattering information it was necessary to correct the raw data using the less accurate first correction method referred to in §2.3.2.

After the *ac-9* data was corrected the absorption of CDOM at the *ac-9* wavelengths was subtracted to leave the absorption of phytoplankton and tripton. Calculations based on the Burdekin Falls Dam SIOP set showed that for the relative concentrations measured at the Fairbairn Dam stations the phytoplankton absorption accounts for approximately 0.3% of the absorption at 412nm. Given the error associated with the *in situ* absorption measurements the absorption associated with phytoplankton could be safely disregarded. The tripton absorption model was then fitted to the tripton absorption spectra. An example of a fitted function is shown in Figure 2-31 and the final fitted parameters are shown in Table 2-13.

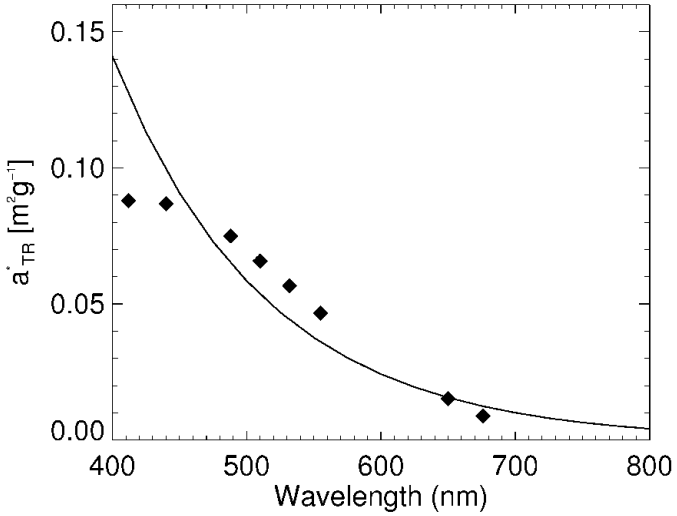

Figure 2-31 An example absorption for tripton for FB1. The points show absorption as measured by the *ac-9* after being corrected by the CDOM absorption and the scaled by the tripton concentration. The line of best fit using the tripton absorption model is shown.

Table 2-13 The mean fitted parameters for the tripton and CDOM absorption for the Fairbairn Dam observation stations.

Station Name	CDOM slope (S) (nm^{-1})	$a^*_{TR}(\lambda_0)$ (m^2g^{-1})	Tripton slope (S) (nm^{-1})	R^2
FB1	0.0181	0.038	0.0088	0.91
FB3	0.0177	0.036	0.0086	0.91
FB4	0.0156	0.037	0.0089	0.92
FB5	0.0179	0.034	0.0086	0.91
FB6	0.0179	0.036	0.0087	0.91
FB8	0.0178	0.036	0.0088	0.92
FB9	0.0179	0.038	0.0089	0.92

Inspection of Figure 2-31 shows that the fit is at its worst at wavelengths less than 450 nm. This is not to be unexpected when we compare the results of laboratory measurements for other sites. For comparison Figure 2-32 shows the unfitted specific tripton absorption for WV5 at Wivenhoe Dam.

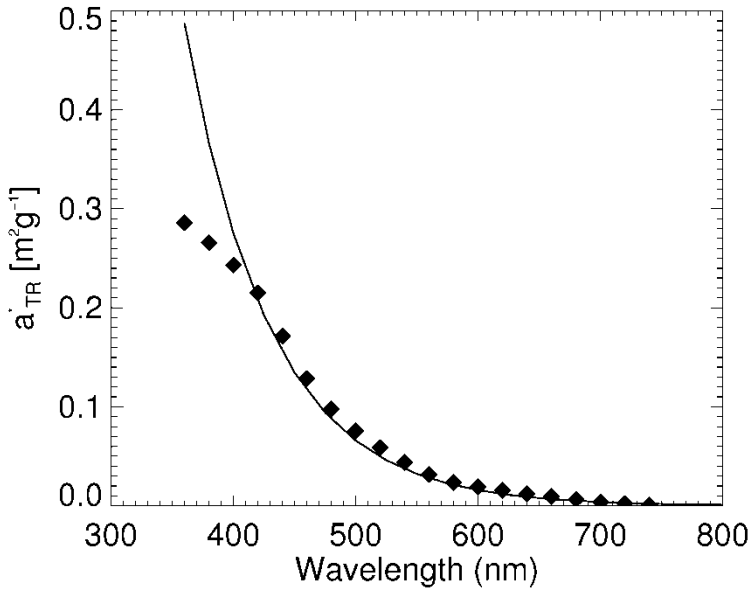

Figure 2-32 An example absorption for tripton for Wivenhoe Dam WV5. The points show absorption as measured in the laboratory then scaled by the tripton concentration. The line of best fit using the tripton absorption model is shown.

Specific Backscattering Spectra

The unreliability of the attenuation measurements of the *ac-9* meant that it was not possible to obtain a value for the scattering of the water quality parameters to correct the *Hydroscat-6* measurements. In the absence of measured scattering values the scattering can be estimated from

$$b = \frac{\left(b_{bu} - b_{bw}\right)}{\tilde{b}_b} \tag{2-18}$$

where b_{bu} is the uncorrected backscattering measured by the *Hydroscat-6*, b_{bw} is the backscattering of pure water and $\tilde{b}_b$ is the backscattering probability, which was approximated by the mean backscattering ratio of similar water. In this case the water of Fairbairn Dam is clearly dominated by terrigenous particles so the value selected (0.093) was the backscattering ratio of the Burdekin Falls dam with the highest percentage of inorganic material in the tripton (Stn1). The results are shown in Table 2-14 and Table 2-15.

Table 2-14 The parameters associated with the tripton backscattering in Fairbairn Dam. The data has been processed using all six *Hydroscat-6* wavelengths and then the four wavelengths used by Oubelkheir et al. (2006).

Station	All Wavelengths			Four wavelengths		
	γ	$b^*_{bTR}(\lambda_0)$	R^2	γ	$b^*_{bTR}(\lambda_0)$	R^2
FB1	-1.35	0.012	0.60	-0.89	0.013	0.66
FB2	-1.25	0.011	0.54	-0.77	0.011	0.55
FB3	-1.14	0.011	0.52	-0.66	0.012	0.52
FB4	-1.38	0.013	0.63	-0.88	0.013	0.81
FB5	-1.11	0.010	0.50	-0.65	0.011	0.46
FB6	-1.24	0.011	0.55	-0.76	0.012	0.61
FB7	-1.16	0.011	0.52	-0.68	0.012	0.55
FB8	-1.29	0.011	0.59	-0.82	0.012	0.68
FB9	-1.37	0.012	0.63	-0.88	0.012	0.77
FB10	-1.30	0.011	0.59	-0.82	0.012	0.66

Table 2-15 The parameters associated with the phytoplankton backscattering in Fairbairn Dam. The data has been processed using all six *Hydroscat-6* wavelengths and then the four wavelengths used by Oubelkheir et al. (2006).

Station	All Wavelengths			Four wavelengths		
	γ	$b_{bTR}(\lambda_0)$	R^2	γ	$b_{bTR}(\lambda_0)$	R^2
FB1	-1.35	0.001	0.60	-0.89	0.001	0.66
FB2	-1.25	0.001	0.54	-0.77	0.001	0.55
FB3	-1.14	0.001	0.52	-0.66	0.001	0.52
FB4	-1.38	0.001	0.63	-0.88	0.001	0.81
FB5	-1.11	0.001	0.50	-0.65	0.001	0.46
FB6	-1.24	0.001	0.55	-0.76	0.001	0.61
FB7	-1.16	0.001	0.52	-0.68	0.001	0.55
FB8	-1.29	0.001	0.59	-0.82	0.001	0.68
FB9	-1.37	0.001	0.63	-0.88	0.001	0.77
FB10	-1.30	0.001	0.59	-0.82	0.001	0.66

As a comparison the reflectance method described in §2.5.2 was applied to Fairbairn Dam reflectance measurements. In this case the forward reflectance spectra generated were unable to recreate the correct shape of the measured spectra in the NIR region. Inspection of the forward model showed that the *ac-9* measured absorption in the 650-715 nm bands was not sufficient to reproduce the shape of the spectra as shown in Figure 2-33. Figure 2-31 shows that the curve of best fit for the tripton absorption for FB1 shows a non-zero absorption at 715nm, contrary to the assumption made in the absorption correction. In an attempt to circumvent this problem the *ac-9* spectra were replaced by calculated spectra using the previously measured CDOM, tripton and water specific absorption spectra. Once again the anisotropy factors were held fixed. The results for the six stations with spectroradiometric observations are shown in Table 2-16.

There are a number of factors evident within these results that require them to be treated with caution. The empirical equation used for the σ correction for the *Hydroscat-6* measurements is likely to be outside its usable bounds due to the extreme turbidity and hence high scattering and absorption of the water being measured. The exponential character of this function means that small differences in the measured absorption and scattering result in large changes in the σ correction. This sensitivity to measurement error is likely to result in an irregular error between wavelengths and affect the correlation coefficient of the fit and the fitted slope. This is

demonstrated by the large difference in the calculated slopes when comparing the six wavelengths and four wavelength fits.

Table 2-16 The parameters associated with the tripton backscattering in Fairbairn Dam. The data has been processed using the reflectance method.

Station	All Wavelengths	
	Gamma	b^*_{bTR}@ 542nm
FB1	-2.39	0.020
FB2	-2.14	0.020
FB3	-2.21	0.016
FB5	-1.92	0.014
FB6	-2.48	0.018
FB9	-2.45	0.018

The very high sediment load in the standing water body that had not received significant inflows suggests that the sediment is dominated by very fine particles as they have a sufficiently low terminal velocity that can be countered by Brownian motion. This domination by fine particles should have the effect of increasing the spectral slope of the tripton backscattering. The fact the *Hydroscat-6* determinations show slopes consistent with those measured at Wivenhoe Dam was unexpected.

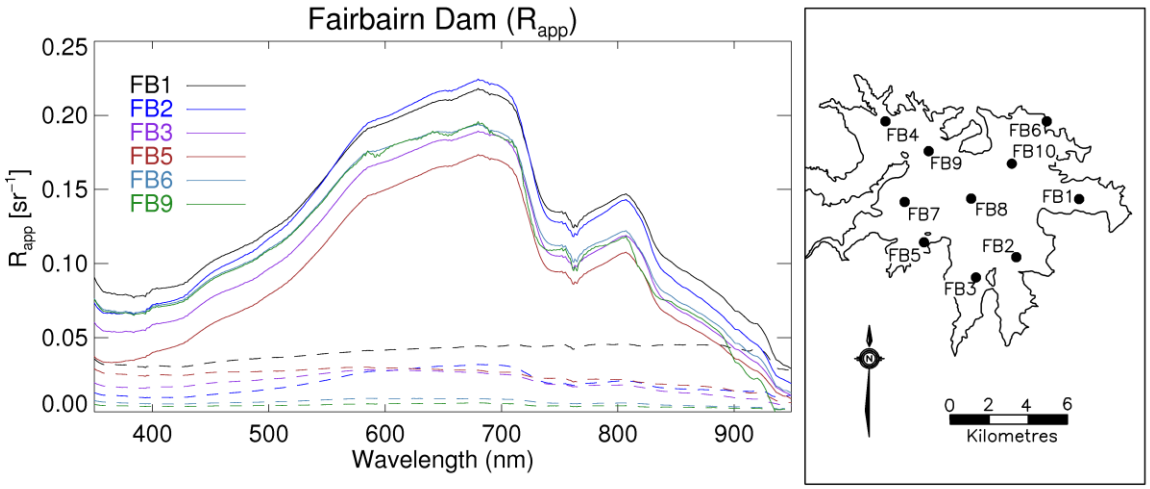

Figure 2-33 The mean remote sensing reflectance (R_{app}) spectra for six stations at Fairbairn Dam. Dashed lines show the standard deviation of the measured spectra.

The values obtained using the reflectance method were more in line with expectations. Due to the choppy conditions on the first two field days the reflectance measurements displayed

relatively high signal to noise ratios for four of the reflectance measurements (Figure 2-33). This concern along with the result in §2.5.2 that showed the reflectance method overestimated the spectral slope and underestimated b_{bp0} means that it is unwise to utilise these results.

IOP Set

Due to the failure to acquire valid measurements of some of the required IOPs it was not possible to obtain an IOP set for Fairbairn Dam.

2.6 Assumptions Related to Phytoplankton

Although their effect on the final remote sensing algorithm performance is likely to be small, this chapter makes two assumptions in relation to phytoplankton properties that should be made explicit. Firstly, that the Dutch lakes' (Buiteveld 1995) relationship between chlorophyll *a* concentration and phytoplankton dry weight biomass can be used in other environments and secondly, that the backscattering of phytoplankton has the same spectral shape as that of tripton.

Due to the difficulties associated with calculating a site specific value the Dutch lakes' value has been widely used in other environments (Erm et al. 2002; Herlevi 2002b; Kutser 2004; Zhang et al. 2009). Even if this ratio was as low as 0.03 to 0.06 as reported for some Finnish lakes (Kutser et al. 2001) the effect on the calculation of the tripton concentration would be negligible for the majority of measured stations and still small for stations WV5-7.

An alternative method to using the second assumption would be to estimate the tripton backscattering from the total backscattering by subtracting previously published chlorophyll *a* specific backscattering of phytoplankton values. The reported backscattering spectra (Ahn et al. 1992; Kutser et al. 2006; Metsamaa et al. 2006) have been measured for laboratory cultured single species. The latter two studies used a *Hydroscat-6* for the measurement. This instrument uses an assumed VSF (Maffione & Dana 1997). It has been shown that the phytoplankton VSF is variable and that the San Diego Harbour VSF (Petzold 1972) was shown to represent the VSF of only 3 out the 17 species investigated by Volten et al. (1998). Vaillancourt et al. (2004) found that the chlorophyll *a* specific backscattering increased as cells decreased in size but this was also dependent on the particulate organic carbon to chlorophyll *a* ratio. This ratio varies with

species composition and light and nutrient conditions. Not only do the optical properties differ between species, but the properties of pure cultures will differ from natural assemblages due to the differences in the prevailing light and nutrient conditions. The errors associated with this alternative method are comparable to the assumption that has been made.

Nevertheless, the effect of errors associated with both these assumptions on a final remote sensing algorithm performance is likely to be small as the backscattering of tripton will dominate the scattering processes.

2.7 International Comparisons

The description of SIOPs for inland waters in the literature is often incomplete because researchers are either focussing on one particular colour-producing agent or on the remote sensing of water quality parameters. The former case provides a detailed examination of the optical properties of a single water quality parameter to the exclusion of the others and the latter case often involves merely graphical representations of SIOP sets. Table 2-17 shows a comparison of the measured Queensland tropical and sub-tropical SIOP values to published values in other environments.

The direct comparison of spectral slopes between studies is difficult if the slopes have been calculated over different spectral ranges, but the present measured values for the spectral slope of the specific absorption of CDOM are comparable to values measured in New Zealand lakes (Davies-Colley & Vant 1987) and Lake Superior, North America (Minor & Stephens 2008)). In general they are larger than mean slopes for Murchison Bay in Lake Victoria (Okullo et al. 2007), Lake Mälaren, Sweden (Strömbeck & Pierson 2001), Finnish lakes (Kallio et al. 2005) and Dutch inland water (Rijkeboer et al. 1997). Values measured in Lake Taihu, China were reported using a hyperbolic model but transformation of those results show the Queensland lakes had spectral slopes that were considerably larger (Zhang et al. 2007). The range of slopes measured in the three lakes is smaller than that measured in a single lake Laguna Ibeŕa, Argentina (Loiselle et al. 2009a).

The direct comparison of phytoplankton absorption spectra is limited by the predominance of graphical rather than numerical reporting. The measured range of the specific phytoplankton absorption at the 670-676nm peak in the Queensland water bodies is comparable to measurements made for New Zealand freshwater (Belzile et al. 2004; Davies-Colley et al. 1986) and the mean measured values for Dutch lakes (Rijkeboer et al. 1997) and Lake Taihu (Le et al. 2009) but considerably lower than that measured for Lake Erie in North America (Binding et al. 2008). The measured values are within the range measured in a variety of lakes in Nebraska and Iowa (Dall'Olmo & Gitelson 2005).

The measured range of the spectral slope of the specific tripton absorption for the Queensland water bodies bracket the values measured at Chinese lakes Taihu (Ma et al. 2006) and Tianmuhu (Zhang et al. 2009), Lake Taupo, New Zealand (Belzile et al. 2004), Finnish and Estonian Lakes (Paavel et al. 2007), Lake Mälaren, Sweden (Pierson & Strömbeck 2001) and the mean measured values for Dutch lakes (Rijkeboer et al. 1997). The values of $a^*_{TR}(550)$ are predominately within the range of values reported for Lake Erie (Binding et al. 2008) and the Nordic lakes (Paavel et al. 2007; Pierson & Strömbeck 2001) (the published a^*_{TR} values were transformed to $a^*_{TR}(550)$ using their quoted slopes).

Table 2-17 Comparison of the Queensland SIOP values to literature values.

Location	a^*_{CDOM} *Slope* (nm^{-1})	*Slope Range* (nm)	$a^*_{\varphi}(670\text{-}676)$ (m^2mg^{-1})	$a^*_{TR}(550)$ (m^2g^{-1})	a^*_{TR} *Slope* (nm^{-1})	$b^*_{bTR}(542)$ (m^2g^{-1})	γ_{TR} (nm^{-1})	$b^*_{b\varphi}(620)$ (m^2mg^{-1})	Reference
Wivenhoe Dam	0.0173-0.0190	350-680	0.010-0.014	0.035-0.145	0.0080 – 0.0088	0.008-0.021	0.49-1.00		
Burdekin Falls Dam	0.0171-0.0185	350-680	0.012-0.025	0.014-0.022	0.0123 – 0.0153	0.031-0.061	1.14-1.57		
Fairbairn Dam	0.0156-0.0181	350-680	n.d.	0.034-0.038	0.0086 – 0.0089	n.d.	n.d.	n.d.	
New Zealand lakes	0.0151-0.0205	280-460	0.01-0.033						(Davies-Colley et al., 1987; Davies-Colley et al., 1986; Belzile et al., 2004)
Lake Superior, North America	0.0183-0.0215	290-400							(Minor et al., 2008)
Murchison Bay, Lake Victoria	0.016 ± 0.001	200-900							(Okullo et al., 2007)
Lake Mälaren, Sweden	0.015 ± 0.002	n.d.		0.02-0.05	0.009-0.013	0.008-0.047	1.52-2.84		(Strömbeck et al., 2001; Pierson et al., 2001)
Finnish lakes	0.015 ± 0.001	400-750							(Kallio et al., 2005)
Dutch Lakes	0.016 ± 0.002	350-750	0.013		0.009				(Rijkeboer et al., 1997)
Lake Taihu, China	0.011 ± 0.002	300-600	0.021		0.009-0.0129				(Zhang et al., 2007; Le et al., 2009)
Laguna Ibeŕa, Argentina	0.0115-0.0205	270-400							(Loiselle et al., 2009)
Lake Erie, North America			0.04	0.004-0.063					(Binding et al., 2008)
Nebraska, Iowa Lakes			0.005-0.050						(Dall'Olmo et al., 2005)
Lake Tianmuhu, China					0.0094-0.0123				(Zhang et al., 2009)
Lake Taupo, New Zealand					0.08 – 0.0.012		0.41-0.79		(Belzile et al., 2004)
Finnish and Estonian Lakes				0.01-0.09	0.006-0.0109		0.13-2.53		(Herlevi, 2002b; Paavel et al., 2007)
Cultured specimens								0.00001-0.001	(Ahn et al., 1992; Kutser et al., 2006; Metsamaa et al., 2006)

Published values for the specific backscattering of tripton and phytoplankton are rare but once again by transforming the published $b_b^*{}_{TR}$ *(400)* values to $b_b^*{}_{TR}$ *(542)* using their published slopes, the Lake Mälaren measurements of Pierson and Strömbeck (2001) show similar values for $b_b^*{}_{TR}$ *(542)*. The range of spectral slopes measured for Wivenhoe Dam and Burdekin Falls Dam were lower than that measured in Lake Mälaren but they are comparable to values measured for Finnish and Estonian lakes (Herlevi 2002a; Paavel et al. 2007) and Lake Taupo, New Zealand (Belzile et al. 2004).

The specific backscattering of phytoplankton at 620 nm values measured for Wivenhoe Dam were comparable to the values obtained for cultures by Ahn et al. (1992) and Vaillancourt et al. (2004) but exceeded the values reported by Kutser et al. (2006) and Metsamaa et al. (2006). The values for Burdekin Falls Dam were higher than these other recorded values. The spectral slope of a power law model for the specific backscattering of phytoplankton has been shown to have a mean of -1.4 ± 0.5 nm^{-1} (Vaillancourt et al. 2004) and the slope for cyanobacterial species has been shown to be higher than phytoplankton species (Ahn et al. 1992; Metsamaa et al. 2006). The total backscattering slopes measured for the study sites fall within this range and the cyanobacteria-dominated Burdekin Falls Dam samples show a greater slope but the domination of backscattering by tripton means these spectra should be treated with caution.

2.8 Conclusions

This chapter described one partial and two complete Australian inland water SIOP sets to allow international and national comparison. In general terms, limited differences were observed between the shapes of the specific phytoplankton absorption spectra measured at different stations across Wivenhoe Dam; however there was a significant difference between specific phytoplankton absorption spectra measured across Burdekin Falls Dam. As might be expected, there were differences between the spectra measured in the tropical and sub-tropical impoundments. The measured spectral slopes of the specific absorption of CDOM showed limited variation within and between impoundments. The measured spectral slopes of the specific absorption of tripton were similar in Wivenhoe and Fairbairn Dams and showed limited variation within the water bodies. In contrast, the specific absorption of tripton spectral slopes for

Burdekin Falls Dam stations were larger and showed a greater variation within the impoundment. There was greater variation within and between the impoundments for the value on $a^*_{TR}(550)$. Among the eleven stations measured at Burdekin Falls Dam there was a greater spatial variation in the tripton backscattering spectral slope, $b^*_{bTR}(542)$ and the backscattering ratio values than Wivenhoe Dam. Both sites deviated from the conventional Petzold (1972) turbid water backscattering ratio (0.019) with Burdekin Falls Dam being higher and Wivenhoe Dam being lower. The measured values were within the ranges of measured values in other environments and the difference is most likely due to the relative concentrations of phytoplankton and tripton (Kirk 1994).

There was sufficient intra-impoundment variation in the specific absorption and specific scattering of phytoplankton and tripton to require a well distributed network of measurement stations to fully characterise the SIOPs of the optical water quality parameters. The variation in catchment soil, land-cover and land-use conditions and impoundment substrate mineralogy resulted in significantly different SIOP sets for each of the study sites. The significance of these variations on the accuracy and precision of optical water quality parameters has been estimated by simulation and is described in Chapter 4, the results of which is confirmed by application to satellite imagery in Chapters 5 and 6.

3. Atmospheric Correction of MERIS Images over Inland Water Bodies

Key Points

- *Atmospheric correction methods for inland waters cannot rely on site independent* a priori *knowledge of the water leaving radiance.*
- *When converting from a radiance image to a reflectance image the reference sun irradiance spectrum that is used to calibrate the sensor must be used in the correction.*
- *MERIS images of inland water bodies can be corrected accurately by taking advantage of dense dark vegetation surrounding the impoundment.*

3.1 Introduction

Many relationships have been established between the concentrations of colour producing water quality parameters and the sub-surface irradiance reflectance ($R(0^-)$). As 90% of the total radiance from a scene over a water body entering a sensor comes from the atmospheric path radiance (Vidot & Santer 2005) the accuracy of the atmospheric correction has a significant effect on the final accuracies of estimated water quality parameter concentrations. The purpose of the atmospheric correction is to convert top of atmosphere (TOA) radiances into water leaving radiance, thence above water reflectance (R_{app}), and then into the below surface water reflectance $R(0^-)$. There are many ways to approach the correction procedure, but they all rely on *a priori* knowledge of either the atmospheric properties or the water leaving radiance.

Three strategies for the atmospheric correction were considered:

1. Use the MERIS standard normalised surface reflectance product (MER_FR_2P) and correct for the air-water interface to obtain an $R(0^-)$ image.

2. Use the MERIS Calibrated TOA Radiance product (MER_FR_1P) and correct to $R(0^-)$ using *c-WOMBAT-c* (coastal Waters and Ocean MODTRAN-4 Based Atmospheric correction) software (Brando & Dekker 2003).

3. Use the MERIS MER_FR_1P product and the BEAM MERIS Case-2 Waters Eutrophic Lakes Processor (MC2WEUL) Plug-in (Doerffer & Schiller 2008) to correct to R_{app} and then correct for the air-water interface to obtain a $R(0^-)$.

These three strategies are representatives of global, regional and site specific atmospheric correction approaches. The MERIS standard normalised surface reflectance product uses a single algorithm for all seasons and environments, the BEAM MERIS Case-2 Waters approach has three parameterisations to deal with different lake water types and the c-WOMBAT-c approach allows the user to tune the parameters to suit either image or *in situ* data. The approaches also vary in terms of the required knowledge of the user and their ability to control the outcome.

This chapter addresses the first objective listed in §1.3. It details the *in situ* spectroradiometric observations that were made as part to the fieldwork that was described in Chapter 2. The chapter describes the theoretical basis of the three atmospheric correction approaches and applies those approaches to MERIS images of the three study sites. The chapter shows that the MERIS standard normalised surface reflectance product was unsuitable for the study sites as the difference between the assumed and actual suspended particulate matter (SPM) and NIR reflectance relationship was too large. Likewise, the BEAM MERIS Case-2 Waters Eutrophic Lakes Processor substantially over-corrected the spectra in the visible wavelengths. For Burdekin Falls Dam the shape of the resultant spectra were consistent with the *in situ* observations, but a marked difference in both the shape and scale of the corrected Fairbairn Dam images was found. In both cases the differences were substantial enough to exclude this approach. The *c-WOMBAT-c* correction approach was examined and then modified to replace the MODTRAN-4 (Berk et al. 1999) radiative transfer code with faster and more accurate 6S code (Kotchenova & Vermote 2007; Kotchenova et al. 2006). The dense dark vegetation (DDV) that was adjacent to the water bodies was then used as a reference to allow the most appropriate aerosol optical thickness to be selected for the atmospheric correction.

3.2 Fieldwork Activities

In situ data for the atmospheric correction assessment were collected at the study sites during 2008 and the obtained data are summarised in Table 3-1 and the station locations are shown in Figure 3-2 and Figure 3-1. Due to instrument malfunction no spectroradiometric observations were made at Wivenhoe Dam.

Table 3-1 The *in situ* data measured at the two study sites.

Study site	Fieldwork dates	Measurement Stations	Water Quality Parameter Concentrations	AOP Measurements	Station Locations
Fairbairn Dam	8-10 Oct 2008	6	Yes	Yes	Figure 3-1
Burdekin Falls Dam	13-15 Oct 2008	11	Yes	Yes	Figure 3-2

Two RAMSES spectroradiometers were mounted in a cage. One spectroradiometer was fitted with a cosine collector and was orientated in the cage to measure the downwelling irradiance (E_d) and one radiance collector was orientated to measure the upwelling radiance (L_u). The cage was lowered on the unshaded side of the vessel to minimize the shading effects. For each station with spectroradiometric observations, simultaneous measurements of downwelling irradiance (E_d) and upwelling radiance (L_u) were combined to calculate the above surface irradiance reflectance (R_{app}). Observations for stations 9-11 at Burdekin Falls Dam were made within ninety minutes of the acquisition of the 15th October MERIS image.

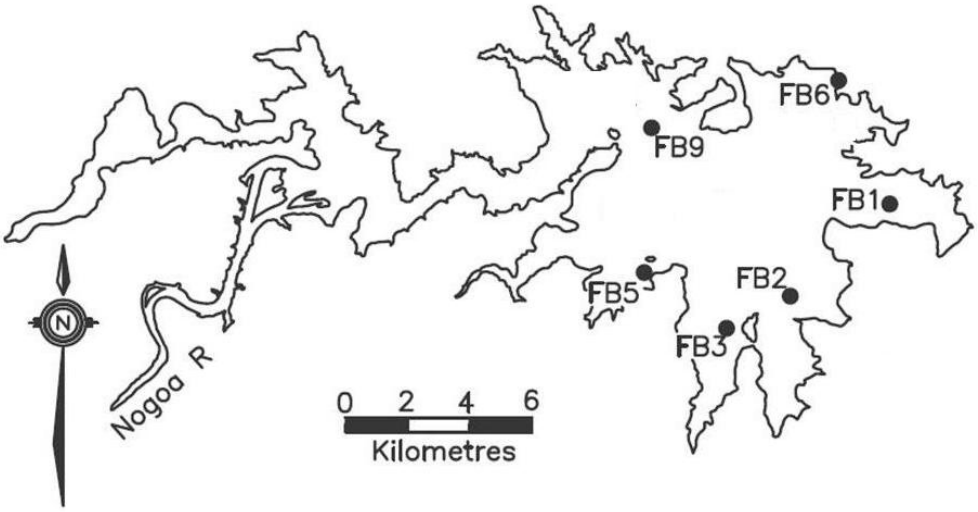

Figure 3-1 Location of the in situ spectroradiometric observation sites for the October 2008 fieldwork activities on Fairbairn Dam. Due to adverse wave conditions spectroradiometric observations were not taken at Stations 4, 7, 8 and 10.

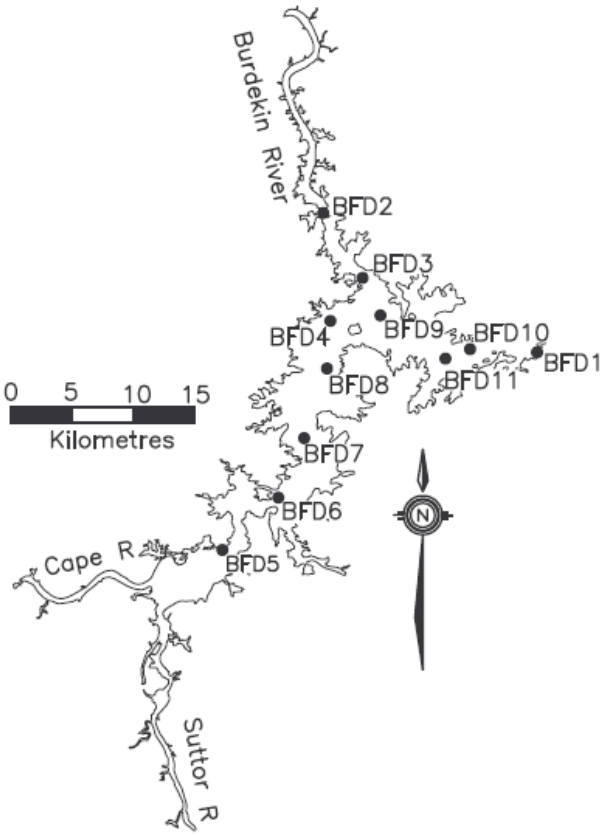

Figure 3-2 Location of the *in situ* spectroradiometric observation sites for the October 2008 fieldwork activities on Burdekin Falls Dam. Observations at stations 9-11 were made within 1½ hours of the MERIS image of 15th October.

3.3 Image Data

Appendix B details the level 1b full resolution cloud free MERIS images obtained for the study sites.

3.4 *In situ* Spectroradiometric Data

The results of the *in situ* spectroradiometric observations are shown below in Figure 3-3 and Figure 3-4. The plotted spectra are the mean spectra for the observations at each station; the standard deviation of the mean is shown to indicate the variability in the observations. The higher variability in the spectra for the first four stations at Fairbairn Dam is a result of the choppy surface conditions at the time of the observations.

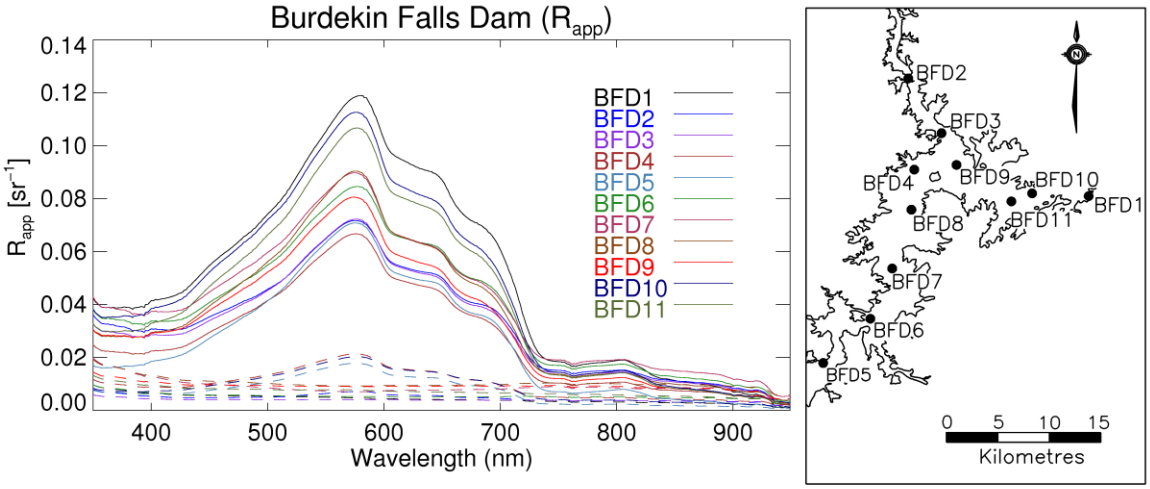

Figure 3-3 The mean R_{app} spectra for the eleven stations at Burdekin Falls Dam. Dashed lines show the standard deviation of the measured spectra.

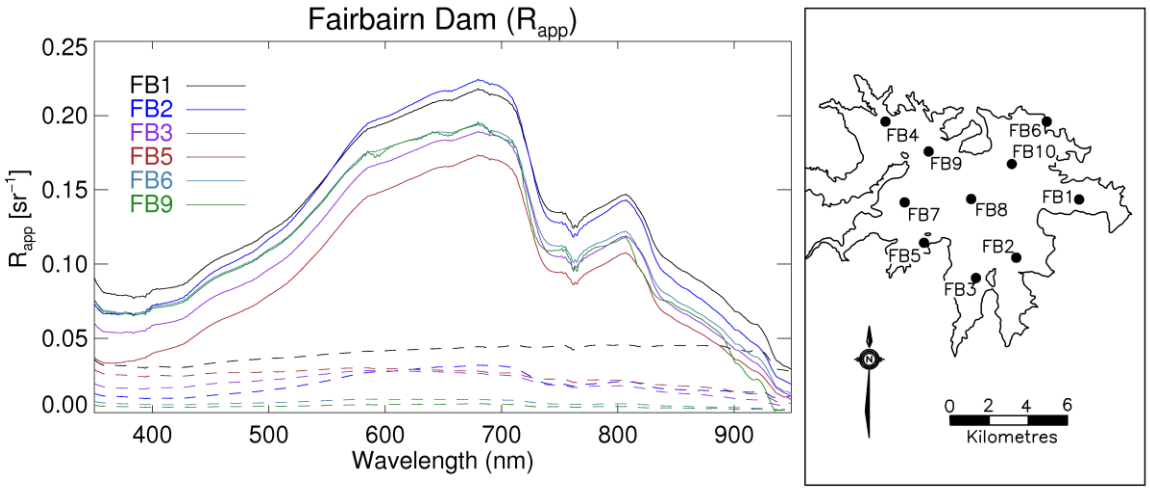

Figure 3-4 The mean R_{app} spectra for six stations at Fairbairn Dam. Dashed lines show the standard deviation of the measured spectra.

The observed spectra were convolved with the MERIS band response function (Bourg 2004) to create spectra for comparison with the image data set.

3.5 MERIS Standard Product

3.5.1. Theoretical Basis

The MERIS case-II water atmospheric correction (Moore et al. 1999) uses reflectance ratios of three NIR wavelengths and tunes the values for optical depth, Ångström coefficient and SPM concentration using two non-linear equations. It uses a devised *a priori* relationship between the above water reflectance ratio ($\frac{\rho_w(775nm)}{\rho_w(865nm)}$) and the SPM concentration. This presumes that the SPM SIOP is known prior to the correction.

The simplest atmospheric correction algorithms for case-I waters presume that the water leaving reflectance in the NIR (700-1000nm) is negligible and use the radiance measured in this range to derive properties of the atmosphere. However, the MERIS case-II water atmospheric correction considers case-II waters as bright pixels that still have appreciable reflectance in the NIR.

The algorithm considers that the TOA reflectance (ρ_t) is made up of contributions from five sources; Rayleigh scattering (ρ_r), aerosol scattering (ρ_a), the interaction of Rayleigh scattering

and aerosol scattering (ρ_{ra}), sun glint (ρ_g) and water (ρ_w) multiplied by the diffuse atmospheric transmittance (t) .

$$\rho_t(\lambda) = \rho_r(\lambda) + \rho_a(\lambda) + \rho_{ra}(\lambda) + \rho_g(\lambda) + t\rho_w(\lambda) \quad (3\text{-}1)$$

Sun glint can be eliminated by correct sun, target and sensor geometric screening, ρ_{ra} is ignored (Gordon & Wang 1994) and the single scattering approximation (Gordon 1978) is made to turn ρ_a into ρ_{as}:

$$\rho_t(\lambda) = \rho_r(\lambda) + \rho_{as}(\lambda) + t\rho_w(\lambda) \quad (3\text{-}2)$$

In case-I waters ρ_w becomes zero in the NIR and ρ_r can be calculated. The ratio of two Rayleigh corrected NIR bands ($\varepsilon_{as}[\lambda_1, \lambda_2] = \frac{\rho_{as}(\lambda_1)}{\rho_{as}(\lambda_2)}$) can be used to calculate the Gordon and Wang (1994) spectral exponent (c):

$$c = \ln\left(\frac{\varepsilon_{as}[\lambda_1, \lambda_2]}{\left(\lambda_1 / \lambda_2\right)}\right) \quad (3\text{-}3)$$

Furthermore ρ_{as} can be extrapolated at any wavelength to retrieve the water leaving reflectance.

$$\rho_w(\lambda) = \frac{\left\{\rho_t(\lambda) - \rho_r(\lambda) - \rho_{as}[\lambda_2]\exp\left[c\frac{\lambda}{\lambda_2}\right]\right\}}{t} \quad (3\text{-}4)$$

In this case the transmission can be approximated by $t = \exp\left[-\frac{(\tau_r 0.5 + \tau_{oz})}{\cos\theta_V}\right]$ where τ_r is the Rayleigh optical thickness, τ_{oz} is the ozone optical thickness and the cosine of the view angle ($\cos\theta_v$) is an approximation of the path length.

In the case of $\rho_w(NIR) \neq 0$, the ratio of the Rayleigh corrected NIR bands is not just dependent on the aerosol scattering.

$$\varepsilon[\lambda_1,\lambda_2]=\frac{\rho_{as}(\lambda_1)+t\rho_w(\lambda_1)}{\rho_{as}(\lambda_2)+t\rho_w(\lambda_2)} \tag{3-5}$$

The Moore et al. (1999) algorithm assumes that the reflectance in the NIR bands is a function of the SPM concentration.

$$\rho_w = f\frac{b_{bw}+b_{bSPM}SPM}{a_w+a_{SPM}SPM} \tag{3-6}$$

The case-1 water simplification ($\frac{b_b}{a+b_b}\approx\frac{b_b}{a}$ if it is < 0.3) is made because the absorption of water dominates strongly in the NIR. Because water absorption increases, then the ratio of ρ_w will be greater than 1 and approximately equal to 2 for the MERIS bands. Then $\varepsilon[\lambda_1,\lambda_2]$ will be close to 1 and can be approximated to

$$\varepsilon[\lambda_1,\lambda_2]=\varepsilon_{as}[\lambda_1,\lambda_2]+0.5t\frac{\rho_w(\lambda_1)}{\rho_{as}(\lambda_2)} \tag{3-7}$$

Since the measured ratio (ε) is always greater than the actual ratio (ε_{as}) in turbid waters the Ångström exponent will be overestimated, meaning that ρ_{as} is overestimated and ρ_w is underestimated or even negative. This error will be worse at lower wavelengths.

Turbid water is identified by processing $\rho_w(705)$ based on the false no NIR reflectance assumption for an approximation. If this is above 0.001 (about 1g m^{-3}) then it is flagged.

If the band ratio at a given concentration of SPM is defined as

$$\varepsilon_w(SPM)=\varepsilon_w[\lambda_1,\lambda_2]=\frac{\rho_w[\lambda_1,SPM]}{\rho_w[\lambda_2,SPM]} \tag{3-8}$$

From Equation (3-4) the Rayleigh corrected reflectance (ρ_{rc}) becomes

$$\rho_{rc}[\lambda_1]=t\rho_w[\lambda_1,SPM]+\rho_{as}[\lambda_1]=t\rho_w[\lambda_2,SPM]\varepsilon_w(SPM)+\rho_{as}[\lambda_2]\exp\left\{c\left[\frac{\lambda_1}{\lambda_2}\right]\right\} \tag{3-9}$$

where the ρ_w value is modelled by an *a priori* relationship.

The reflectance can be modelled by three parameters, SPM, *c* and $\rho_{as}[\lambda_2]$ and can be estimated using an iterative solution of three pairs of NIR bands.

3.5.2. Application to MERIS Images

Two MERIS standard normalised surface reflectance product (MER_FR_2P) images were obtained. The first was of Wivenhoe Dam (5th July 2007) and the second contained Burdekin Falls Dam and Fairbairn Dam (15th October 2008). Transects were taken down the centre of the three water bodies and example spectra are shown in Figure 3-5.

The transect taken down the centre of the Wivenhoe Dam 5th July 2007 image shows consistently negative reflectances for wavelengths below 500 nm. The vast majority of these pixels have been flagged as going through the case-II water correction. (Some pixels that appear to be mixed pixels with water and land go through the case-I correction). It would appear that the Ångström exponent is being overestimated even though the pixel has been through the case-II correction that should account for this.

The transect taken down the centre of the Burdekin Falls Dam 15th October 2008 image shows the majority of the pixels going through the case-II water correction and returning positive reflectance values. By comparing these spectra to the measured spectra shown in Figure 3-3 it can be seen that the algorithm has still over-corrected the spectra, but the brightness of the target has allowed the majority of the spectra to retain positive values.

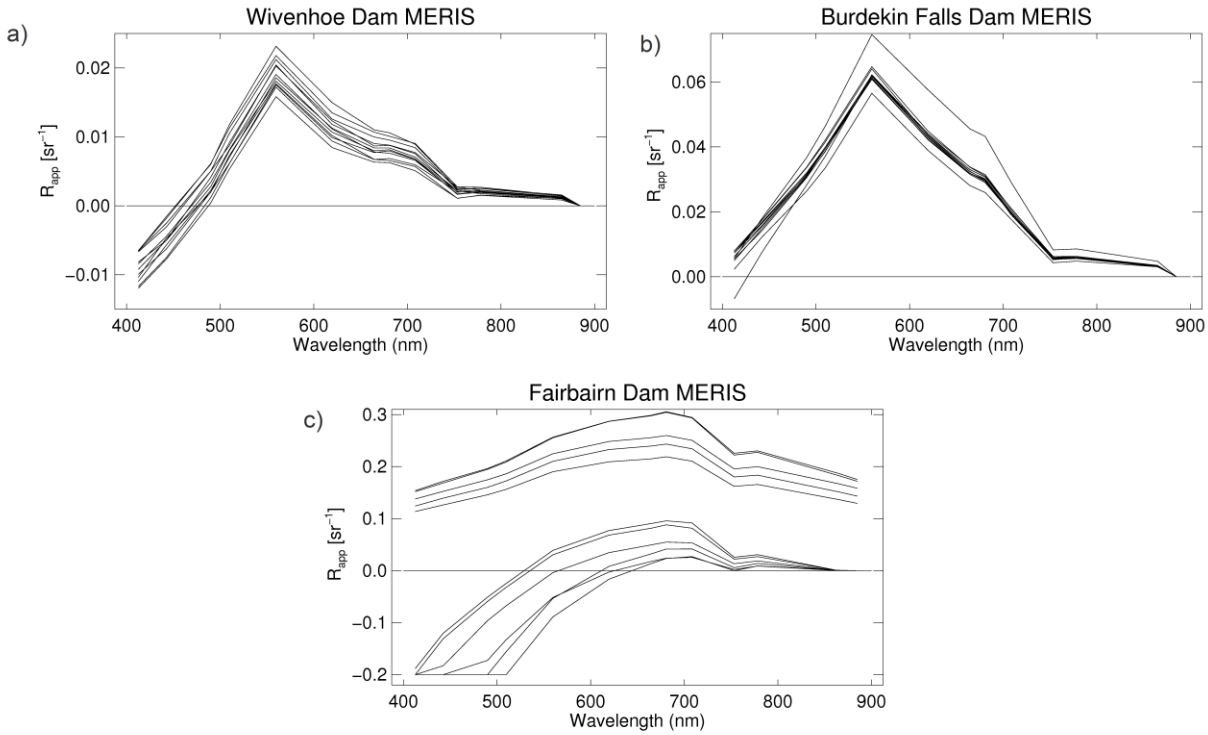

Figure 3-5 Example spectra for water pixels for the MERIS standard normalised surface reflectance product (MER_FR_2P) images. a) Wivenhoe Dam 5th July 2007, b) Burdekin Falls Dam 15th October 2008 and c) Fairbairn Dam 15th October 2008.

The example spectra shown for Fairbairn Dam show two distinct behaviours. Those spectra that were processed using the case-II water correction have been over-corrected in a similar way to the other two study sites. The other spectra have been identified as land pixels by the MERIS processor and have been corrected as such. Although there is 5-7 days difference between the *in situ* measurements and the image acquisition, the resultant spectra are similar to the *in situ* measured spectra shown in Figure 3-4. The MERIS land atmospheric correction uses dense dark vegetation in the scene to obtain the aerosol model parameters for the scene (Santer et al. 2006).

For all three study sites it was apparent that the Ångström exponent was being overestimated. To examine the reflectance ratios between 708nm, 778nm and 865nm on which the correction relies, reflectances were calculated using the simplified Gordon model and the measured Wivenhoe IOPs. The effect of chlorophyll *a* at these wavelengths was ignored, although it is not actually valid at 708nm, so the absorption and the backscatter should be proportional to the TSM only.

Figure 3-6 shows a variation of 35-80% in 708:865 and 9-38% in 778:865 with the most marked variation at lower TSM concentrations. These variations from an assumed constant relationship would flow through to the value for SPM, then $\rho_w(865)$, hence $\rho_{as}(865)$ and c as well.

The difference between the *a priori* SPM and NIR reflectance relationship and one that would be appropriate for the Wivenhoe water body is obviously too large to allow the MERIS standard reflectance product to be used.

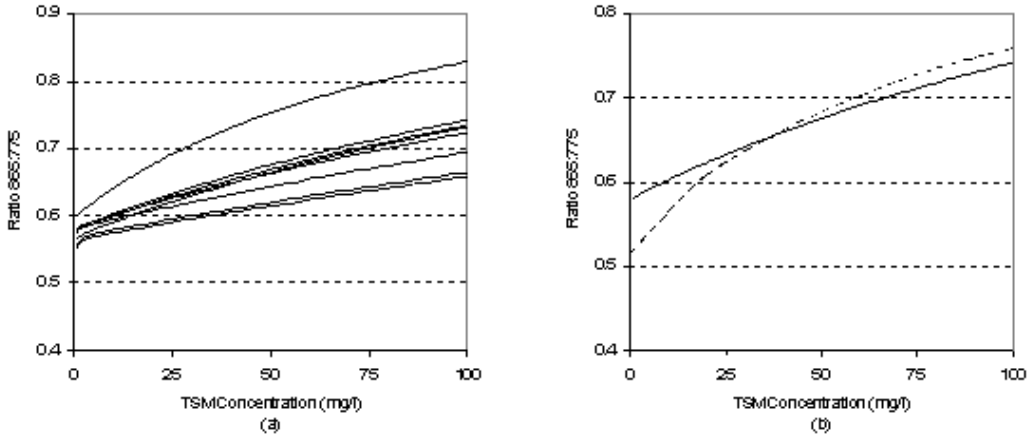

Figure 3-6 (a) The *ρ(865):ρ(778)* ratio calculated using the linear Gordon model and the measured Wivenhoe IOPs. (b) A typical *ρ(865):ρ(778)* ratio curve for the measured Wivenhoe IOPs (solid) plotted with the assumed *ρ(865):ρ(778)* ratio curve reported by Moore et al. (1999) (dashed).

3.6 c-WOMBAT-c

3.6.1. Theoretical Basis

The c-WOMBAT-c algorithm uses the theoretical framework established by de Haan et al. (1999) using atmospheric parameters generated by the radiative transfer code MODTRAN-4.

Top of Atmosphere Radiance to R_{app}

The algorithm considers the TOA radiance seen by the sensor ($L_{rs,t}$) to be the sum of the target radiance (L_t), the atmospheric path radiance (L_{pa}) and the background path radiance (L_{pb}). The target radiance is made up from contributions by the direct solar flux reflected by the target and directly transmitted to the sensor, the scattered flux from the background reflected by the target

and directly transmitted to the sensor and the scattered solar flux reflected by the target and directly transmitted to the sensor.

For unidirectional monochromatic sunlight having a flux per unit area equal to πF, the path radiance for a sensor at the top of the atmosphere is a function of the sensor viewing angle (θ_v) and a reflectance function that is dependent on the sun-target-sensor geometry.

$$L_{pa} = R(\theta_v, \theta_s, \phi_v - \phi_s)\theta_v F \tag{3-10}$$

If the target reflectance is denoted by R_{app} and the average background reflectance by A_{app} then the total surface irradiance (E_{ad}) for an atmosphere of optical depth b is:

$$E_{ad} = \frac{\cos(\theta_s)\left[\exp\left(\frac{-b}{\cos(\theta_s)} + t_d(\theta_s)\right)\right]\pi F}{1 - s^* A_{app}} \tag{3-11}$$

where t_d is the diffuse transmittance from the sun towards the surface, θ_s is the sun zenith angle and s^* is the spherical reflectance for illumination from below which is a measure of the average reflection properties of the atmosphere.

Making use of the reflectances, the target and background radiance contributions become:

$$L_b = \frac{1}{\pi} A_{app} \exp\left(\frac{-b}{\cos(\theta_v)}\right) E_{ad} \tag{3-12}$$

$$L_t = \frac{1}{\pi} R_{app} \exp\left(\frac{-b}{\cos(\theta_v)}\right) E_{ad} \tag{3-13}$$

Lastly the background path radiance is

$$L_{pb} = \frac{1}{\pi} A_{app} d_d^*(\theta_v) E_{ad} \tag{3-14}$$

where d_d^* is the diffuse transmittance from the surface to the top of the atmosphere (Equation 12 of de Haan et al.(1999) shows this as the total transmittance (d^*) but the derivation of subsequent relationships show it must be d_d^*). The preceding equations are combined to solve for the target reflectance:

$$R_{app} = \frac{L_{rs,t} - L_{pa} - \left[L_{rs,t} - L_{rs,b}\right]\exp\left[\frac{-b}{\cos(\theta_v)}\right] d_d^*(\theta_v)}{\cos(\theta_s)\, d^*(\theta_v)\, t(\theta_s) F + s^*\left[L_{rs,b} - L_{pa}\right]} \quad (3\text{-}15)$$

R_{app} to $R(0^-)$

R_{app} is made up of the reflectance from the surface R_{int} and R_{app} :

$$R_{app} = R_{\text{int}}(\theta_v) + \frac{t_{\text{int}}^*(\theta_v)\, R(0^-)\left[\left(1 - F_{diff}\right) t_{\text{int}}(\theta_s) + F_{diff} < t_{\text{int}} >\right]}{1 - s_{\text{int}}^* R(0^-)} \quad (3\text{-}16)$$

where t^* is the transmission from water to air, t the transmission from air to water (this differs from diffuse and direct sources) and s^* which is the reflectance of the diffuse upwelling radiation back down (Austin (1974) calculates it at 0.485 to 0.463 as the wind speed goes from 0-16 m/s and Dekker (1993, p. 68) chooses it to be 0.48). The v is the viewing angle and s is the solar angle.

The transmittance from below is a function of the radiance to irradiance conversion factor (Q), the refractive index of the water (n_w) and the Fresnel reflectance ($r(\theta_v)$).

$$t_{\text{int}}^*(\theta_v) = \frac{\pi\left[1 - r(\theta_v)\right]}{Q n_w^2} \quad (3\text{-}17)$$

The n_w^2 factor describes change in the solid angle by refraction and π/Q describes the bidirectional effects of the water body. The other transmittances are 1- r either in that direction or averaged over all angles.

R_{app} is obtained after the atmospheric correction and rearranging this gets the $R(0^-)$

$$R(0^-) = \frac{d_1 + d_2 R_{app}}{d_3 + d_4 R_{app}} \tag{3-18}$$

where d_1- d_4 are the interface correction co-efficients:

$$d_1 = -\pi r(\theta_v) L_{ad}(\theta_v, \varphi_v) / E_{ad} \tag{3-19}$$

$$d_2 = 1 \tag{3-20}$$

$$d_3 = t^*_{\text{int}}(\theta_v)[(1 - F_{dif}) t_{\text{int}}(\theta_s) + F_{dif} < t_{\text{int}} >] - s^*_{\text{int}} \pi r(\theta_v) L_{ad}(\theta_v, \varphi_v) / E_{ad} \tag{3-21}$$

$$d_4 = s^*_{\text{int}} = 0.48 \tag{3-22}$$

3.6.2. Implementation with MODTRAN-4

After the user defines the viewing geometry, the target reflectance, the aerosol, atmospheric and illumination parameters MODTRAN-4 will return four radiance spectra:

1. $L_{rs,t}$ the radiance seen by the sensor
2. L_{path} the total path radiance
3. L_{gd} the total ground radiance that has been reflected by the ground
4. L_{dir} that portion of the ground radiance that is a result of the direct illumination of the surface.

When the simulation is looking towards space then MODTRAN-4 only returns the path radiance.

Top of Atmosphere Radiance to R_{app}

Sufficient information to solve the functions in §3.6.1 is generated by running the MODTRAN-4 code six times using the conditions shown in Table 3-2.

Table 3-2 The purposes and conditions for the six MODTRAN-4 runs used by the c-WOMBAT-c atmospheric correction algorithm.

Correction Purpose	Surface albedo	Viewer position	View direction
Radiance to R_{app}	0.05	Sensor	Sensor to Target
Radiance to R_{app}	0.0	Sensor	Sensor to Target
Radiance to R_{app}	0.5	Sensor	Sensor to Target
Radiance to R_{app}	1.0	Sensor	Sensor to Target
R_{app} to $R(0^-)$	0.05	At ground	Sensor to Target
R_{app} to $R(0^-)$	0.05	At ground	Target to Zenith

The equation for R_{app} shown previously (Equation 3-15) is rearranged.

$$R_{app} = \frac{c_1 + c_2 L_{rs,t} + c_3 L_{rs,b}}{c_4 + c_5 L_{rs,b}} \tag{3-23}$$

The co-efficients c_1-c_5 are defined as follows:

$$c_1 = -L_{pa} \tag{3-24}$$

$$c_2 = 1 + \exp[(b-\tau)/\cos(\theta_v)]d_d^*(\tau,\theta_v) \tag{3-25}$$

$$c_3 = 1 - c_2 \tag{3-26}$$

$$c_4 = \cos(\theta_s)d^*(\tau,\theta_v)t(\theta_s)F - L_{pa}s^* \tag{3-27}$$

$$c_5 = s^* \tag{3-28}$$

The values of the co-efficients are obtained from the MODTRAN-4 runs of target reflectance 0.0, 0.5 and 1.0.

$$c_1 = -L_{path}(0.0) \tag{3-29}$$

$$c_2 = 1 + \frac{L_{path}(0.5) - L_{path}(0.0)}{L_b(0.5)} \tag{3-30}$$

$$c_3 = 1 - c_2 \tag{3-31}$$

$$c_4 = (1-c_5)\left(L_{ground}(1.0) + L_{pa}(1.0) - L_{pa}(0.0)\right) - L_{pa}(0.0)c_5 \tag{3-32}$$

$$c_5 = s^* = \frac{2L_{gd}(0.5) - L_{gd}(1.0)}{L_{gd}(0.5) - L_{gd}(1.0)} \tag{3-33}$$

R_{app}* to *$R(0^-)$

From before (Equation 3-18) the subsurface radiance is:

$$R(0^-) = \frac{d_1 + d_2 R_{app}}{d_3 + d_4 R_{app}} \tag{3-18}$$

where d_1- d_4 are the interface correction co-efficients:

$$d_1 = -\pi r(\theta_v) L_{ad}(\theta_v, \varphi_v) / E_{ad} \tag{3-19}$$

$$d_2 = 1 \tag{3-20}$$

$$d_3 = t^*_{\text{int}}(\theta_v)[(1 - F_{dif})t_{\text{int}}(\theta_s) + F_{dif} < t_{\text{int}} >] - s^*_{\text{int}}\, \pi r(\theta_v) L_{ad}(\theta_v, \varphi_v) / E_{ad} \tag{3-21}$$

$$d_4 = s^*_{\text{int}} = 0.48 \tag{3-22}$$

$r(\theta_v) = \frac{1}{2}\left[\frac{\sin^2(\theta_v - \theta_w)}{\sin^2(\theta_v + \theta_w)} + \frac{\tan^2(\theta_v - \theta_w)}{\tan^2(\theta_v + \theta_w)}\right]$, $\sin(\theta_v) = n_w \sin(\theta_w)$ and n_w =1.333 for fresh water

and $t^*_{\text{int}}(\theta_v) = \frac{\pi[1 - r(\theta_v)]}{Q n_w^2}$, $t_{\text{int}}(\theta_s) = 1 - r(\theta_v)$ and $< t_{\text{int}} >= 1.0 - 0.0615$

Two simulations are made to calculate the *d* coefficients, one pointing along the sensor view at 1.0 metre above a surface of reflectance 0.05 (↓) and the other at the surface looking up (↑).

L_{ad} will be the path radiance looking up ($L_{path}(\uparrow)$).

The diffuse fraction will equal $F_{diff} = 1 - F_{dir} = 1 - \frac{L_{dir}(\downarrow)}{L_{gd}(\downarrow)}$ and the downwelling irradiance be

$$E_{ad} = \frac{\pi L_{rs,t}(\downarrow)}{\rho} = \frac{\pi L_{rs,t}(\downarrow)}{0.05}.$$

3.6.1. Application to MERIS Images

The MODTRAN-4 code requires the user to specify a number of geometric and aerosol characteristics. Table 3-3 below shows the final parameters used for the 15th October 2008 image of Burdekin Falls Dam. The visibility parameter is the most significant and quickly varying parameter, as it controls the aerosol optical thickness (AOT). This value was chosen to give the closest match to the *in situ* overpass stations. To make allowance for image noise and

geo-referencing uncertainty the image spectra for each station are taken to be the average spectra from the four pixels that are closest to the co-ordinates for the *in situ* measurement.

The corrected Burdekin Falls Dam water pixels were compared with the *in situ* spectroradiometric observations and are shown in Figure 3-7. There is a significant anomaly below 500 nm which appears in the spectra corrected with the de Haan et al. formulation in other published work (Bagheri et al. 2005; Sterckx & Debruyn 2004) and is also apparent in Figure 3-8 which is shown in Candiani et al. (2007a). The MERIS instrument performs a calibration every two weeks using diffuser plates illuminated by the Sun. The absolute radiometric gains are calculated by comparing the averaged signal to the on-ground characterisation of the diffuser (ESA 2006). The MERIS sensor is calibrated using the Thuillier et al. (2003) reference sun irradiance spectrum as recommended by the Committee on Earth Observation Satellites (CEOS) (CEOS 2008). This model was compared to the default solar MODTRAN-4 illumination database and a major difference was found around 440 nm (see Figure 3-9). As the sensor gains are calculated with reference to this model the same model must be used to calculate the reflectance spectrum. Figure 3-7 shows that when the correction was re-run using the new reference sun the anomaly was eliminated.

Table 3-3 The initial MODTRAN-4 parameters for the 15th October 2008 image of Burdekin Falls Dam.

Parameter	Value	Source
Atmosphere Model	Tropical†	
Multiple Scattering	At H2	
T-Boundary Temperature	293.15°K	Bureau of Meteorology (BOM) Charters Towers
Illumination	Standard Sun	
CO_2	360ppm	Average Value (No effect in Visible Region)
H_2O	2.971	Obtained from MODIS 07 Product
O_3	0.289 ATM-cm	Obtained from MODIS 07 Product
Aerosol Model	Maritime	Prevailing wind was from the SW
Visibility	75km	Tuned on *in situ* overpass stations
Ground Altitude	0.154km	Burdekin Falls Dam water level RL
Sensor Altitude	799km	MERIS Specifications
Sensor Zenith, Observer φ & λ , UTC time	11.07°	MERIS Image

†Selected Tropical because the main constituent is the water content.

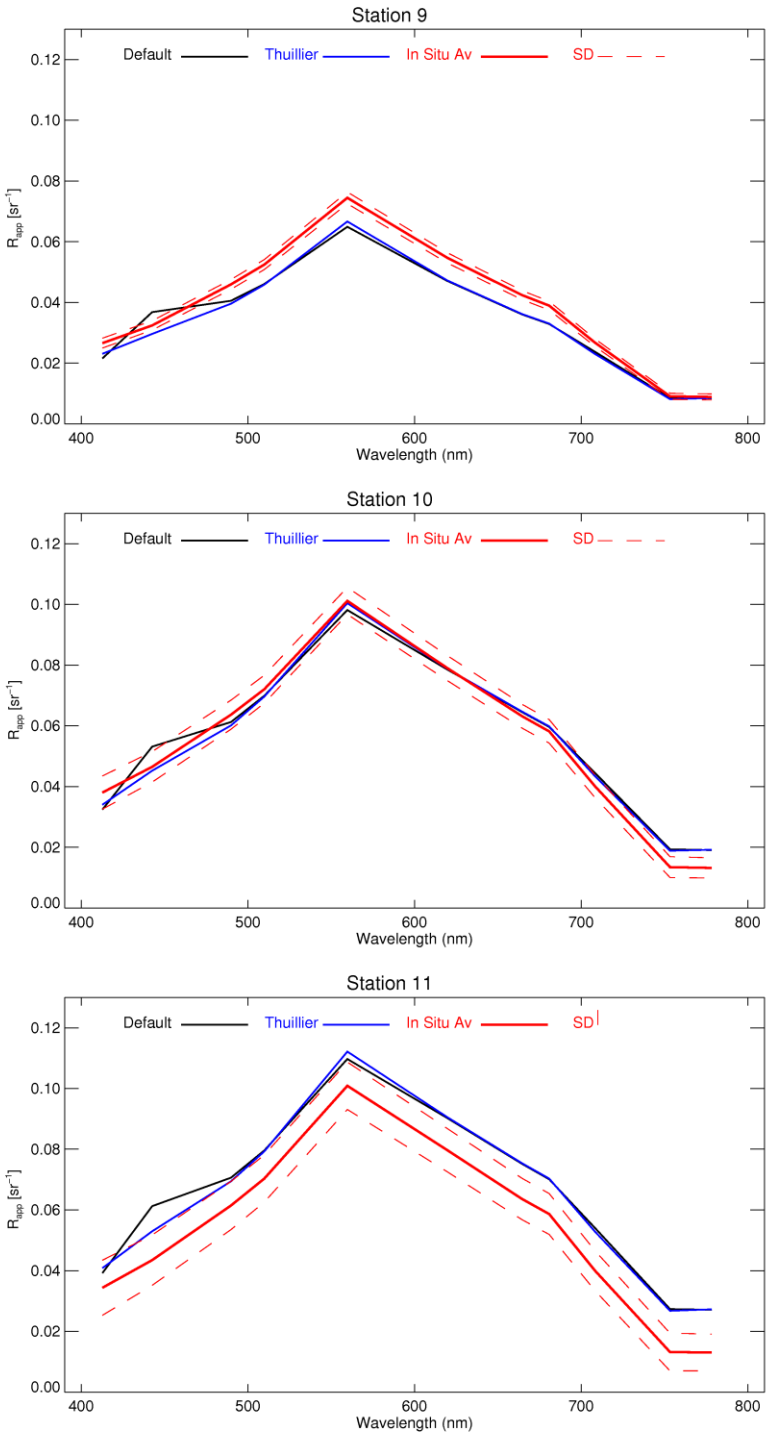

Figure 3-7 Mean above surface reflectance spectra of the corrected Burdekin Falls Dam water pixels at Stations 9-11. The image was corrected using the MODTRAN-4 two stream model and the Thuillier et al (2003) and the MODTRAN-4 default reference sun irradiance. No correction for the adjacency effect has been made.

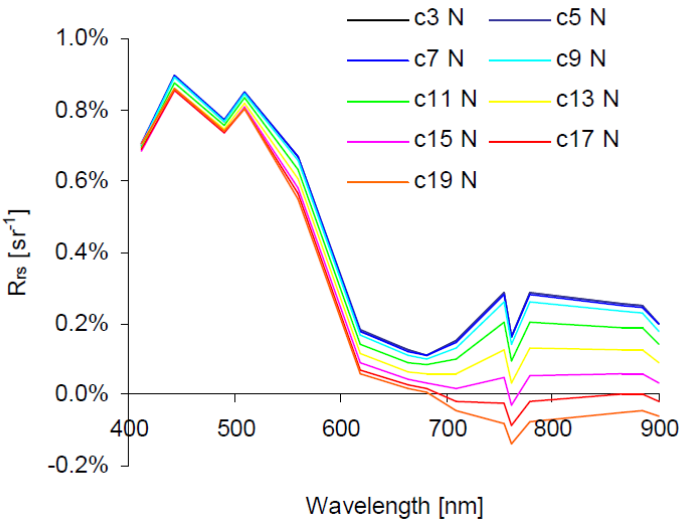

Figure 3-8 Example corrected spectra from Lake Garda as reported by Candiani et al.(2007a)

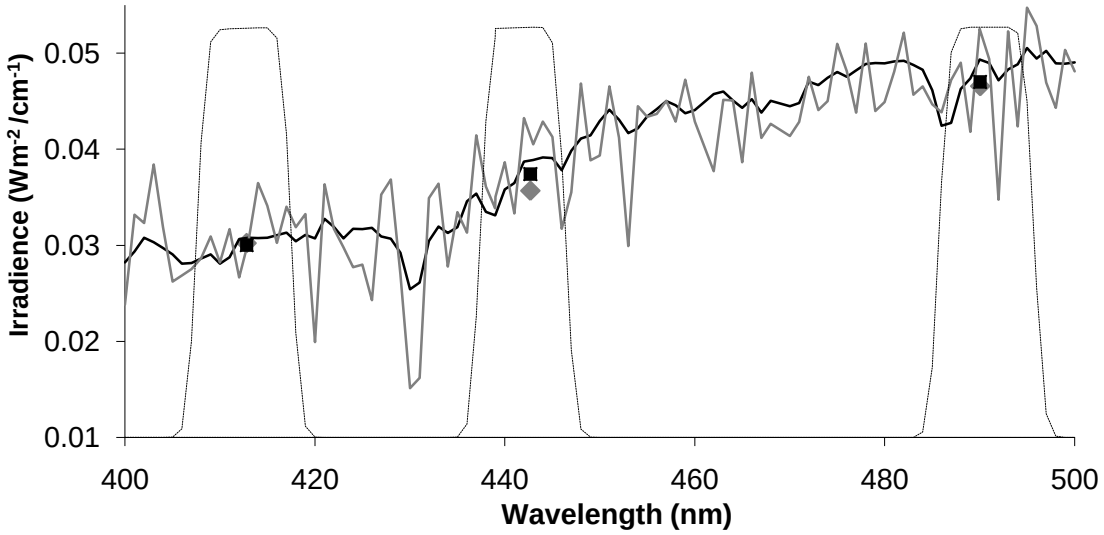

Figure 3-9 Comparison of two MODTRAN solar irradiance databases. The default MODTRAN database (newkur.dat) is shown in grey and the Thuiller database (thurkur.dat) is shown in black. The databases were convolved with the MERIS band response function (shown dotted) to produce estimated values for the default database shown by diamonds and the Thuiller database depicted by squares.

MODTRAN-4 neglects to include the effect of polarisation on the radiance (Kotchenova et al. 2008; Levy et al. 2004) and it is postulated that in the blue section of the visible spectrum the Rayleigh optical thickness is large enough to introduce errors in modelled TOA reflectance. These errors range from 0-0.003 reflectance units and can be positive or negative depending on

the scattering geometry. From Figure 1 in Levy (2004) (reproduced below) it can be seen that at reasonable aerosol loading of AOT = 0.25 there is around 5-8 times the error at 466 nm MODIS channel than there is at 660 nm. Levy uses RT3 radiative transfer code. If this is true, then the size of the anomaly should change with the sun-target-sensor geometry. It was not possible to test this assertion as there are no available *in situ* spectroradiometric observations available for other MERIS images.

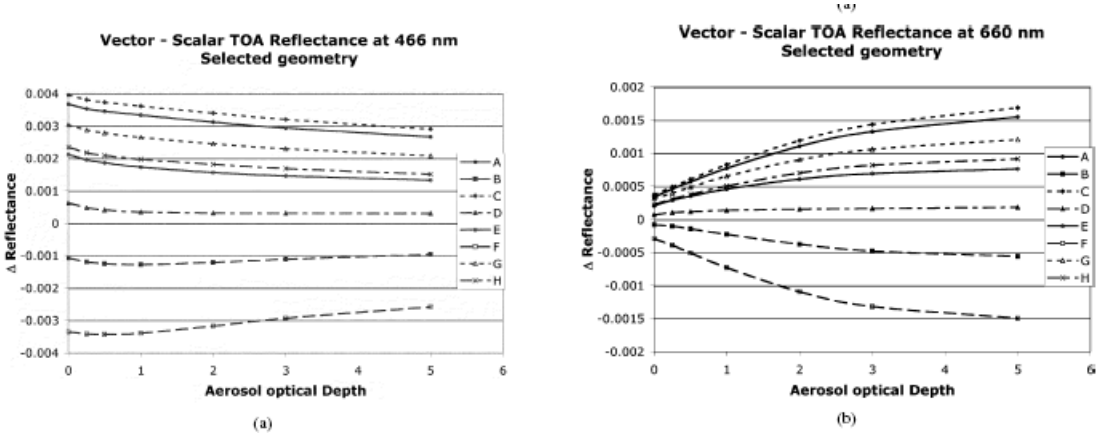

Figure 3-10 Figure 1 from Levy (2004) reflectance error for differing geometries and aerosol loadings at two wavelengths λ = 466nm and λ = 660nm.

An extensive test between 6S, MODTRAN, RT3 and SHARM radiative transfer codes (Kotchenova et al. 2008) found that 6S was the most reliable code for calculations of solar radiation reflected and transmitted by a plane-parallel, non-absorbing molecular atmosphere and so the code was used as a reference to examine the effect of the errors of the other codes.

The errors associated with the retrieved surface reflectance at three wavelengths 412, 440 and 670nm were calculated. The final results have been made available in Excel® files downloadable from http://rtcodes.ltdri.org/Main.htm. In Figure 3-11 below is shown the absolute error for a target reflectance of 0.05 at 90° angle between the view and sun azimuths for sun zenith angles between 58.67° and 23.07° and an AOT = 0.2. These are the closest values reported to the geometry of the MERIS images.

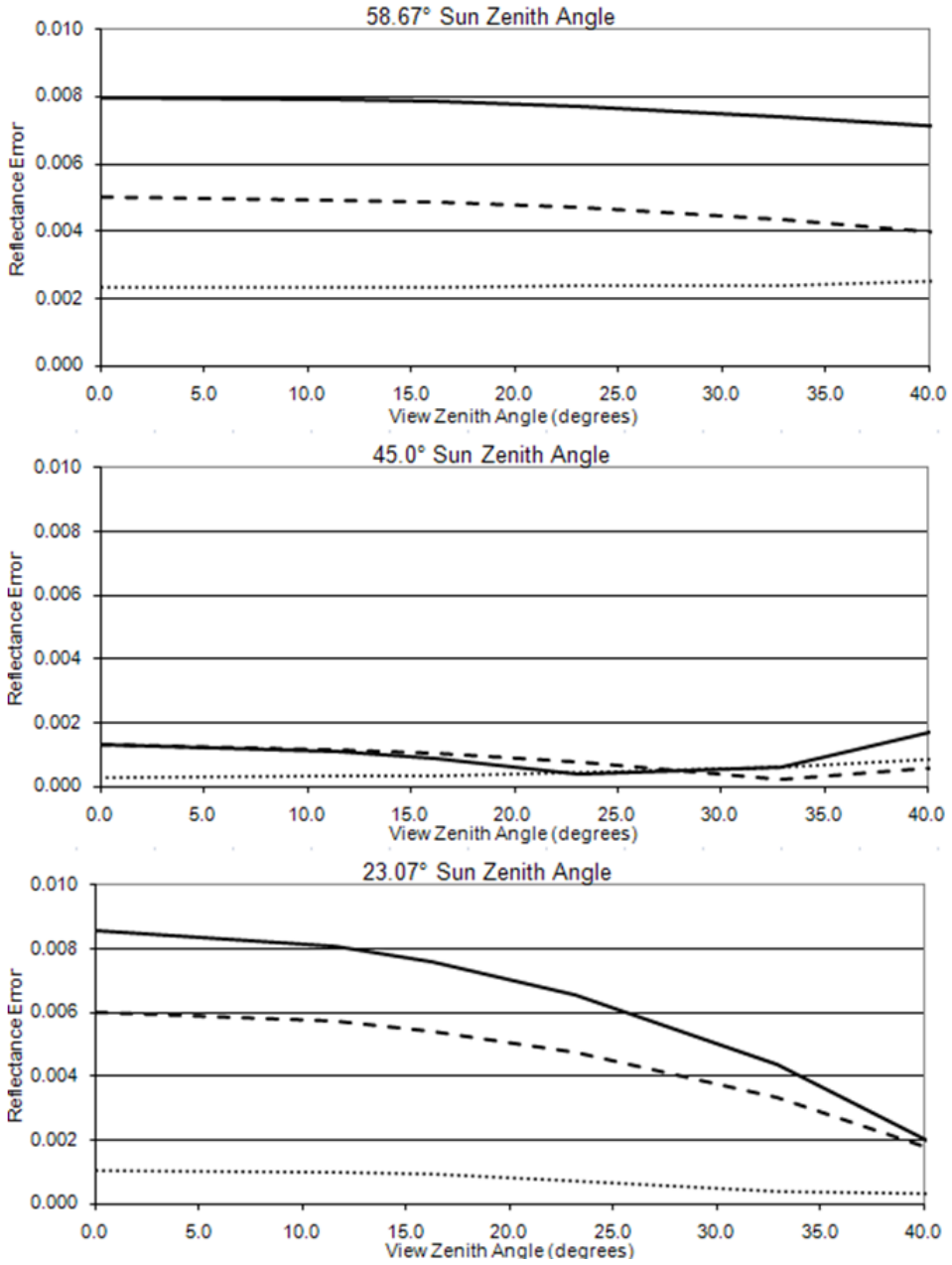

Figure 3-11 The absolute error for a target reflectance of 0.05 at 90° angle between the view and sun azimuths for a sun zenith of angles between 58.67° and 23.07° and a AOT = 0.2 for wavelengths of 412nm (solid), 440nm (dashed) and 670nm (dotted) (Kotchenova et al. 2008).

The error ($\Delta\rho_{surf}$) is defined as $\rho^{bm}\left(\rho_{surf}\right)=\rho^{code}\left(\rho_{surf}\right)+\Delta\rho_{surf}$ where $\rho^{bm}\left(\rho_{surf}\right)$ is the TOA reflectance as a function of the surface reflectance. If $\Delta\rho_{surf}$ is positive then the code is under-calculating the TOA reflectance. That would mean that for a given measured TOA reflectance the code would compensate for the under-calculated modelled TOA reflectance by increasing the

surface reflectance to match this difference. The result would be corrected surface spectra that were too high. Figure 3-12 shows the result of errors for the first two bands being interpolated and the spectra corrected. This only provides a reasonable gross estimate but it is sufficient to show the general trend. In the diagram the dashed lines are the corrected reflectance spectra.

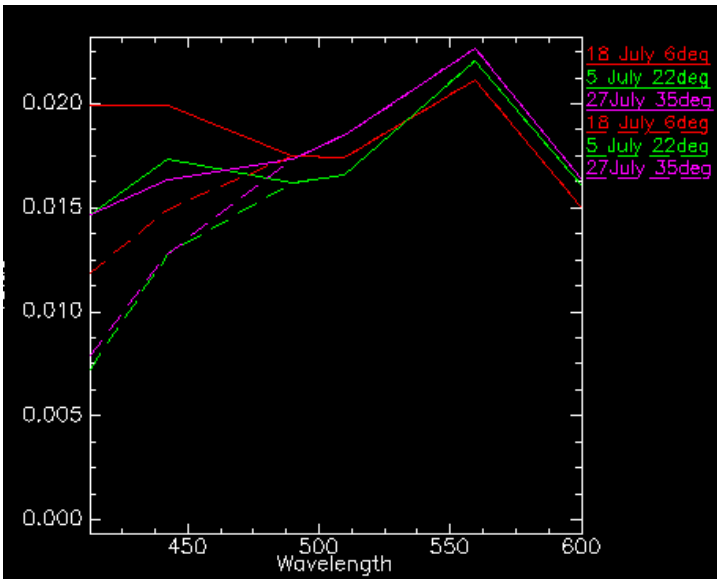

Figure 3-12 Original average reflectance values for three Wivenhoe Dam images (solid lines) and a reasonable gross estimate of the result when the MODTRAN-4 error is removed. The view zenith angles for the images are 18th July = 5.70°, 5th July = 21.73° and 27th July =35.40°.

An alternative explanation may be that the relatively fast scalar option within MODTRAN-4 does not account for the azimuthal dependence of the multi-scattering solar contribution (Acharya et al. 1999). To take this into account the user must select the more accurate but much slower DISORT N-stream method. The primary effect of running the DISORT option is to greatly increase the spherical albedo of the atmosphere for illumination from below and hence the proportion of the TOA radiance that is assigned to the effect of the adjacent surfaces.

The c-WOMBAT-c code was modified to use the 6S radiative transfer code. Once again it was necessary to substitute the default solar irradiance spectrum with the CEOS standard sun irradiance spectrum (Thuillier et al. 2003) to minimise the below 500 nm anomaly. This resulted in reflectance spectra that were a more acceptable fit to the simulated spectra. Examples of these corrected spectra are shown in Figure 3-13.

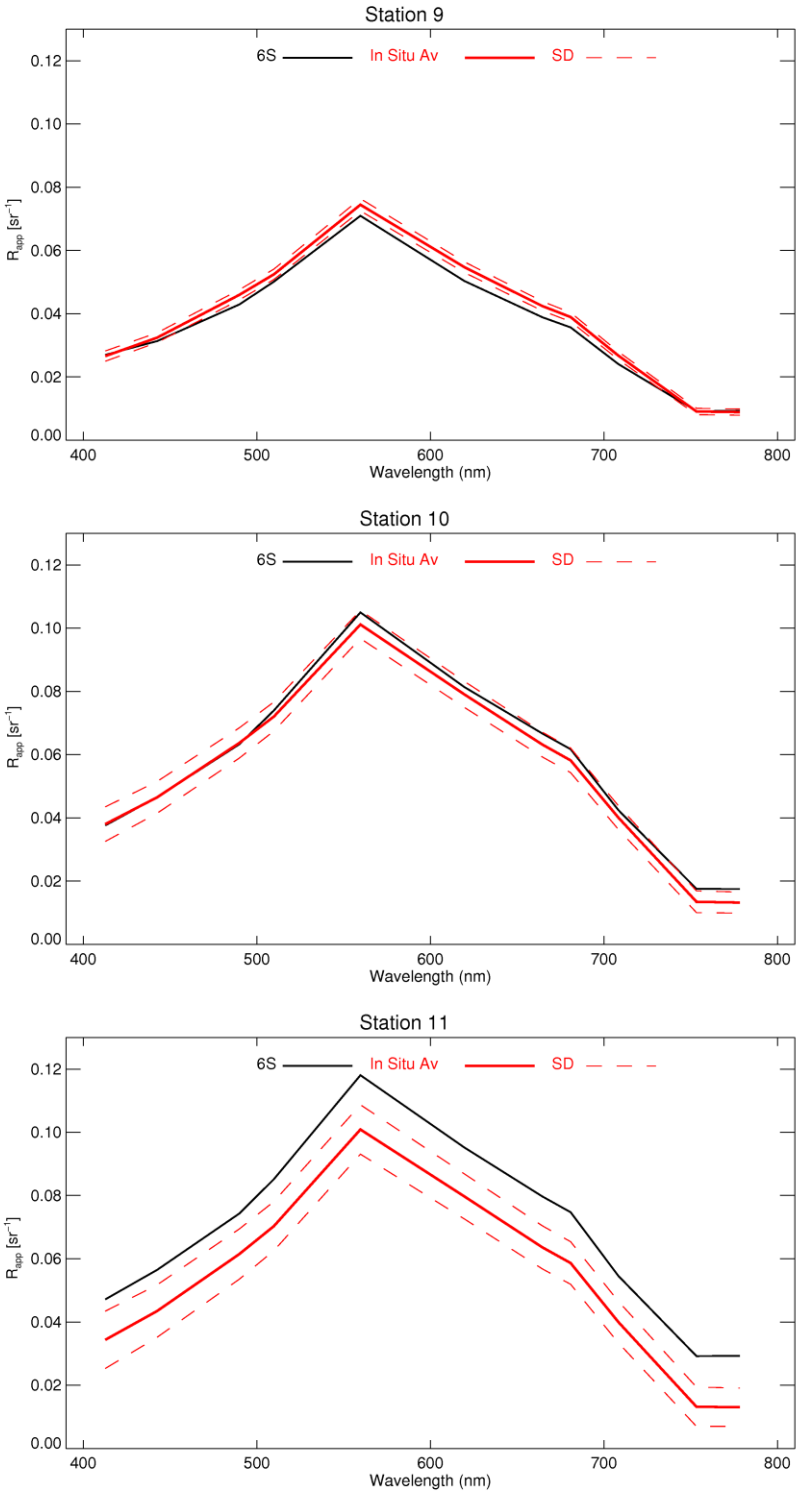

Figure 3-13 Mean above surface reflectance spectra of the corrected Burdekin Falls Dam water pixels at Stations 9-11. The image was corrected using the 6S atmospheric model and the Thuillier et al (2003) reference sun irradiance. No correction for the adjacency effect has been made.

3.7 BEAM Case-2 Regional Processor (Eutrophic Lakes)

The BEAM Case-2 Regional Processor (Doerffer & Schiller 2008) uses a neural network of four hidden layers that was trained on reflectance spectra of unstratified and optically deep water that were generated with the radiative transfer numerical model *Hydrolight*® (Mobley & Sundman 2001). A large range of aerosols and vertical distributions are used in the forward calculations as well as scattering by cirrus clouds at the top of the troposphere. Sunglint and skylight glint have been taken into account but a standard profile of air pressure and ozone has been used. In a separate procedure prior to the application of the neural network the radiance reflectance at the top of the standard atmosphere is calculated from the measured radiance reflectance at the top of the atmosphere by allowing for deviations from the standard profile of the measured ozone and air pressure. However, in the neural network there are no allowances made for polarisation, inelastic scattering or the adjacency effect. The *Hydrolight*® simulated spectra were generated with site specific SIOP values which means the correction procedure will not necessarily be effective above all water bodies.

3.7.1. Application to MERIS Images

The BEAM corrected Burdekin Falls Dam water pixels were compared with the *in situ* spectroradiometric observations and are shown in Figure 3-14. Although there was a substantial over correction in the visible wavelengths the shape of the resultant spectra was consistent with the *in situ* observations.

In contrast, there is a marked difference is both the shape and scale of the corrected Fairbairn Dam images. Due to the cloud cover that was present during the site visit it was not possible to get a direct image-field matchup. The mean of the corrected reflectance from the 29th September and the 15th October 2008 have been used for comparison in Figure 3-15. On all pixels examined the processing flag ATC_OOR (atmospheric correction out of range) is false but the OOTR (out of training range) flag is true. This means that the output of the atmospheric correction neural network (path radiance reflectances and transmittances) were within the expected range, but the water leaving radiance reflectance as submitted to the water NN was outside the range of the

spectra used for training of the NN. As the reflectance inversion part of the processor was not being considered, this warning flag was disregarded.

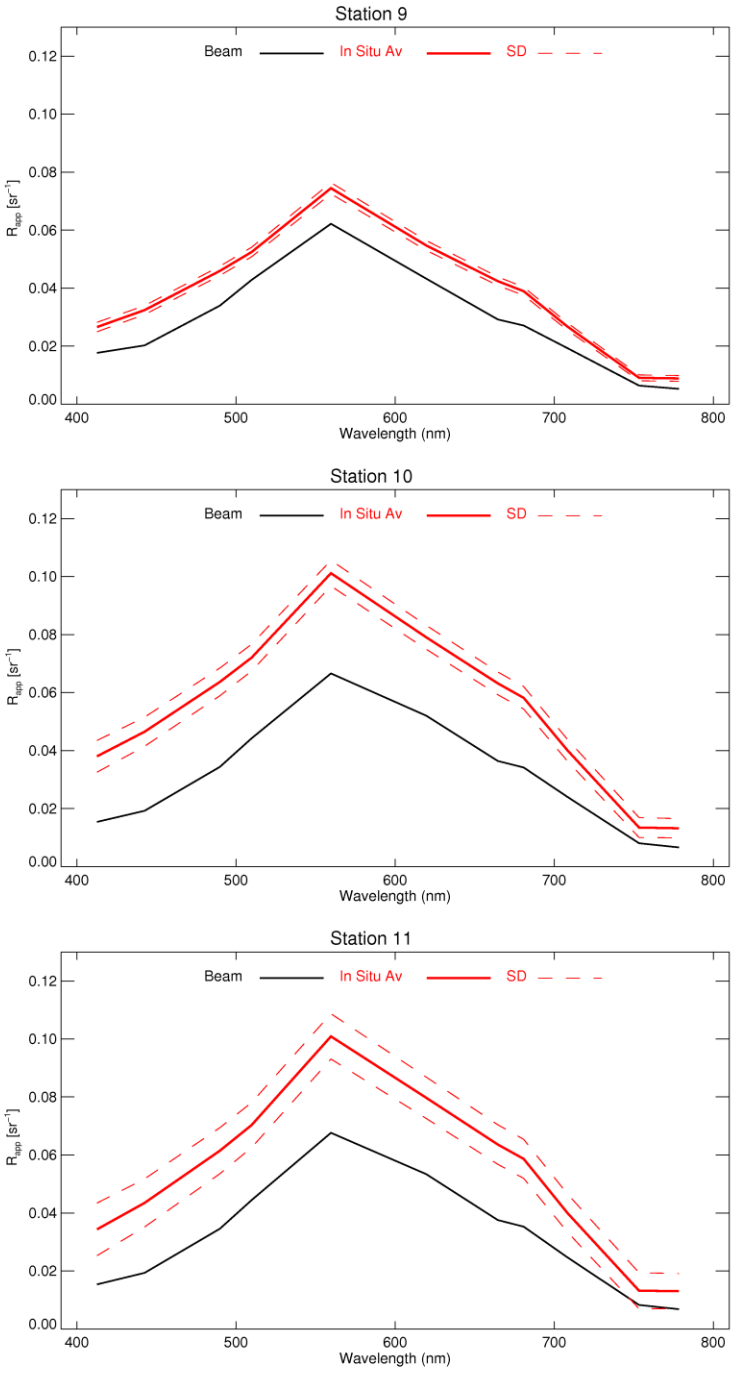

Figure 3-14 Mean above surface reflectance spectra of the corrected Burdekin Falls Dam water pixels at Stations 9-11. The image was corrected using the BEAM Case-2 Regional Processor (Eutrophic Lakes). No correction for the adjacency effect has been made.

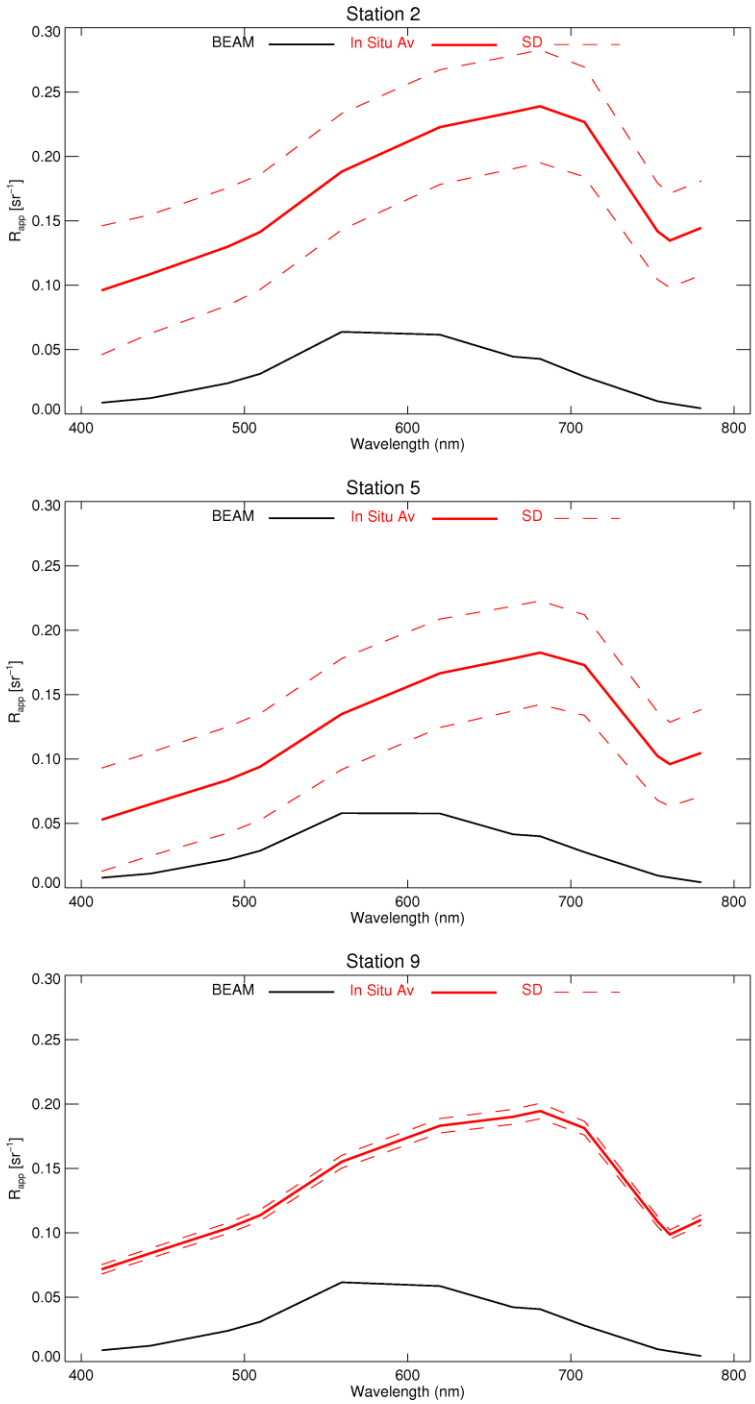

Figure 3-15 Mean above surface reflectance spectra of the corrected Fairbairn Dam water pixels at Stations 2, 5 and 9 compared to the *in situ* observations. The image pixels were corrected using the BEAM Case-2 Regional Processor (Eutrophic Lakes) and averaged between images on either side of the *in situ* observation dates. No correction for the adjacency effect has been made.

3.8 Adjacency Effect

Adjacency effects occur when atmospheric multiple scattering makes photons reflected from the area around the target pixel appear to be originating from the target pixel. This is particularly pronounced when the target pixel is much darker than the surrounding area and the aerosol loading in the atmosphere is high. Due to the size and shape of the target water bodies and inland waters in general, a substantial proportion of pixels can be contaminated by the adjacency effect.

The c-WOMBAT-c approach to correcting for the adjacency effect applies an *n x n* low pass filter to the image to supply the average radiance ($L_{rs,b}$) image. The implicit assumption is that every part of that area contributes the same to the environmental radiance. The size of *n* has previously been nominated arbitrarily to a figure that produces the appropriate amount of adjacency effect. However, the effect of the background reflectance (ρ_b) is more complicated and can be represented by the integration of small contributions over the background area (Vermote et al. 2006)

$$\langle \rho_b(M) \rangle = \frac{1}{t_d(\theta_v)} \int_{-\infty}^{\infty} \int_{-\infty}^{\infty} \rho'(x,y)\, e(x,y,\theta_v)\, dx\, dy \tag{3-34}$$

where ρ' is the reflectance of a small section of the background at coordinates of (x,y) from the centre of the target and t_d is the diffuse transmittance. The function *e* is the contribution to the diffuse transmittance from that position (x,y). This expression can be converted to deal with polar co-ordinates of near vertical observation (θ_v <30°).

$$\langle \rho_b(M) \rangle = \frac{1}{t_d(\theta_v)} \int_{0}^{2\pi} \int_{0}^{\infty} \rho'(r,\phi)\, e(r,\phi,\theta_v)\, dr\, d\phi \tag{3-35}$$

If the background reflectance is assumed homogenous (to eliminate one of the integrations) a division can be made between the target of radius *r* and the background. The fraction of the diffuse transmittance that the target is responsible for becomes:

$$F(r) = 2\pi \int_0^r e(r, \phi, \theta_v) dr \tag{3-36}$$

This reasoning can be applied to model the average background radiance as $\langle L_b(M) \rangle = L_c F(r) + (1 - F(r)) L_b$ where L_c is the image and L_b is an *n x n* pixel low pass filter. Vermote et al. (2006) evaluate the *F(r)* for a particular *e* which shows it has a small spectral dependence with a maximum in the blue part of the spectrum and a minimum in the NIR part. For *r* = 0.15km (for MERIS) an average value of *F(r)* = 0.118 was used.

An understanding of the scale of the adjacency effect was obtained by running the c-WOMBAT-c algorithm using background images described above with values of *n* from 3 to 15 and comparing it to a run which uses the image itself as a background file. Using the image as background has the effect of eliminating the adjacency term in Equation 3-15. Figure 3-16 shows that for three Burdekin Falls Dam stations the effect of neglecting adjacency is to overestimate R_{app} of up to 33%, predominately in the NIR part of the spectrum. It should be noted that for Stations 9 and 10 there is a not insubstantial contribution in the blue part of the spectrum.

Keller (2001b) conducted an experiment to evaluate the theoretically expected adjacency effect, but found no significant contribution. In contrast Candiani et al. (2007b) found the steep forested hills that border the northern section of the Lake Garda in Italy, contributed a noticeable contamination of the water spectra and Vos et al. (2003) eliminated all pixels within 1 km of the shoreline as they found that spectra were too corrupted for an accurate retrieval of the water quality parameter concentrations. The gentle topography that typifies the study sites is likely to keep any adjacency effect to a minimum. By comparing the co-incident *in situ* spectra with the images processed with alternative values of *n* it should be theoretically possible to nominate an optimal value for *n*, but comparing Figure 3-16 and Figure 3-13 shows that the standard deviation in the *in situ* observations in the case of Stations 10 and 11 is larger than the range of the calculated adjacency effect. Relying solely on Station 9 a value of *n* = 9 was adopted, resulting in a 2.7 km x 2.7 km adjacency window.

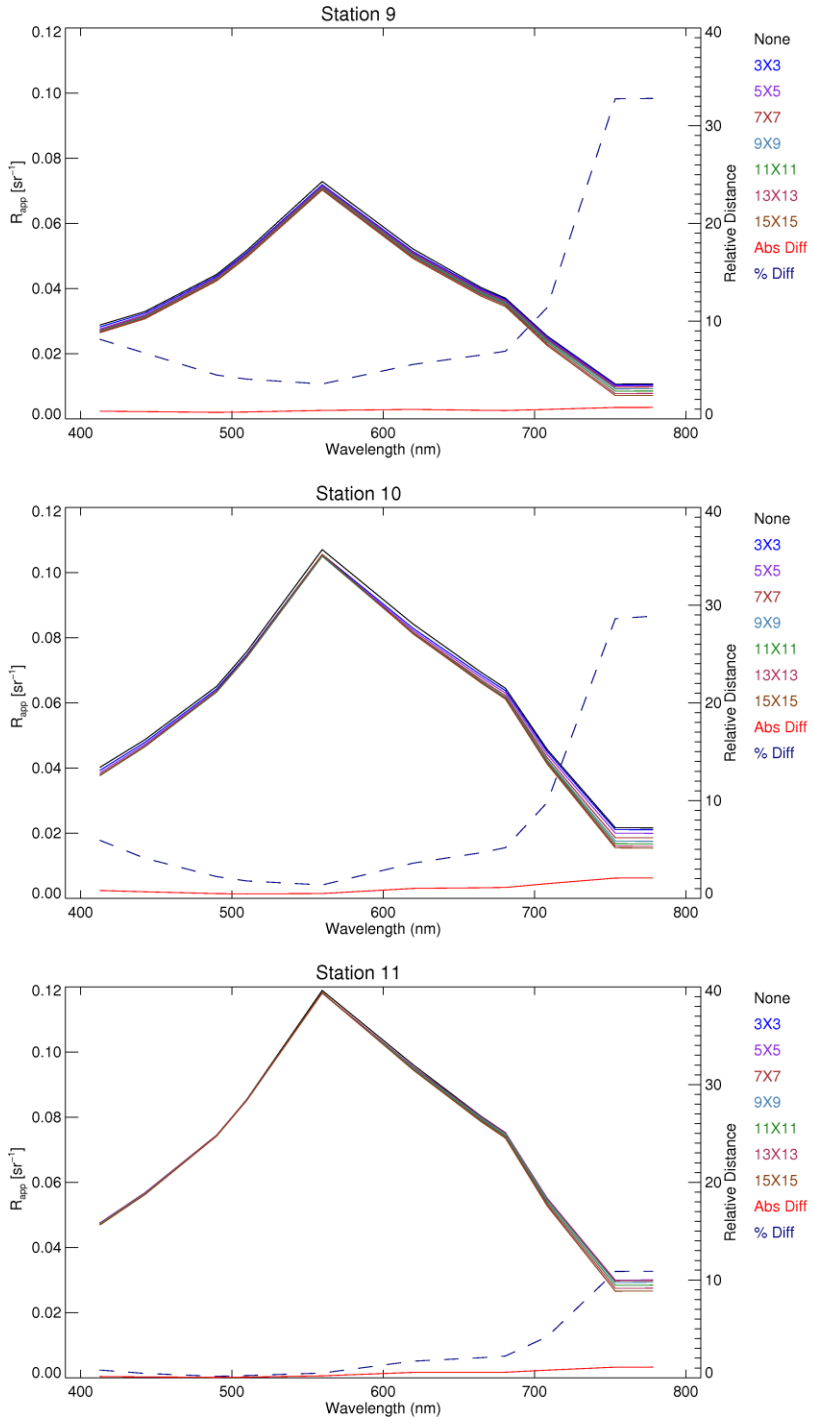

Figure 3-16 The effect of varying the contribution ascribed to the adjacency effect for Stns 9 (top) to Stn 11(bottom). The corrected spectra using no adjacency widow is show as black lines. The other lines show the corrected spectra using 3x3 (blue), 5x5 (violet), 7x7 (brown), 9x9 (light blue), 11x11 (green), 13x 13 (maroon) and 15 x15 (light brown) pixel adjacency windows. The absolute (red line) and relative (dashed line) difference between using no correction and a 15x15 correction window is shown.

3.9 Image Based Correction

The assessment of the correction parameters of the October 15th 2008 image was possible because of the *in situ* spectroradiometric observations taken at Burdekin Falls Dam. The collection of these measurements is both time consuming and expensive. Any long term or archival monitoring project needs to come to terms with how the images can be corrected in the absence of *in situ* data. The image based approaches all rely on the assumption that there is some quality of the water reflectance spectrum that is known or invariant. Figure 3-3 and Figure 3-4 show how the assumption of a zero or constant NIR reflectance value is untenable and Figure 3-6 shows how the within water body variation in the spectral dependence of the water leaving radiance in the NIR is too variable to be reliable. Other approaches take advantage of the homogeneity of aerosols over small spatial scales of 50-100 kms (Vidot & Santer 2005) to calculate the correction parameters and then apply them to the water body. The near-coastal setting of Wivenhoe Dam may make it feasible to use the clear water to the east of Stradbroke and Moreton Islands as a reference to ascertain the predominant visibility over Wivenhoe Dam. As the prevailing wind is from the south-east in the majority of images the same aerosol mass may well be present above both sites. This would not be a reasonable assumption to make at the other two sites as their distance from coast (> 200 km) means overextending the homogeneity of aerosols assumption beyond reasonable limits. Vidot and Santer (2005) use an approach to extract the aerosol properties over land close to the water body and then assume that the same conditions exist over the water. A simplified version of this approach was used where the aerosol model is pre-selected rather than estimated from the image.

3.9.1. Dense Dark Vegetation Correction at Burdekin Falls Dam

The Burdekin Falls Dam study site was used to test the adapted Vidot and Santer approach as there were *in situ* spectroradiometric observations that were co-incident with the image acquisition.

The Vidot and Santer approach assumes that the reflectance value of the dense dark vegetation (DDV) in the blue and red regions is known and uses these values to identify the aerosol type and retrieve the aerosol optical thickness. The atmospheric correction approach described in §3.6

uses a limited number of standard aerosol models that are selected by the user based on the water body location and the prevailing wind conditions prior to the image acquisition.

Pixels were designated as DDV pixels if their Atmospherically Resistant Vegetation Index (ARVI) (Kaufman & Tanre 1992) was above a given threshold. The ARVI was calculated by

$$ARVI = \frac{\rho_{aG}^{NIR} - \rho_{aG}^{rb}}{\rho_{aG}^{NIR} + \rho_{aG}^{rb}} \tag{3-37}$$

$$\rho_{aG}^{rb} = \rho_{aG}^{r} - \gamma\left(\rho_{aG}^{b} - \rho_{aG}^{r}\right) \tag{3-38}$$

where ρ_{aG} is the reflectance in the blue (443 nm), red (665 nm) and NIR (865 nm) bands that has been corrected for molecular scattering and gaseous absorption. This image is created by running the c-WOMBAT-c code described above with an AOT of 0.0. The selection of γ is left to the discretion of the user and a value of $\gamma = 1.3$ was used (Floricioiu & Rott 2005; Santer et al. 1999; Vidot & Santer 2005).

The DDV captured in the image is not a Lambertian surface so the sun-sensor geometry should be considered when selecting an ARVI threshold. While the calculation of a bi-directional reflectance distribution function (BRDF) for forests is possible it is a non trivial exercise that is beyond the scope of this project.

A simple ARVI threshold is prone to select normal vegetation that is shadowed by cloud at the time of the image acquisition. The reflectance value in the 865nm band was used to separate cloud shadow from DDV using a minimum reflectance of 17%.

Figure 3-17 shows the DDV pixels identified with thresholds that result in approximately 5% (0.24), 1% (0.33) and 0.5% (0.4) of the image subset selected. The effect of the threshold selection is demonstrated in Figure 3-18 which shows the change in the mean spectra for an image that has been corrected using the maritime aerosol with an AOT at 550 nm of 0.09.

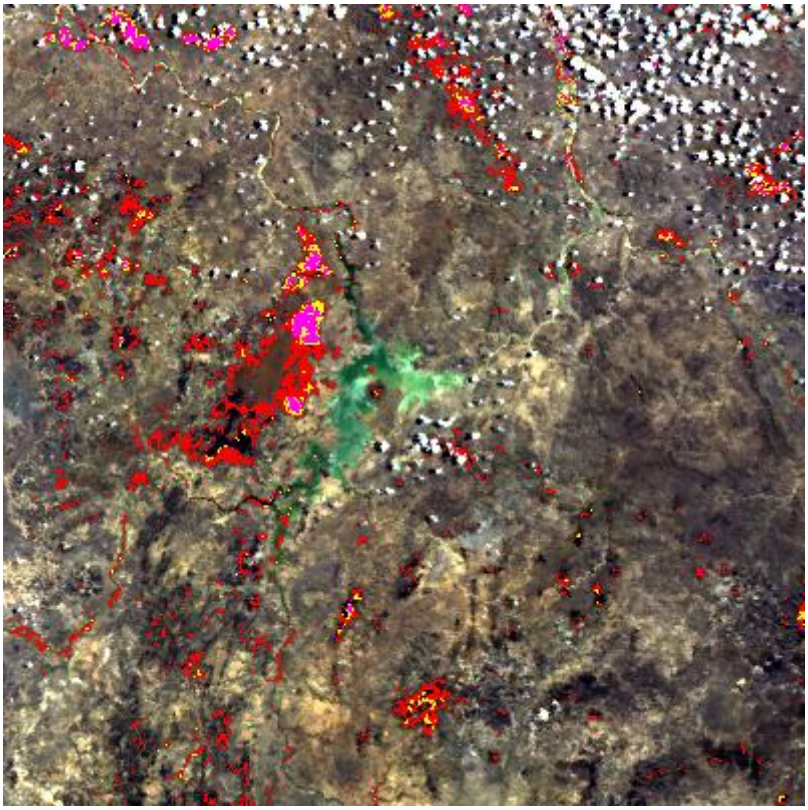

Figure 3-17 A MERIS FR image of Burdekin Falls dam showing the DDV pixels selected with an ARVI threshold of 0.4 (magenta), 0.33 (yellow) and 0.24 (red).

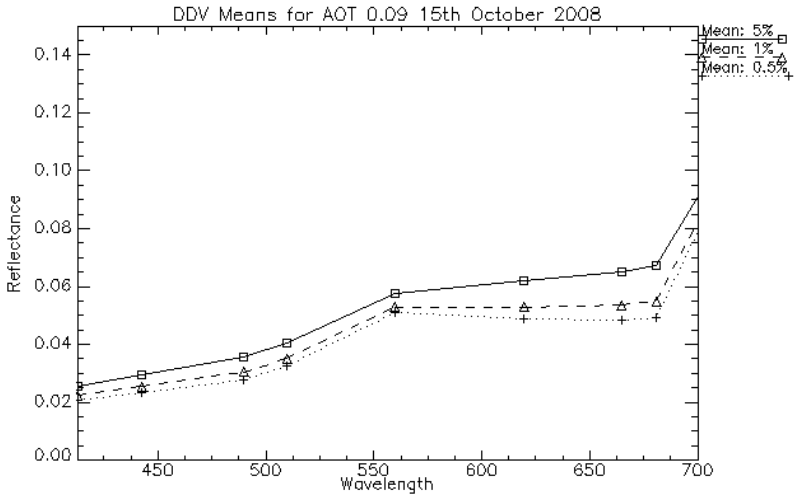

Figure 3-18 The mean reflectance spectra of the DDV thresholds that select 5% (0.24), 1% (0.33) and 0.5% (0.4) of the available pixels.

Reference DDV threshold values are stored in the auxiliary file MER_LAP_AX and the DDV threshold values were corrected for 78 combinations of solar and view zenith angles at 19 relative azimuth angles to make allowance for the BRDF. The thresholds relate to an ARVI calculated for a standard rural model with an AOT of 0.25 at 550 nm. This threshold selected 0.2% and 0% of the pixels in the images of the 29th September and 15th October respectively. As a result the MER_LAP_AX thresholds were disregarded and the DDV pixels were identified as the highest 0.5% of ARVI values in the 400 x 400 pixel subset.

3.9.2. Reference Reflectance Values

Using DDV pixels to tune the atmospheric correction parameters presupposes that the reflectance value of the DDV pixels is known. Vidot and Santer (2005) use mean values of 1.5% in the blue and 2% in the red bands. It is clear that the expected DDV reflectance spectra will vary with biome, vegetation type and its physical state. The MERIS atmospheric correction over land utilises a look up table of reflectance values in three bands (412, 443 and 665 nm). It uses 20 models with each reflectance value corrected for the BRDF for the vegetation (Santer et al. 2006). The model that is used for an image is chosen based on the location of the pixel and the time of acquisition. For the Queensland sites the appropriate models are model 9 *equatorial_asia_nov* for September – February and model 20 *equatorial_asia_june* for March – August. Like the DDV threshold values the LUT values are stored in the auxiliary file MER_LAP_AX and the DDV reflectance values are corrected for 78 combinations of solar and view zenith angles at 19 relative azimuth angles to make allowance for the BRDF using the Leroy et al. (1998) model.

The gentle change in reflectance with angular geometry shows that it is reasonable to adopt a single value for all DDV pixels in the target's vicinity and to make a linear interpolation between the two nearest documented values for the angles in question.

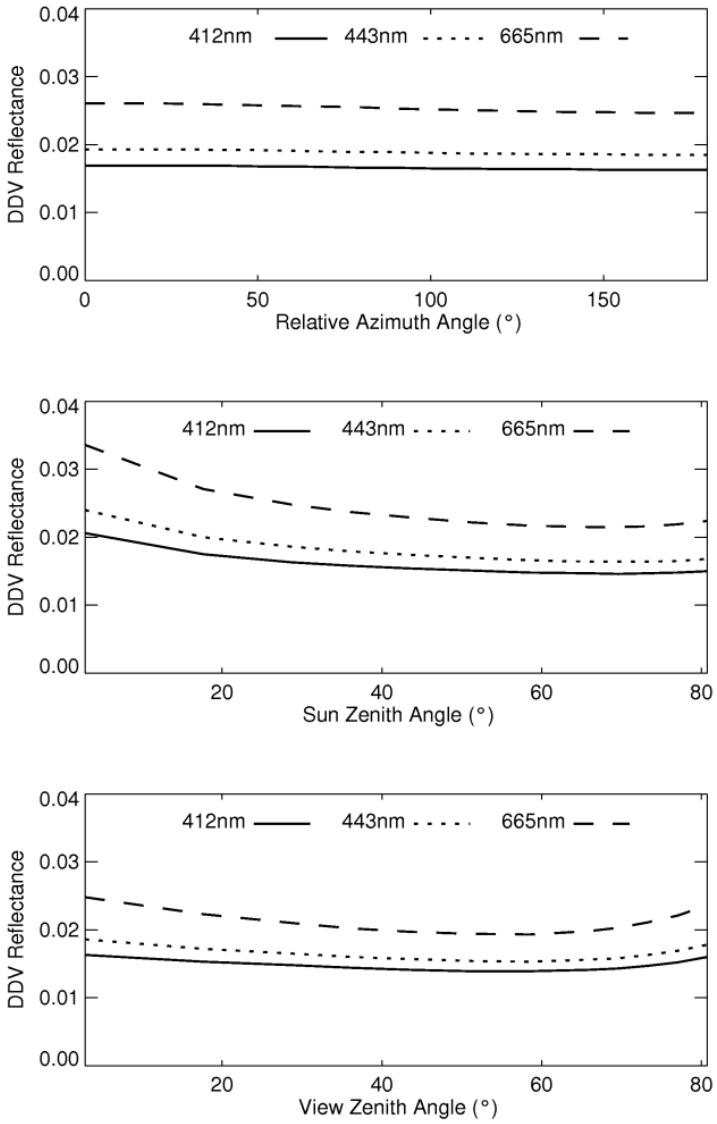

Figure 3-19 The effect of sun-sensor geometry on the reflectance values of DDV for the *equatorial_asia_nov* model. The example values were chosen as those that most closely match the geometry of the 15th October 2008 image. The top plot shows the change of reflectance with relative azimuth for a θ_v= 2.8° and θ_s=28.7°. The middle plot shows the change of reflectance with sun zenith angle for a θ_v= 28.7° and φ=150.0°. The middle plot shows the change of reflectance with view zenith angle for a θ_s= 2.8° and φ=150.0°.

The effect on the DDV mean of the adjacency correction is illustrated in Figure 3-20. This shows that change in the mean spectra for an image that has been corrected using the maritime aerosol with an AOT at 550 nm of 0.09 can be of the order of 13% in the 413nm band down to 5% in the 665 nm band. Notwithstanding this variation, the background image recommended in §3.8 was adopted.

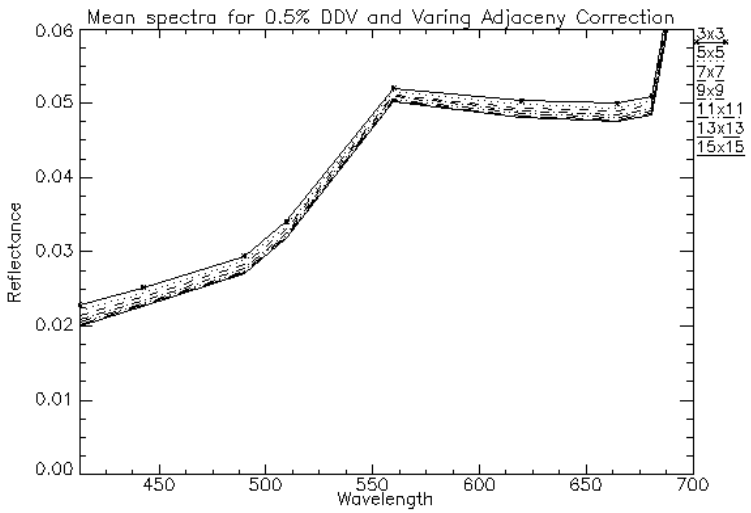

Figure 3-20 The effect of the adjacency correction on the value of the DDV mean.

3.9.3. AOT at 550nm selection

Using the tropical atmospheric model, as the main constituent is the water content and the maritime aerosol model as the prevailing wind was from the south-west prior to the image capture the atmospheric correction was performed with AOT at 550 nm values that varied between 0.04 and 0.18. The average reflectance for the DDV pixels were compared with the auxiliary file MER_LAP_AX DDV values. The results are shown in Figure 3-21. It is clear that no realistic value of the AOT at 550 nm will allow a match in the 665 nm band but an AOT at 550 nm value of 0.15 gives excellent agreement at the remaining two bands.

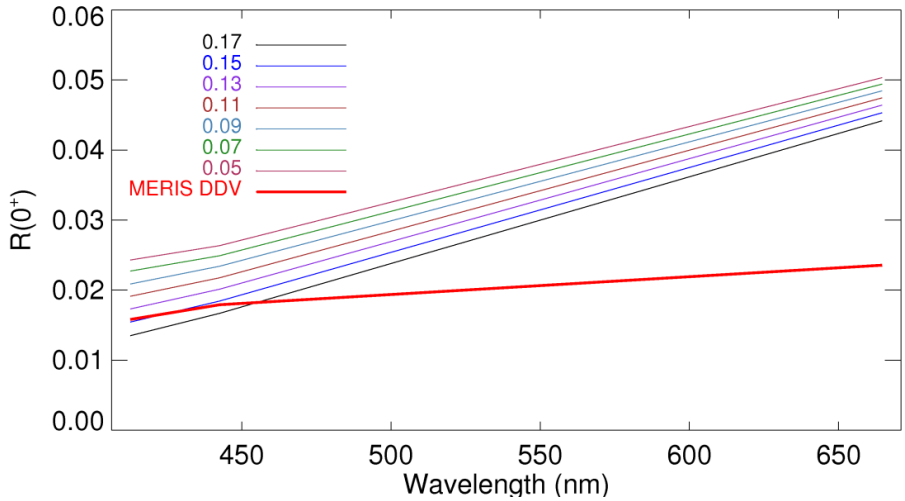

Figure 3-21 The reflectance at 413nm, 443nm and 665nm of the 0.5% DDV pixels compared to the auxiliary file MER_LAP_AX DDV values. The atmospheric correction was performed with the tropical atmospheric model and the maritime aerosol model with AOT at 550nm values was varied between 0.04 and 0.18.

The image corrected with an AOT at 550 nm value of 0.15 was compared to the *in situ* measurements for stations 9-11. The comparison is shown in Figure 3-22. It should be noted that the direct comparison of *in situ* measurements and the image pixel is hampered by complications arising from the homogeneity of the water, the difference in the instantaneous field of view of the sensors and the inherent noise in the image. Even if it is assumed that the adjacency effect has been fully accounted for, the MERIS image pixel still represents an average spectrum for an area of 290 m x 260 m. The environmental noise-equivalent reflectance difference ($NE\Delta R(0^-)_E$) is a measure of the inherent noise in an image and is calculated as the standard deviation of the subsurface reflectance in each band over a homogeneous area of optically deep water (Brando and Dekker 2003). Using a MERIS full resolution image acquired on the 2nd July 2007 corrected using c-WOMBAT-c (Brando and Dekker 2003) ($NE\Delta R(0^-)_E$) was estimated to be a constant 0.1% in all bands. After consideration of these uncertainties it is reasonable to say that the correction procedure has overcorrected for Station 9 and under corrected for Station 11.

Due to the cloud cover that was present during the site visit it was not possible to get a direct image-field matchup for the Fairbairn Dam site. To obtain a merely indicative comparison the 29th September 2008 image was corrected using the same procedure. There were no recorded inflows into the storage between the image date and the *in situ* measurements. There was approximately ten days between image and *in situ* measurements and the ratio of diffuse to direct illumination will have been substantially different. The comparison for the same three stations shown in Figure 3-15 is shown in Figure 3-23.

In general terms the image is being under corrected much like Station 11 at Burdekin Falls Dam.

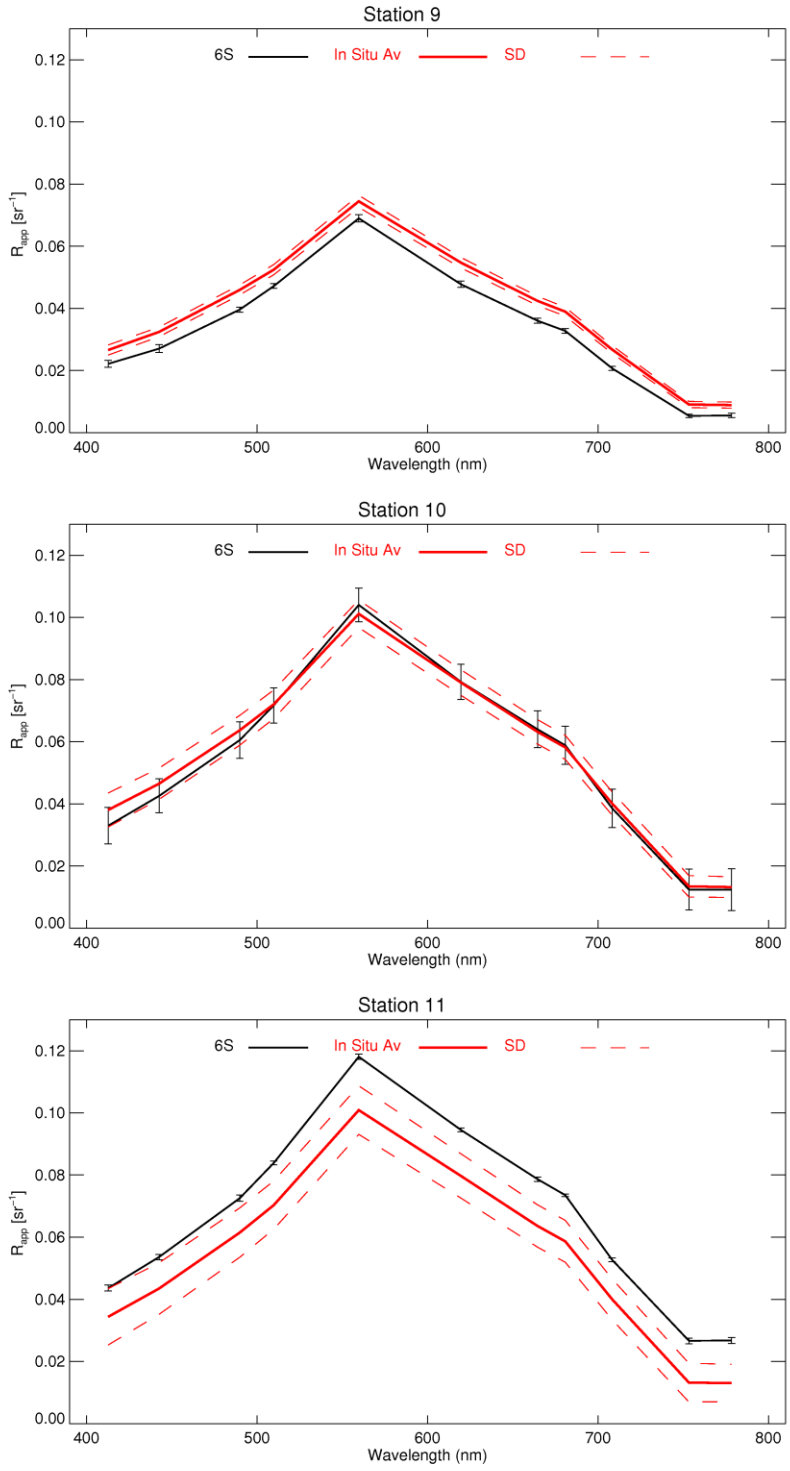

Figure 3-22 Comparing the *in situ* spectroradiometric measurements with the corrected image for 15th October at Burdekin Falls Dam. The dotted lines represent one standard deviation either side of the mean for the *in situ* measurements. The black spectra show the mean spectra of four pixels closest to the *in situ* measurement with the error bars representing one standard deviation of the sample.

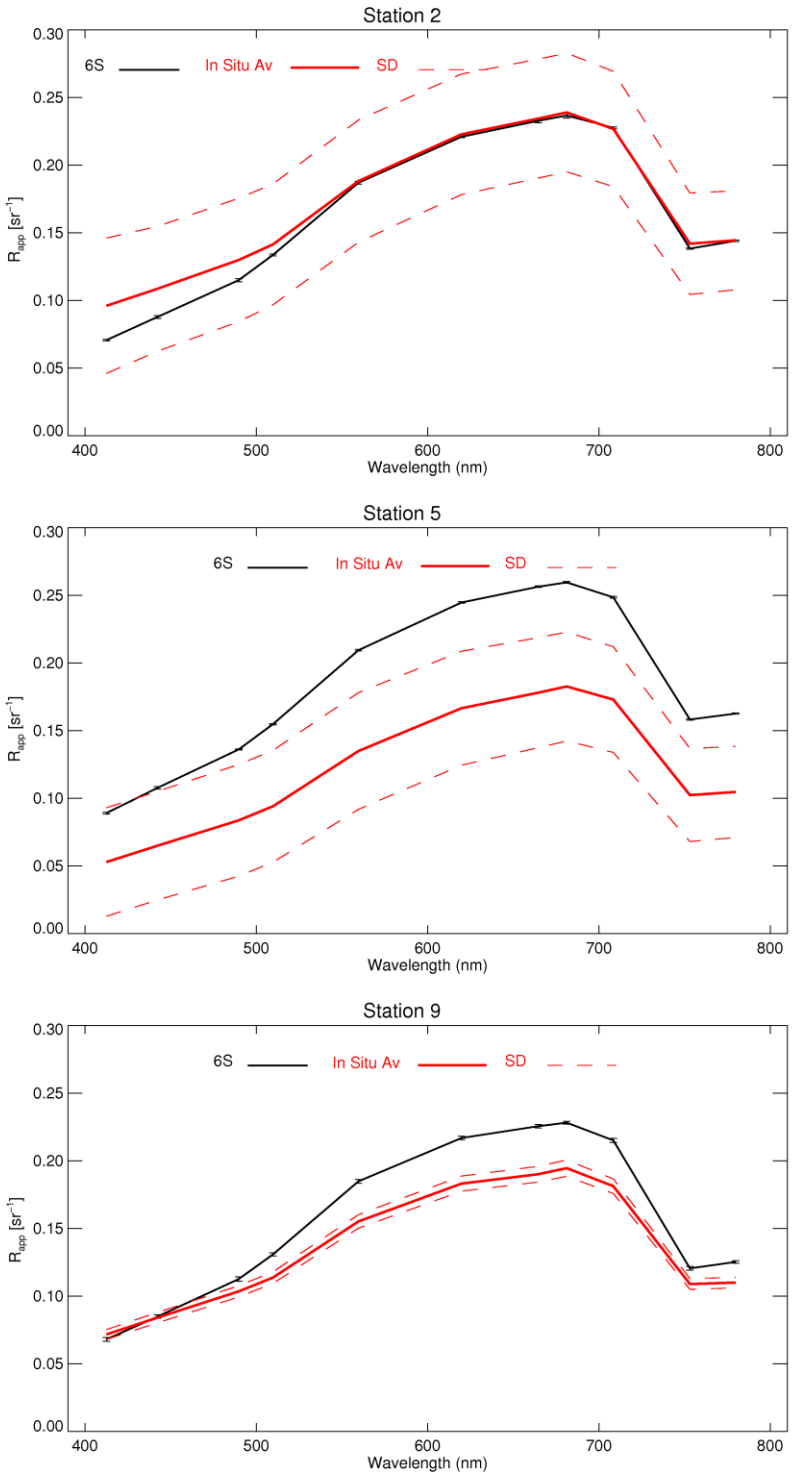

Figure 3-23 Comparing the in situ spectroradiometric measurements with the corrected image for 29th September and Fairbairn Dam. The dotted lines represent one standard deviation either side of the mean for the *in situ* measurements. The black spectra show the mean spectra of four pixels closest to the *in situ* measurement with the error bars representing one standard deviation of the sample.

3.10 Conclusions

Using MERIS images of Wivenhoe, Fairbairn and Burdekin Falls Dams it was shown that substantial errors can be made if the corrections are applied without attention to the limits of their validity. The MERIS standard product assumes knowledge of the SPM SIOPs that may be inappropriate for some water bodies as is the case with the chosen study sites. It is therefore not possible to utilise the MERIS standard product to provide the images for the final water quality parameter retrieval.

In general the BEAM Case-2 Regional Processor (Eutrophic Lakes) substantially over-corrected the spectra in the visible wavelengths. For Burdekin Falls Dam the shape of the resultant spectra is consistent with the *in situ* observations but there is a marked difference is both the shape and scale of the corrected Fairbairn Dam images. In both cases the differences are substantial enough to exclude this approach.

The default sun irradiance spectra that are used with MODTRAN-4 and 6S introduce an anomaly in the lower wavelengths of the water spectrum and the CEOS international standard (Thuillier et al. 2003) should be used. If MODTRAN-4 is to be used to simulate the atmospheric conditions then it is necessary to use the computationally costly DISORT scattering option. This can be alleviated by utilising the faster, more accurate 6S code. Notwithstanding this it was not possible to definitively establish the optimal allowance that must be made for the adjacency effect.

A necessary precondition to establishing a long term water quality monitoring program is the ability to correct images without the assistance of *in situ* observations. §3.9 showed it was possible to correct the MERIS images of inland water bodies by taking advantage of the DDV surrounding the impoundment. The expected DDV reflectance spectra vary with biome, vegetation type and its physical state. A global mean for equatorial Asia was used and appears to be adequate within the limitations of the *in situ* observations. There is a direct relationship between the accuracy of the DDV model and the accuracy of the atmospheric correction. A DDV model specific to the Queensland tropical savannah vegetation would be required to increase the accuracy of the atmospheric correction; however it was beyond the scope of this project.

4. Algorithms and Errors for Retrieving Water Quality Parameters

Key Points

- *Significant improvements in the accuracy and precision of retrieved water quality constituent values can be obtained by using semi-analytically estimated values for the anisotropy factor (f) that are calculated for each band separately in contrast to a single value approach.*
- *The calculated anisotropy factors are SIOP and site specific.*
- *The minimum detection limits and retrieval accuracy of water quality parameters are dependent on the concentrations of the other colour producing agents in the water.*
- *Over-determined systems of equations can be used to mitigate the effect of unknown and inherent sources of error in the remote sensing system.*

4.1 Introduction

The reflectance spectrum of water is a result of the cumulative interactions of light with the water itself and the contents of the water column. To retrieve the water quality parameter concentrations it is necessary to invert the reflectance spectrum. The water quality parameter concentrations and the reflectance spectrum are linked by the inherent optical properties (IOPs) of the water. The IOPs have magnitudes that are independent of the geometric structure of the light field. The absorption coefficient a describes the chances of a photon being absorbed, the scattering coefficient b describes the chances of a photon being scattered and the volume scattering function (VSF) $\beta(\theta)$ describes the probability of a scattered photon being scattered in a particular direction. Any successful semi-analytic inversion approach needs to relate the reflectance to the IOPs and then the IOPs to the water quality parameter concentrations.

This chapter addresses the third objective listed in §1.3. It describes two models of water reflectance and demonstrates how these models can be inverted using a direct and a stochastic iterative method to retrieve the water quality parameter concentrations. The chapter details how those approaches were applied to simulations of the subsurface water reflectance that were generated using the *Hydrolight*® numerical model and the SIOP spectra described in Chapter 2. The *Hydrolight*® simulations were used to show that the anisotropy factor (*f*) is not only dependent on the illumination conditions but is affected by the scattering and absorption of the water and the water quality parameters. The chapter reveals how the concentrations of the other colour producing agents in the water affect the retrieval accuracy of a particular water quality parameter concentration. Finally, the *Hydrolight*® simulations were used to show that empirical modelling of the anisotropy factor combined with the over-determined systems of equations improves the water quality parameter retrieval in the presence of image noise, atmospheric correction uncertainty and SIOP measurement errors.

4.2 Models of Reflectance

4.2.1. Gordon, Brown and Jacobs (1975)

The most common semi-analytical model for in-water reflectance was developed by Gordon, Brown and Jacobs (1975) using the optical depth τ as the independent variable.

$$R(\tau,-)=\sum_{n=0}^{N} f_n(\tau)X^n \quad , \quad X=\frac{\omega_0 B}{(1-\omega_0 F)},\ \tau=\int_0^z c(z)dz \tag{4-1}$$

B and *F* are the backscattering and forward scattering probabilities and ω_0 is the ratio between the total scattering co-efficient *b* and the total attenuation co-efficient *c*. The constants in the polynomial equation $f_n(\tau)$ are dependent on the illumination conditions. The dependence on wavelength has been omitted for clarity. As $B=1-F$ the equation can be represented in the more common form (Whitlock et al. 1981).

$$R(0^-)=\sum_{n=0}^{n=3} f_n(0)\left(\frac{b_b}{a+b_b}\right)^n \tag{4-2}$$

For convenience ω_b will be defined as

$$\omega_b = \frac{b_b}{a + b_b} \tag{4-3}$$

It was further shown for $\theta_s \geq 20°$ the third power term can be dropped and the co-efficients $f_0(0)$=0, $f_1(0)$=0.0949Q and $f_2(0)$=0.0794Q , where Q is the ratio of upwelling irradiance to upwelling radiance, can be used (Gordon 1986). This has been applied in a number of case studies (Gordon et al. 1988; Hoge & Lyon 1996; Keller 2001a) using various expressions for the factor Q.

The non-linear nature of the relationship and the effect of illumination conditions are clearly displayed in Figure 4-1.

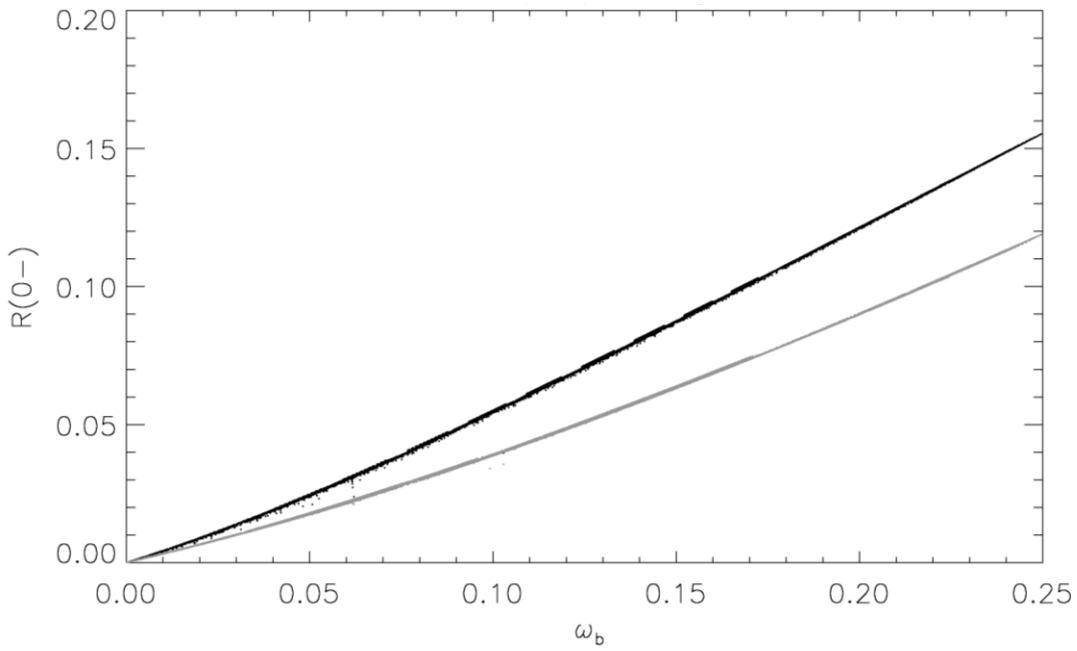

Figure 4-1 *R(0⁻)* as a function of ω_b modelled with *Hydrolight*®. The reflectance was modelled between 400nm and 800nm using θ_s=61.1° (black) and θ_s=0° (grey), a clear sky and an average IOP set for Wivenhoe Dam. The resulting spectra were convolved with the MERIS band response functions.

The error from leaving out the second order term is approximately $\frac{\omega_b}{1+\omega_b}$ (Gordon et al. 1988) which equates to 20% for the simulation shown in Figure 4-1. Approximating the reflectance model by neglecting higher order terms was a computational necessity that no longer exists.

4.2.2. Lee, Carder and Du (2004)

Because of the different scattering phase functions for the water (*w*) and the particulate matter (sum of phytoplankton and tripton (*p*)) suspended in it, Lee et al (2004) partitioned the f factor into:

$$r_{rs} = f_w \frac{b_{bw}}{a + b_b} + f_p \frac{b_{bp}}{a + b_b} \quad (4\text{-}4)$$

Call $\omega_w = \frac{b_{bw}}{a + b_b}$ and $\omega_p = \frac{b_{bp}}{a + b_b}$

They proceeded to solve the parameters for a single solar angle and two viewing angles using a large variety of values for scattering and absorption.

Using their model parameters and the typical water quality parameter values for Wivenhoe Dam the difference in reflectance due to the viewing angle was calculated to be a maximum of 3.8%. It is shown later that this variation is much less than the variation with respect to the change in the sun angle, which can be greater than 22%, so for these purposes the view angle variation has been disregarded.

4.2.3. Water Quality Parameter Inherent Optical Property Models

Absorption

A four part absorption model was used.

$$a(\lambda) = a_w(\lambda) + a_{CDOM}(\lambda) + a_{TR}(\lambda) + a_\phi(\lambda) \quad (4\text{-}5)$$

The values for $a_w(\lambda)$ were obtained from Pope and Fry (1997) and Smith and Baker (1981). The absorption due to the water quality parameters is proportional to the concentration of the constituent. This is normally represented by the use of a specific absorption coefficient:

$$a_i(\lambda) = C_i a_i^*(\lambda). \quad (4\text{-}6)$$

The specific spectra were sourced from the field measurements of Wivenhoe Dam in July 2007 and Burdekin Falls in October 2008 derived in Chapter 2.

Scattering

A three part backscattering model was used.

$$b_b(\lambda) = b_{bw}(\lambda) + b_{bTR}(\lambda) + b_{b\phi}(\lambda). \quad (4\text{-}7)$$

The scattering coefficient for pure water was obtained from Morel (1974) and the of b_w:b_{bw} ratio of 0.5 was used. The backscattering of tripton and phytoplankton is proportional to the concentration of the constituent and were obtained from the field measurements of Wivenhoe Dam in July 2007 and Burdekin Falls in October 2008 described in Chapter 2.

4.3 Inversion Methods

The inversion approaches that have been used in the past were described in §1.2.1. This thesis concentrated on two methods, an over-determined MIM approach and optimisation that used the particle swarm intelligence search algorithm.

4.3.1. Matrix Inversion Method

After omitting the spectral dependence for the anisotropy factor, the linearised version of the Gordon et al. model is:

$$R(0^-, \lambda_i) = f(\omega_b, \mu_0)\frac{b_b(\lambda_i)}{a(\lambda_i) + b_b(\lambda_i)} \quad (4\text{-}8)$$

where μ_0 is the cosine of the sun zenith angle. By substituting Equations 4-5 to 4-7 into Equation 4-8 and rearranging (Hoge & Lyon 1996)

$$\frac{R(0^-)}{f(\omega_b, \mu_0)} = \frac{b_{bw} + TR \cdot b_{bTR} + CHL \cdot b_{b\phi}}{a_w + CDOM \cdot a_{CDOM} + TR \cdot a_{TR} + CHL \cdot a_\phi + b_{bw} + TR \cdot b_{bTR} + CHL \cdot b_{b\phi}} \quad (4\text{-}9)$$

This can be represented in a matrix form for all wavelengths of the spectra as:

$$\begin{bmatrix} a_w(\lambda_1)\frac{R(\lambda_1)}{f} - b_{bw}(\lambda_1)\left(1-\frac{R(\lambda_1)}{f}\right) \\ \cdot \\ \cdot \\ a_w(\lambda_n)\frac{R(\lambda_n)}{f} - b_{bw}(\lambda_n)\left(1-\frac{R(\lambda_n)}{f}\right) \end{bmatrix} = \begin{bmatrix} a^*_\phi(\lambda_1)\frac{R(\lambda_1)}{f} - b^*_{b\phi}(\lambda_1)\left(1-\frac{R(\lambda_1)}{f}\right) & \cdot\cdot \\ \cdot & \cdot\cdot \\ \cdot & \cdot\cdot \\ a^*_\phi(\lambda_1)\frac{R(\lambda_1)}{f} - b^*_{b\phi}(\lambda_1)\left(1-\frac{R(\lambda_1)}{f}\right) & \cdot\cdot \end{bmatrix} \begin{bmatrix} CHL \\ TSM \\ CDOM \end{bmatrix} \quad (4\text{-}10)$$

or

$$\mathbf{y} = \mathbf{A}\mathbf{x} \quad (4\text{-}11)$$

Where **A** is a 3 x N dimension matrix with N being the number of bands utilised by the inversion.

The standard solution for this problem is

$$\mathbf{x} = \left[\mathbf{A}^{\mathbf{T}}\mathbf{A}\right]^{-1}\mathbf{A}^{\mathbf{T}}\mathbf{y} \quad (4\text{-}12)$$

It has been asserted but not demonstrated that application of the weighted least-squares method significantly improves the accuracy of the results (Hakvoort et al. 2002).

The weight matrix is a square (NxN) diagonal matrix (W) where W_{ii}= relative weight of band *i*. The weights are chosen to give greater influence to those bands which are deemed to be more reliable.

The solution then becomes

$$\mathbf{x} = \left[\mathbf{A}^{\mathbf{T}}\mathbf{W}\mathbf{A}\right]^{-1}\mathbf{A}^{\mathbf{T}}\mathbf{W}\mathbf{y} \quad (4\text{-}13)$$

Weighting Schemes

The interplay between the band weights and the performance of the MIM is too complex to be characterised analytically, instead a number of suppositions are tested to see which returns the most accurate and precise results.

The first family of weighting schemes represent the conventional approach where all bands are given equal weighting (ALL & NO_IR) or where exactly determined systems of equations of *a priori* selected bands have been used (3BANDS). In this case the three bands selected were as close as possible to those used by Phinn et al. (2005): two centred at 490 and 670 nm and one in the 700-740 nm range.

The next family of weighting schemes assumes that there is a uniform noise in reflectance (Hakvoort et al. 2002) meaning that those bands with a high value of reflectance should have a higher signal to noise ratio and thus will be more reliable (HAK & REF). As the shape of the reflectance spectrum changes with the concentrations of the water quality parameter, weights representing low, mid and high water quality parameter concentrations were selected.

Giardino et al. (2007) make the argument that bands that exhibit the greatest change in reflectance when an increase in a water quality parameter concentration occurs should be of greater use in determining the concentration. The change in reflectance with a change in a water quality parameter concentration is measured by the first derivative of the reflectance spectra with respect to the water quality parameter concentration (DER). Using the *Hydrolight*® simulations the derivatives were calculated and used to create the next family of weighting schemes.

The last family were derived empirically (RAN). The weights were allowed to vary randomly and those that performed the best were retained and the commonalities of the best performed schemes were combined.

The weighting scheme names and short descriptions are listed in Table 4-1.

Table 4-1 Weighting scheme names and descriptions.

Weight Scheme	Description	Weight Scheme	Description
MER_ALL	All bands equally weighted	MER_REF1	Reflectance based (clear water)
MER_NO_IR	No NIR bands used and all the remaining bands equally weighted	MER_REF2	Reflectance based (turbid water)
MER_3BANDS	Conventional three band approach	MER_RAN1	Empirically derived
MER_DER1	Based on spectrum derivative with respect to chlorophyll *a* (low chlorophyll *a*)	MER_RAN2	Empirically derived
MER_DER2	Based on spectrum derivative with respect to chlorophyll *a* (high chlorophyll *a*)	MER_RAN3	Empirically derived
MER_DER3	Based on spectrum derivative with respect to TSM (low TSM)	MER_RAN4	Empirically derived
MER_DER4	Based on spectrum derivative with respect to TSM (high TSM)	MER_RAN5	Empirically derived
MER_DER5	Based on spectrum derivative with respect to CDOM (low CDOM)	MER_RAN6	Empirically derived
MER_DER6	Based on spectrum derivative with respect to CDOM (high CDOM)	MER_RAN7	Empirically derived
MER_HAK	Hakvoort et al. (2002) weighting scheme	MER_RAN8	Empirically derived

4.3.2. Particle Swarm Optimisation (PSO)

The PSO is a stochastic search technique which includes a random element in the search approach. The algorithm represents the solution as an *n*-dimensional vector in an *n*-dimensional solution space. It then mimics the action of a swarm by generating a number of potential solutions or 'particles' and after each iteration having them react to the closest match in its local area as well as the best match from all the particles. The best match can be defined by any appropriate cost function.

Let $\mathbf{x_j}$ be a particle and the position of $\mathbf{x_j}$ after the next iteration as $\mathbf{x_j}+\mathbf{\Delta x_j}$ where $\mathbf{\Delta x_j}$ is referred to as the trajectory. The trajectory is related to the value of two vectors, the vector connecting $\mathbf{x_j}$ to the best match that it has previously made ($\mathbf{x_{j,best}}$) and the vector connecting $\mathbf{x_j}$ to the best match that any of the particles have made ($\mathbf{x_{G,best}}$). The random element is introduced by generating random number multiples of the components of $\mathbf{x_{j,best}}$ and $\mathbf{x_{G,best}}$. The bias towards each component vector is controlled by two weight constants c_1 and c_2. To aid in the convergence the sum of the vectors is multiplied by a constriction factor χ.

Formally,

$$\mathbf{x_j}(t+1) = \mathbf{x_j}(t) + \Delta\mathbf{x_j}(t+1) \tag{4-14}$$

$$\Delta\mathbf{x_j}(t+1) = \chi\left(\Delta\mathbf{x_j}(t) + \Phi_1\left(\mathbf{x_{j,best}} - \mathbf{x_j}(t)\right) + \Phi_2\left(\mathbf{x_{G,best}} - \mathbf{x_j}(t)\right)\right) \tag{4-15}$$

In this case the search space is three dimensional so

$\Phi_m = c_m \begin{bmatrix} r_{m,1} & 0 & 0 \\ 0 & r_{m,2} & 0 \\ 0 & 0 & r_{m,3} \end{bmatrix}$ where $r_{m,i}$ are random scalars uniformly distributed between 0 and 1.

$$\chi = \frac{2}{\left|2 - \phi - \sqrt{\phi^2 - 4\phi}\right|} \qquad \phi = c_1 + c_2, \quad \phi > 4 \tag{4-16}$$

The $\phi > 4$ restriction is required to prevent the values of the trajectories from becoming cyclical and hence not randomly searching the solution space (Clerc & Kennedy 2002). The parameters c_1 and c_2 were set at 2.05 (Slade et al. 2004). Figure 4-2 shows a graphical representation of the particle trajectory update.

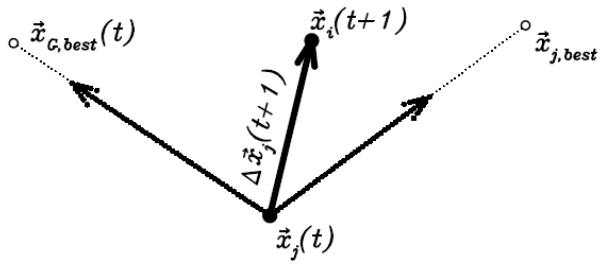

Figure 4-2 Graphical representation of the calculation of the particle trajectory.

Similarity Measures

The PSO determines the direction of the search based on the values of the best spectrum match. These values can be provided by any number of similarity measures. Four similarity measures and their combinations were tested to see which returned the most accurate and precise results.

Spectral Angle Mapper

The Spectral Angle Mapper (SAM) measure treats the two spectra as *n*-dimensional column vectors and uses their dot product normalised for the magnitude of the vectors as a measure of their similarity.

Formally let **x** and **x'** be two spectra with *n* bands then:

$$SAM(\mathbf{x},\mathbf{x}') = \cos^{-1}\left(\frac{\sum_{i=1}^{n} x_i\, x_i'}{\sqrt{\sum_{i=1}^{n} x_i^2}\cdot\sqrt{\sum_{i=1}^{n} x_i'^2}}\right). \tag{4-17}$$

Spectral Information Divergence

The Spectral Information Divergence (SID) is a stochastic, rather than deterministic measure of similarity (Du et al. 2004). It reduces the vectors to probability vectors before comparing them. This is achieved by normalising the vector by dividing by the sum of its components. For a given band this probability can be converted into its self-information. In broad terms this describes the unlikeliness of the predicted outcome. The discrepancy in a particular band is the difference between the self information of the comparable bands in the two spectra. The discrepancy of the spectra is the sum of the band discrepancy weighted by that band's probability. For this reason the discrepancy is not commutative so the SID is calculated as the sum of the discrepancies of the two combinations.

Formally, let **x** and **x'** be two spectra with *n* bands with probability vectors **p** and **q** respectively. The probability for a given band is:

$p_i = \dfrac{x_i}{\sum_{i=1}^{n} x_i}$ and the self-information for each band is $I_i(\mathbf{x}) = -\log(p_i)$.

The discrepancy of a band is $D_i(\mathbf{x} \parallel \mathbf{x}') = I_i(\mathbf{x}) - I_i(\mathbf{x}') = \log\left(\dfrac{p_i}{q_i}\right)$ and the discrepancy of the spectrum is $D(\mathbf{x} \parallel \mathbf{x}') = \sum_{i=1}^{n} p_i \log\left(\dfrac{p_i}{q_i}\right)$.

Lastly,

$$SID(\mathbf{x},\mathbf{x}') = D(\mathbf{x} \parallel \mathbf{x}') + D(\mathbf{x}' \parallel \mathbf{x}) \quad (4\text{-}18)$$

Spectral Correlation Mapper

The Spectral Correlation Mapper (SCM) is a modification of the SAM that takes into account the sign of the correlation not just the magnitude (Carvalho & Menezes 2000).

$$SCM(\mathbf{x},\mathbf{x}') = \cos^{-1}\left(\frac{\sum_{i=1}^{n}(x_i - \bar{x})(x_i' - \bar{x}')}{\sqrt{\sum_{i=1}^{n}(x_i - \bar{x})} \cdot \sqrt{\sum_{i=1}^{n}(x_i' - \bar{x}')}} \right) \quad (4\text{-}19)$$

Minimum Distance (MINDIST)

The three previous measures mathematically eliminate the magnitude of the reflectance spectra from the calculation and focus on its shape. However, as the TSM concentration increases in water, the increased scattering leads the reflectance spectra to increase in magnitude rather than change in shape. The minimum distance measure only considers the magnitude of the two spectra by calculating the Euclidean distance between their vectors in band space.

$$MIN(\mathbf{x},\mathbf{x}') = \sqrt{\sum_{i=1}^{n}\left(x_i^2 - x_i'^2\right)} \quad (4\text{-}20)$$

Combined Measures

The combined measures were as follows:

$$SIDSAM = SID.\tan(SAM) \text{ (Du et al. 2004)} \quad (4\text{-}21)$$

$$SIDMIN = SID.MINDIST \quad (4\text{-}22)$$

$$SAMMIN = SAM.MINDIST \quad (4\text{-}23)$$

4.4 Parameterising the Models

4.4.1. *Hydrolight*® Simulations

Based on monitoring data, 1089 *Hydrolight*® simulations were run for each sun position at the water quality constituent concentration values shown in Table 4-2 and Table 4-3.

As water managers do not regularly measure CDOM absorption at 440nm values, the range was estimated based on field measurements from Appendix A.

Table 4-2 Water quality constituent concentrations and modelling parameters used in simulation of the reflectance spectra for Wivenhoe Dam.

Water quality constituent	Concentration
Chlorophyll *a* (μgl^{-1})	0, 2 ,4, 6, 8, 10, 12, 14, 16, 18, 20
TSM (mgl^{-1})	0, 2, 4, 6, 8, 10 ,12, 14, 16, 18, 20
CDOM (a_{CDOM} @440 nm [m^{-1}])	0, 0.1, 0.2, 0.3, 0.4, 0.5, 0.6 ,0.7 ,0.8
Sun zenith Angle (°)	0, 9.5, 19.1, 29.0, 36.9, 43.5, 49.5, 54.9, 61.1

Table 4-3 Water quality constituent concentrations and modelling parameters used in simulation of the reflectance spectra for Burdekin Falls Dam.

Water quality constituent	Concentration
Chlorophyll *a* (μgl^{-1})	0, 2, 4, 6, 8, 10, 12, 14, 16, 18, 20
TSM (mgl^{-1})	0, 2, 4, 6, 8, 10, 12, 14, 16, 18, 20
CDOM (a_{CDOM} @440 nm [m^{-1}])	0, 0.2 ,0.4 ,0.6, 0.8, 1.0, 1.2, 1.4, 1.6
Sun zenith Angle (°)	0, 9.5, 19.1, 29.0, 36.9, 43.5, 49.5, 54.9, 61.1

The simulations used the final SIOP values from the 2007 and 2008 site visits (shown in Figure 4-3) at 1nm steps between 401-799nm using a clear sky with the default *Hydrolight*® atmosphere, an infinite depth and a wind speed of 1m/s. To model the effect of the sun position, nine simulation sets were run for clear skies with the sun zenith angle varying from 0° to 61.1°. The angles were selected so that their cosines were well distributed. The simulated spectra were then convolved with the first twelve MERIS bands (412.5, 442.5, 490, 510, 560, 620, 665, 681.25, 708.75, 753.75, 760.625 and 778.75 nm).

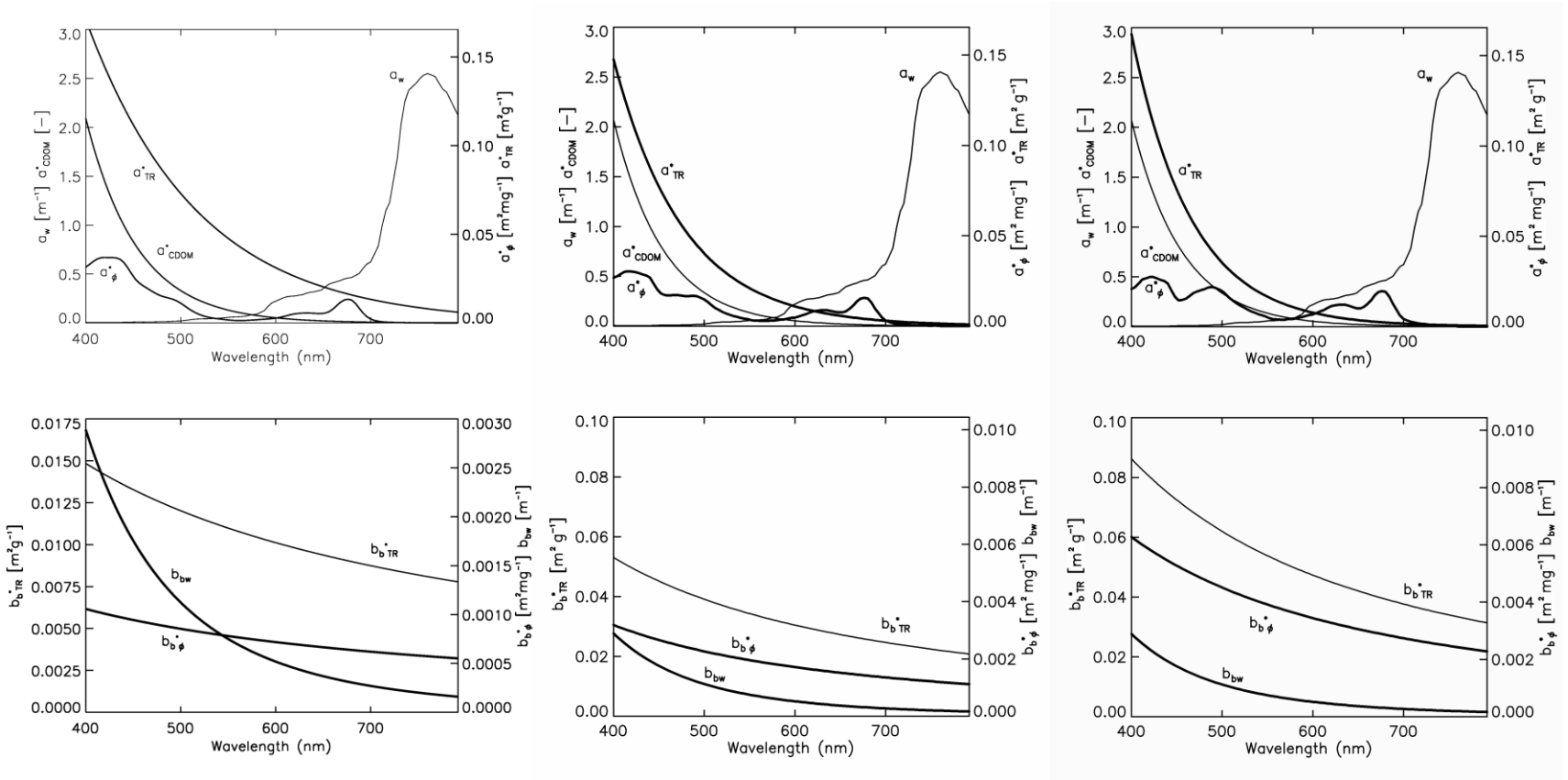

Figure 4-3 Average SIOPs for Wivenhoe and Burdekin Falls Dam (left: Wivenhoe Dam, centre: Burdekin Falls Dam Upper basin, right: Burdekin Falls Dam Lower basin): The upper graph shows the spectral absorption of water (*w*) and the chlorophyll *a* specific absorption spectra of phytoplankton (ϕ), total suspended material (*TSM*) and coloured dissolved organic matter (*CDOM*). The lower shows the spectral backscattering of water (*w*) and the specific backscattering spectra of chlorophyll *a*(ϕ) and total suspended material (TSM).

4.4.2. Matrix Inversion Method

There are two ways to account for the non-linear nature of the reflectance and ω_b relationship. Non-linear systems of equations can still be solved using a least-squares approach but this involves using an iterative solution that comes at a computational cost. Alternatively, the model can be linearised by truncating the higher order terms. In this case a portion of the IOP dependence can be transferred to the anisotropy factor *f*. In this approach *f* becomes the ratio of reflectance to ω_b and it should have a shape that can be easily modelled by a polynomial. An example of the relationship is plotted in Figure 4-4.

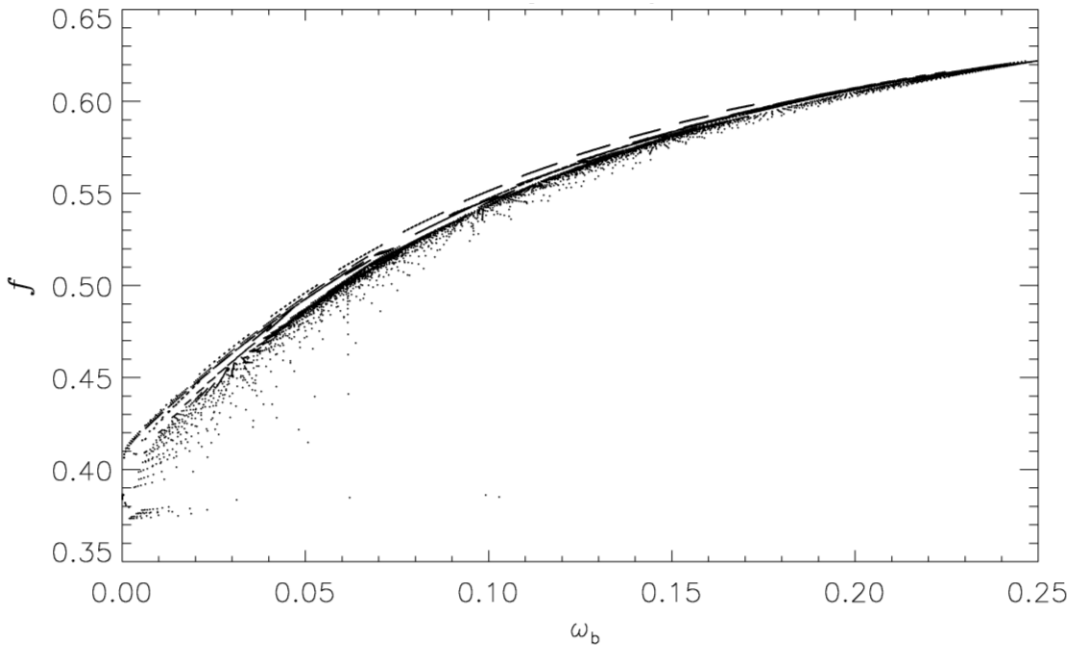

Figure 4-4 *f* as a function of ω_b modelled with *Hydrolight*®. The reflectance was modelled between 400nm and 800nm using θs=61.1°, a clear sky and an average IOP set for Wivenhoe Dam. The resulting spectra were convolved with the MERIS band response functions.

This relationship can be used to evaluate *f* for a forward model as the value of ω_b will be known but it is of no use in inverting the measured reflectance spectra. Clearly another approach needs to be found to calculate *f* for a backward model.

It has already been shown that for the first order approximation reflectance is proportional to ω_b. If this is the case then a plot of *f* against reflectance should have a very similar shape to that shown in Figure 4-4. An example of the relationship is plotted in Figure 4-5.

The parameters of the polynomial fit will be dependent on the IOP set of the water in question as well as the illumination properties. To model the effect of the sun position nine simulation sets were run for clear skies with the sun zenith angle varying from 0° to 61.1°. For each set a quadratic and cubic function were used to model *f* as a function of subsurface reflectance. The results of these simulations are shown in Table C-1 and C-2 in Appendix C.

The co-efficients detailed in Appendix C were then plotted against the multiplicative inverse of the cosine of the in-water sun zenith angle ($1/\mu_w$) as shown in Figure C-1 and Figure C-2 in the appendix to obtain functions to generate co-efficients for any sun position.

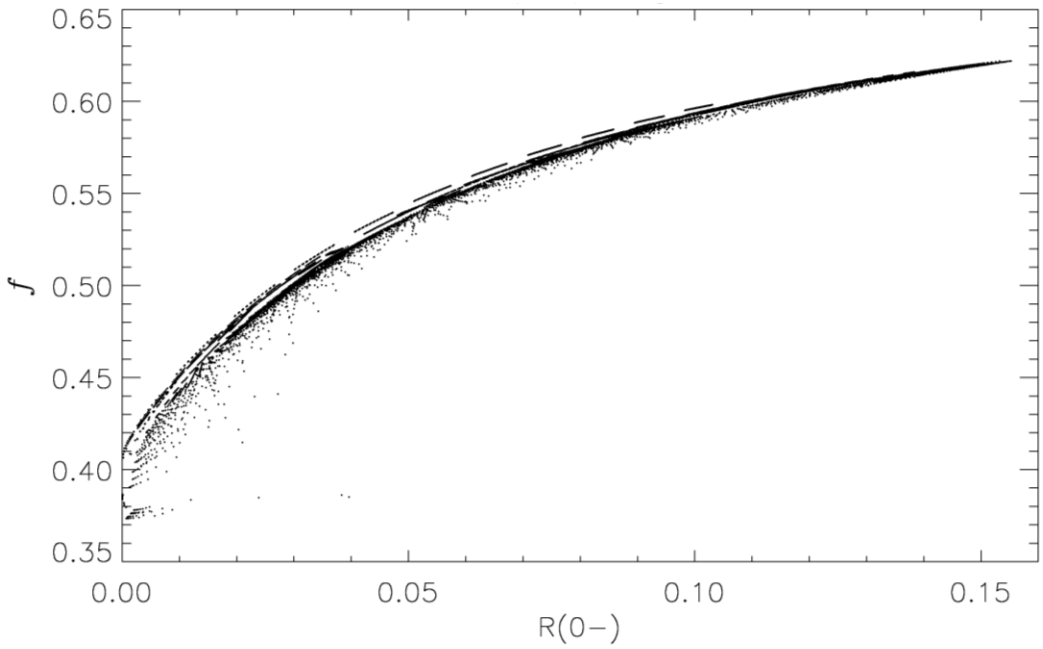

Figure 4-5 *f* as a function of *R(0-)* modelled with *Hydrolight*®. The reflectance was modelled between 400nm and 800nm using θs=61.1°, a clear sky and an average IOP set for Wivenhoe Dam. The resulting spectra were convolved with the MERIS band response functions.

4.4.3. PSO

By using the forward model and a spectrum matching approach it is easier to deal with the effect of the non-linear nature of the model. Three approaches were used to model the reflectance from the IOP values. The first used the Lee et al. (2004) approach and the other two used the Gordon et al. (1975) formulation in a quadratic and cubic form.

Lee et al. (2004) Form

The Lee et al. paper used an approximation method to solve for the values of *f* but a more robust result can be achieved by treating the reflectance like a surface with two dimensions: the water part and the particle part. Figure 4-6 shows one of the simulations where the black points are the simulated values and the blue surface is the fitted surface. Because the points are irregularly spread over the surface the validity of the fit is less than ideal. The figure shows the surface as being an essentially an inclined plane but with a very slight curve.

The difference is more notable in Figure 4-7 which shows a scatter plot of the residuals of the two fitted options. The distinctive quadratic shape of the residuals of the planar fit show that a higher degree polynomial surface is required.

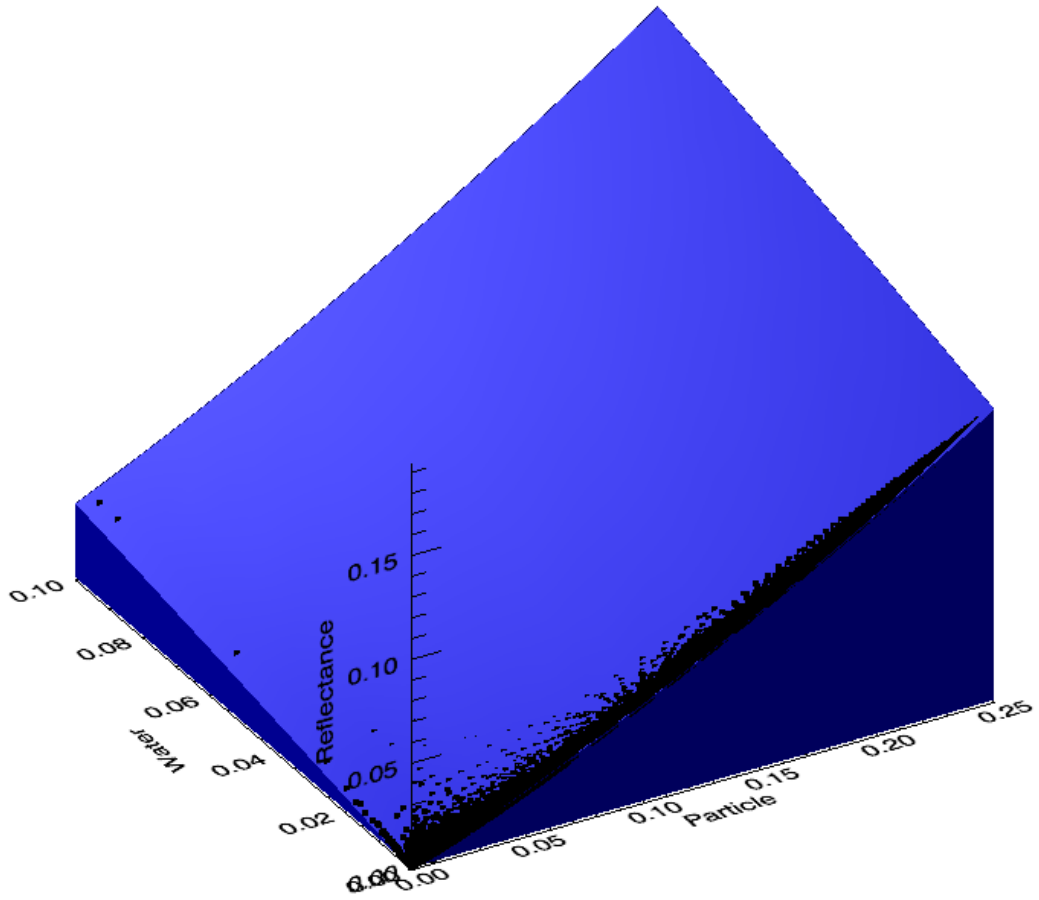

Figure 4-6 Example showing the fitted reflectance surface (coloured blue) and the original simulated data (coloured black).

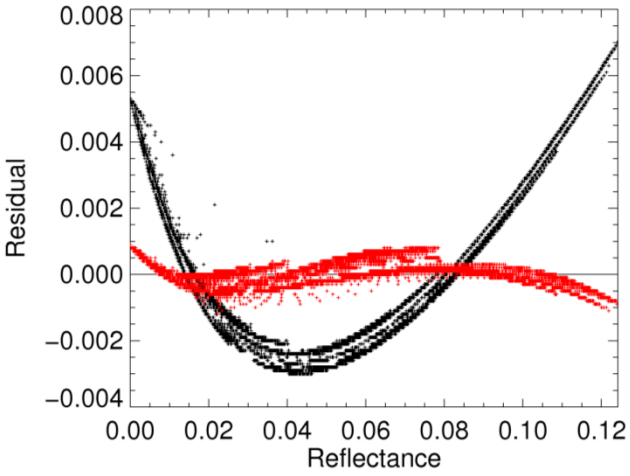

Figure 4-7 Example of a graph showing the residuals remaining after fitting a three dimensional surface with b_{bp} and b_{bw} as x and y axes. The black dots represent the residuals when a plane was fitted and the red dots show the residuals when a curved surface was fitted.

As the surface is dependent on the sun angle a surface was generated for each of the nine simulated data sets. The results of the planar fit are shown in Table C-3 and the curved surface in Table C-4 of Appendix C.

Gordon et al. (1975) Form

To see whether the added complexity of the Lee et al. (2004) approach increased the accuracy of the ensuing data retrieval the co-efficients of the traditional Gordon et al. (1975) approach were calculated by fitting $R(0^-) = \sum_{n=0}^{n=3} f_n(0)\left(\frac{b_b}{a+b_b}\right)^n$ for n = 2 and n =3. The final fitted parameters and equations are shown in Tables C-5 and C-6 and Figures C-4 and C-5 in Appendix C.

Plotting the residuals for selected sun positions shows that the cubic form is preferable (Figure 4-8).

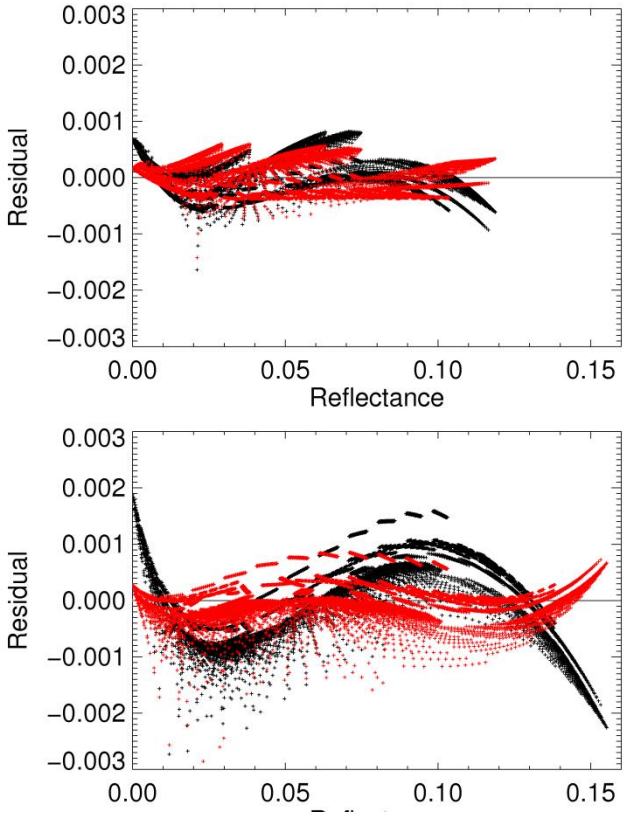

Figure 4-8 Example of residual scatter plots showing the residuals for the quadratic model (black) and the cubic model (red). The upper plot is for a zenith sun and the lower plot is for a sun angle of 61.1°.

Accuracy Check of Forward Models

After using numerous fitting routines it was necessary to check how the forward model matches its *Hydrolight*® simulation. The percentage error between the reflectance calculated by *Hydrolight*® and the forward model was calculated for the nine sun positions. Figure 4-9 shows histograms of the results for each forward model.

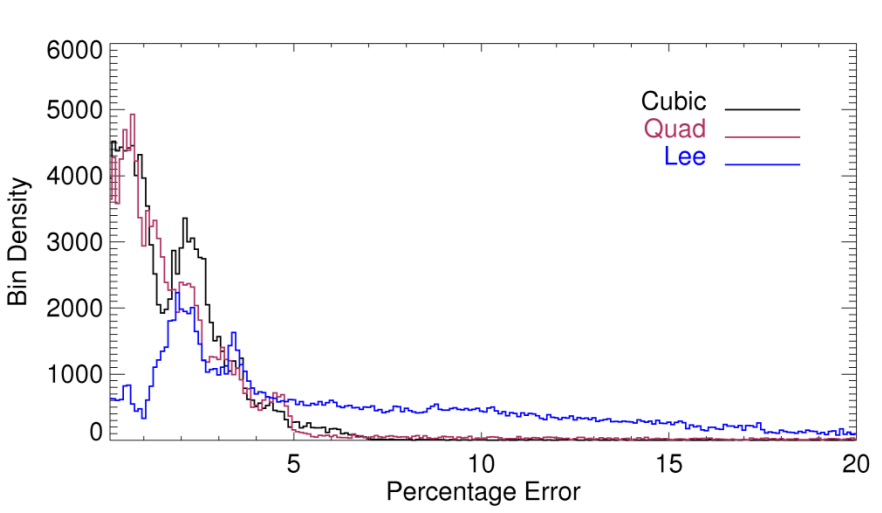

Figure 4-9 Histogram of the percentage error over the nine sun positions. For clarity only those errors below 20% are shown. This excludes 0.5% for the cubic function, 5.8% for the quadratic function and 8.0% for the Lee function.

4.4.4. MERIS Band Specific Functions

The anisotropy factor is related to the scattering and absorption of the water and the water quality parameters and as the IOPs vary with wavelength so too must the anisotropy factor.

To look at the wavelength effect on the anisotropy factor a cubic function was fitted to a *Hydrolight*® run and the residuals were separated by wavelength. Figure 4-10 shows the histogram of MERIS Bands 1 (412.5 nm), 3 (442.5 nm), 5 (560 nm), 8 (681.25 nm), 9 (708.75 nm), and 12 (778.75 nm). The mean residual of the fit for all bands was zero.

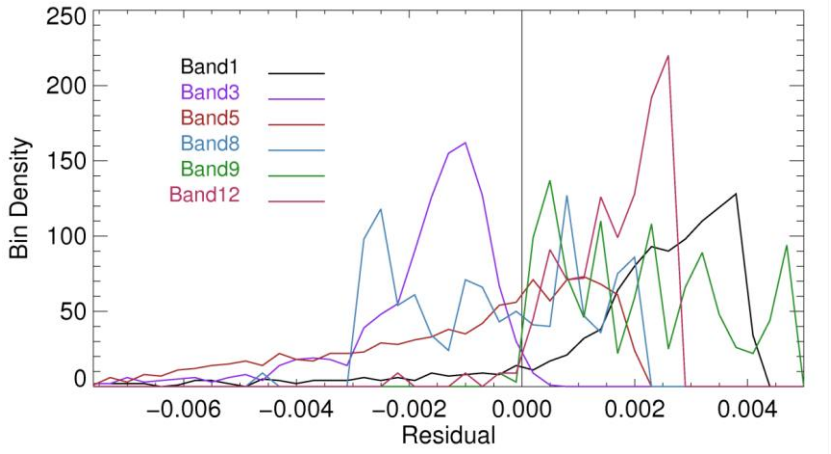

Figure 4-10 Histogram of the residuals of a cubic fit of *f* against *R(0-)* for MERIS Bands 1 (412.5 nm), 3 (442.5 nm), 5 (560 nm), 8(681.25 nm), 9 (708.75 nm), and 12 (778.75 nm).

It can be seen that the peak in the residuals for Band 1 (412.5 nm) and 12 (778.75 nm) is greater than zero and the peak in the Band 3 (442.5 nm) residuals is definitely less than zero. Band 8 (681.25 nm) shows a distribution around zero. For display purposes the bins for the histogram were chosen from residuals that were within two standard deviations from the mean. This means that while no positive residuals were excluded, 2.5% of negative residuals were omitted. Furthermore 1.6% of the values were more than three standard deviations away from the mean. Further investigation into these values showed that they all occurred when the amount of scattering was very low. They were all simulations without any TSM and 75% were where the Chlorophyll *a* value was less than 2 μgl^{-1}. The effect of those outliers is minimal. When the cubic and quadratic fit were recalculated with all the spectra with TSM = 0 mgl^{-1} and chlorophyll *a* less than 2 μgl^{-1} removed, the recalculated relationship only varied from the original relationship by a maximum of 0.5% for very low reflectances.

The simulation sets were used to recalculate the f and $R(0^-)$ relationship using reflectances from single bands. Figure 4-11 and Figure 4-12 show the resulting functions. Each function has been cropped to only show the range of $R(0^-)$ for which it is valid.

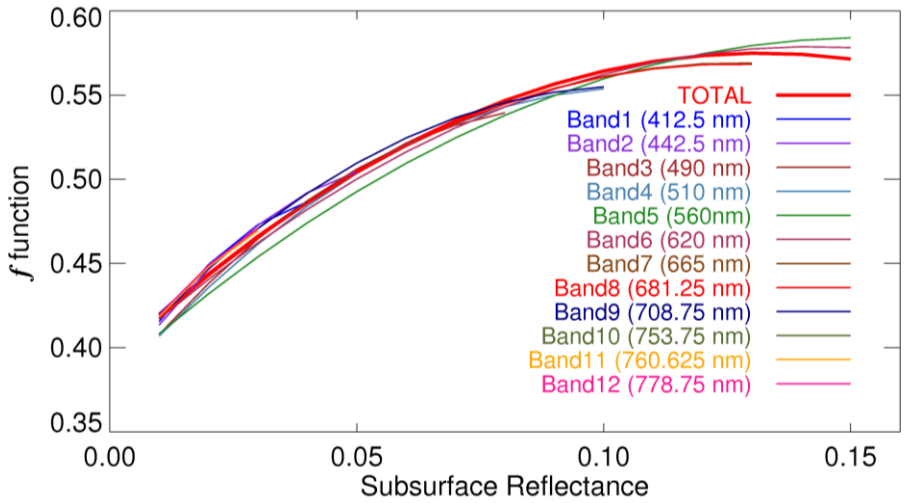

Figure 4-11 f as a quadratic function of $R(0-)$ modelled within each MERIS band with *Hydrolight*®. The reflectance was modelled between 400nm and 800nm using θs=54.9°, a clear sky and an average IOP set for Wivenhoe Dam. The functions have been trimmed to show only the valid range for $R(0-)$. The function calculated for the set as a whole is shown in bold red.

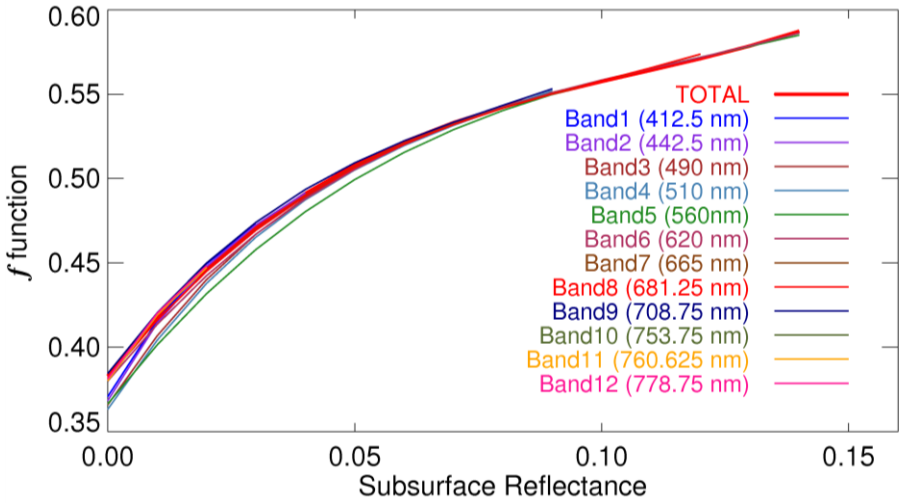

Figure 4-12 *f* as a quadratic function of *R(0-)* modelled within each MERIS band with *Hydrolight*®. The reflectance was modelled between 400nm and 800nm using θs=54.9°, a clear sky and an average IOP set for Wivenhoe Dam. The functions have been trimmed to show only the valid range for *R(0-)*. The function calculated for the set as a whole is shown in bold red.

To investigate the effect of splitting the fitting into band specific functions the difference between the *Hydrolight*® calculated *f* and the model calculated *f* were compared. Figure 4-13 shows plots of the residuals using the single function and the band split function. It is clear that there was considerable improvement in the quadratic function but less so in the cubic function. Further investigation showed that only 59.8% of the residuals were reduced and the rest were increased. However, the median value of reduction was 45% larger than the median value of increase. In short, residuals were reduced and the amount of improvement in residual size was greater.

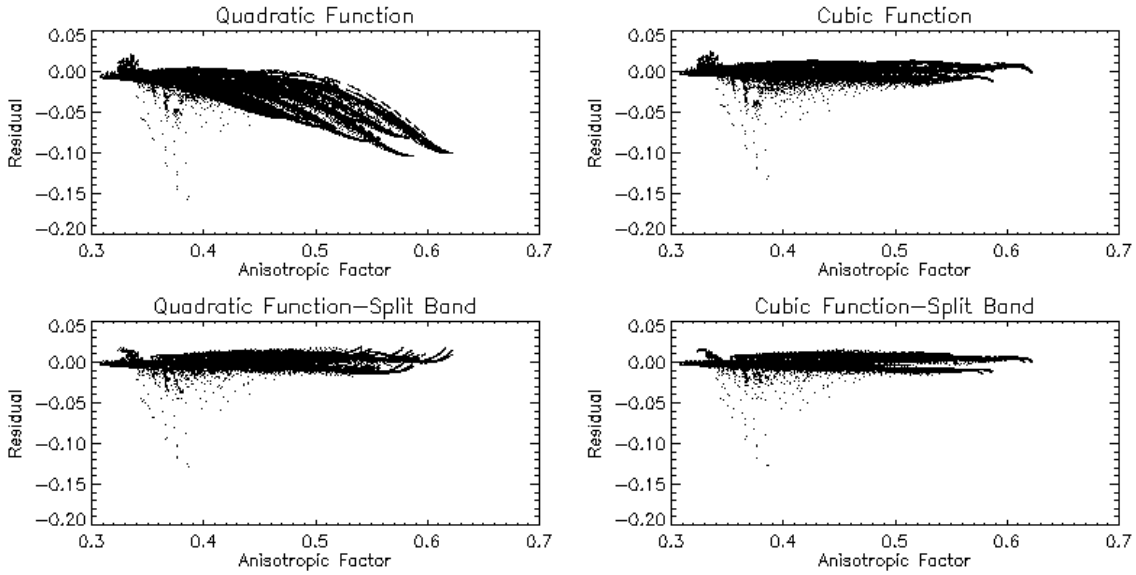

Figure 4-13 The residuals for all sun positions using the single function and the band split function for the quadratic and cubic inverse model.

The exercise was repeated for the PSO models and the results are shown in Figure 4-14. The Lee formulation requires a surface to be fitted to the reflectance, but because the water backscattering reduces with wavelength the solution becomes unstable once the extent of the b_{bw} axis becomes too small. As a result the single band function was only used for the first five bands and the previous single function was substituted for the other bands.

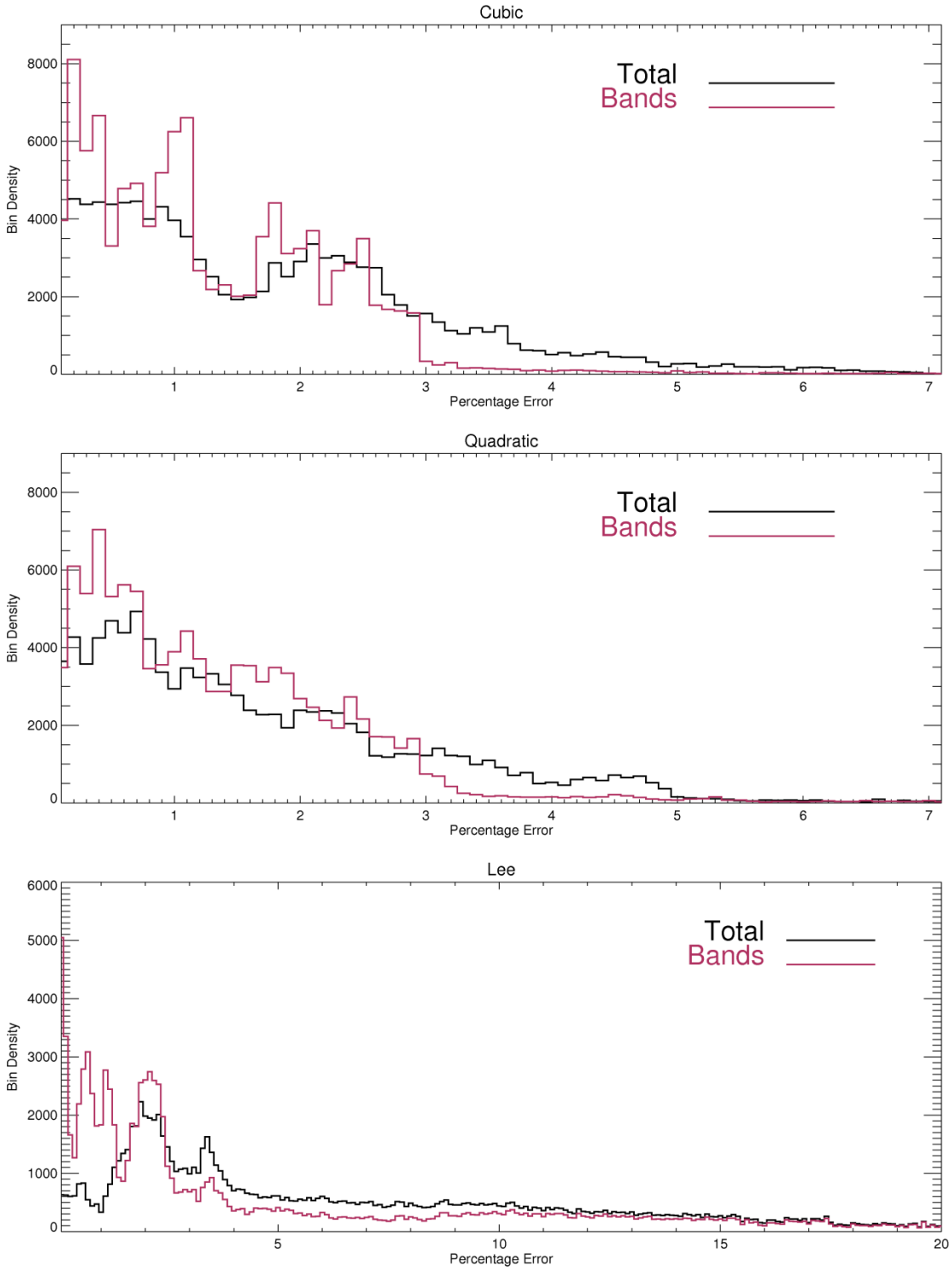

Figure 4-14 Histograms comparing the percentage error in reflectance for the single function and the band specific functions.

4.5 Minimum Detection Limits

The environmental noise-equivalent reflectance difference ($NE\Delta R(0^-)_E$) (Brando & Dekker 2003) is the standard deviation of the sub-surface reflectance in each band over a homogeneous area of optically deep water. This is a useful measure of the inherent noise in the image. For a change in water quality parameter value to be detectable in an image the change in the reflectance brought about by the concentration change must exceed the noise associated with the image (Hoogenboom et al. 1998a). Mathematically this means that the first derivative of the sub-surface reflectance with respect to the water quality parameter must exceed the $NE\Delta R(0^-)_E$. Analytical expressions of the first derivative of reflectance with respect to chlorophyll *a*, TSM and CDOM concentrations were derived using the simple quadratic model for reflectance. The quadratic model was used because the anisotropy factor *f* in the linear model is not independent of the water quality parameter concentration and the cubic model added a layer of needless complexity.

$$R(0^-) = c_0 \frac{b_b}{a+b_b} + c_1 \left(\frac{b_b}{a+b_b} \right)^2 \tag{4-24}$$

where

$$a(\lambda) = a_w(\lambda) + CDOM a^*_{CDOM}(\lambda) + TSM a^*_{TSM}(\lambda) + CHL a^*_{CHL}(\lambda) \tag{4-25}$$

$$b_b(\lambda) = b_{bw}(\lambda) + TSM b^*_{bTSM}(\lambda) + CHL b^*_{bCHL}(\lambda) \tag{4-26}$$

Finding the derivative with respect to CHL:

$$\frac{\partial R(0^-)}{\partial CHL} = c_0 \frac{b^*_{bCHL} a - b_b a^*_{CHL}}{(a+b_b)^2} + c_1 \frac{2\left(a b^*_{bCHL} b_b - b_b^2 a^*_{CHL}\right)}{(a+b_b)^3} \tag{4-27}$$

With respect to TSM:

$$\frac{\partial R(0^-)}{\partial TSM} = c_0 \frac{b^*_{bTSM} a - b_b a^*_{TSM}}{(a+b_b)^2} + c_1 \frac{2\left(a b^*_{bTSM} b_b - b_b^2 a^*_{TSM}\right)}{(a+b_b)^3} \tag{4-28}$$

with respect to CDOM:

$$\frac{\partial R(0^-)}{\partial CDOM} = c_0 \frac{-b_b a^*_{CDOM}}{(a+b_b)^2} + c_1 \frac{-2 b_b^2 a^*_{CDOM}}{(a+b_b)^3} \tag{4-29}$$

The analytical expression allowed an incremental change in the signal for any given water quality parameter concentrations to be calculated. A MERIS full resolution image of Wivenhoe

Dam acquired on the 2nd July 2007. As Wivenhoe Dam is the study site closest to the coast the image also showed a large expanse of optically deep water. The image was corrected using c-WOMBAT-c (Brando & Dekker 2003) and the assumption that there was no near infrared reflectance for optically deep case-I waters. A large homogenous area of water was selected and the standard deviation of the sub-surface reflectance in each band was calculated. The $NE\Delta R(0^-)_E$ was estimated to be a constant 0.1% in all bands.

Previous work has displayed the signal sensitivity for water quality parameters with families of curves on two dimensional plots (Giardino et al. 2007). This approach necessitated holding one water quality parameter constant and allowing the other two to vary. It was clear from the initial sensitivity calculations that the choice of the value for the constant parameter was critical in determining the shape and scale of the sensitivity curves. To allow the whole relationship to be seen, Figures 4-15 – 4-17 below were developed to represent the sensitivity as a volume. For a change in a water quality parameter to be detectable, the change in concentration must bring about a resulting change in the reflectance signal of least 0.001 reflectance units. That is, the first derivative with respect to that water quality parameter must be greater than 0.001 reflectance units. Each volume element that is coloured shows a combination of water quality parameter values for which the first derivative with respect to the water quality parameter value was equal to or greater than 0.001 reflectance units. The displayed volume shows the water quality parameter values that are useable if it is wished to resolve concentrations down to 1 μgl^{-1}, 1 mgl^{-1} and 0.1 m^{-1} for Chlorophyll *a*, TSM and CDOM respectively. In general the larger the volume the more useful the band is and the more reliable the water quality parameter value retrieved will be. Figures 4-15 – 4-17 were calculated with the quadratic model for reflectance that was derived from the θ_s =61.1° simulation calculated with the Burdekin Falls Dam lower SIOP set (c_0 = 0.4825, c_1 = 0. 2117). Similar figures were calculated for the other SIOP sets and are shown in Appendix D. There is one volume for each MERIS band.

Figure 4-15 demonstrates the complexity of the interaction of the three colour producing agents. For the bands 620-681.25 nm a sensitivity minimum in the first derivative of reflectance with respect to chlorophyll *a* appears for TSM values around 4 mg l^{-1} that is maintained irrespective of the chlorophyll *a* or CDOM values.

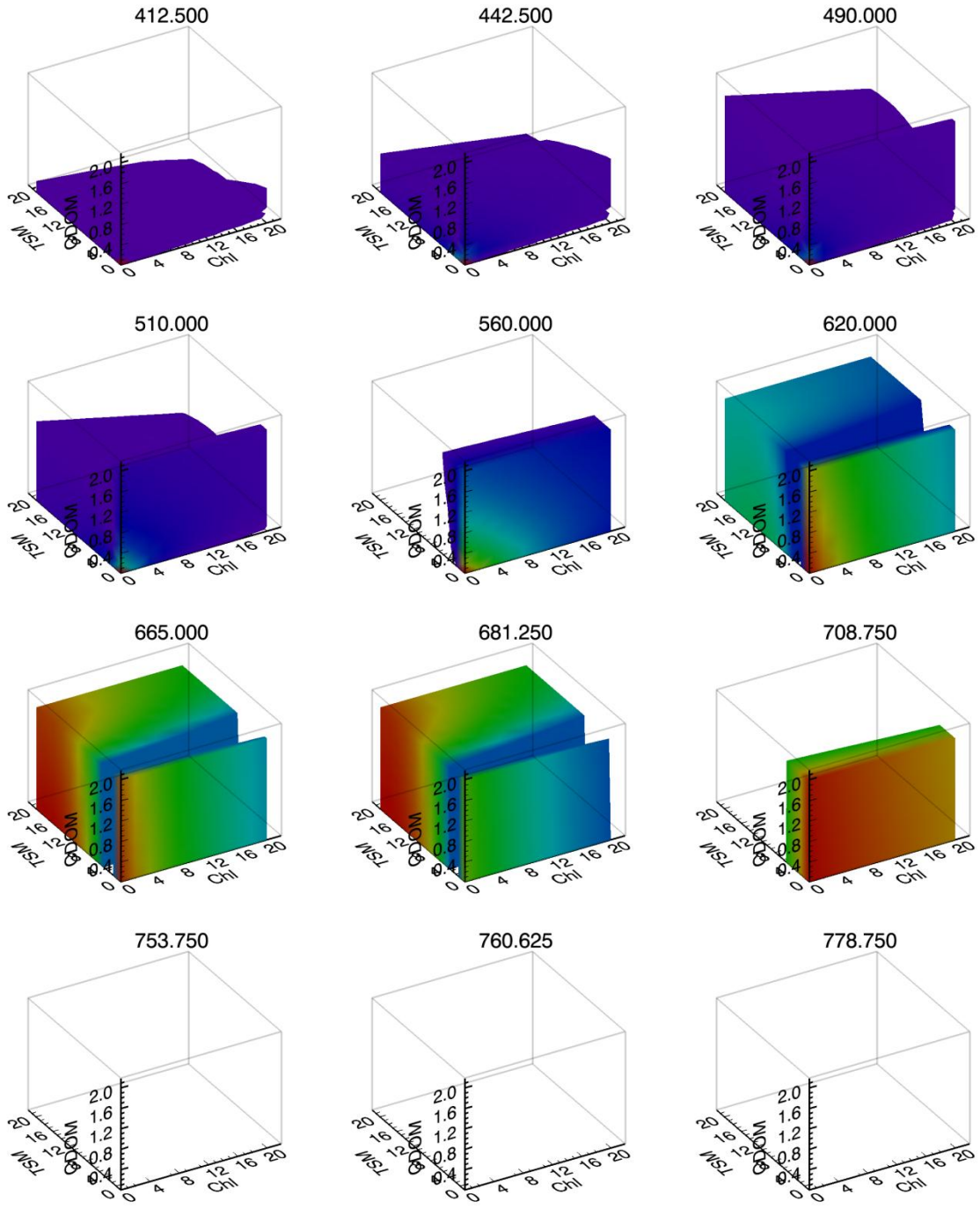

Figure 4-15 Acceptable water quality parameter combinations that allow the change in the reflectance spectra for that wavelength to be distinguished from environmental noise with a change in concentration of Chlorophyll *a* by 1µgl^{-1}. The volumes were calculated with the quadratic model for reflectance that was derived from the θ_s = 61.1° simulation calculated with the Burdekin Falls Dam upper SIOP set.

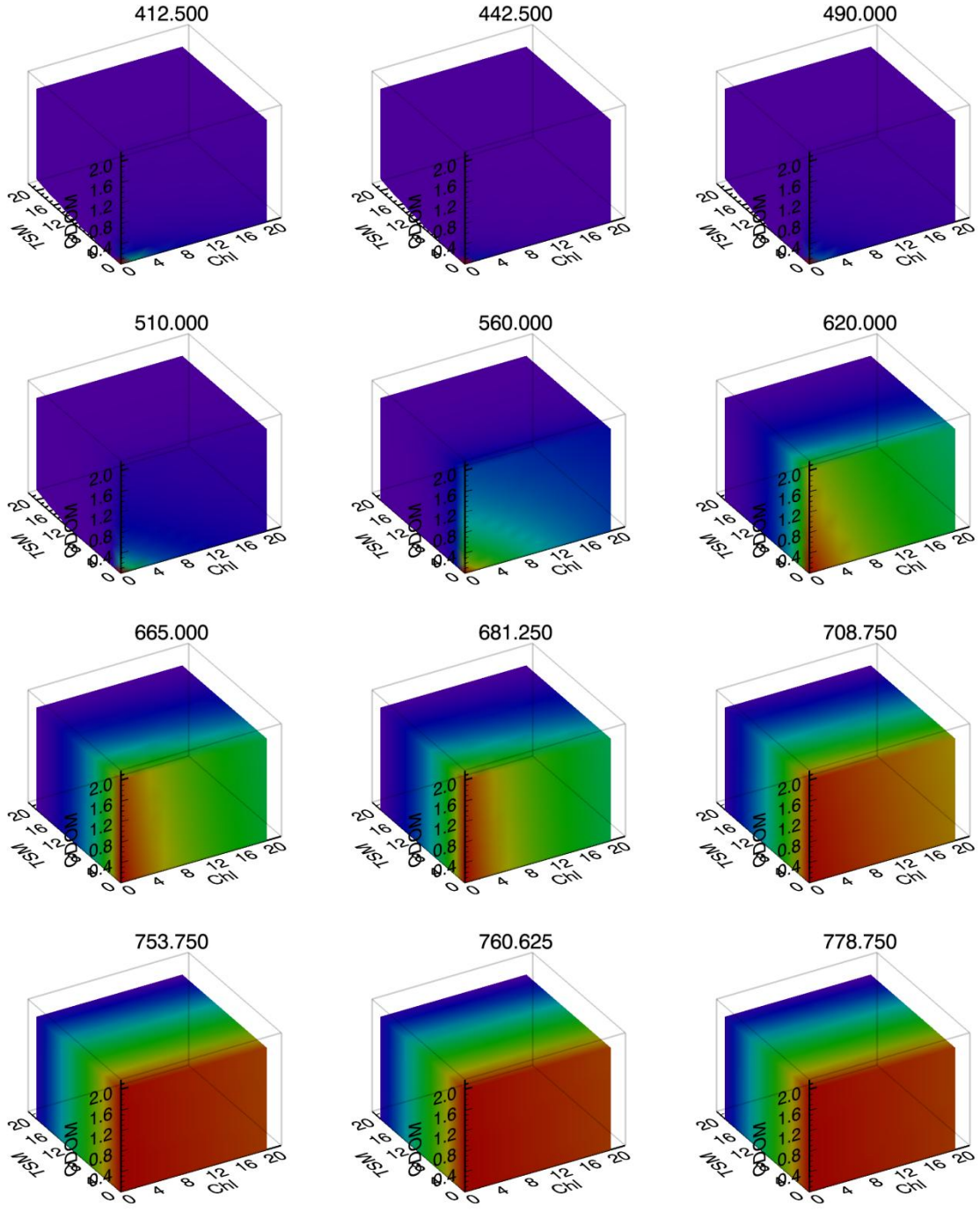

Figure 4-16 Acceptable water quality parameter combinations that allow the change in the reflectance spectra for that wavelength to be distinguished from environmental noise with a change in concentration of TSM by 1mgl^{-1}. The volumes were calculated with the quadratic model for reflectance that was derived from the θ_s = 61.1° simulation calculated with the Burdekin Falls Dam upper SIOP set.

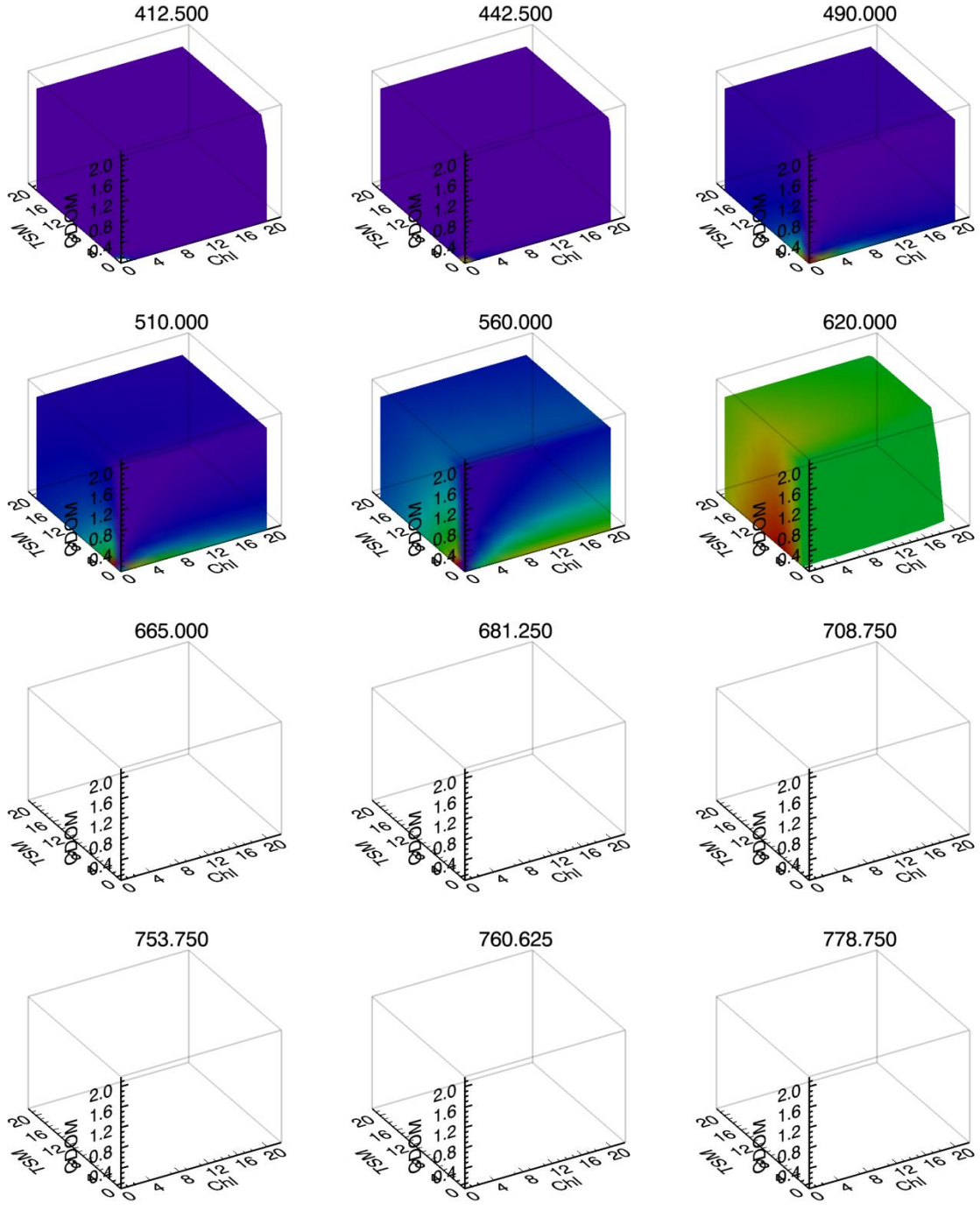

Figure 4-17 Acceptable water quality parameter combinations that allow the change in the reflectance spectra for that wavelength to be distinguished from environmental noise with a change in concentration of CDOM by 0.1 m^{-1}. The volumes were calculated with the quadratic model for reflectance that was derived from the θ_s = 61.1° simulation calculated with the Burdekin Falls Dam upper SIOP set.

It can be seen from the figures that the TSM can be most reliably discriminated to a sufficient level whilst the CDOM and chlorophyll *a* pose greater problems. The signal sensitivity is clearly affected by the SIOP set. By comparing Figures 4-15 – 4-17 to the Appendix Figures D-1 – D-6 it is apparent that the chlorophyll *a* retrieval for Wivenhoe Dam will be far more susceptible to instrument and environmental noise than the Burdekin Falls Dam site, because a greater change in the chlorophyll *a* concentration is required to bring about a similar change in the water reflectance signal.

In practical terms it would be more useful to ask how much a water quality parameter must vary, given the combination of water quality parameter concentrations, before the change in the signal is sufficient to be differentiated from noise. Due to the complex nature of the mathematical interactions in the MIM and PSO it is not possible to arrive at an analytical solution for this question, but the next section uses the *Hydrolight*® simulations to estimate the effect of different noise sources on the expected retrieval accuracy and precision.

4.6 Accuracy and Precision of Inversions

The accuracy and precision of the inversion methods were established by inverting the spectra simulated with the *Hydrolight*® code and comparing the resultant water quality parameter concentrations to the concentrations that were used to simulate the reflectance spectrum. The accuracy of any given concentration estimate derived from spectrum inversion was evaluated by the absolute value of the difference between the retrieved water quality parameter value and the value used to simulate the spectrum. The average value over all the spectra in all nine simulations was considered the accuracy of that water quality parameter for that inversion routine. The precision was measured by the standard deviation of all the absolute values of the differences between the retrieved water quality parameter values and the values used to simulate the spectra. These accuracies and precisions represent the baseline or best possible values.

The bio-optical models described above relate the subsurface reflectance to the absorption and backscattering of the water and water quality parameters. As a remote sensor measures the top of atmosphere radiance the effect of the atmosphere and the air-water interface must be eliminated before the subsurface reflectance spectra can be used. In addition the inversions rely on having

accurate specific absorption and backscattering spectra. Any measurement errors, approximations or assumptions made in this process will introduce error into the retrieved water quality parameter concentrations. The ability of a weighting scheme or similarity measure to reduce the effect of these errors will be a useful measure of its efficacy.

The interaction between these error sources and forward inverse model for remote sensing of water quality is shown conceptually in Figure 4-18

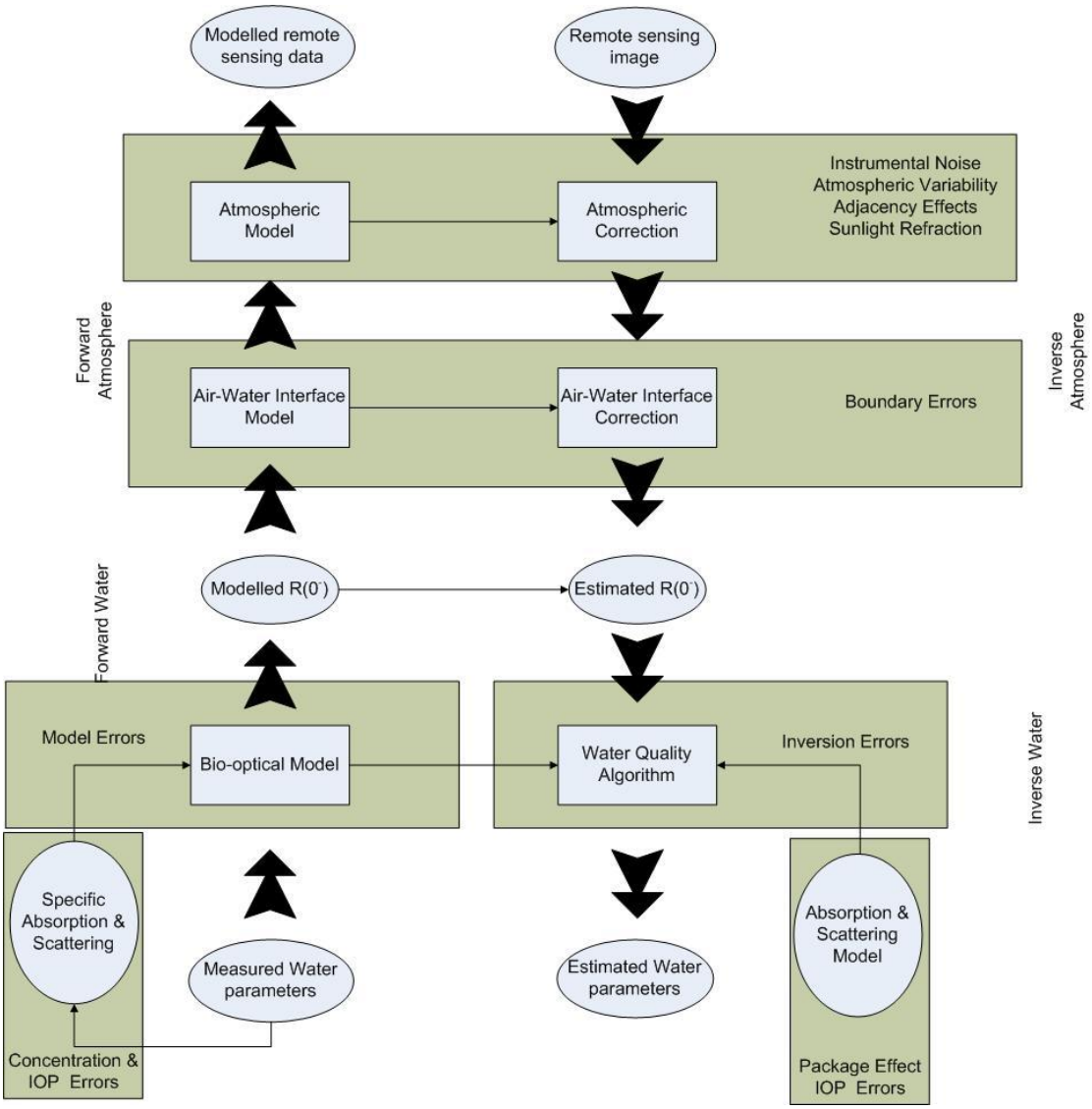

Figure 4-18 The effect of error on the forward and inverse model for remote sensing of water quality. Adapted from (Dekker et al. 2001)

To simulate the effect of three broad types of error the following distortions were made to the simulated spectra or the SIOPs:

Environmental noise errors

Some errors act separately in each band, meaning the reflectance spectra is distorted in shape as well as scale. Some of the sources of this variation are:

- A single value of the ratio of upwelling irradiance to upwelling radiance (Q) is used in the air-water interface correction of de Haan & Kokke (1996) but the *Hydrolight*® simulations show this value varies by approximately 4.6% (range 4.52–4.96).
- The average error between the fitted curve and the raw data for the anisotropy factor f was 1%.
- The environmental noise-equivalent reflectance difference ($NE\Delta R(0^-)_E$) (Brando & Dekker 2003) is the standard deviation of the subsurface reflectance in each band over a homogeneous area of optically deep water. The same $NE\Delta R(0^-)_E$ value of a constant 0.1% in all bands estimated from the 2nd July 2007 MERIS image was used.

For eight noise levels between 0-7% these errors were imitated by adding to each band in a simulated spectrum a normally-distributed, pseudo-random number with a mean of zero and a standard deviation of one that was scaled to the particular noise level. An offset representing the $NE\Delta R(0^-)_E$ was then applied. As each band had a different scale factor applied to it, the effect was to distort the shape as well as the scale of the spectra. The inversion was run on the 9801 simulated spectra with 50 applications of the noise. The inversion algorithm was applied and the mean of the 50 mean errors was calculated for each water quality constituent value at each noise level.

Atmospheric correction errors

The errors associated with the atmospheric correction involve a scale error and a shape error as before but in this case the amount of the error will be band dependent. In broad terms the scale error will occur when an incorrect estimate has been made of the visibility and the shape error will occur from making a poor estimation of the aerosol types or their mixing ratio. The spectral

dependence of the path radiance conforms to a power law so the spectra were modified by a single multiplicative scale factor (varying from unity by 0% to 20%, normally distributed) as well as a value for the power slope (varying from unity by 0% to 10%). The inversion was run as described in the previous section.

SIOP measurement errors

The MIM method requires that the spectra for a^* and b_b^* be calculated from field measurement of the total absorption and backscattering for each constituent and the water quality constituent concentration. Measurement errors in the water quality constituent concentration, due to the limitations of the laboratory techniques, will result in a consistent scale error across all bands as the water quality constituent concentration is used as a divisor for each band when the SIOP is calculated. In addition, the measurement of absorption and backscattering for each constituent will have a shape error associated with it due to random errors in their measurement because the errors are not necessarily consistent across the spectrum. For the phytoplankton absorption, the shape change was modelled in the same way as the signal shape error. The other water quality constituents' absorption and the backscattering calculations involve fitting a function with slope and scale parameters to the raw observation so their errors were modelled using a variation of spectral slope in the same way as the atmospheric correction error. After considering the variation in SIOPs measured during the July 2007 site visit, the phytoplankton SIOP scale error bounds were set to 0% and 20%, and the noise applied to the slope was set at half the value for the scale. The absorption and scattering of pure water was not varied. The inversion was run as described in the previous section.

4.6.1. MIM

Baseline Accuracy

The baseline values for the MIM are reported in Table 4-4 and Table 4-5 for both the quadratic and cubic formulations of the f value. The cubic function is superior for all of the weighting schemes. It was used in the estimation of effects of the other noise sources. The weighting schemes were evaluated based on their relative performance across the three water quality

parameter types. The individual band weights for the weighting schemes are shown in Figure 4-19.

Table 4-4 The means of the means of the absolute values of error for inversions at nine different sun angles using a single parameter function for all bands. *†‡§ denotes the difference is not significant at 95% for pairwise comparisons. Names and short descriptions for the weighting schemes are given in Table 4-1.

Weight Scheme	Quadratic						Cubic					
	Chl (μgl^{-1})		TSM (mgl^{-1})		CDOM(m^{-1})		Chl (μgl^{-1})		TSM (mgl^{-1})		CDOM(m^{-1})	
	Av	SD	Av	SD	Av	SD	Av	SD	Av	SD	Av	SD
MER_ALL	2.49	1.88	0.98	0.8	0.03	0.03	0.23*	0.16	0.17	0.14	0.02	0.02
MER_NO_IR	1.99	1.13	1.64	1.42	0.05	0.04	0.22	0.15	0.17	0.16	0.02*	0.02
MER_3BANDS	2.94	1.55	1.09	0.96	0.09	0.07	0.3	0.2	0.15	0.15	0.02	0.02
MER_DER1	2.13	1.33	1.47	1.24	0.08	0.05	0.23*	0.18	0.17	0.15	0.02†	0.02
MER_DER2	1.69	1.19	1.36	1.14	0.08	0.05	0.23	0.17	0.17	0.15	0.02§	0.02
MER_DER3	1.47	0.88	1.26	1.05	0.1	0.05	0.22	0.16	0.17	0.15	0.02§	0.02
MER_DER4	8.35	4.61	3.57	2.98	0.06	0.05	0.43	0.38	0.29	0.27	0.02	0.02
MER_DER5	1.64	1.14	1.38	1.18	0.08	0.05	0.22	0.17	0.17	0.15	0.02‡	0.02
MER_DER6	1.53	1.08	1.35*	1.16	0.08	0.05	0.21	0.17	0.17	0.15	0.02‡	0.02
MER_HAK	1.42	0.86	1.27	1.07	0.1	0.05	0.22	0.16	0.17	0.15	0.02	0.02
MER_REF1	4.63	1.83	1.83	1.56	0.11	0.07	0.28	0.23	0.19	0.17	0.02	0.02
MER_REF2	1.47	1.03	1.37	1.15	0.09	0.05	0.22	0.17	0.17	0.15	0.02	0.02
MER_RAN1	0.54	0.39	1.49	1.29	0.05	0.05	0.25	0.14	0.16	0.16	0.02†	0.02
MER_RAN2	0.84	0.69	1.36	1.18	0.05	0.04	0.27	0.15	0.16*	0.15	0.02*	0.02
MER_RAN3	1.02	0.75	1.18	1.06	0.04	0.03	0.25	0.16	0.16	0.15	0.02	0.02
MER_RAN4	1.18	0.75	1.19	1.04	0.05	0.03	0.2	0.15	0.16*	0.15	0.02	0.02
MER_RAN5	1.6	1.16	1.26	1.07	0.03	0.03	0.23	0.16	0.16	0.15	0.02	0.02
MER_RAN6	2.5	1.76	1.00	0.81	0.13	0.07	0.26	0.17	0.17	0.14	0.02	0.02
MER_RAN7	6.42	4.13	1.03	0.78	0.05	0.04	0.37	0.26	0.17	0.14	0.02	0.02
MER_RAN8	12.19	7.68	1.35*	0.95	0.14	0.09	0.64	0.45	0.19	0.15	0.02	0.02

Table 4-5 The means of the means of the absolute values of the error for inversions at nine different sun angles using separate parameter functions for each band. * denotes the difference is not significant at 95% for pairwise comparisons. Names and short descriptions for the weighting schemes are given in Table 4-1.

Weight Scheme	Quadratic						Cubic					
	Chl (μgl^{-1})		TSM (mgl^{-1})		CDOM (m^{-1})		Chl (μgl^{-1})		TSM (mgl^{-1})		CDOM(m^{-1})	
	Av	SD	Av	SD	Av	SD	Av	SD	Av	SD	Av	SD
MER_ALL	0.21	0.18	0.15	0.15	0.01	0.01	0.1	0.09	0.14	0.14	0.01	0.01
MER_NO_IR	0.15	0.15	0.16	0.18	0.01	0.01	0.08*	0.09	0.16	0.16	0.01	0.01
MER_3BANDS	0.22	0.2	0.15	0.15	0.02	0.02	0.16	0.13	0.14	0.14	0.02	0.02
MER_DER1	0.19	0.17	0.16	0.17	0.02	0.01	0.1	0.1	0.16	0.16	0.02	0.01
MER_DER2	0.19	0.17	0.16	0.17	0.02	0.01	0.1	0.1	0.15*	0.16	0.02	0.01
MER_DER3	0.19	0.16	0.15	0.16	0.02	0.02	0.08*	0.09	0.15	0.15	0.02	0.02
MER_DER4	0.41	0.43	0.27	0.33	0.01	0.01	0.34	0.34	0.26	0.28	0.01	0.01
MER_DER5	0.18	0.16	0.16	0.17	0.02	0.01	0.09	0.09	0.15	0.15	0.02	0.01
MER_DER6	0.18	0.16	0.15	0.17	0.02	0.01	0.09	0.09	0.15	0.15	0.02	0.01
MER_HAK	0.19	0.16	0.15	0.16	0.02	0.02	0.08	0.09	0.15	0.15	0.02	0.02
MER_REF1	0.24	0.21	0.18	0.19	0.02	0.02	0.18	0.15	0.17	0.18	0.02	0.02
MER_REF2	0.19	0.16	0.16	0.17	0.02	0.01	0.09	0.09	0.15*	0.16	0.02	0.01
MER_RAN1	0.13	0.14	0.15	0.17	0.01	0.01	0.07	0.07	0.15	0.15	0.01	0.01
MER_RAN2	0.14	0.15	0.15	0.16	0.01	0.01	0.08	0.08	0.15	0.15	0.01	0.01
MER_RAN3	0.15	0.15	0.15	0.16	0.01	0.01	0.07	0.07	0.14	0.14	0.01	0.01
MER_RAN4	0.16	0.15	0.15	0.16	0.01	0.01	0.08	0.08	0.15	0.15	0.01	0.01
MER_RAN5	0.17	0.16	0.15	0.16	0.01	0.01	0.1	0.09	0.15	0.15	0.01	0.01
MER_RAN6	0.22	0.19	0.15	0.15	0.02	0.02	0.1	0.1	0.15	0.15	0.02	0.02
MER_RAN7	0.34	0.31	0.15	0.15	0.01	0.01	0.27	0.22	0.15	0.15	0.01	0.01
MER_RAN8	0.62	0.59	0.17	0.17	0.01	0.01	0.49	0.45	0.16	0.16	0.01	0.01

For reference Figure 4-20 shows the result of the single quadratic and cubic function against the band specific results.

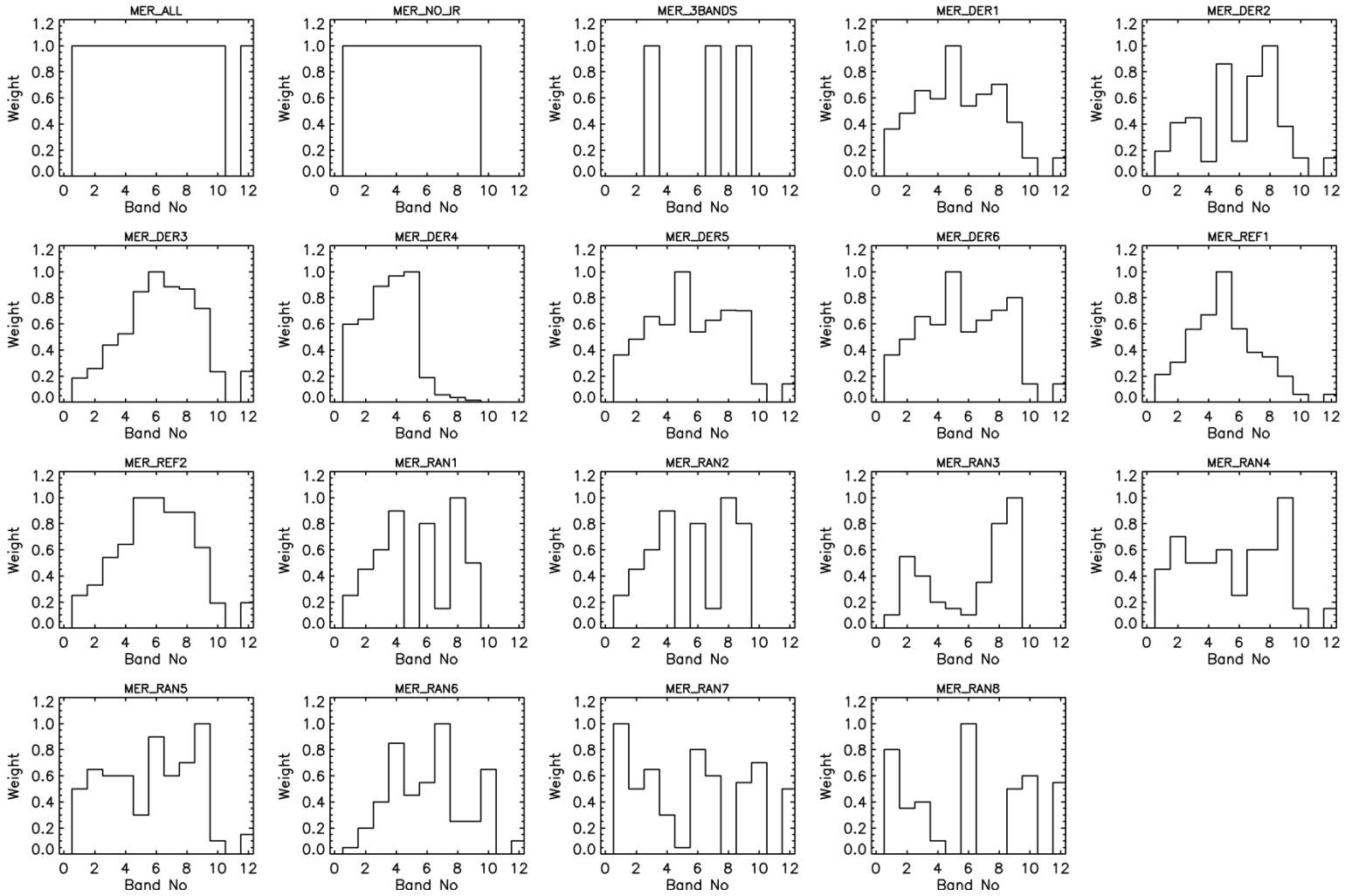

Figure 4-19 The weights for the weighting schemes. Names and short descriptions for the weighting schemes are given in Table 4-1.

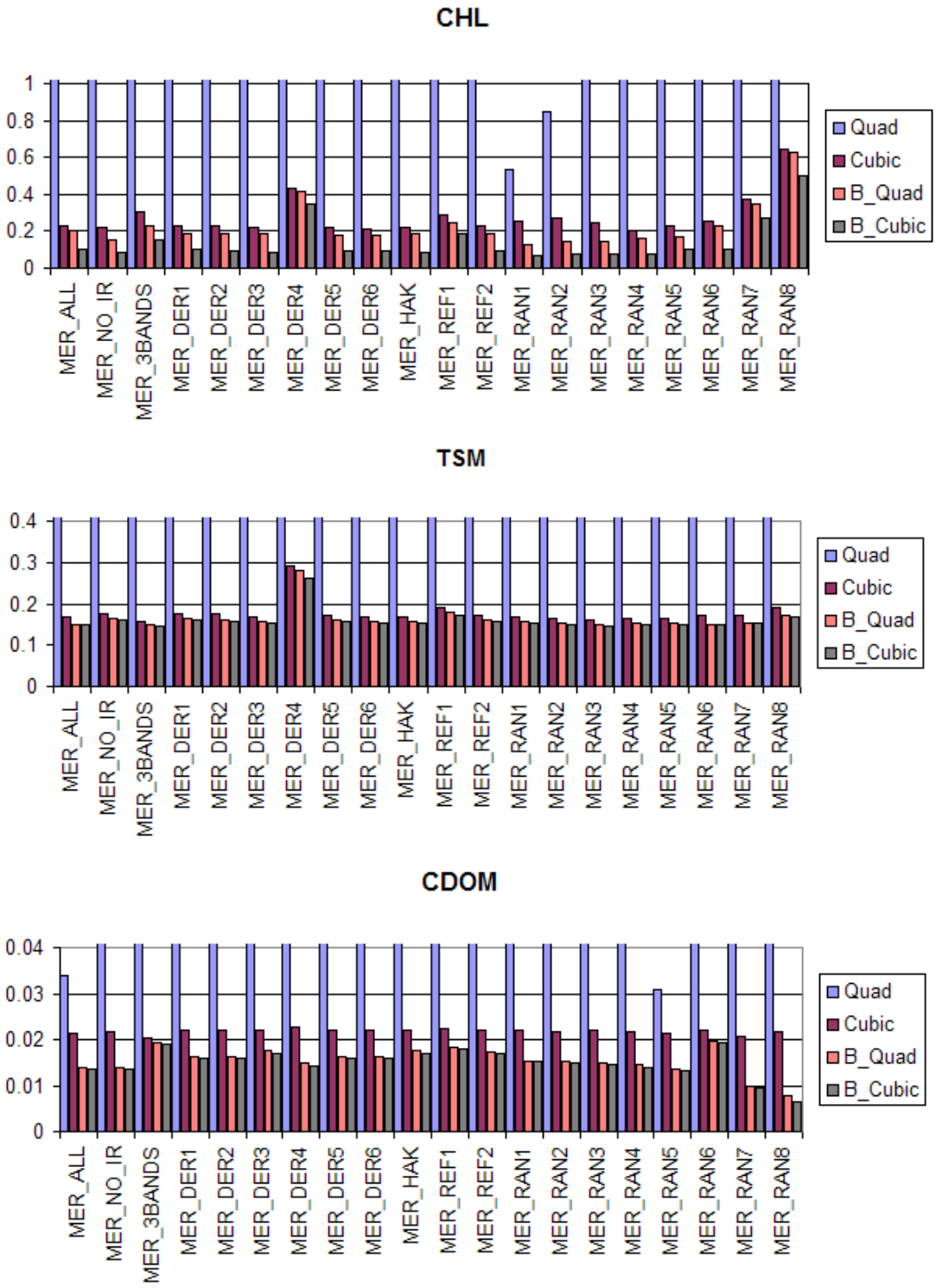

Figure 4-20 The mean retrieval accuracy for chlorophyll *a*, TSM and CDOM for the quadratic and cubic single functions as well as the quadratic and cubic band specific functions. Names and short descriptions for the weighting schemes are given in Table 4-1.

Table 4-1Accuracy and Precision Values after the Addition of Environmental Noise

Before introducing simulated error from the other sources the offset representing the $NE\Delta R(0^-)_E$ was applied. Figure 4-21 compares the average error before the application of the noise against the average error after the noise is applied. The most obvious feature is that the standard three band approach has performed very poorly with the addition of the $NE\Delta R(0^-)_E$. However there has also been a change in the best performed weighting schemes.

Previous work (Campbell & Phinn 2008) has shown differences in the behaviour of the weighting schemes with respect to the introduced noise. This behaviour was ascribed to the weighting schemes themselves, but it now appears to be an artefact of the poor fitting of the *f* function to the individual bands. Using the band specific *f* function ensures that nearly all the weighting schemes behave in essentially the same manner when environmental noise is added. Figure 4-22 shows examples of the error-noise relationship. It can be seen that the three band approach has a large variability in the water quality parameter retrievals. For all three water quality constituents the MER_ALL weighting scheme is the least affected by the increase in the environmental noise but its overall utility is limited by its response to the $NE\Delta R(0^-)_E$ offset.

If we exclude the three band weighting scheme, the addition of the $NE\Delta R(0^-)_E$ offset increased the standard deviation of the absolute error by between 10-30 times for chlorophyll *a*, 1.2-16 times for TSM and 1.9-2.6 times for CDOM. In the case of chlorophyll *a* and CDOM the addition of the other noise sources had a negligible effect on the retrieval precision. However, in the case of the TSM retrieval the precision varies in proportion to the accuracy.

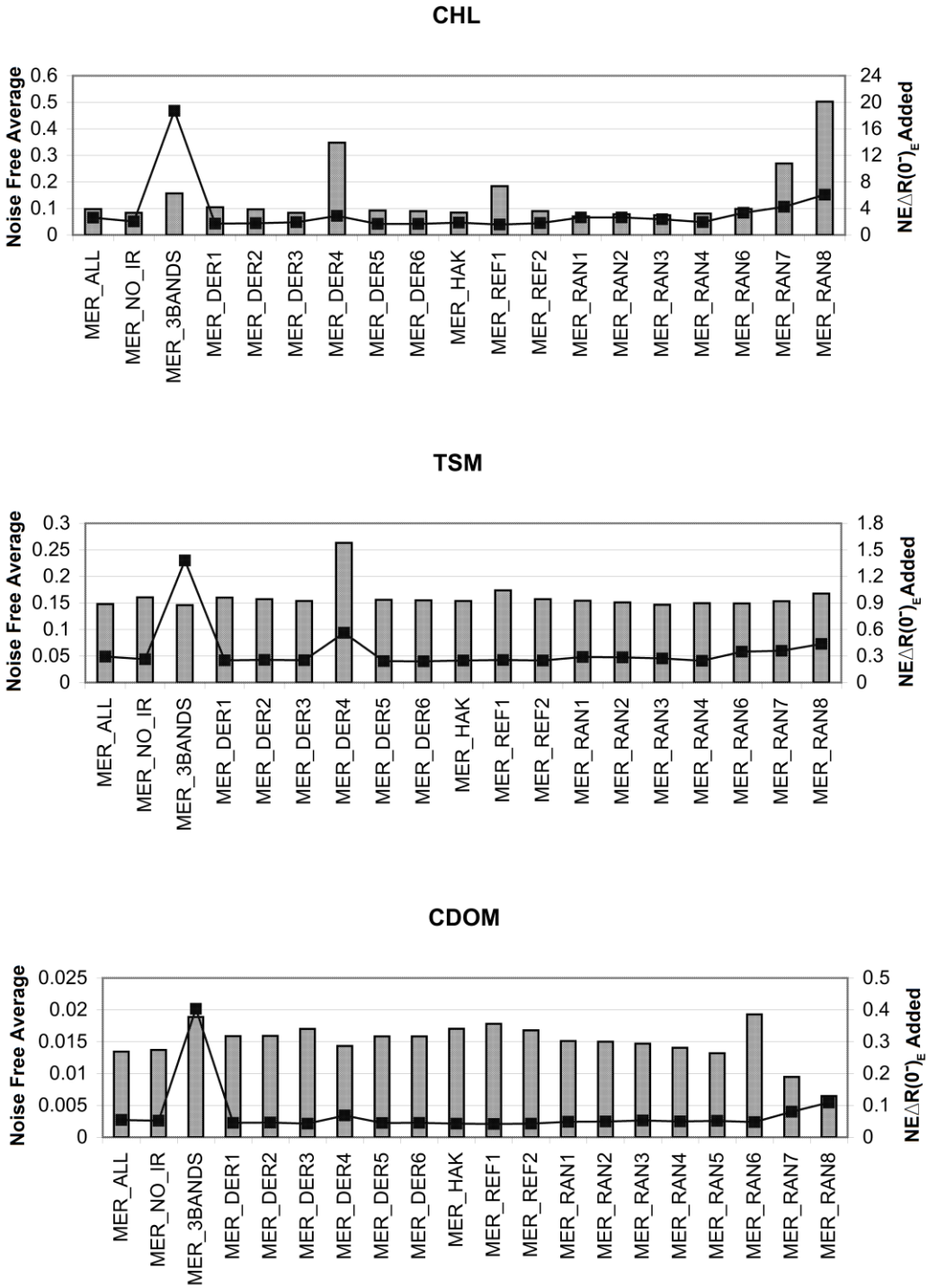

Figure 4-21 Comparing the mean retrieval accuracy for chlorophyll *a*, TSM and CDOM with and without added noise. The retrieval was done using the band specific cubic *f* function. The bars are the noise free averages and the line is the average after addition of a NE$\Delta R(0^-)$ of 0.001. Names and short descriptions for the weighting schemes are given in Table 4-1.

Table **4-1**

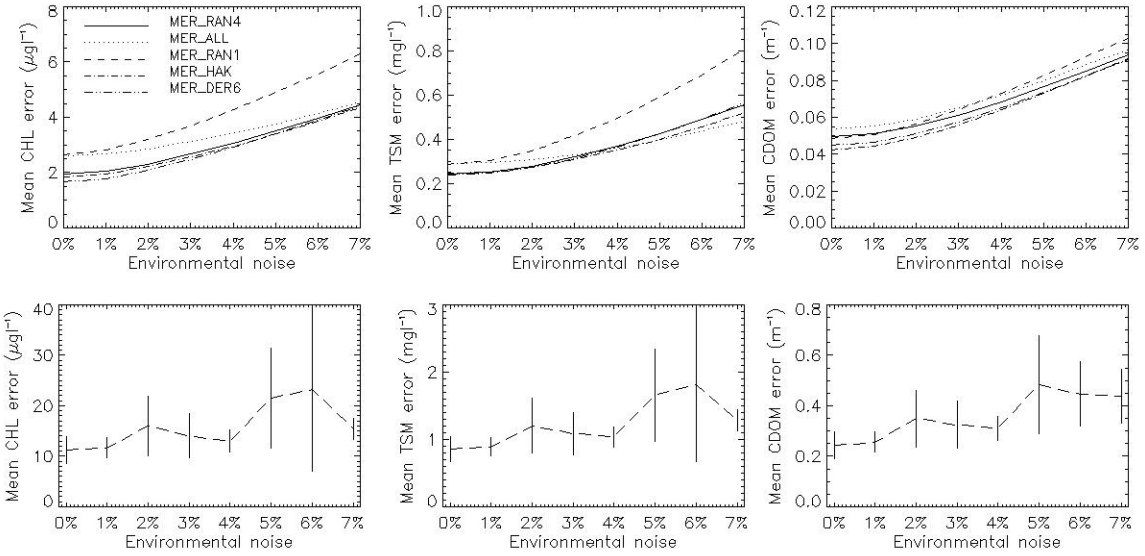

Figure 4-22 The average error of chlorophyll *a* (left), TSM (centre) and CDOM (left) retrieval against the environmental noise level for selected weighting schemes. MER_3BANDS has been plotted separately for clarity and is shown with its 95% confidence intervals.

Accuracy and Precision Values after the Addition of Atmospheric Noise

Sample plots of the atmospheric noise-error relationship are shown in Figure 4-23. For all intents and purposes the water quality constituent error values follow a linear trend with the increase in atmospheric noise. The water quality constituent retrieval precision varies in proportion to the accuracy.

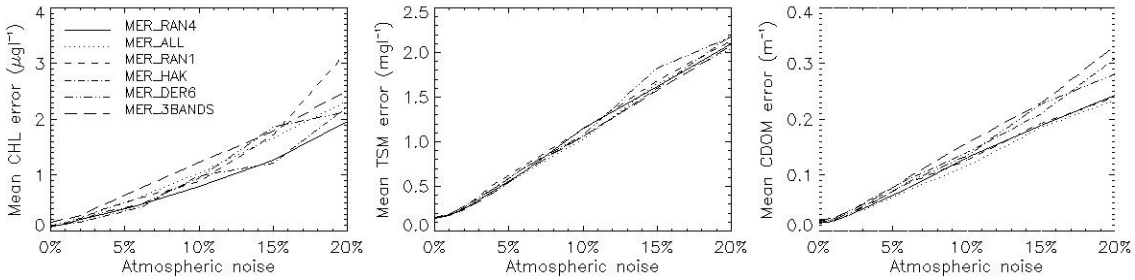

Figure 4-23 The average error of chlorophyll *a* (left), TSM (centre) and CDOM (left) retrieval against the atmospheric correction noise level for selected weighting schemes.

Accuracy and Precision Values after the Addition of SIOP Noise

Sample plots of the SIOP noise-error relationship are shown in Figure 4-24. Like the effect of atmospheric noise, the error increase is linear, for the most part, with the addition of noise in the

SIOP set. It is clear that none of the weighting schemes are superior in relation to the retrieval of TSM but once again the three band scheme performance is degraded more sharply by the addition of SIOP noise. The water quality constituent retrieval precision varies in proportion to the accuracy.

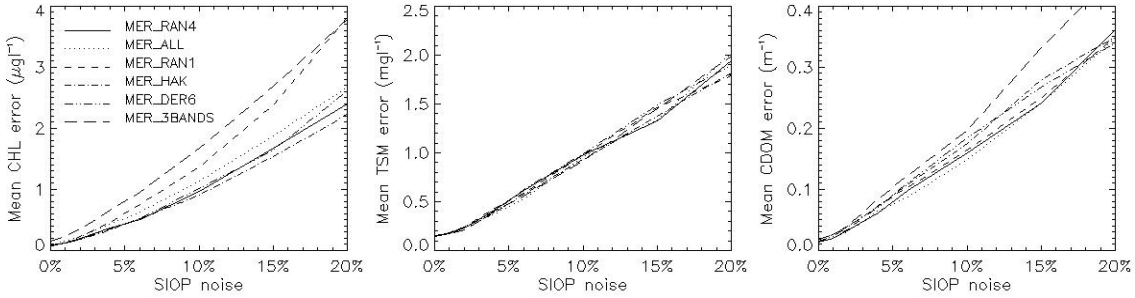

Figure 4-24 The average error of chlorophyll *a* (left), TSM (centre) and CDOM (left) retrieval against the SIOP noise level for selected weighting schemes.

The preceding results were used to rank the weighting schemes to identify those that give the best all-round performance for the three water quality constituent types and the three sources of noise. The six best performed weighting schemes are shown in Figure 4-25. With the exception of the three band approach and a few other exceptions there was little difference between the performances of the weighting schemes.

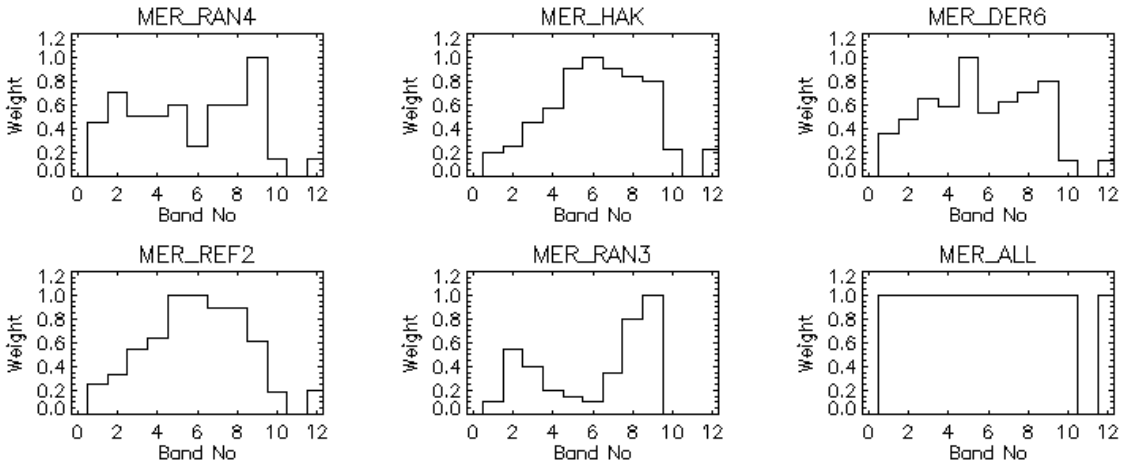

Figure 4-25 The weights for the six best performed weighting schemes. The schemes are shown in rank order from the best performed in the top left hand corner and the sixth best performed in the bottom right.

4.6.2. PSO

The PSO is a stochastic search technique which includes a random element in the search approach. This means the path of each particle is different each time the optimisation is run. As an example Figure 4-26 below shows the four search paths for the same starting particle matching the same input spectra using the SID matching condition. The starting point is chlorophyll *a* 5 μgl^{-1}, TSM 5 mgl^{-1}, and CDOM 0.25 m^{-1}. The final solution is the same chlorophyll *a* 3.66 μgl^{-1}, TSM 16.08 mgl^{-1}, and CDOM 0.64 m^{-1} and the true value is chlorophyll *a* 4 μgl^{-1}, TSM 16mgl^{-1}, and CDOM 0.6 m^{-1}

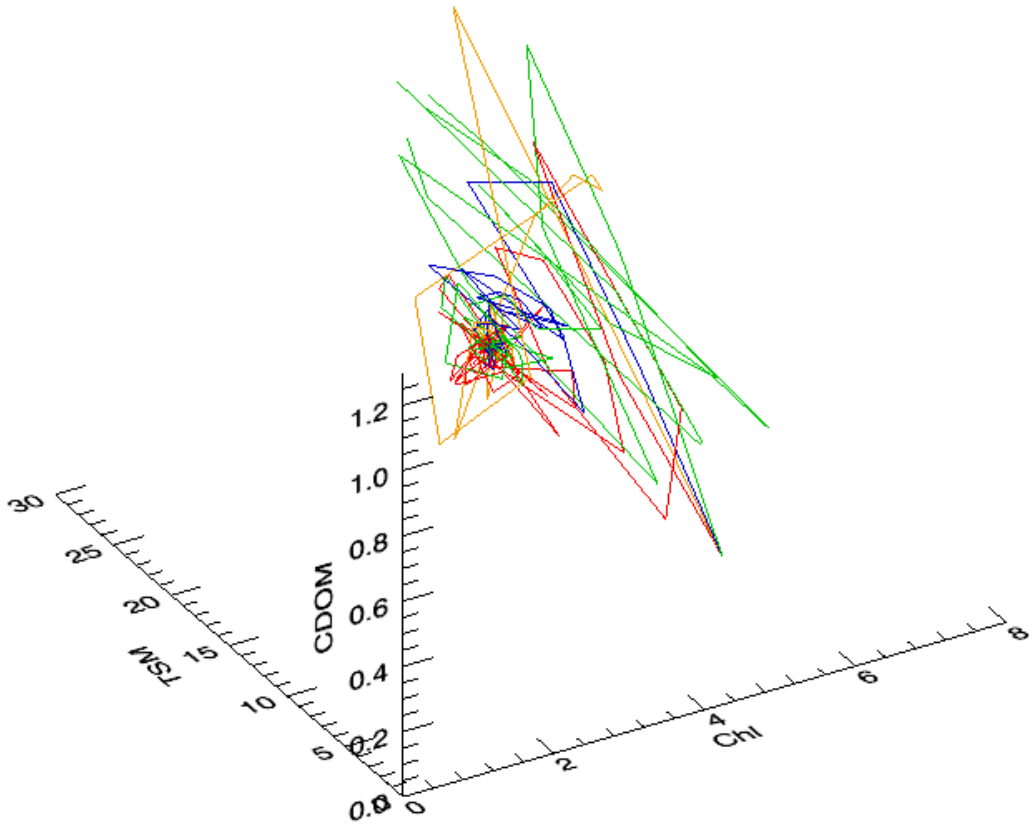

Figure 4-26 The trajectory of a single particle during four inversions of the same spectrum.

Effect of Starting Points

To compare the effect of the number of particles in the swarm, 30 *Hydrolight*® spectra were selected at random and then optimised 100 times to solve for the water quality parameters using a PSO with 8, 27 and 64 starting particles. The matching was done by the SID. A maximum of

100 iterations were used and the solution was considered converged when the range of all the particle concentrations were less than $0.05\ \mu gl^{-1}$ for chlorophyll *a*, $0.05\ mgl^{-1}$ for TSM and $0.01\ m^{-1}$ for CDOM. For each spectrum the standard deviation of the 100 solutions was calculated as a measure of the consistency of the optimisation. The mean standard deviations are shown tabulated in Table 4-6.

Table 4-6 Comparison of the performance of the PSO with 8, 27 and 64 starting points. For each starting point value the average time to complete the inversion and the average number of iterations required before convergence is tabulated.

No of particles	Avg Time	Avg Iterations	Mean Chl Stdev (μgl^{-1})	Mean Tripton Stdev (mgl^{-1})	Mean CDOM Stdev (m^{-1})
8	0.017s	73	0.219	0.056	0.0112
27	0.06s	86	0.009	0.001	0.0003
64	0.145s	89	0.002	0.001	0.0001

There is no noteworthy difference between the performance of the 64 and 27 point approaches except for the 2.5 fold time advantage of the 27 point approach. Reducing the number of starting points to eight led to an increase in the variability of the result as evidenced by the increase in the standard deviation.

The convergence test sometimes allowed outliers to be selected so it was not used in the following tests.

Baseline Accuracy

The baseline values for the PSO are reported in Table 4-7 and Table 4-8 for the quadratic, cubic and Lee formulations of the forward model. The band specific cubic function is superior for all of the matching criteria. It was used in the estimation of effects of the other noise sources.

Table 4-7 The means of the means of the absolute values of error for inversions at nine different sun angles using a single parameter function for all bands. * denotes the difference is not significant at 95% for pairwise comparisons.

	Lee et al. Approach						Gordon Approach Cubic						Gordon Approach Quadratic					
	Chl (μgl^{-1})		TSM (mgl^{-1})		CDOM (m^{-1})		Chl (μgl^{-1})		TSM (mgl^{-1})		CDOM (m^{-1})		Chl (μgl^{-1})		TSM (mgl^{-1})		CDOM (m^{-1})	
	Av	SD	Av	SD	Av	SD	Av	SD	Av	SD	Av	SD	Av	SD	Av	SD	Av	SD
SID	2.22	0.90	1.42	0.49	0.20	0.08	0.29	0.41	0.16	0.18	0.02	0.05	1.35	1.75	0.31	0.36	0.06	0.09
SAM	1.46	0.86	1.05	0.41	0.16	0.07	0.19	0.46	0.11	0.20	0.03*	0.06	0.80	1.23	0.22	0.35	0.05	0.08
MIN_DIST	1.22	1.27	0.46	0.26	0.06	0.05	0.28	0.96	0.19	0.16	0.03	0.03	0.67	1.26	0.19	0.16	0.03	0.04
SIDSAM	1.95	0.92	1.28	0.46	0.19	0.07	0.25	0.47	0.14	0.20	0.02	0.06	1.13	1.49	0.25	0.35	0.05	0.09
SIDMIN	1.52	0.90	0.53	0.29	0.06	0.05	0.20	0.30	0.18	0.15	0.02	0.02	0.87	1.24	0.24	0.30	0.04	0.08
SAMMIN	1.24	1.37	0.47	0.25	0.06	0.09	0.22	0.72	0.18	0.14	0.03*	0.06	0.63	1.00	0.18	0.15	0.03	0.04
SCM	0.33	0.58	0.59	0.43	0.10	0.08	0.32	0.44	0.22	0.24	0.05	0.06	0.34	0.60	0.60	0.44	0.10	0.08

Table 4-8 The means of the means of the absolute values of the error for inversions at nine different sun angles using separate parameter functions for each band. * denotes the difference is not significant at 95% for pairwise comparisons.

	Lee et al. Approach						Gordon Approach Cubic						Gordon Approach Quadratic					
	Chl (μgl^{-1})		TSM (mgl^{-1})		CDOM (m^{-1})		Chl (μgl^{-1})		TSM (mgl^{-1})		CDOM (m^{-1})		Chl (μgl^{-1})		TSM (mgl^{-1})		CDOM (m^{-1})	
	Av	SD	Av	SD	Av	SD	Av	SD	Av	SD	Av	SD	Av	SD	Av	SD	Av	SD
SID	2.10	0.82	1.03	0.33	0.07	0.08	0.16	0.63	0.09	0.21	0.02*	0.07	0.23	0.35	0.12	0.20	0.02	0.06
SAM	1.16	0.69	0.75	0.26	0.05	0.07	0.23	1.12	0.11	0.28	0.02	0.08	0.21	0.36	0.13	0.22	0.02	0.06
MIN_DIST	0.87	1.10	0.47	0.28	0.05	0.05	0.24	1.04	0.17	0.16	0.03	0.03	0.40	1.05	0.18	0.16	0.03	0.04
SIDSAM	1.74	0.90	0.93	0.36	0.06	0.08	0.17*	0.71	0.09	0.22	0.02*	0.07	0.22	0.38	0.13	0.21	0.02*	0.06
SIDMIN	1.32	0.98	0.54	0.30	0.05	0.05	0.12	0.48	0.07	0.12	0.01	0.04	0.29	0.53	0.12	0.16	0.02	0.05
SAMMIN	0.90	1.11	0.48	0.27	0.05	0.06	0.17*	0.64	0.14	0.15	0.02	0.03	0.36	0.78	0.16	0.15	0.03	0.04
SCM	0.44	0.82	0.55	0.55	0.17	0.10	0.21	0.91	0.11	0.27	0.02	0.08	0.20	0.85	0.15	0.37	0.02*	0.06

Accuracy and Precision Values after the Addition of Environmental Noise

Before introducing simulated error from the other sources the offset representing the $NE\Delta R(0^-)_E$ was applied to one simulation set (θ_s = 19.1°). The results are shown in Figure 4-27.

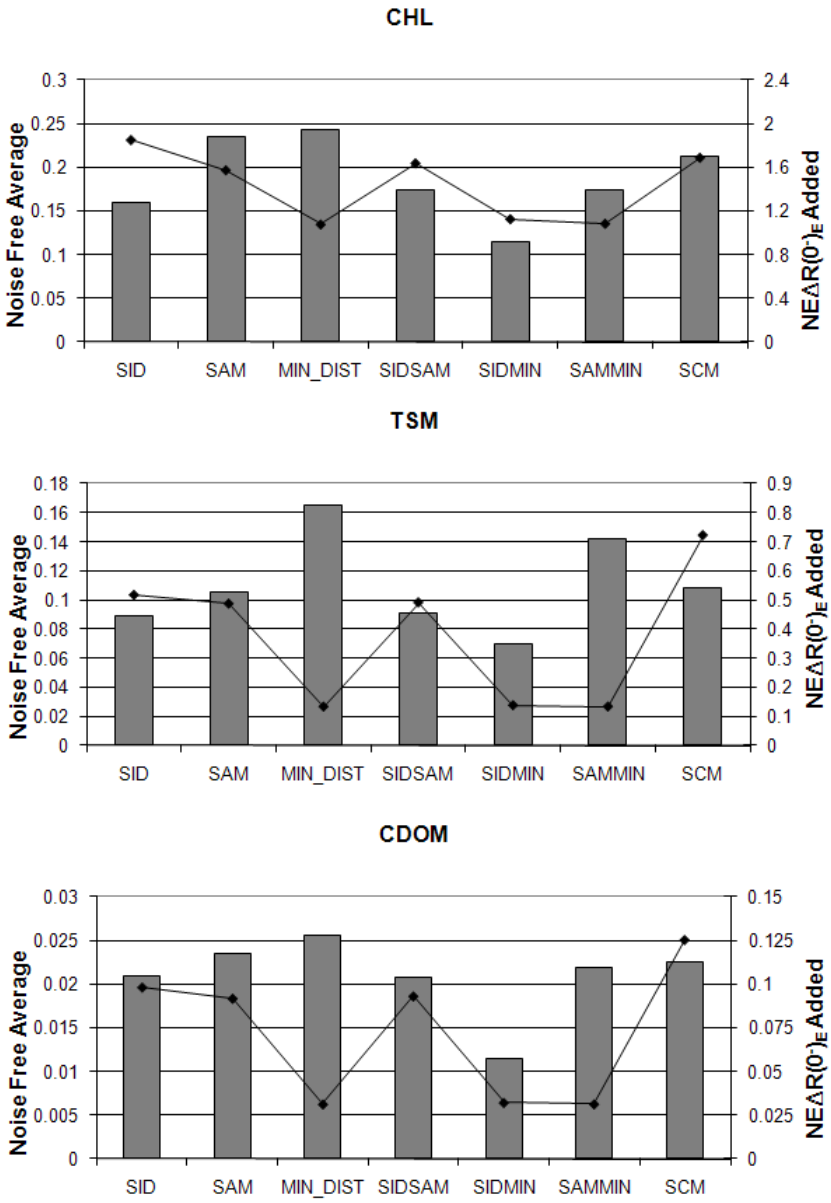

Figure 4-27 Mean retrieval accuracy for chlorophyll a, TSM and CDOM with and without added noise. The retrieval was done using the band specific cubic forward model. The bars are the noise free averages and the line is the average after addition of a NE$\Delta R(0^-)$ of 0.001

Before the addition of the noise it was clear that similarity measures that used SID delivered superior results (Table 4-8). However, after the addition of the noise the minimum distance measure was the most accurate. The reason for this can be deduced if the effect of the noise on the simulated spectrum is considered. With the SAM and SCM measures the denominator was more sensitive to increases in the large values of the vector rather than the numerator. The SID, SAM and SCM measures, however, considered the band reflectance value in relation to the other bands within the spectrum. The minimum distance measure was influenced the most by those bands that had the highest value. The effect of the small change in these large values was less pronounced so the effect on the retrieval was also be limited.

Sample plots of the environmental noise-error relationship are shown in Figure 4-28. In general terms the TSM and CDOM retrieval errors behaved in the same somewhat exponential manner. In both cases the minimum distance criterion showed the best response in terms of the accuracy and precision, and the SCM measure showed the worst. The apparently less regular relationships between the chlorophyll *a* retrieval errors are deceptive, as almost none of the differences are significant at 95%. Notwithstanding this, the precision of chlorophyll *a* retrieval for the minimum distance criterion is on average 2.0, 2.5 and 3.7 times more precise than SCM, SAM and SID respectively.

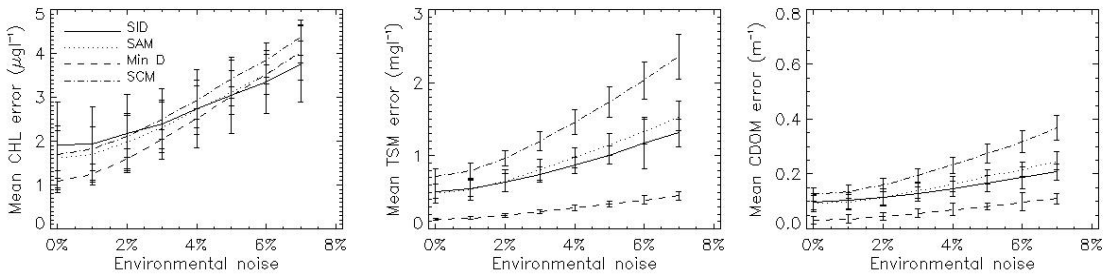

Figure 4-28 **Average error of chlorophyll *a* (left), TSM (centre) and CDOM (left) retrieval, with its 95% confidence intervals, against the environmental noise level for selected weighting schemes.**

Accuracy and Precision Values after the Addition of Atmospheric Noise

Sample plots of the atmospheric noise-error relationship are shown in Figure 4-29. It is clear that the minimum distance criterion had the greatest sensitivity to the increase in atmospheric noise and the water quality parameter error values follow a linear trend, whereas the other three criteria

appeared relatively insensitive to the increase. For the SID, SCM and SAM criteria the water quality parameter retrieval precision remained constant but the minimum distance criterion had an exponential relationship between the water quality parameter retrieval precision and the atmospheric noise.

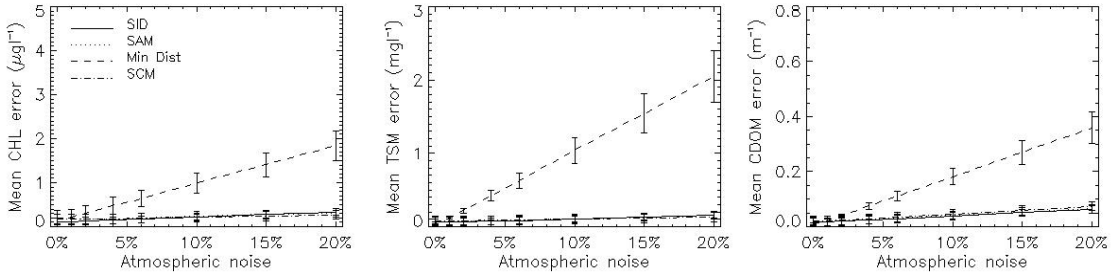

Figure 4-29 Average error of chlorophyll *a* (left), TSM (centre) and CDOM (left) retrieval, with its 95% confidence intervals, against the atmospheric correction noise level for selected weighting schemes.

Accuracy and Precision Values after the Addition of SIOP Noise

Sample plots of the atmospheric noise-error relationship are shown in Figure 4-30. The minimum distance criterion had the greatest sensitivity to the increase in noise, but the difference between it and the other three criteria was greatly reduced. In the case of TSM retrieval there is no discernable difference between the four criteria. The water quality parameter retrieval precision varied in proportion to the accuracy.

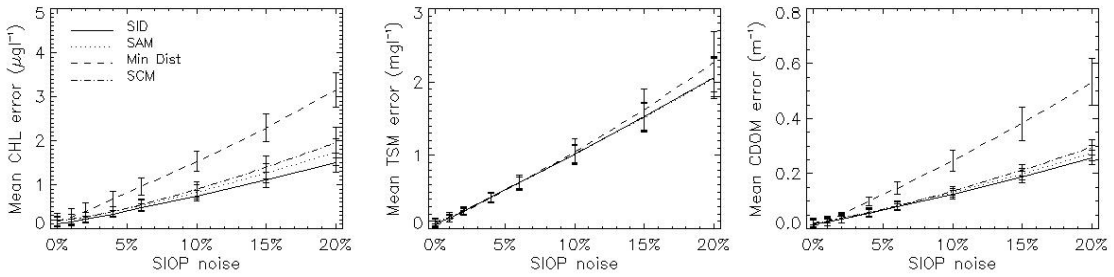

Figure 4-30 Average error of chlorophyll *a* (left), TSM (centre) and CDOM (left) retrieval, with its 95% confidence intervals, against the SIOP correction noise level for selected weighting schemes.

4.7 Conclusions

This chapter described two models of water reflectance and demonstrated how these models can be inverted using a direct and a stochastic iterative method to retrieve the water quality

parameter concentrations. *Hydrolight*® simulations were used to show that the anisotropy factor (*f*) is not only dependent on the illumination conditions but is affected by the scattering and absorption of the water and the water quality parameters. The chapter showed how the concentrations of the other colour producing agents in the water affected the retrieval accuracy of a particular water quality parameter concentration. The *Hydrolight*® simulations were used to show that empirical modelling of the anisotropy factor combined with the over-determined systems of equations improved the water quality parameter retrieval in the presence of image noise, atmospheric correction uncertainty and SIOP measurement errors.

In the case of the MIM, the results were used to rank the weighting schemes to identify those that give the best all-round performance for the three water quality parameter types and the three sources of noise. With the exception of the three band approach and a small number of other schemes there was little difference between the performance of the weighting schemes. No single supposition about the relationship between the band weights and modelled reflectance spectrum was found to be superior.

With regards to the PSO, the minimum distance criterion was shown to be the most resistant to the introduction of environmental noise in general and the $NE\Delta R(0^-)_E$ in particular, but to perform poorly when noise associated with the atmospheric correction or SIOP measurement was introduced. Of the other criteria there is no discernable difference between performance of the SID and SAM measures which both have equal or sometimes superior performance to the SCM measure.

5. Field Validation of the MIM Algorithm at Wivenhoe and Burdekin Falls Dam, Queensland, Australia

Key Points

- *Optical closure can be used to identify the most appropriate SIOP set in water bodies that have multiple SIOP domains.*
- *The over-determined weighted MIM algorithm was more accurate and precise than the conventional three band or unweighted approach.*
- *There is no weighting scheme that is optimal for all water quality parameters.*

The previous chapters established a method for atmospheric correction of images of Queensland inland water bodies, along with working SIOP sets for Wivenhoe and Burdekin Falls Dams and refined the MIM and PSO algorithms. This chapter describes the work done to test and validate the findings of the previous chapters.

Whilst it is possible to make a rudimentary validation using the same measurements for the parameterisation and the validation, ideally the validation measurements should be independent of those used to parameterise the algorithm. The observations taken at Wivenhoe Dam in July 2007 and at Burdekin Falls Dam in October 2008 were limited in their effectiveness for the purposes of validation due to their lack of independence. To counter this problem another field campaign to Burdekin Falls Dam was mounted in August 2009 to obtain an independent validation set. The first portion of the chapter used the *in situ* measurements of above surface reflectance and water quality parameter measurement to examine the optical closure between the measured and modelled spectra. Next, the chapter describes how the optical closure was used to identify the most appropriate SIOP set in Burdekin Falls Dam. After that, the laboratory measured water quality parameter concentrations were used to calculate the accuracy and precision of the MIM.

5.1 Wivenhoe Dam July 2007

Due to the protracted period of below average rainfall experienced in the South-East of Queensland prior to the field visit the volume of water stored in the water body was reduced to 17% of the storage capacity (see Figure 5-1). It was not possible to establish enough SIOP measurement stations that were sufficiently removed from the shoreline to be represented by pure water pixels in the image. As a result it was not possible to examine the accuracy and precision of the retrieved concentration maps so the Wivenhoe Dam validation was not pursued.

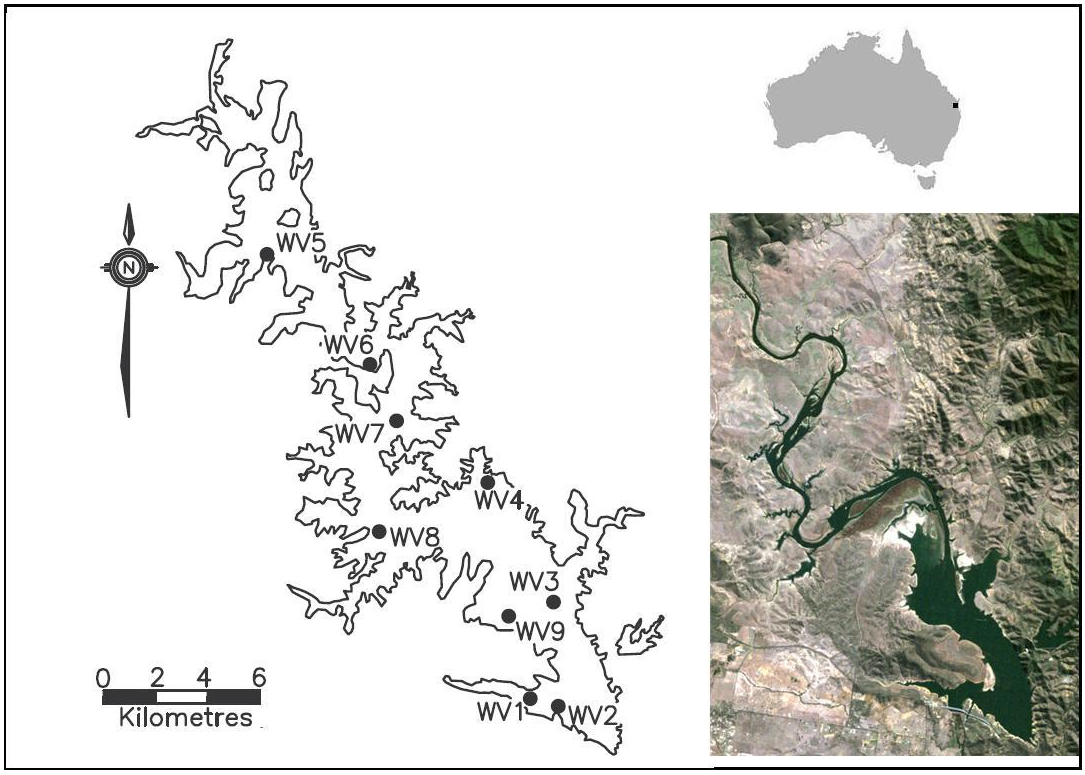

Figure 5-1 Location of the SIOP sample sites for the July 2007 fieldwork activities on Wivenhoe Dam, Australia. The left hand image shows the calculated full supply level and the right hand side shows a true colour Landsat 5 Thematic Mapper (TM) image, at the same scale captured on 16th July 2007. Note the reduced water extent at the time of the fieldwork activities.

5.2 Burdekin Falls Dam October 2008

5.2.1. Laboratory Measurements

The water quality parameter concentrations for the Burdekin Falls Dam in October 2008 were measured using the methods described in §2.2. The range of the measured chlorophyll *a* values

was 2.8 – 7.7 μgl^{-1}, the range of the measured tripton was 5.6 – 10.3 mgl^{-1}, the measured CDOM range was 0.88 – 1.21 m^{-1} and the Secchi depth range was 0.9 – 1.3 m. A table showing the individual measurements is shown in Appendix A.

5.2.2. Image Processing

The image used was the same image as in Chapter 3. Table 5-1 shows the final parameters used in the atmospheric correction.

Table 5-1 The S6 parameters for the 15th October 2008 image.

Parameter	Value	Source
Atmosphere Model	Tropical†	
Illumination	Thuillier Sun	
CO_2	360ppm	Average Value (No effect in Vis. Region)
H_2O	2.971	Obtained from MODIS 07 Product
O_3	0.289 ATM-cm	Obtained from MODIS 07 Product
Aerosol Model	Maritime	Prevailing wind was from the SW
AOT at 550nm	0.15	Tuned on *in situ* overpass stations
Ground Altitude	0.154km	Burdekin Falls Dam water level RL
Sensor Altitude	799km	MERIS Specifications
Sensor Zenith,	11.07°	MERIS Image
Sensor Azimuth	282.33°	MERIS Image
Solar Zenith Angle	29.88°	MERIS Image
Solar Azimuth	70.41°	MERIS Image
Low pass filter size for Background File	9 x 9	
Radiance to irradiance conversion factor (Q)	4.0	*Hydrolight*® simulations

†Selected Tropical because the main constituent is the water content.

The atmospheric correction was tuned using 0.5% DDV pixels compared to the auxiliary file MER_LAP_AX DDV values. Figure 5-3 compares the *in situ* measured above surface reflectance and the reflectance measured from the nearest pixel in the image for the measurement stations shown in Figure 5-2. These plots are indicative only because the field observations were taken over a period of three days and they compare a measurement of a single position with an approximately 300 m square image pixel. With respect to the image, Stations 1-4 were observed two days before the image and Stations 5-8 the day before. On both these days there was moderate cloud cover of 5-6 octa. Stations 9-11 were taken on the day of the image (Station 11 at

the time of the image) during clear conditions with a maximum cloud cover of 1 octa. Station 5 was too close to the shore to get a pure water pixel from the image.

The match between in the *in situ* and satellite retrieved reflectances was comparable to recent observations made at European lakes using the SCAPE-M (Guanter et al. 2010) and the BEAM Case-2 Regional atmospheric corrections. (Odermatt et al. 2010).

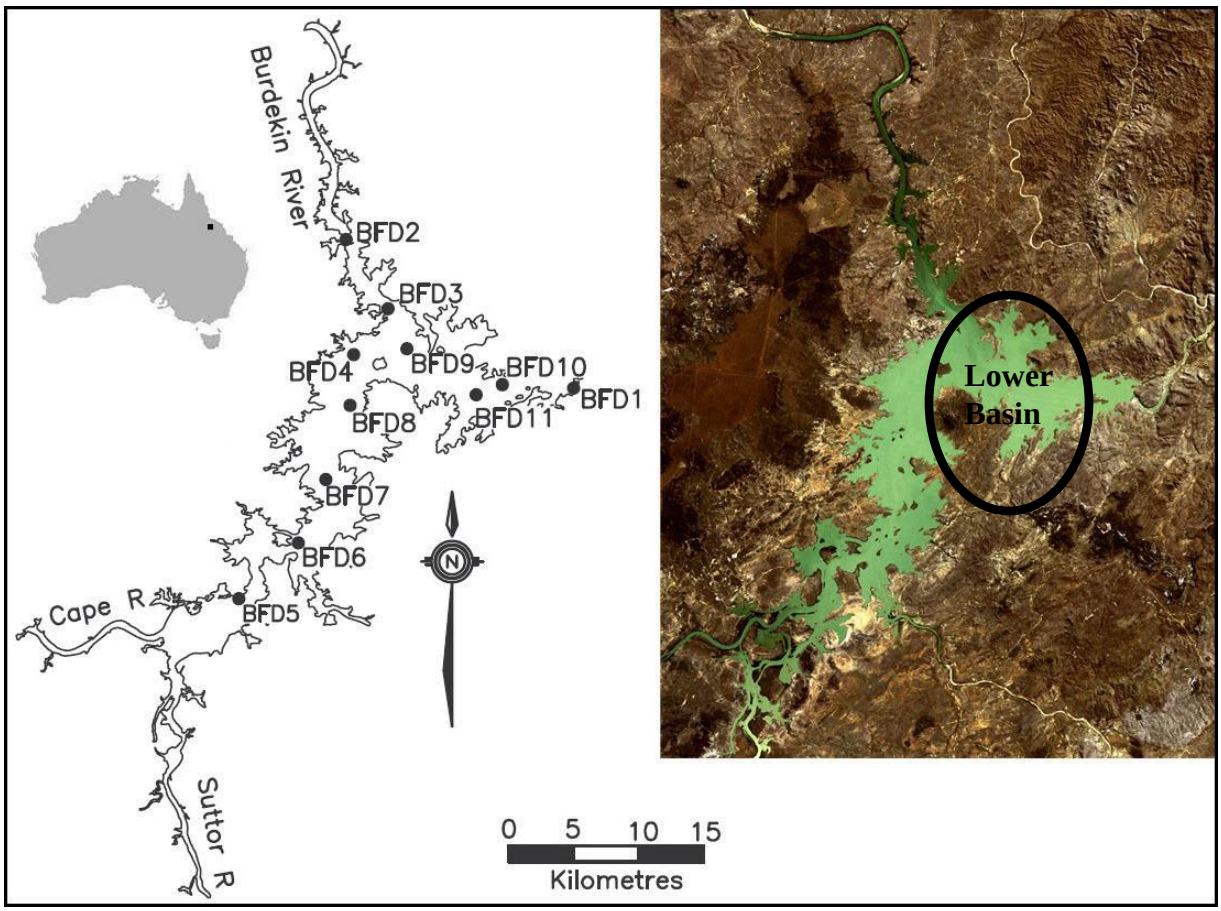

Figure 5-2 Location of the SIOP sample sites for the October 2008 fieldwork activities on Burdekin Falls Dam, Australia. The left hand image shows the calculated full supply level and the right hand image shows a Landsat 5 TM true colour image at the same scale as the map, captured on 22nd August 2008.

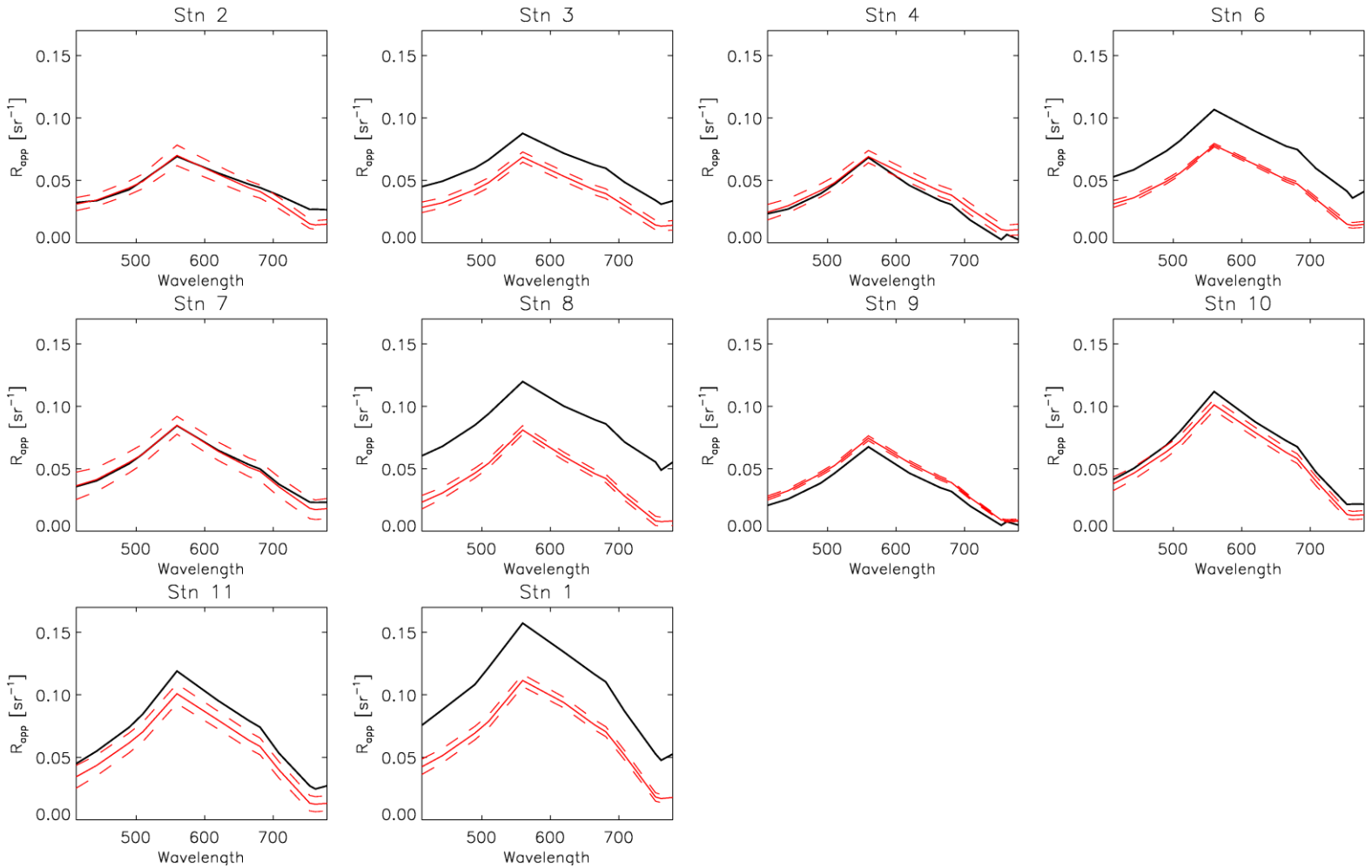

Figure 5-3 The *in situ* measured above surface reflectance (red lines with one standard deviation each side of the mean shown dashed) and the reflectance measured from the nearest pixel in the image (black line). With respect to the image, Stations 1-4 were observed two days before the image and Stations 5-8 the day before. Stations 9-11 were taken on the day of the image (Station 11 at the time of the image). Station 5 was too close to the shore to get a pixel that was water only from the image.

5.2.3. Algorithm Application

SIOP Sets

The inversions were performed using the upper and lower SIOP set as described in the §2.5.2 and shown in Figure 5-4 overlaid with the MERIS bands.

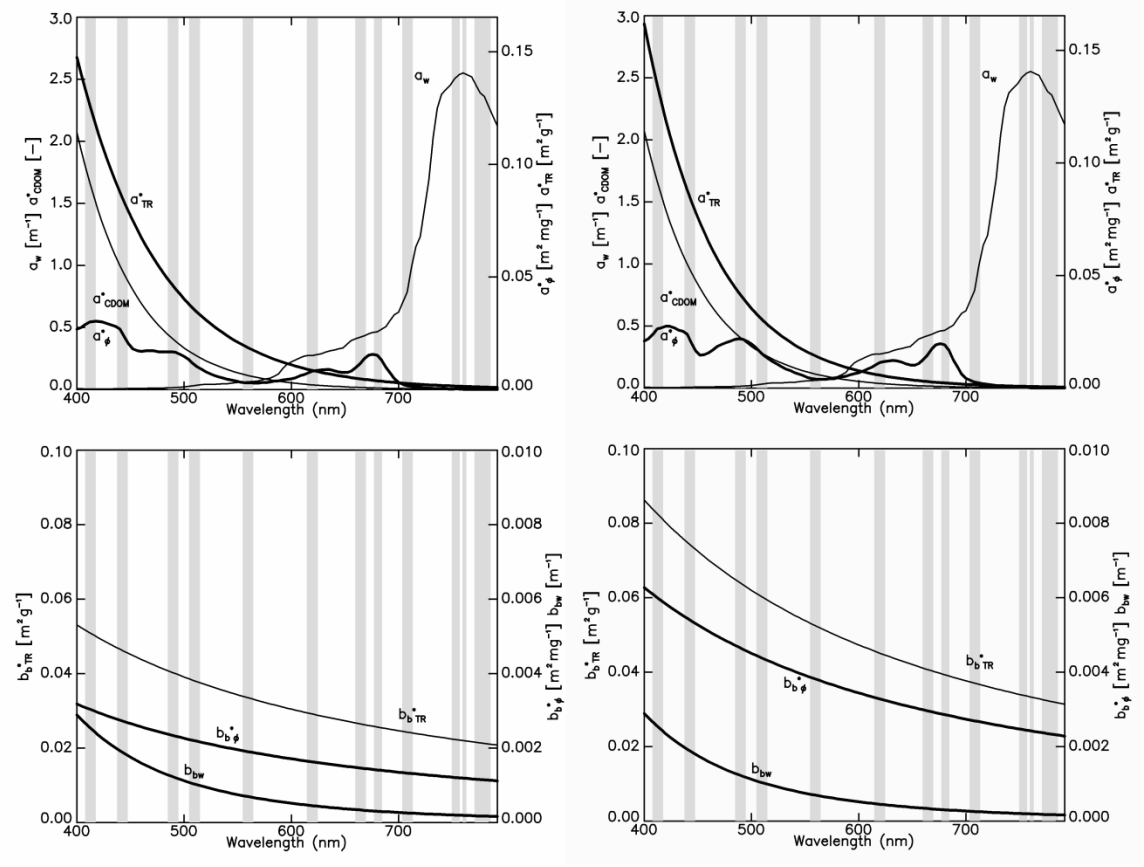

Figure 5-4 SIOP sets upper basin (left) and lower basin (right) for Burdekin Falls Dam measured during the October 2008 field work. The upper graph shows the spectral absorption of water (*w*) and the chlorophyll *a* specific absorption spectra of phytoplankton (ϕ), total suspended material (*TSM*) and coloured dissolved organic matter (*CDOM*). The lower shows the spectral backscattering of water (*w*) and the specific backscattering spectra of chlorophyll *a*(ϕ) and total suspended material (TSM).The shaded areas represent the MERIS bands.

Optical Closure

The optical closure for each of the stations was examined. Optical closure is the difference between the measured and modelled spectra. Each of the plots shown in Figure 5-5 and Figure 5-6 show six spectra. The solid dark line is from the MERIS pixel that contains the station. The

dark broken line shows a *Hydrolight*® run using the SIOP set measured for that station and the laboratory measured concentrations. Two of the lighter lines show *Hydrolight*® runs for each station using the averaged SIOP sets and the laboratory measured concentrations. The last two light lines show $R(0^-)$ modelled using the f function calculated using the process described in Chapter 4 using the laboratory measured concentrations.

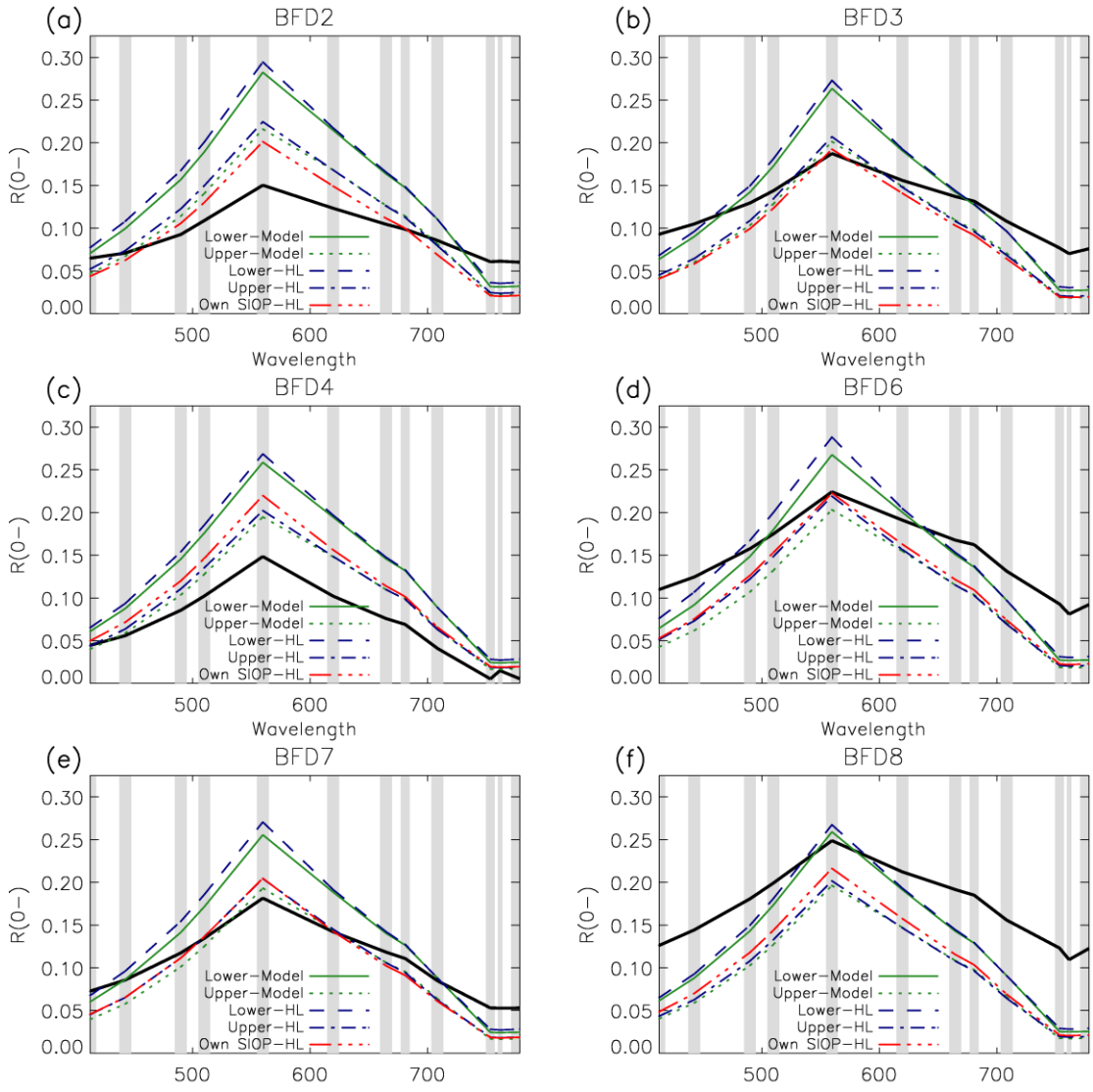

Figure 5-5 The optical closure for Stations 2-4 ((a)–(c)) and 6-8 ((d)–(f)) between the image measured spectra and the spectra modelled with *Hydrolight*® and the f function calculated using the process described in Chapter 4 using the SIOP sets and the laboratory measured concentration values. The shaded areas represent the MERIS bands. The solid black line is from the MERIS pixel that contains the station. The red broken line shows a *Hydrolight*® run using the SIOP set measured for that station and the laboratory measured concentrations. The two blue lines show *Hydrolight*® runs for each station using the averaged SIOP sets and the laboratory measured concentrations. The two green lines show *R(0-)* modelled using the f function calculated using the process described in Chapter 4 using the laboratory measured concentrations.

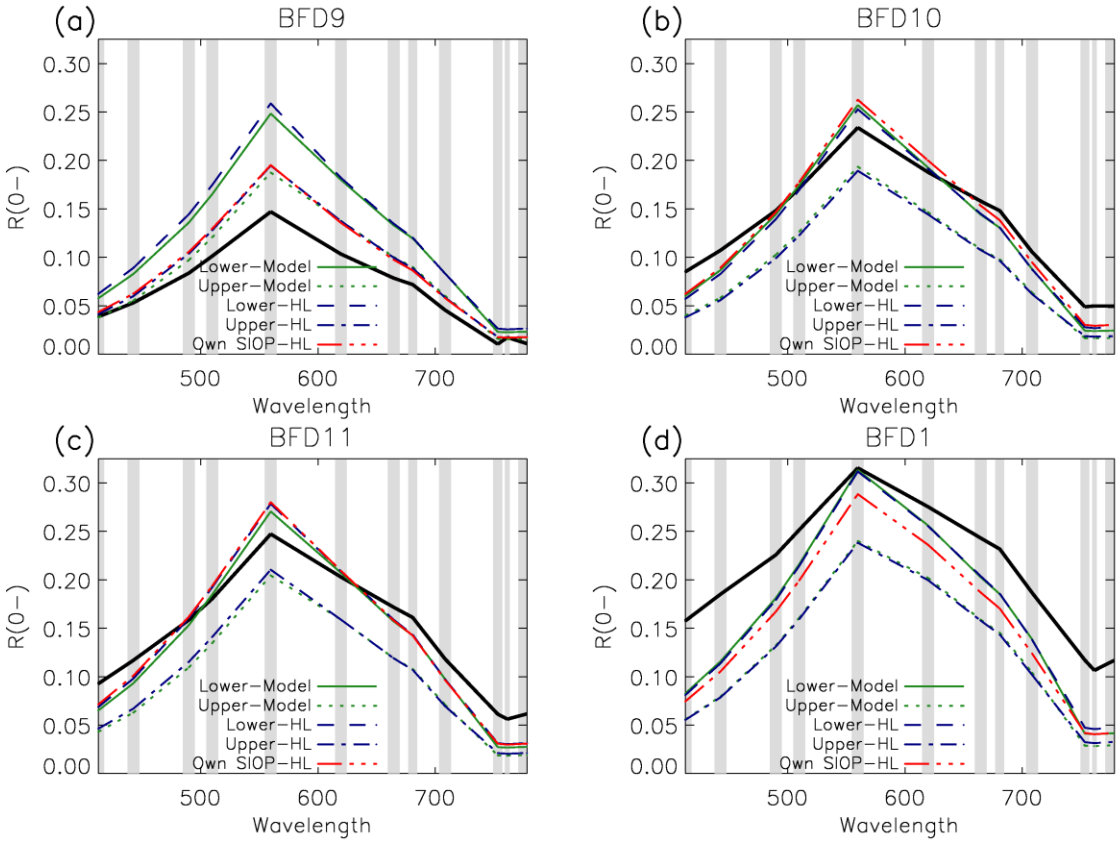

Figure 5-6 The optical closure for Stations 1 (d) and 9-11 ((a)–(c)) between the image measured spectra and the spectra modelled with *Hydrolight*® and the *f* function calculated using the process described in Chapter 4 using the SIOP sets and the laboratory measured concentration values. The solid black line is from the MERIS pixel that contains the station. The red broken line shows a *Hydrolight*® run using the SIOP set measured for that station and the laboratory measured concentrations. The two blue lines show *Hydrolight*® runs for each station using the averaged SIOP sets and the laboratory measured concentrations. The two green lines show *R(0-)* modelled using the *f* function calculated using the process described in Chapter 4 using the laboratory measured concentrations.

The most obvious difference is that the MERIS spectra have a central peak that is lower with respect to the blue and NIR wavelengths. The measured spectra appear flattened with respect to the modelled spectra. This phenomenon has been noted previously with satellite images of Wallis Lake on the central coast of New South Wales (Dekker et al. 2005). The possibility that a systematic error has been introduced into the processing chain was investigated.

Air-Water Interface Correction

The first possibility was that the de Haan et al. (1999) method of converting above water reflectance to below water reflectance may be overestimating in the blue and NIR part of the

spectrum. For example, the radiance to irradiance conversion factor (*Q)* should be dependent on the sun zenith angle, view angle and the SIOP set. Albert and Mobley (2003) made an attempt to model this but they could find no suitable parameterisation. Examination of the *Hydrolight*® simulations for Burdekin Falls Dam showed that there was an SIOP and a sun zenith angle effect (All simulations have the same view zenith angle so no effect due to that parameter could be examined.) The average *Q* value over the simulations seemed to be band dependent and inversely proportional to the reflectance value. The variation was approximately 7% but since the *Q* value was larger in the blue & NIR regions of the spectrum a band specific value of *Q* would have the effect of marginally increasing the observed difference. A modification of the above to below surface correction to account for this difference would introduce a greater level of complexity for a minimal effect.

Stratification of the Water Column

The measured laboratory concentrations come from a 10L sample of water taken from the surface. The *Hydrolight*® simulations are based on a completely mixed homogenous water column. It is not unreasonable to suspect that there may be some stratification of the water constituents. It has been shown for Lake Constance (Europe) that the assumption of a constant concentration of phytoplankton and suspended matter with depth meant the irradiance reflectance was underestimated by 12-15% for the range of 2-5 μgl^{-1} of chlorophyll and 2-5 mgl^{-1} for suspended material (Albert & Mobley 2003). This work did not indicate whether this difference was spectrally constant but Kutser et al. (2008) did show that the simulated reflectance spectra varied in shape with changes in the vertical distribution of cyanobacteria. Griffiths and Faithful (1996) measured profiles of turbidity at three positions in the dam (corresponding to the stations BFD1, BFD2 (river sites) and BFD7 (lake site)). They found during periods of high river inflow the greater turbidity values occurred in the lower part of the water column for the river sites while the opposite was true for the lake site. After a long period of no flow the stratification of turbidity disappeared in the river sites but the turbidity slowly increased with depth at the lake site. The general applicability of these results to the optically active part of the water column can be questioned as that paper measured the turbidity at 2m depth intervals and the maximum Secchi disk depth measured in October 2008 was 1.3m.

SIOP Measurement Systematic Errors

There is also the possibility that the SIOP sets used for the modelling suffer from some systematic errors. Firstly, solvent pigment extraction has limitations with respect to freshwater phytoplankton. An important fraction of the freshwater phytotoplankton populations (Wivenhoe Dam see Burford and O'Donohue (2006)) are chlorophyceae (green algae) whose thick cellulose cell-walls hinder the penetration of solvents (Tassan & Ferrari 1995). Schagerl and Künzl (2007) found that cell disruption was necessary for the effective extraction of chlorophyll *a* for freshwater samples. No cell disruption was performed as part of the pigment extraction described in Chapter 2.

Secondly, there is a missing tripton and phytoplankton absorption fraction in the conventional SIOP measurement method. The glass fibre filters used for the SIOP measurement are rated at a nominal pore size of 0.7μm but they have been shown to have a smaller effective pore size that is closer to 0.5 μm (Chavez et al. 1995). Notwithstanding the precise pore size Laanen (2007) found a 13% difference in absorption at 440 nm between the filtrate left from a 0.7 μm glass fibre filtration and a 0.2 μm membrane filtration. This absorption difference was ascribed to the absorption and scattering of the 0.2 – 0.7 μm fraction water sample. The missing fraction may have an effect on the optical closure by affecting the SIOPs in the following ways:

1. If the missing fraction is merely smaller particles of the predominant phytoplankton and tripton types, then although the measured concentration of each water quality parameter will be lower than the true concentration the absorption that would be contributed by this fraction will missing as well. This will mean the effect on the specific absorption will be limited. The lower overall absorption will mean that the modelled spectra will be somewhat higher than they would otherwise be.

2. If the phytoplankton or tripton in the missing fraction have different absorption properties to the predominant types, the shape of the specific absorption spectra will be different as well as their size. It is not possible to predict the effect on the modelled spectra.

3. Since the scattering is measured *in situ* the only effect on the specific values will be the lower than true concentration of phytoplankton and tripton. For both tripton and phytoplankton this will lead to overestimation of specific scattering values and the modelled spectra will be overestimated.

Thirdly, Chavez et al (1995) found that similar numbers of prochlorophytes (0.54-0.67 μm equivalent spherical diameter) pass through 0.2 μm filters as 0.7 μm glass fibre filters. It is reasonable to assume that tripton particles of a similar size also pass through the membranes. As mentioned in §2.5.2 there is an increase in the backscattering ratio when particle size distributions are dominated by smaller particles. This suggests that the assumption that there is no backscattering associated with the CDOM fraction may not be valid. This unmodelled scattering may affect the optical closure at the blue end of the spectrum.

Fourthly, as discussed more fully in §2.6, two assumptions were made in relation to phytoplankton, either of which could affect the optical closure. An error in the relationship between chlorophyll *a* concentration and phytoplankton dry weight biomass will lead to an overestimation or underestimation in the specific absorption and backscattering of tripton and a resultant effect on the modelled reflectance spectrum. Since the tripton dominates the scattering processes the effect of this assumption is likely to be greater than the effect of the assumption that the backscattering of phytoplankton has the same spectral shape as that of tripton.

Representative Scale

Another difficulty to consider is that of representative scale. The satellite spectra and subsequent inversion are the integration of a 290 m x 260 m area of water that is being compared to an *in situ* sub-metre radiometric measurement and 10L sample of water. Kutser (2004) found variations in chlorophyll *a* concentrations within a MERIS sized pixel of two orders of magnitude and he attributed the errors in chlorophyll *a* concentration estimation in past studies to the patchiness of cyanobacterial blooms. Since the reflectance spectra are dependent on the concentration of the water quality parameters the result can be extended to the within pixel variation of the reflectance spectra. In addition there is the potential that the satellite measured spectra have been ‘contaminated’ by other objects within the pixel’s point spread function.

Figure 5-7 is a photograph of the standing timber that is prevalent in the area of the dam south of Station BFD4.

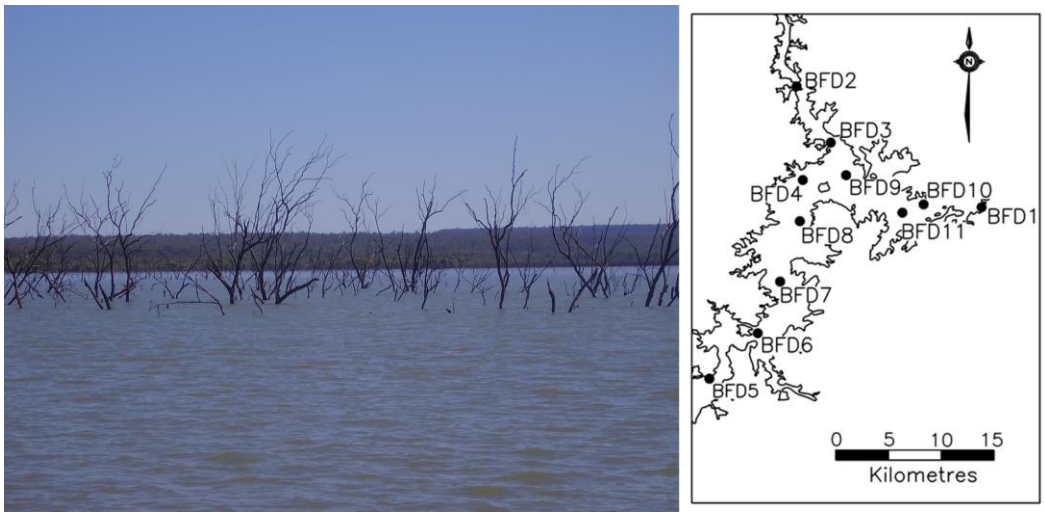

Figure 5-7 Standing timber projecting through the surface of the water. This photograph was taken in an area south of BFD4.

There is no doubt some effect due to the standing timber above and below the water's surface, but since Figure 5-3 shows no discernable trend in difference between timber affected stations (BFD4-8) and the others, the effect must be minor.

Adjacency Effect

It was shown in Chapter 3 that the adjacency effect is most pronounced in the NIR part of the spectrum. An investigation of the adjacency effect was conducted on the Lake Constance in Europe. In general terms the water in Lake Constance is darker than Burdekin Falls Dam water but the *in situ* spectrum reported for station WB by Odermatt et al. (2008b) is similar to those measured in the upper basin. Their work confirmed that the adjacency effect was most pronounced in the NIR part of the spectrum but it also showed that there were examples of the adjacency effect reducing the reflectance signal in the Band 5 (560nm) and Band 7 (665nm) when the water increased in turbidity. Notwithstanding this result, the scale of the effect detected by Odermatt et al (approx 1% at 665 nm) is too small to account for the observed variation.

Phytoplankton and CDOM Fluorescence

When stimulated by sunlight, the chlorophyll *a* emits a roughly Gaussian shaped spectral feature with width at half maximum of about 25 nm, centred at 685 nm (Gower et al. 2005). The phytoplankton fluorescence is attenuated by the CDOM and tripton absorption as well as tripton backscattering. Simulations performed by Gilerson et al. (2007) using a SIOP set with comparable CDOM and lower tripton SIOP values suggested that the fluorescence is very small for tripton concentrations of 2-10 mgl^{-1} and could be ignored for tripton concentrations over 10 mgl^{-1}. The simulated and modelled spectra have made no allowance for a chlorophyll *a* fluorescence which may account for the shape differences at that wavelength exhibited by the measurements of stations BFD3, BFD4, BFD6, BFD8 and BFD9.

Fluorescence from CDOM results in a broad Gaussian-shaped spectral feature centred around 490-520 nm (Bukata et al. 2004). CDOM of low molecular weight has been found to fluoresce more intensely than do those of high molecular weight (Stewart & Wetzel 1980). As mentioned in §2.5.3 the slope of the CDOM absorption curve has been shown to be inversely proportional to the molecular weight of fulvic acids (Carder et al. 1989; Hayase & Tsubota 1985). By extrapolation it would appear that the CDOM with a high spectral absorption slope has a greater quantum yield (defined as the ratio of the number of photons emitted to the number of photons absorbed) and a higher contribution from fluorescence. Notwithstanding that CDOM fluorescence is substantial enough to be used for the retrieval of the CDOM absorption coefficient using an airborne laser (Hoge et al. 1995), the fluorescence effects over the range 400-600 nm are generally very small with respect to the reflectance value for case-II waters as the suspended sediments and organic matter are effective attenuators. Lee et al. (1994) calculated reflectance contributions from the inelastic processes. Their Figure 4 shows the closest reflectance spectrum to those in question and it shows a negligible CDOM fluorescence contribution.

Summary

It is not possible to accurately quantify the contribution of the six identified error sources. The Lee et al. (1994) result would suggest that the CDOM fluorescence contribution would be

minimal and so too the adjacency effect, as a correction for the effect has been performed. It would appear that the chlorophyll *a* fluorescence has had an effect around 685 nm but it would not account for the whole difference in this area of the spectrum. The SIOP measurement errors are likely to be a significant contributor but as they act in different directions there is a chance that they may partially compensate for each other. The work by Albert & Mobley (2003) indicates that the stratification may well be a strong contributor to the misclose. Using depth integrated sampling in future work would be a sensible precaution. The last two error sources have the potential to be significant but it is not possible to estimate their effect here without substantial field and modelling work.

Image Inversion

The MIM algorithm was applied to the 15th October 2008 image and the water quality parameter concentrations were retrieved. The mean absolute errors for the ten *in situ* measurement stations were calculated for all the weighting schemes being examined. The results for a selection of weighting schemes are shown in Table 5-2 and Figure 5-8 - Figure 5-10. The results for the other weighting schemes are shown in Appendix E.

Table 5-2 The means of the absolute values of error between the laboratory measured concentrations and those retrieved from the 15th October 2008 image for selected weighting schemes.

	Upper Basin SIOP set						Lower Basin SIOP set					
	Chl (μgl^{-1})		TR (mgl^{-1})		CDOM(m^{-1})		Chl (μgl^{-1})		TR (mgl^{-1})		CDOM(m^{-1})	
	Av	SD	Av	SD	Av	SD	Av	SD	Av	SD	Av	SD
NO_WEIGHTS	3.84	2.30	3.56	2.97	0.68	0.41	5.17	2.36	2.15	1.43	0.39	0.29
3_BANDS	7.89	5.41	4.66	3.65	0.38	0.42	6.50	3.96	2.60	1.68	0.35	0.25
MER_BL_RAN1	13.7	5.79	2.13	1.36	0.23	0.30	12.5	4.81	2.43	1.25	0.19	0.11
MER_BL_REF3	3.93	3.29	3.11	2.50	0.56	0.39	2.43	1.88	1.98	1.49	0.33	0.26
MER_BU_DER6	3.97	2.26	3.16	1.89	0.94	0.25	2.70	1.69	4.63	1.18	0.80	0.24
MER_BU_RAN1	1.71	1.55	4.07	3.15	0.35	0.34	1.46	1.62	2.13	1.26	0.49	0.25
MER_BU_RAN2	1.75	1.59	4.04	3.13	0.34	0.36	2.01	1.68	2.11	1.26	0.43	0.24

To investigate the effect of the SIOP choice, concentration maps for the water quality parameters (Figures 5-11, 5-13 and 5-15) were created using the MER_BU_RAN2 weighting scheme. Any pixels that had a Band 10 (753.75 nm) to Band 5 (560 nm) ratio of greater than 0.6 were masked out as they were most likely land and partial land pixels.

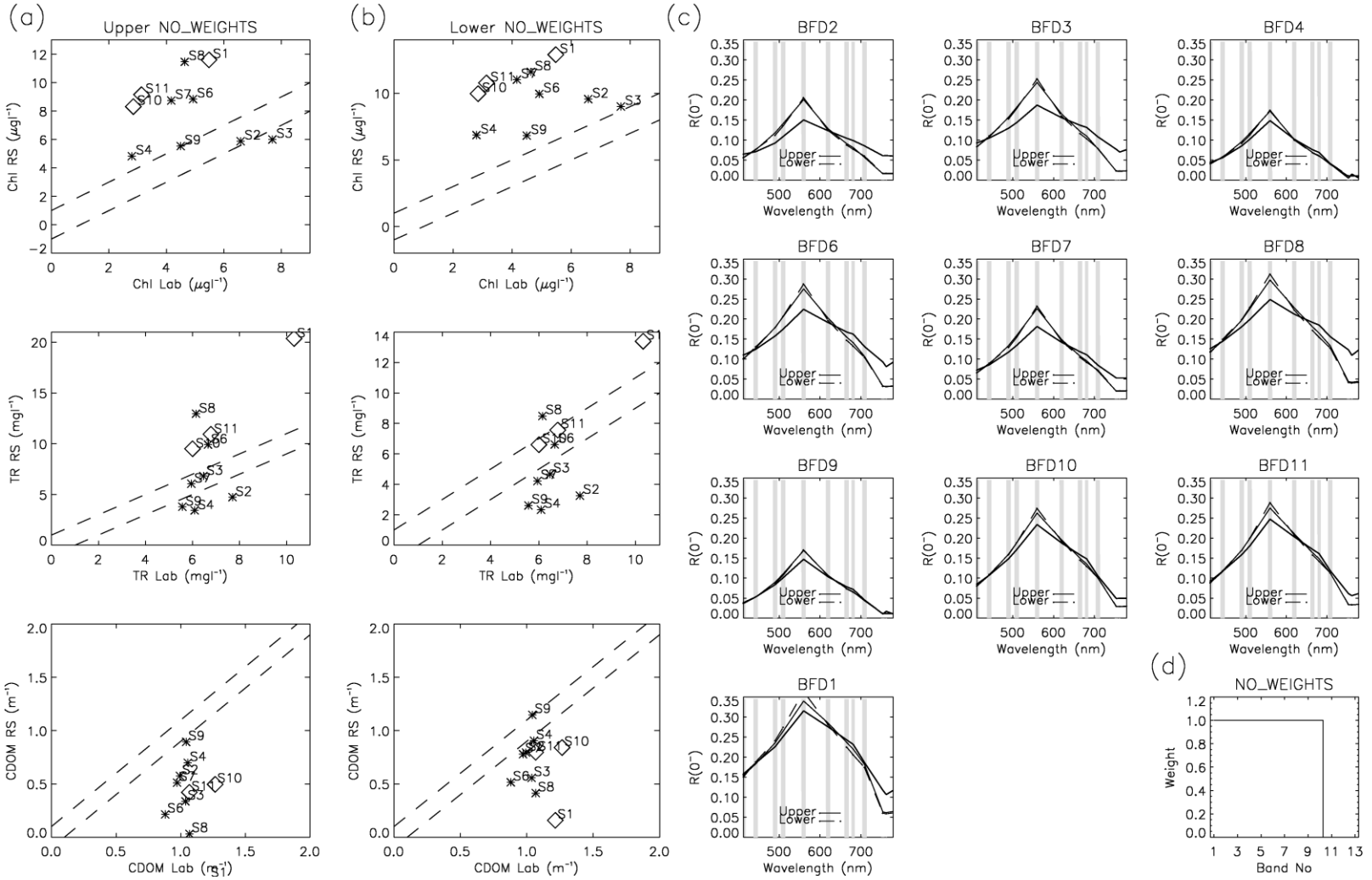

Figure 5-8 The laboratory concentrations vs. image retrieved concentrations using the unweighted first nine bands. (a) Using the Upper basin SIOP set. (b) Using the Lower basin SIOP set. The diamond symbols show the stations that are geographically in the lower basin. The dotted lines show the bounds of 1μgl^{-1} for chlorophyll *a*, 1mgl^{-1} of tripton and 0.1 m^{-1} for CDOM. (c) The optical closure for each station (d) The weighting scheme.

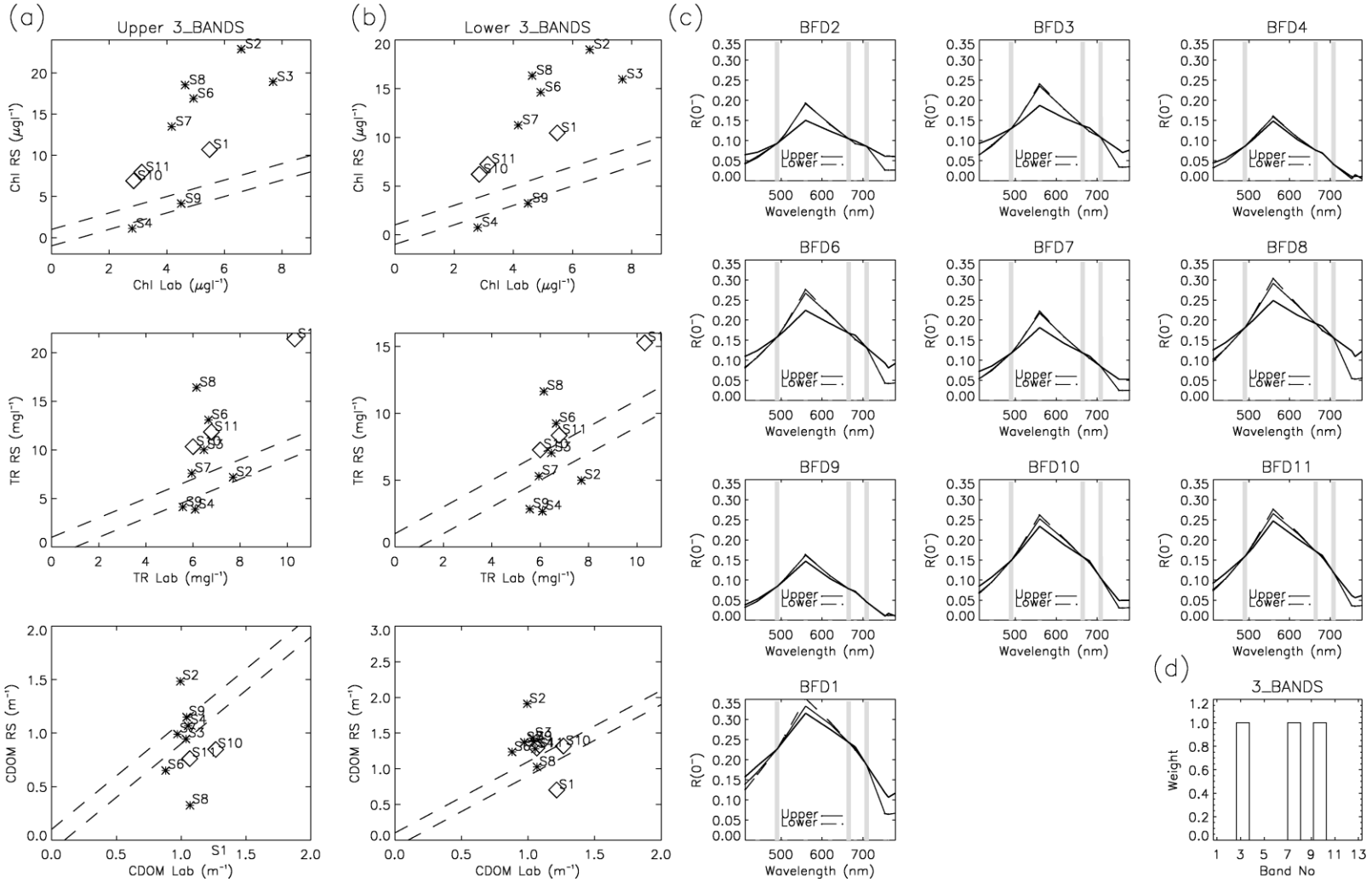

Figure 5-9 The laboratory concentrations vs. image retrieved concentrations using the 3_BANDS weighting scheme. (a) Using the Upper basin SIOP set. (b) Using the Lower basin SIOP set. The diamond symbols show the stations that are geographically in the lower basin. The dotted lines show the bounds of 1μgl^{-1} for chlorophyll *a*, 1mgl^{-1} of tripton and 0.1 m^{-1} for CDOM. (c) The optical closure for each station (d) The weighting scheme.

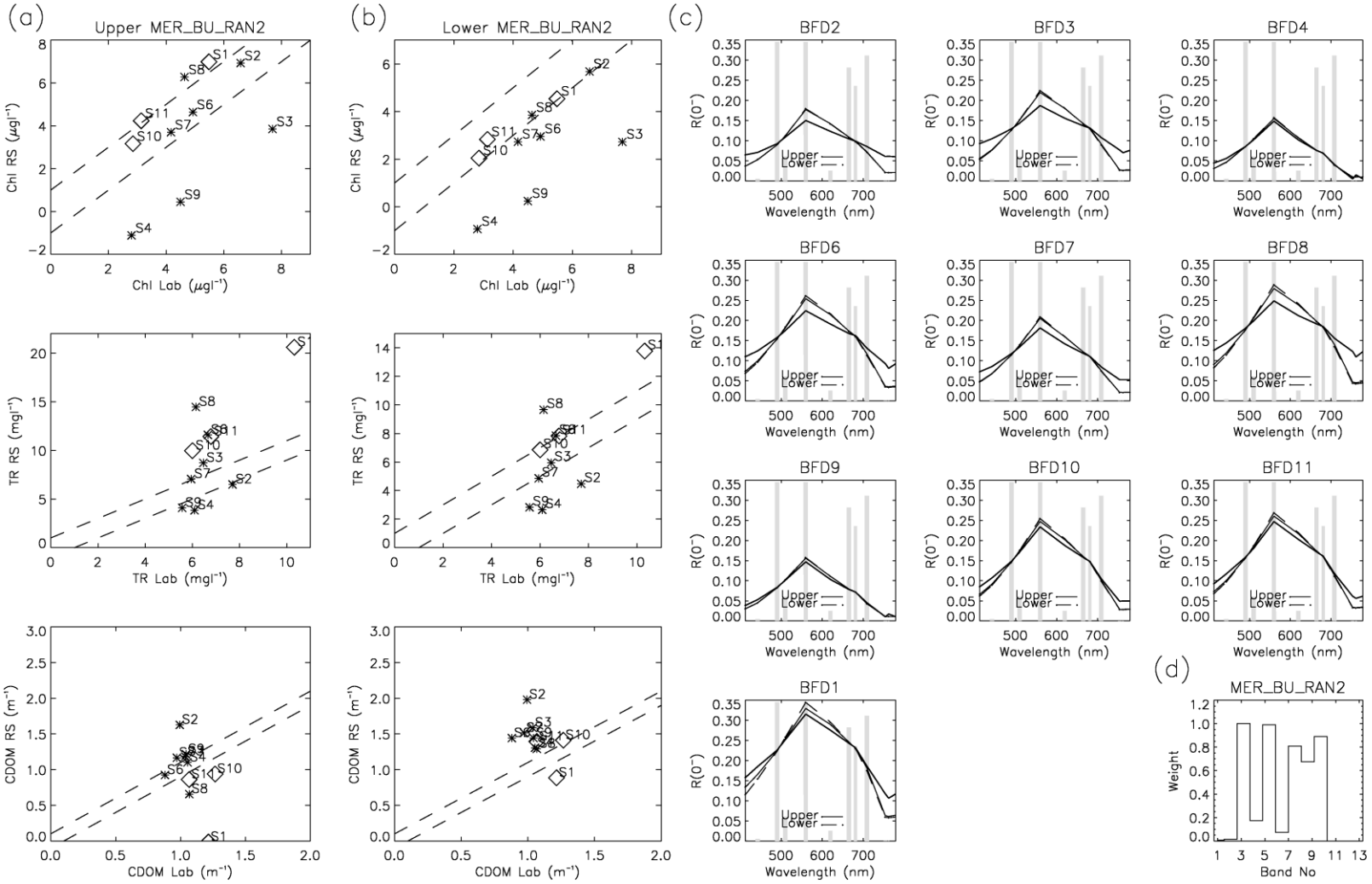

Figure 5-10 The laboratory concentrations vs. image retrieved concentrations using the MER_BU_RAN2 weighting scheme. (a) Using the Upper basin SIOP set. (b) Using the Lower basin SIOP set. The diamond symbols show the stations that are geographically in the lower basin. The dotted lines show the bounds of 1μgl^{-1} for chlorophyll *a*, 1mgl^{-1} of tripton and 0.1 m^{-1} for CDOM. (c) The optical closure for each station (d) The weighting scheme.

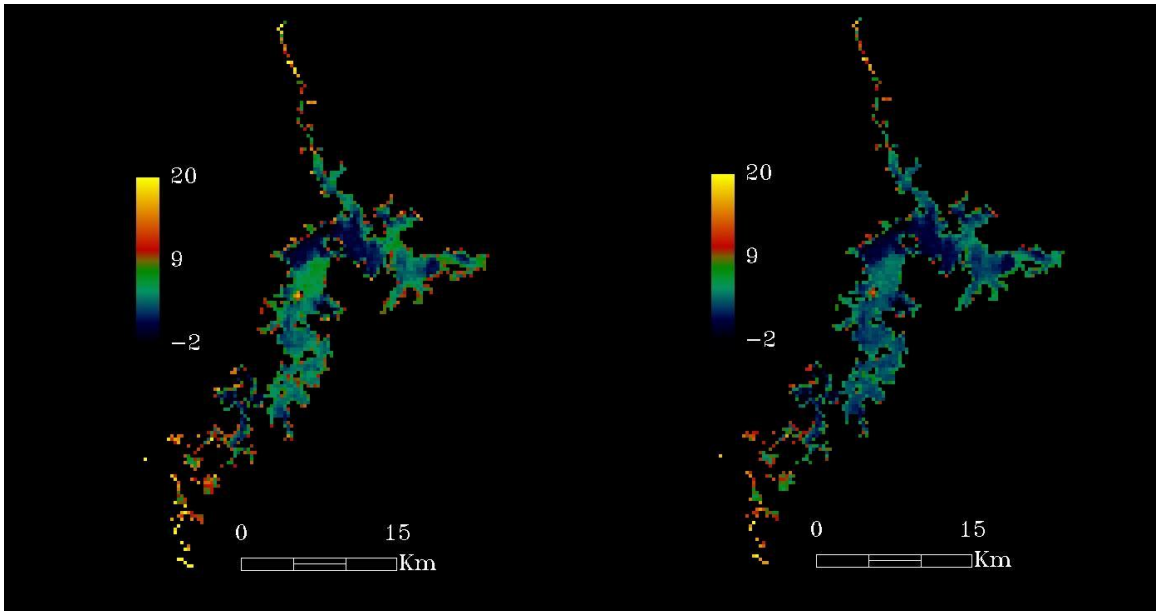

Figure 5-11 Chlorophyll *a* concentration maps derived from the 15th October 2008 MERIS image. The left hand map has been inverted using the Upper SIOP set and the right hand image has been inverted using the Lower SIOP set.

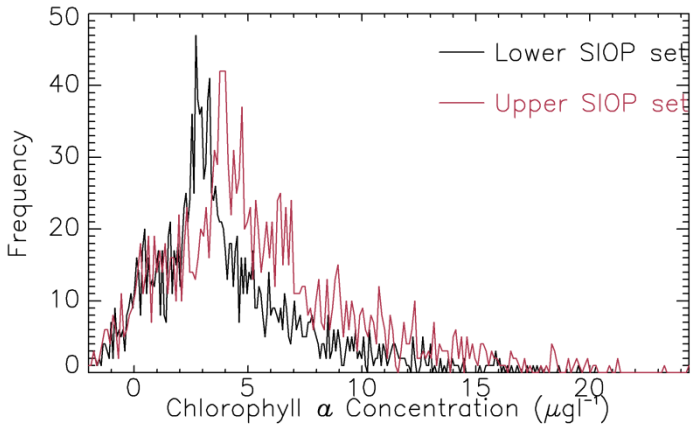

Figure 5-12 Histogram of the chlorophyll *a* concentrations retrieved from the 15th October 2008 MERIS image. In the case of the Upper SIOP set 5% of the pixels returned a negative concentration whilst the Lower SIOP set had negative concentrations for 6% of the pixels.

The distributions of the retrieved chlorophyll *a* concentration for each SIOP set were compared in Figure 5-12. The figure shows that 5-6% of the 1727 pixels have returned a physically impossible negative concentration. Inspection of the original image showed that the negative concentrations coincided with those areas of the image where the water appeared the darkest. Further investigation showed that spectra with differences of the order of the previously measured $NE\Delta R(0^-)_E$ value of MERIS (0.1% in all bands) could return differences in chlorophyll

a concentration up to 1 μgl^{-1}. The equivalent difference for tripton and CDOM was 0.2 mgl^{-1} and 0.07 m^{-1}. This suggests that the negative chlorophyll *a* concentrations are products of the unavoidable image noise rather than the inversion itself. How these pixels would be treated in any final product map would depend on the needs of the final user: either label the pixels as 'no data' or indicate that they are lower than the minimum detection limit. For the purposes of this thesis the values as retrieved are shown.

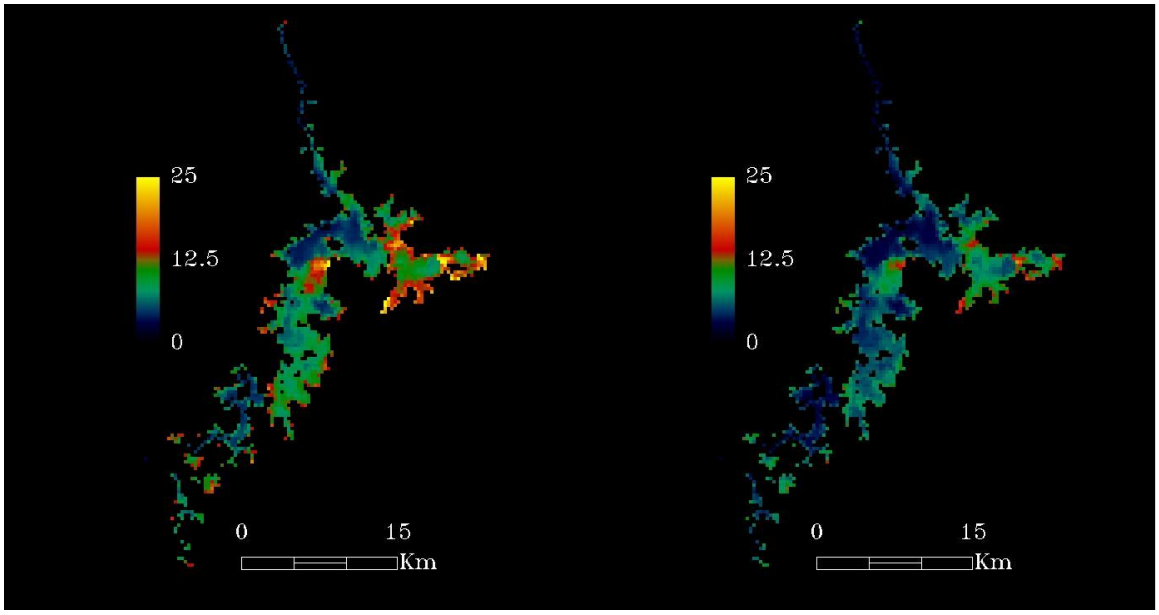

Figure 5-13 Tripton concentration maps derived from the 15th October 2008 MERIS image. The left hand map has been inverted using the Upper SIOP set and the right hand image has been inverted using the Lower SIOP set.

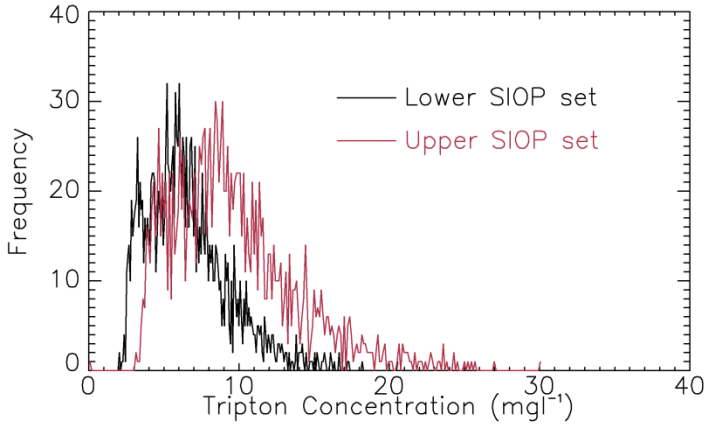

Figure 5-14 Histogram of the tripton concentrations retrieved from the 15th October 2008 MERIS image.

Figure 5-14 shows that the retrieved tripton values for the lower basin SIOP set are lower than those retrieved with the upper basin SIOP set. This is to be expected as the specific absorption and backscattering of tripton for the lower basin SIOP set is larger than the alternative SIOP set at all wavelengths. This means that the same amount of absorption and scattering apportioned to tripton by the inversion will translate into a smaller value for the concentration.

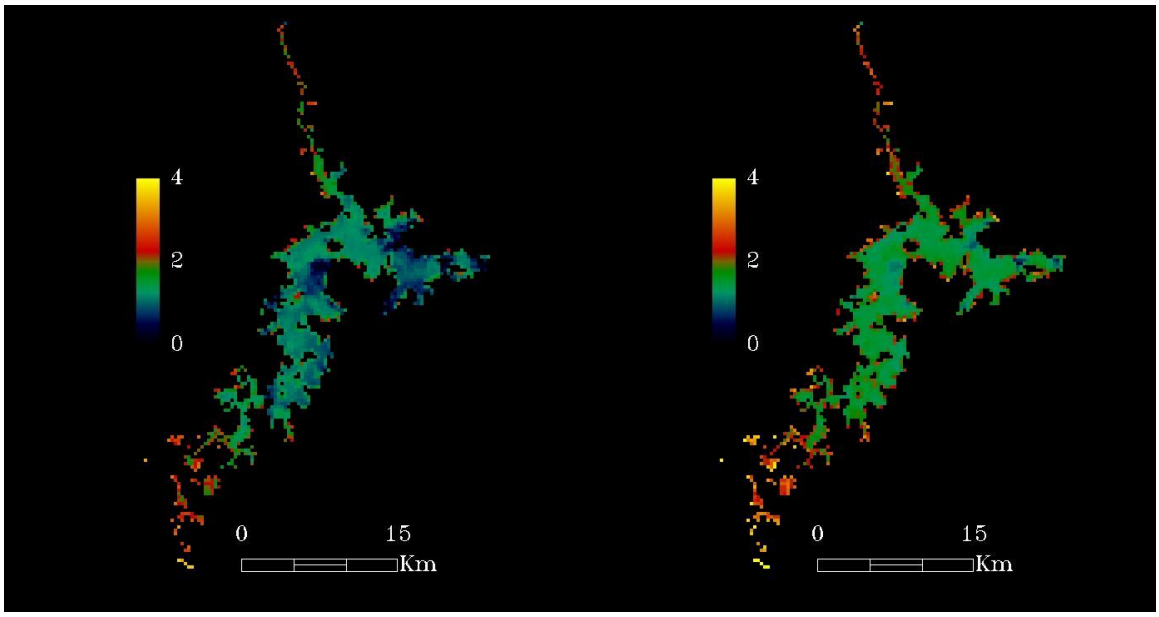

Figure 5-15 CDOM concentration maps derived from the 15th October 2008 MERIS image. The left hand map has been inverted using the Upper SIOP set and the right hand image has been inverted using the Lower SIOP set.

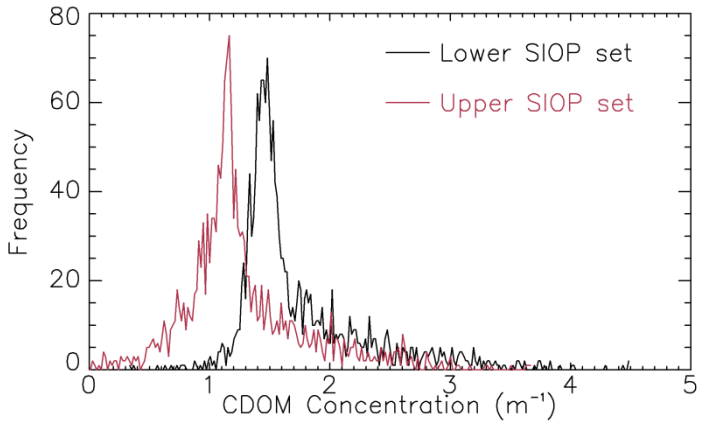

Figure 5-16 Histogram of the CDOM concentrations retrieved from the 15th October 2008 MERIS image.

SIOP Set Selection

The previous section confirmed the assumption made in Chapter 2 that the SIOP variation measured in Burdekin Falls Dam was sufficient to warrant using multiple SIOP sets. Because the SIOPs were reasonably distinct geographically, the simplest option would be to take the upper basin area from the upper basin concentration maps and combine it with the lower basin area from the lower basin map. The risk with this simplistic approach is that it assumes that the distribution of the sediment and phytoplankton types within the water body is temporally constant. A more flexible approach would be to establish an image or inversion based measure that will select the optimal SIOP set. Phinn et al. (2005) used the difference between the imagery $R(0^-)$ and the 'inverse-forward' simulated $R(0^-)$ as a measure of the optical closure of each pixel. This approach was implemented by using the sum of the squares of the difference between the imagery $R(0^-)$ and the 'inverse-forward' simulated $R(0^-)$. For convenience this is called the misclose sum.

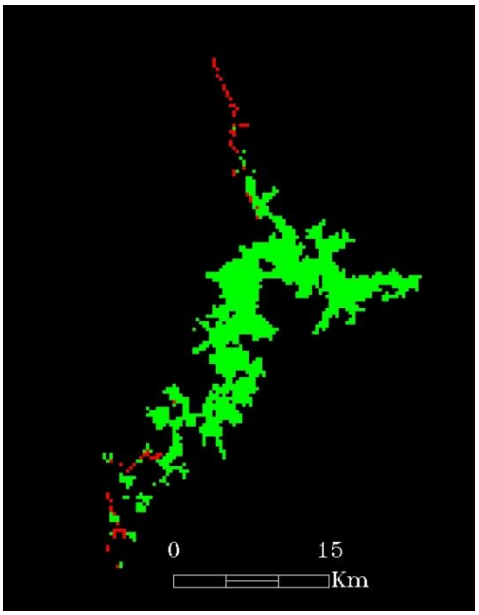

Figure 5-17 The SIOP set selected based on the difference between the imagery $R(0^-)$ and the 'inverse-forward' simulated $R(0-)$. The pixels coloured green selected the upper basin SIOP set while the pixels coloured red selected the lower basin SIOP set.

In selecting the SIOP set that corresponded to the lower of the two misclose sums the lower basin SIOP set was selected for only 4.3% of the pixels and those were in the extreme upstream ends of the water storage (see Figure 5-17). This was an unexpected result as SIOP

measurements made at the time of the image acquisition (Stn 10 &11) measured directly the SIOPs in the water and found them to be closer to the lower basin SIOP set.

To investigate whether the pooling of the individual station SIOP measurements into indicative domains had caused the unexpected results the 15th October 2008 image was inverted using the eleven individual SIOP sets and the best SIOP set was selected using the sum of the squares of the difference between the imagery $R(0^-)$ and the 'inverse-forward' simulated $R(0^-)$. The result of this inversion is shown in Figure 5-18.

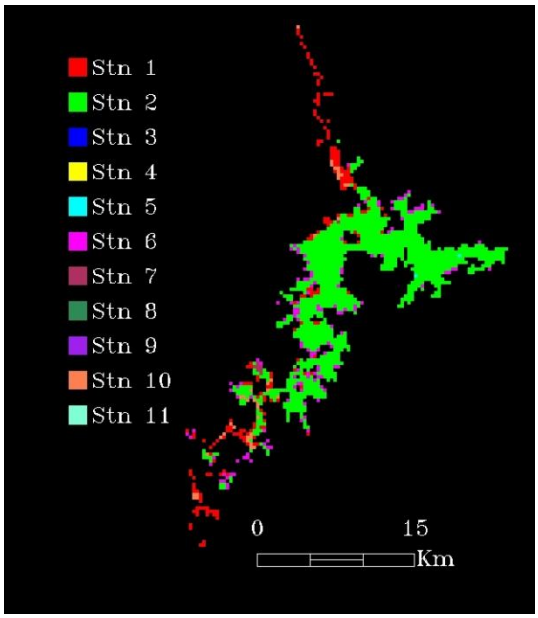

Figure 5-18 The SIOP set selected based on the difference between the imagery *R(0-)* and the 'inverse-forward' simulated *R(0-)* (closure sum). The pixels colours reflect the SIOP sets measured at the eleven measurement stations.

The image was dominated by the Stn 2 SIOP set. This set is characterised by the low tripton specific absorption and specific scattering spectra. That this result is similar to the initial result shows that the pooling of the SIOP sets into indicative domains is unlikely to be the cause of the anomalous result.

The misclose spectra for two of the measurement stations were extracted to appreciate what may be causing this dominance of the low tripton backscattering SIOP sets.

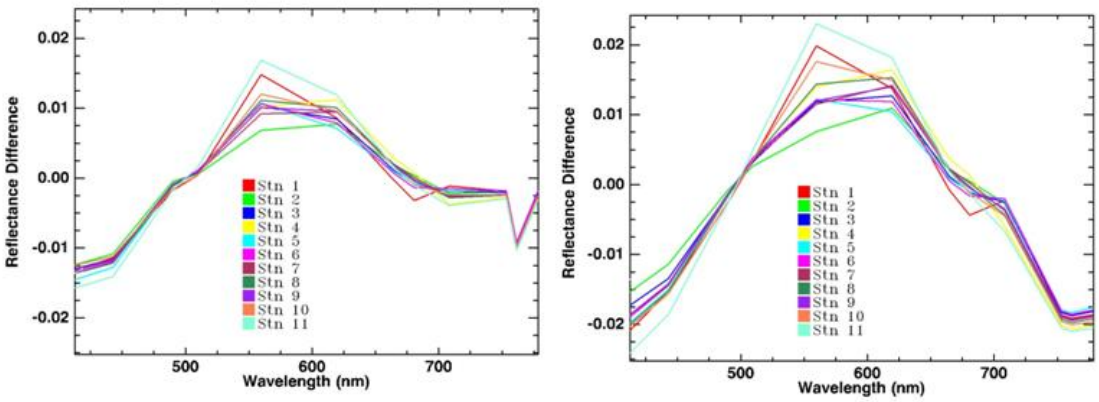

Figure 5-19 The difference between the imagery *R(0-)* and the 'inverse-forward' simulated *R(0-)* (closure sum) for the individual SIOP sets measured at Stn 9 (left) and Stn 11 (right).

Comparing Figure 5-6 and Figure 5-19 shows that the misclose sum is dominated by the apparent model-measurement differences rather than the smaller differences in closure that arise from the difference in SIOP set that is used. To investigate the more subtle differences between the misclose sums of the two SIOP sets the pixels were separated into upper basin and lower basin groups. The comparison between the misclose sums resulting from the two SIOP sets is displayed in Figure 5-20 which shows a clear trend for the ratio between the misclose sums to be lower for the lower basin group of pixels.

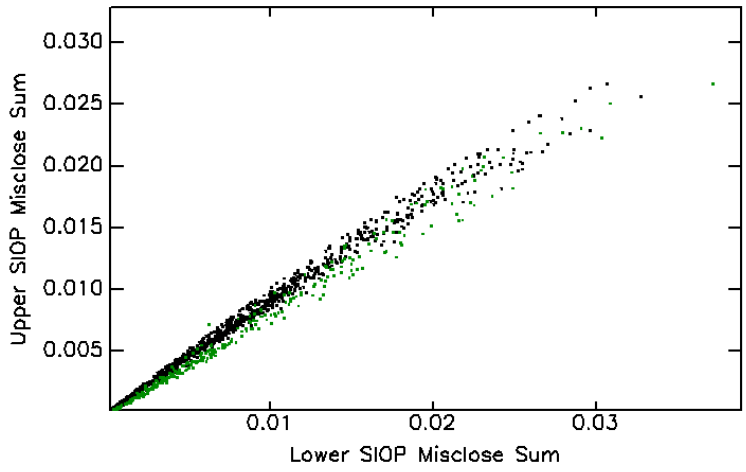

Figure 5-20 The misclose sum that results from the lower basin SIOP set against the misclose sum that results from using the upper basin SIOP set. Those data associated with pixels in the upper basin group are plotted in black and those associated with the lower basin group are plotted in green.

Lines of best fit were calculated for the two groups with gradient and R^2 value of 0.877 and 0.992 for the upper basin SIOP set and 0.818 and 0.986 for the lower basin SIOP set. In both cases the y intercept was negligible, so the ratio of the lower and upper misclose sums was calculated and considered. Histogram plots of the ratio are shown in Figure 5-21. The histograms in the figure have been normalised to the peaks in their distributions for easier comparison and they show that a threshold ratio of 0.847 may be appropriate to separate the two groups.

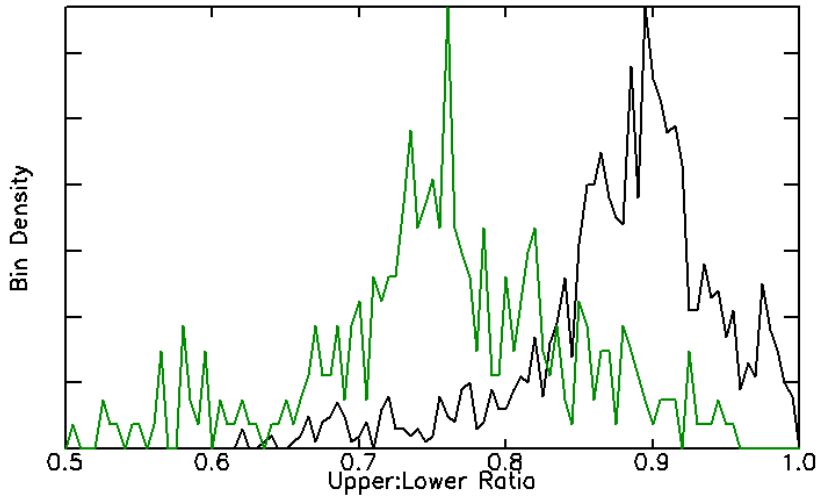

Figure 5-21 Histogram showing the distribution of the Lower : Upper ratio for the upper basin SIOP group of pixels (black) and the lower basin SIOP group of pixels (green). The histograms have been normalised to the peaks in their distributions for easier comparison.

The ratio threshold of 0.847 was applied and the result (Figure 5-22) is much more in keeping with expectations. Aside from the lower area that was used to calculate the threshold, the sorting method identified an area around the former confluence of the Burdekin and Suttor Rivers. The tripton specific backscattering spectrum that was measured in this area (Stn 4) shows the largest slope measured in the upper basin region. Figure 5-23 shows a comparison between part of the SIOP selection map and the October 2008 image. The areas that have been selected for inversion with the lower SIOP set that are in the upper basin can be seen to have a distinctive colour, perhaps indicative of a different domain.

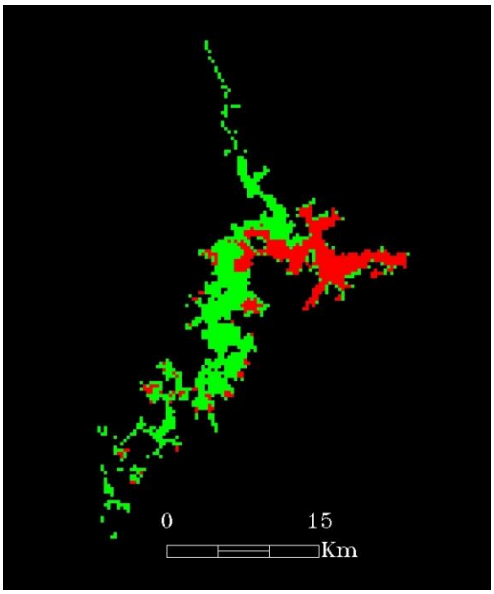

Figure 5-22 The SIOP set selected based on the 0.847 threshold on the ratio of the lower SIOP set to upper SIOP set misclose sum. The pixels coloured green selected the upper basin SIOP set while the pixels coloured red selected the lower basin SIOP set.

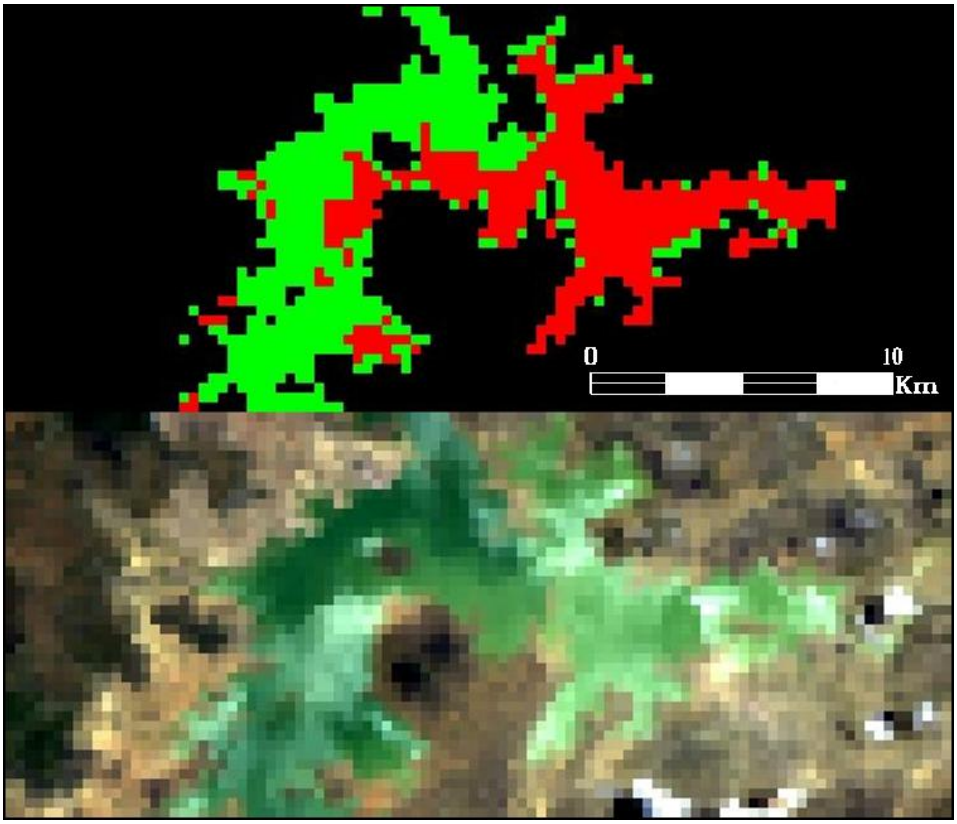

Figure 5-23 Comparison between part of the SIOP selection map and the October 2008 image. The areas that have been selected for inversion with the lower SIOP set that are in the upper basin can be seen to have a distinctive colour.

The inversions were run again using the ratio threshold to select the SIOP set and the accuracy and precision results are shown in Table 5-3 and the resultant water quality parameter maps for the MER_BU_RAN2 weighting scheme are shown in Figure 5-24

Table 5-3 The means of the absolute values of error between the laboratory measured concentrations and those retrieved from the 15th October 2008 image and the ratio threshold for selected weighting schemes.

	Chl (μgl^{-1})		TR (mgl^{-1})		CDOM(m^{-1})	
	Av	SD	Av	SD	Av	SD
NO_WEIGHTS	4.31	2.82	1.79	1.23	0.52	0.26
3_BANDS	7.72	5.53	3.39	3.04	0.25	0.25
MER_BL_RAN1	13.8	5.35	1.74	0.84	0.12	0.11
MER_BL_REF3	3.88	3.31	1.24	1.07	0.39	0.24
MER_BU_DER6	3.28	2.16	4.22	1.12	0.87	0.18
MER_BU_RAN1	1.44	1.68	2.71	2.36	0.28	0.17
MER_BU_RAN2	1.66	1.62	2.69	2.35	0.25	0.18

The most notable improvement from using the ratio threshold has occurred in the retrieval of the tripton concentration. This would be expected as the greatest difference in the SIOP sets are in the specific tripton backscattering.

The highest concentration values for each of the water quality parameters are all associated with pixels that had a Band 10 (753.75 nm) to Band 5 (560 nm) ratio that was close to 0.6. These are most likely mixed water and land pixels or water pixels that have not been fully corrected for the adjacency effect.

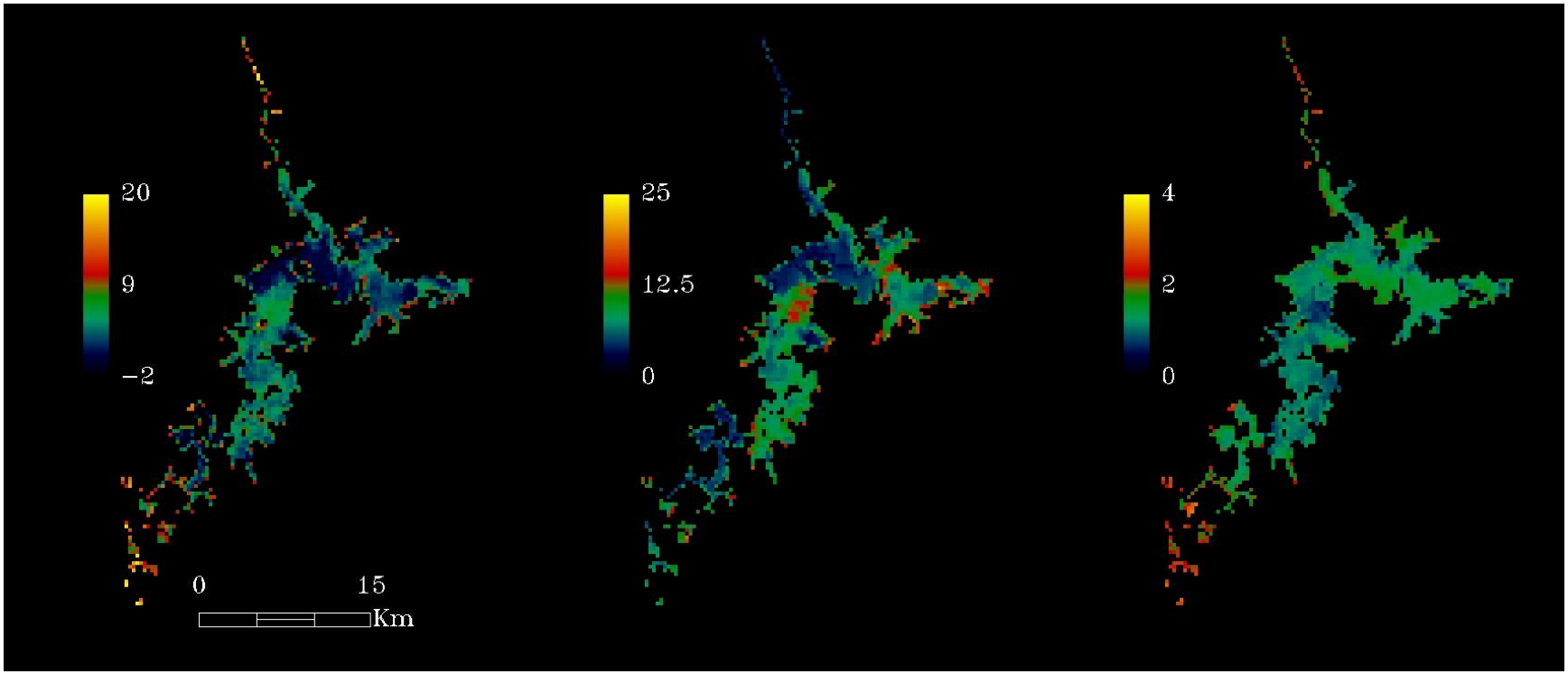

Figure 5-24 Maps of the water quality parameters (Chlorophyll a (left), Tripton (middle) and CDOM (right)) retrieved from the 15th October 2008 image using the ratio threshold and the MER_BU_RAN2 weighting scheme.

5.3 Burdekin Falls Dam August 2009

The intention of the August 2009 fieldwork was to obtain a larger validation dataset that was independent of the measurements used to parameterise the algorithm. As the concentration of CDOM is not of interest to water managers it was decided that it was preferable to allocate the available resources to building a more extensive validation set for the chlorophyll *a* and tripton products.

5.3.1. Observation Stations

Water samples were taken from the surface water at 25 observations stations on the afternoon of 12th August 2009 between 1:40 pm and 4:10 pm. The locations of those observation stations are shown in Figure 5-25.

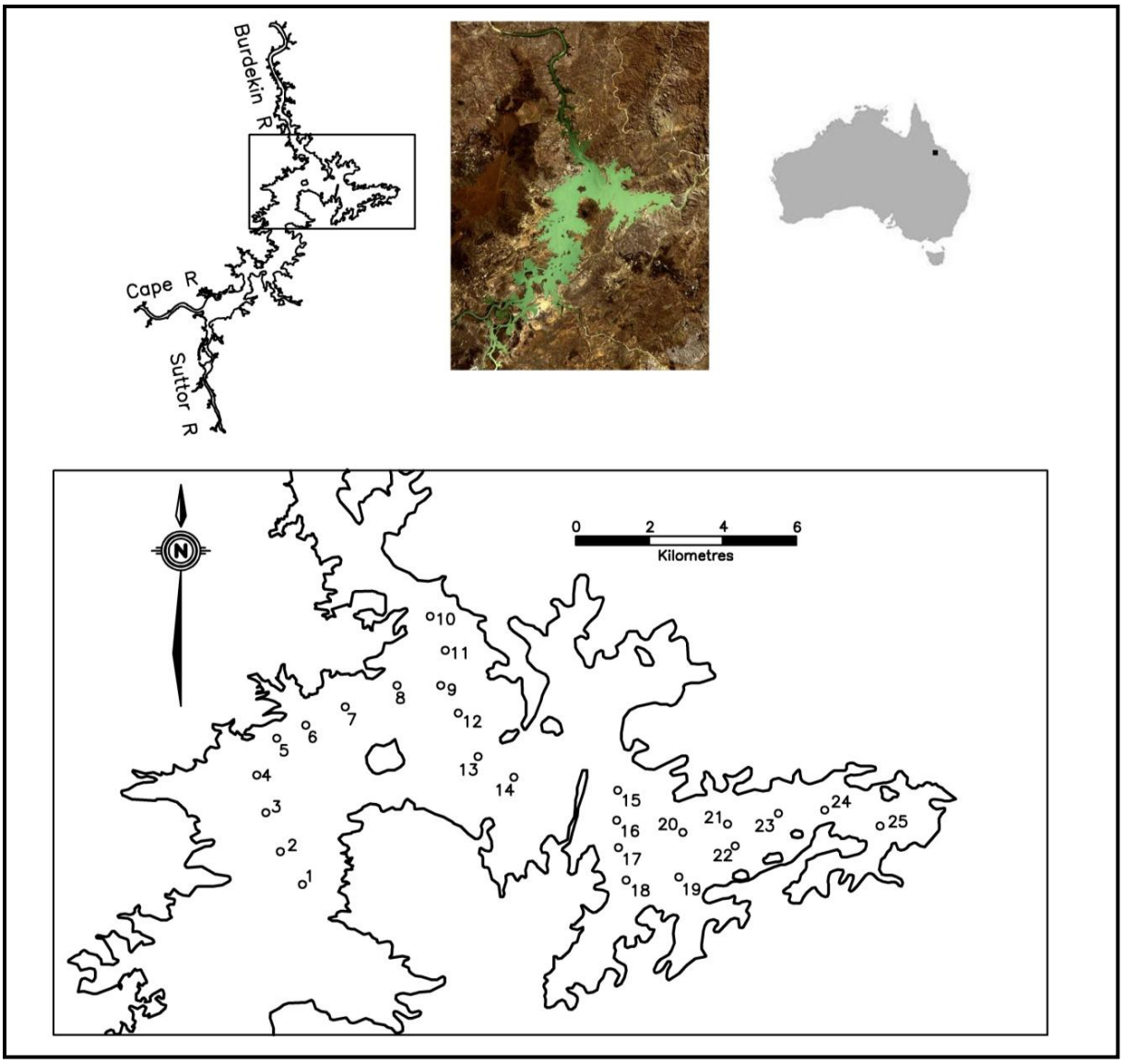

Figure 5-25 Location of the validation sample sites for the August 2009 fieldwork activities on Burdekin Falls Dam, Australia. The upper left hand image shows the calculated full supply level and the upper middle image shows a Landsat 5 TM true colour image captured on 22nd August 2008. The lower image shows the location of the 25 validation sample sites.

5.3.1. Image Processing

Three MERIS full resolution level 1b images were obtained for the 10th, 13th and 14th August 2009. The satellite overpassed the site at approximately 10:00 am on each day. Table 5-4 shows the final parameters used in the atmospheric correction for the MERIS images.

Table 5-4 The S6 parameters for the August 2009 MERIS images.

Parameter	Value			Source
	10th August 2009	**13th August 2009**	**14th August 2009**	
Atmosphere Model	Tropical†	Tropical†	Tropical†	
Illumination	Thuillier Sun	Thuillier Sun	Thuillier Sun	
CO_2	360ppm	360ppm	360ppm	Average Value (No effect in Vis. Region)
H_2O	2.375	2.322	2.112	Obtained from MODIS 07 Product
O_3	0.272 ATM-cm	0.275 ATM-cm	0.272 ATM-cm	Obtained from MODIS 07 Product
Aerosol Model	Maritime	Maritime	Maritime	Prevailing wind was from the SW
ARVI threshold	0.428	0.4	0.425	
AOT at 550nm	0.12	0.09	0.09	Tuned on DDV pixels
Ground Altitude	0.154km	0.154km	0.154km	Burdekin Falls Dam water level RL
Sensor Altitude	799km	799km	799km	MERIS Specifications
Sensor Zenith	16.86°	27.48°	32.70°	MERIS Image
Sensor Azimuth	282.08°	281.60°	104.32°	MERIS Image
Solar Zenith Angle	48.28°	46.61°	51.70°	MERIS Image
Solar Azimuth	43.93°	43.22°	50.53°	MERIS Image
Low pass filter size for Background File	9 x 9	9 x 9	9 x 9	
Radiance to irradiance conversion factor (Q)	4.0	4.0	4.0	*Hydrolight*® simulations

†Selected Tropical because the main constituent is the water content.

The atmospheric correction was tuned using 0.5% DDV pixels compared to the auxiliary file MER_LAP_AX DDV values.

5.3.2. Laboratory Measurements Method

The water samples taken at each station were kept cool in opaque storage containers and were filtered on the day of collection. The chlorophyll *a* analysis was carried out by the Australian Institute of Marine Science (AIMS), Townsville and the tripton analysis was carried out by Townsville City Council's Citiwater Laboratory.

Phytoplankton Pigments

Two replicates were prepared for each water sample by filtering through a 25 mm diameter GF/F glass-fibre filter (Whatman, nominal pore size; 0.7 μm) and then freezing the filter.

The pigments were measured using the US EPA method 445.0 (Arar & Collins 1997). This method measures the combined concentrations of chlorophyll *a* and pheophytin *a*. With the aid of HPLC analysis no pheophytin *a* was detected in the October 2008 samples so it is assumed that the measured concentration is only that of chlorophyll *a*. The pigments were extracted from the phytoplankton in 90% acetone and then centrifuged to clarify the solution. The solution was transferred to a glass cuvette and fluorescence was measured with a Turner Designs 10AU fluorometer before and after acidification to 0.003 N HCl with 0.1 N HCl.

Tripton Mass

Water samples were filtered through 47 mm diameter pre-weighed Whatman GF/F filters. After the sample had been filtered the filter paper was stored flat in a petrislide (Millipore). After collection, the filter papers were oven-dried at 60ºC to constant weight and then weighed to obtain the weight of TSM.

The mass of tripton was obtained by deducting the weight of the phytoplankton from the TSM weight. Once again the phytoplankton dry weight was estimated using the assumption that 1 μgl^{-1} of chlorophyll *a* was approximately equal to 0.07 mgl^{-1} TSM (Buiteveld et al. 1994).

5.3.3. Laboratory Measurements Results

The range of the measured chlorophyll *a* values was 1.83 – 6.88 μgl^{-1} and the range of the measured tripton was 0.8 – 7.7 mgl^{-1}. A table showing the individual measurements is shown in Appendix F.

If the efficacy of the remote sensing algorithm was established by comparing the retrieved water quality parameter concentrations to the values obtained by standard laboratory analyses, then it is important to understand the inherent variability in the sampling technique. In an intercomparison trial to test the full sample processing chain, that is, storage, extraction, measurement,

calibration, interpretation between 20 laboratories Sørensen et al. (2007) found that the overall error for HPLC and spectrophotometric determinations of chlorophyll *a* concentration was 20%. They suggested that the fluorometric method measured lower than the other two but they conceded that their sample size was too small to be certain. This finding was not consistent with Arar & Collins (1997), who whilst only comparing the methods, found the three methods gave a comparable error of 15%. Although the flourometric method has been shown to prone to error when significant amounts of chlorophyll *b* and chlorophyll *c* are present in the phytoplankton (Trees et al. 1985) this is unlikely to have been a obstacle as the HPLC analysis of the 2008 samples showed low levels of both pigments. Raateoja et al. (2004) found that two cyanobacterial taxa from the Baltic Sea showed a low ratio of *in vivo* fluorescence to chlorophyll *a* when measured using a conventional fluorometer. They suggest that any cyanophyte that contains the pigment phycoerythrocyanin rather than phycoerythrin will have inefficient light harvesting in the excitation wave band and thus show a reduced fluorescence signal. Although the results they obtained are not universally applicable to all cyanobacterial taxa, the cyanobacterial presence displayed in the phytoplankton absorption spectra for Burdekin Falls Dam means that chance that the chlorophyll *a* concentrations are underestimated cannot be disreguarded.

To get an indication of the consistency of the measurement method, replicates for each measurement station were created by first dividing the water sample in two before filtering each half onto separate filters. Figure 5-26 compares the measured chlorophyll *a* concentrations for each replicate. The differences between the replicates had a mean of 0.3 μgl^{-1} and a standard deviation of 0.35 μgl^{-1} and the maximum difference was 1.36 μgl^{-1}.

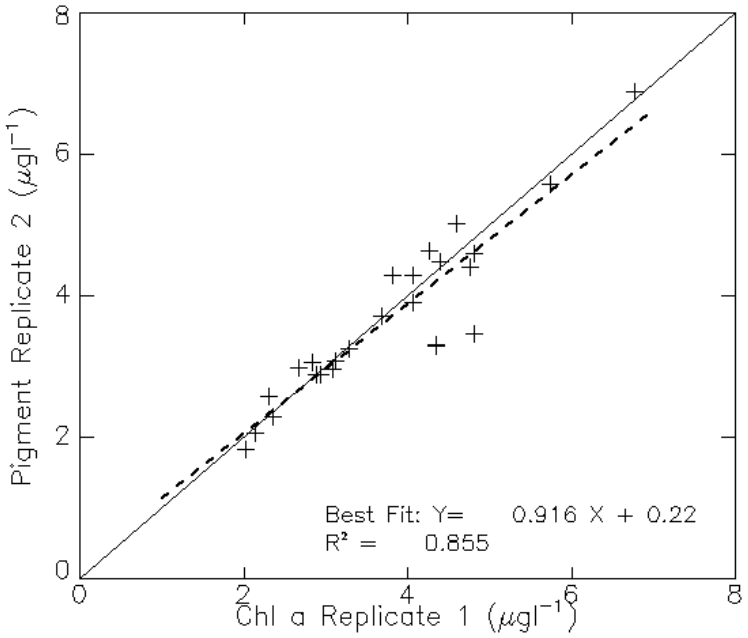

Figure 5-26 Comparing the measured chlorophyll *a* concentrations for the two replicates of each measurement station for the August 2009 Burdekin Falls Dam fieldwork. The dashed line is the line of best fit which has a slope of 0.916, an intercept of 0.22 µgl^{-1} and an R^2 of 0.855. The solid line is the line of 1:1 correspondence.

5.3.4. Algorithm Application

The image that was closest in time to the field observations was the 13th August 2009 image. The MIM algorithm was applied to this image and the water quality parameter concentrations were retrieved. The mean absolute errors for the 25 *in situ* measurement stations were calculated for all the weighting schemes being examined. The results for a selection of weighting schemes are shown in Table 5-5. Results for the other weighting schemes are shown in Appendix G.

Table 5-5 The means of the absolute values of error between the laboratory measured concentrations and those retrieved from the 13th August 2009 image for selected weighting schemes.

	Chl (µgl^{-1})		TR (mgl^{-1})	
	Av	SD	Av	SD
NO_WEIGHTS	5.96	1.26	5.20	2.46
3_BANDS	2.81	1.16	5.74	2.46
MER_BL_RAN1	7.08	1.14	3.61	1.98
MER_BL_REF3	2.73	1.48	4.82	2.36
MER_BU_DER6	4.64	2.14	1.69	1.25
MER_BU_RAN1	0.88	0.61	5.44	2.38
MER_BU_RAN2	0.78	0.70	5.41	2.37

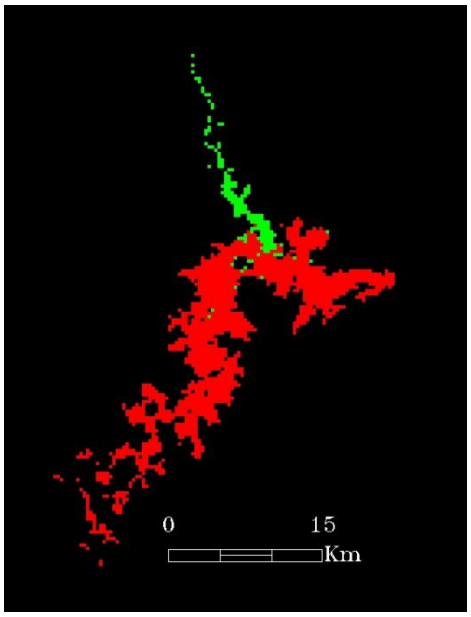

Figure 5-27 The SIOP set selected based on the 0.847 threshold on the ratio of the lower SIOP set to upper SIOP set misclose sum for the 13th August 2009 image. The MER_BU_RAN2 weighting scheme was used. The pixels coloured green selected the upper basin SIOP set while the pixels coloured red selected the lower basin SIOP set.

In this case the area selected for inversion with the lower basin SIOP set (vide Figure 5-27) is far more extensive. Although there was no direct measurement of the SIOPs, at the time of the image acquisition a clear boundary can be seen in the image (Figure 5-28) that coincides with the boundary between the inversion selected SIOP sets. This is similar to the comparison made in Figure 5-23.

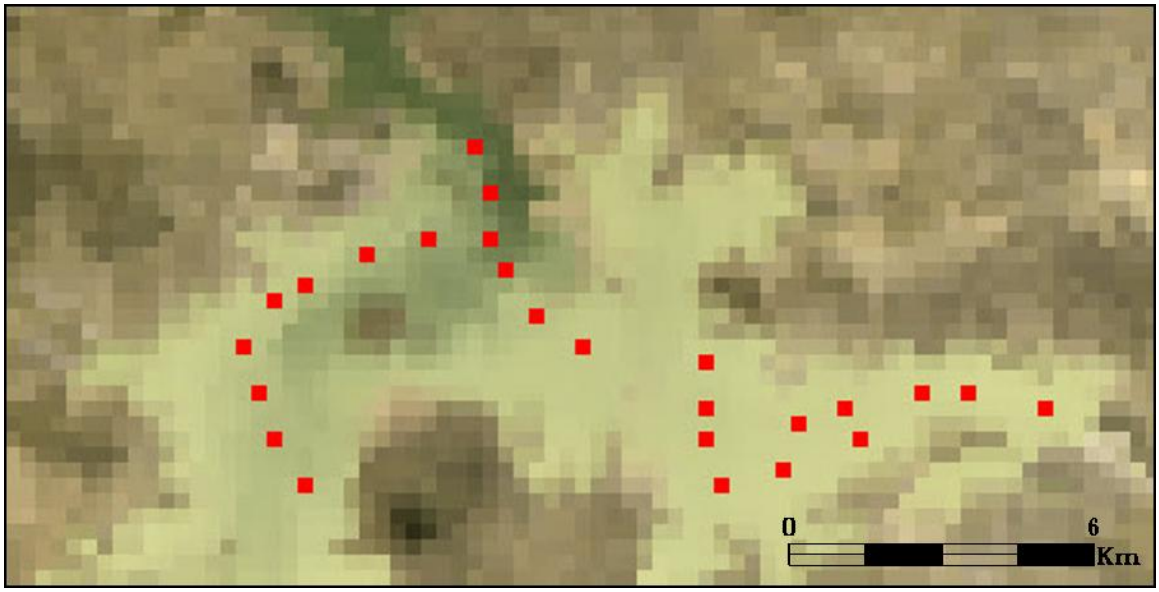

Figure 5-28 True colour image taken from the 13th August MERIS image. The overlaid red squares represent the sample stations. Patterns in tripton can be clearly seen within the water body. The lower basin shows a uniformity of colour that is at odds with measured values of tripton.

Figure 5-29-Figure 5-31 show comparisons on the retrieved and the laboratory measured chlorophyll *a* and tripton concentrations as well as the measured and 'forward – inverse' spectra for each of the measurement stations.

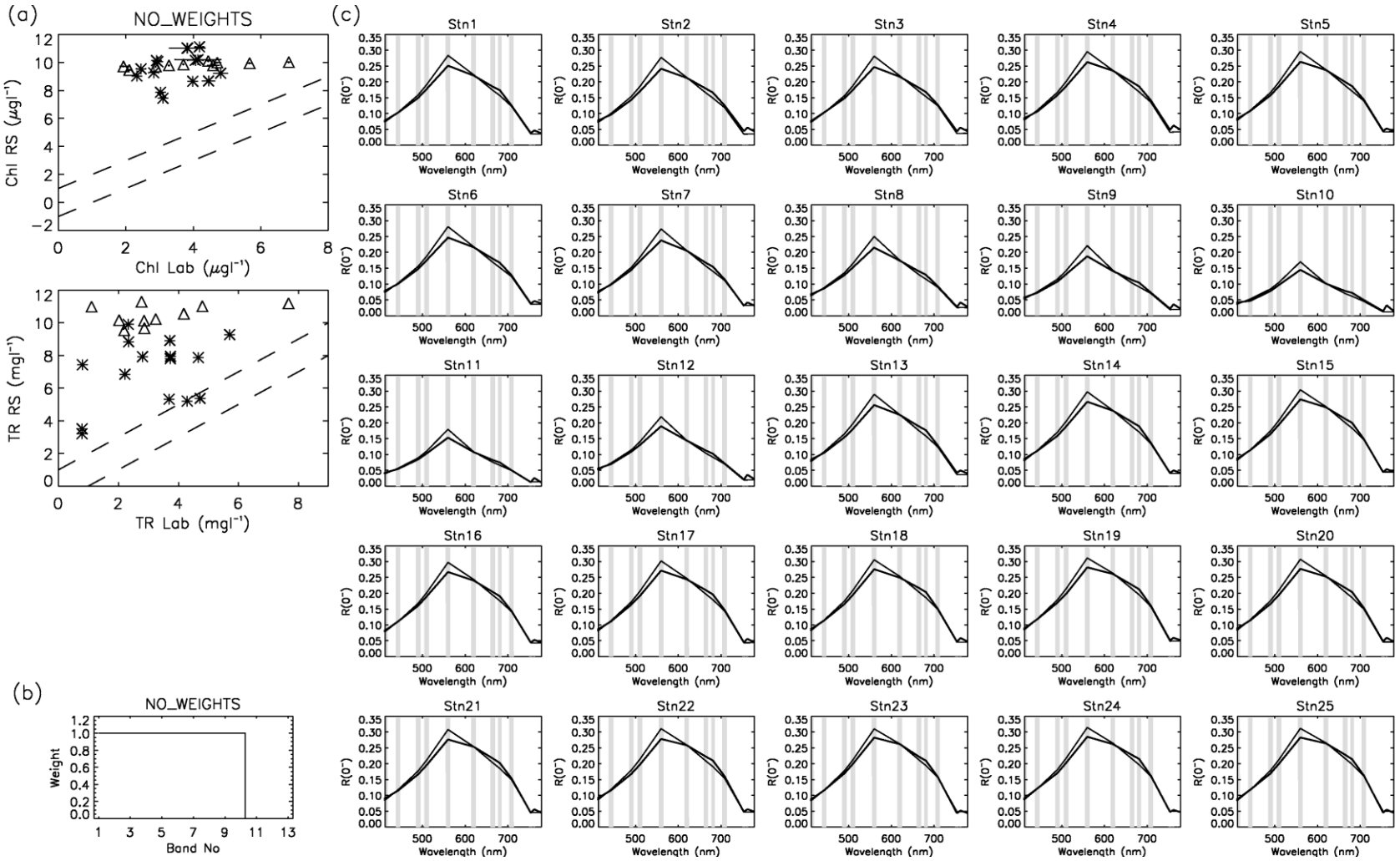

Figure 5-29 (a) The laboratory concentrations vs. image retrieved concentrations using the unweighted first nine bands. The diamond symbols show the stations that are geographically in the lower basin. The dotted lines show the bounds of 1μgl^{-1} for chlorophyll *a* and 1mgl^{-1} of tripton. (b) The weighting scheme. (c) The optical closure for each station.

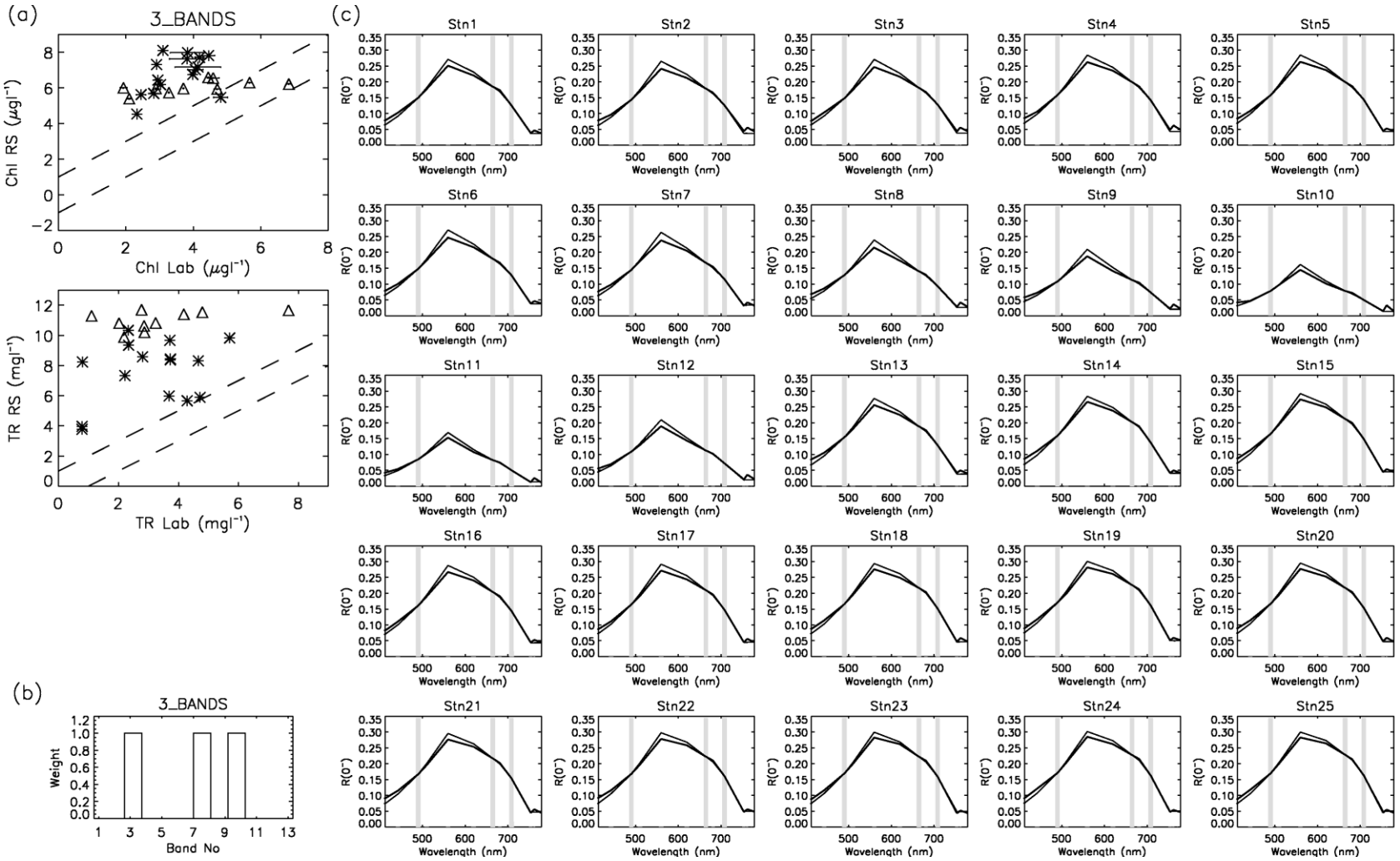

Figure 5-30 (a) The laboratory concentrations vs. image retrieved concentrations using the 3_BANDS weighting scheme. The diamond symbols show the stations that are geographically in the lower basin. The dotted lines show the bounds of 1μgl^{-1} for chlorophyll *a* and 1mgl^{-1} of tripton. (b) The weighting scheme. (c) The optical closure for each station.

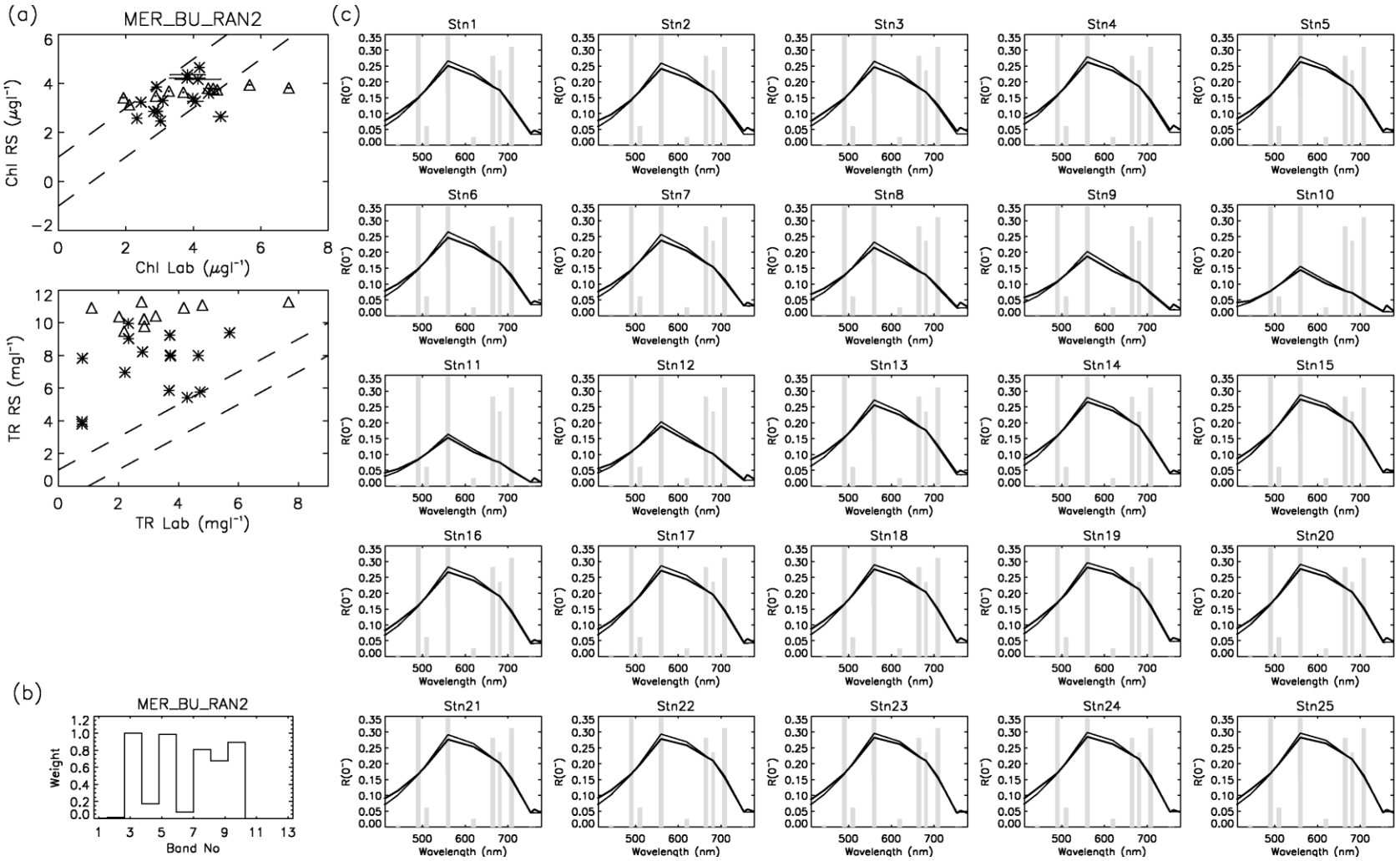

Figure 5-31 (a) The laboratory concentrations vs. image retrieved concentrations using the MER_BU_RAN2 weighting scheme. The diamond symbols show the stations that are geographically in the lower basin. The dotted lines show the bounds of 1μgl^{-1} for chlorophyll *a* and 1mgl^{-1} of tripton. (b) The weighting scheme. (c) The optical closure for each station.

A comparison between Table 5-3 and Table 5-5 shows that the accuracy and precision of the chlorophyll *a* retrieval in the 2009 image is comparable to, if not better than the 2008 image. The difference between the accuracy and precision of the tripton retrieval is more marked. The suitability of the atmospheric correction of the 2008 image was confirmed by comparing it to co-incident *in situ* radiometric measurements at three places in the image. To investigate whether an unreliable atmospheric correction may be responsible for the inferior retrieval accuracy, the 13th August 2009 image was corrected using AOT at 550nm values higher (0.11) and lower (0.07) than the figure provided by the DDV approach. These images were then inverted using the MER_BU_RAN2 weighting scheme and the change in retrieved concentration was calculated. The distributions of difference in the retrieved values for chlorophyll *a* and tripton are plotted in Figure 5-32. To isolate the effect of the atmospheric correction, the differences were only calculated on those pixels that selected the same SIOP set in both inversions. In the comparison of 0.07 AOT at 550nm and 0.09 AOT at 550nm 98.9% of the pixels were used and in the comparison of 0.09 AOT at 550nm and 0.11 AOT at 550nm 99.6% of the pixels were used.

The chlorophyll *a* retrieval had a mean of -0.028 μgl^{-1} (sd 0.222 μgl^{-1}) for the 0.07-0.09 difference and a mean 0.009 μgl^{-1} (sd 0.270 μgl^{-1}) for the 0.09-0.11 difference. The tripton retrieval had a mean of -0.025 mgl^{-1} (sd 0.120 mgl^{-1}) for the 0.07-0.09 difference and a mean -0.010 mgl^{-1} (sd 0.124 mgl^{-1}) for the 0.09-0.11 difference. In all cases the distribution of the differences are centred close to zero but it is clear that the tripton is less sensitive to the atmospheric correction as the standard deviation of the differences is smaller in both the under and over corrected cases. It is unlikely that a poor atmospheric correction is responsible for the consistent overestimation of the tripton concentration with respect to the laboratory measurements.

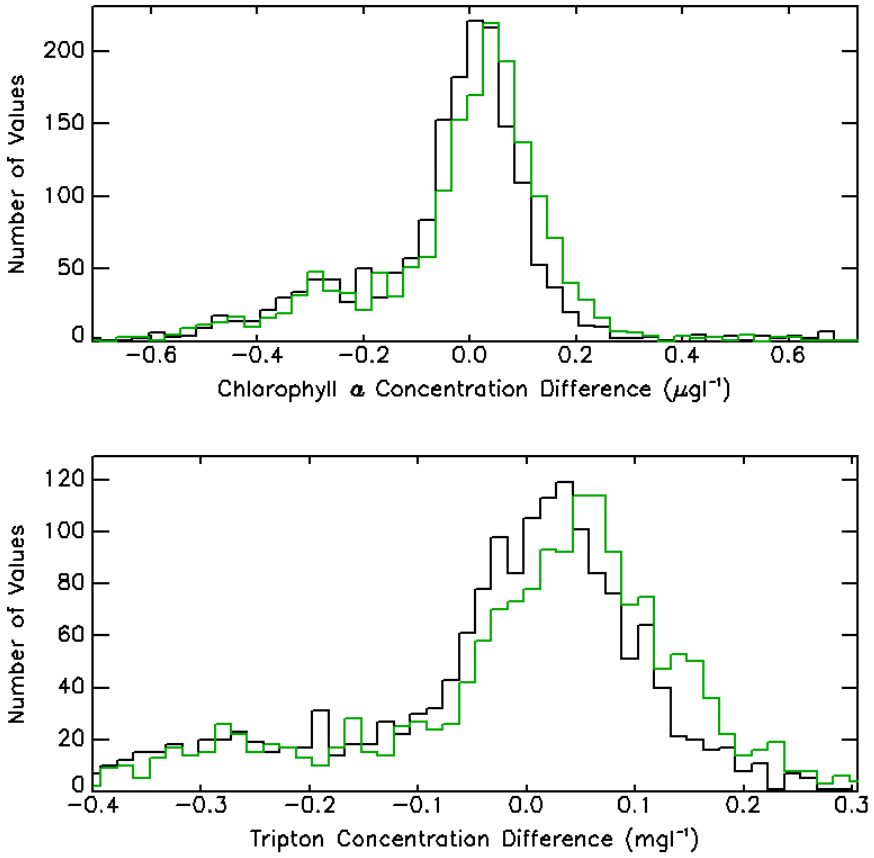

Figure 5-32 The distribution of retrieved chlorophyll *a* (top) and tripton (bottom) concentrations for the 13th August 2009 image. The black lines show the difference in retrieved values when an AOT at 550nm of 0.09 is used for the atmospheric correction instead of an AOT at 550nm of 0.07 and the green lines show the difference in retrieved values when an AOT at 550nm of 0.11 is used for the atmospheric correction instead of an AOT at 550nm of 0.09.

Table 5-6 shows a selection of photographs of the water that were taken at the time of sampling. The *in situ* photographs are consistent with the colours shown in Figure 5-28. The first example illustrates a circumstance where the laboratory measured water quality parameters are very similar and the photographs show a significant difference in colour and the second example shows where the water colour is very similar and the laboratory measured water quality parameters are quite different. The laboratory measured tripton concentration shows the greatest variation. The water quality parameter concentrations retrieved from the image are shown for comparison. In the first case the image retrieved tripton concentration difference is large, which is consistent with difference in turbidity displayed by the photographs, and in the second case the difference is small, which is consistent with colour similarity displayed by the photographs. This

evidence suggests that error displayed by the laboratory-image comparison may not be entirely attributed to errors in the retrieval algorithm.

Table 5-6 Comparison of the observed water colour and the laboratory measured and image retrieved water quality parameters.

Station	Photograph	Laboratory Measurement		Retrieved from Image	
		Chlorophyll *a* mean (μgl^{-1})	Tripton (mgl^{-1})	Chlorophyll *a* (μgl^{-1})	Tripton (mgl^{-1})
2		2.91	0.8	3.86	7.8
10		3.10	0.8	3.30	3.8
23	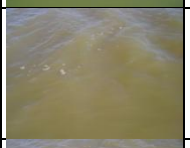	5.67	1.1	3.94	10.9
24	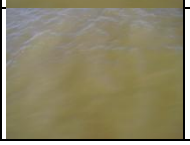	4.71	7.7	3.74	11.3

5.4 Time Series

Figure 5-33 - Figure 5-35 show time series of the optical water quality parameter maps. The tripton concentration maps show an intrusion of clearer water flowing in from the Burdekin River to the north of the storage. The chlorophyll *a* concentration maps show that for the open water areas chlorophyll *a* concentrations range between 0-9 μgl^{-1} with only the 10th August image returning negative concentrations (1% of the pixels).

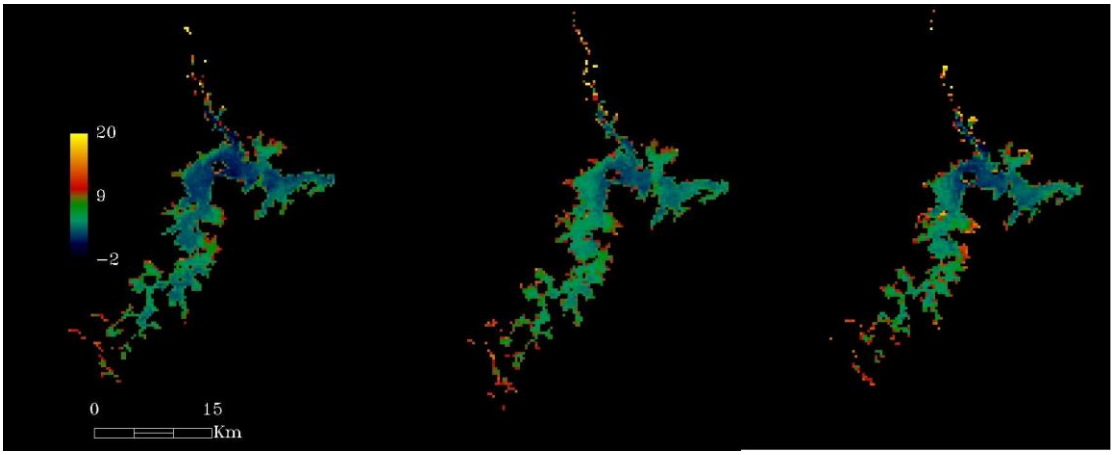

Figure 5-33 Chlorophyll *a* concentration maps derived from the 10th (left), 13th (middle) and 14th (right) August 2009 MERIS image.

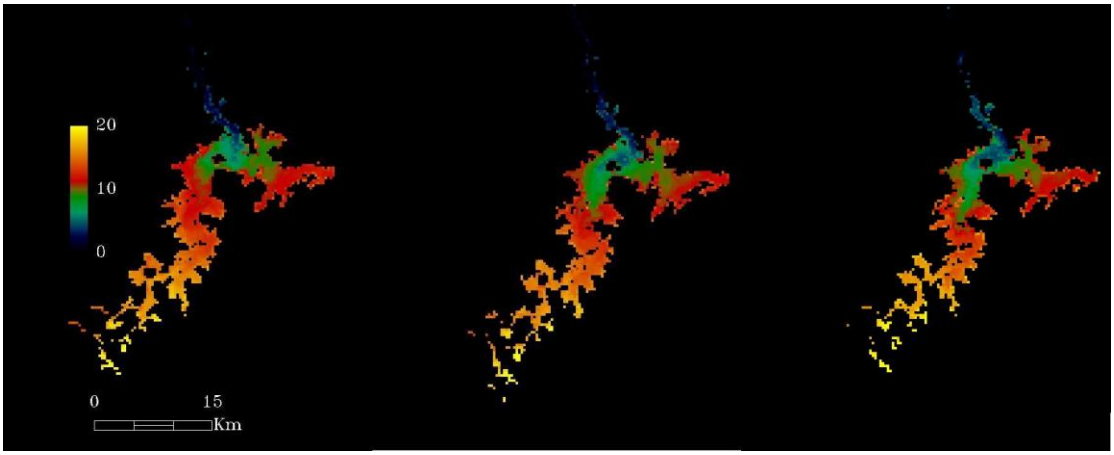

Figure 5-34 Tripton concentration maps derived from the 10th (left), 13th (middle) and 14th (right) August 2009 MERIS images.

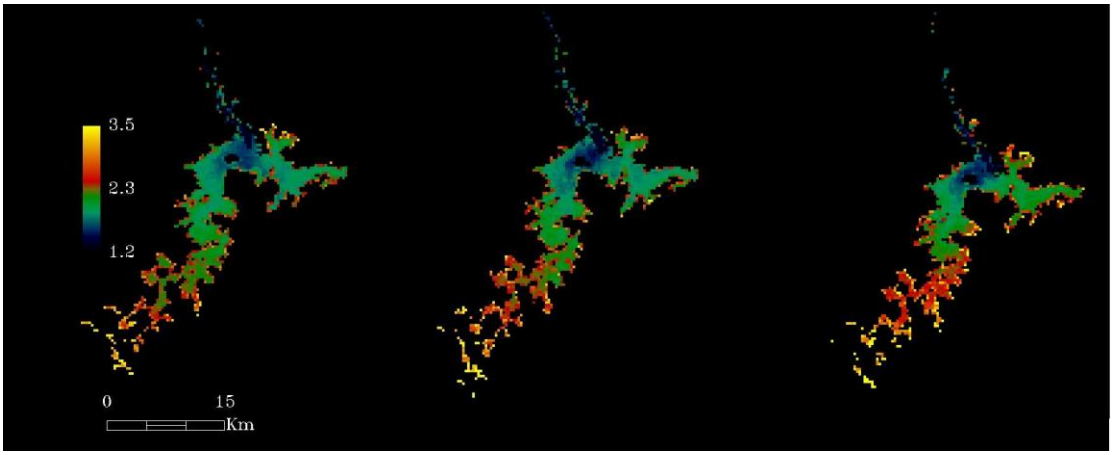

Figure 5-35 CDOM concentration maps derived from the 10th (left), 13th (middle) and 14th (right) August 2009 MERIS image.

5.5 Conclusions

This chapter described the work done to test and validate the findings of the previous chapters in relation to the MIM approach. The MIM was validated against field observations taken at Burdekin Falls Dam in October 2008 and August 2009. The *in situ* measurements of above surface reflectance and water quality parameter measurements were used to examine the optical closure between the measured and modelled spectra. The chapter then showed how that optical closure can be used to identify the most appropriate SIOP set in water bodies like Burdekin Falls Dam that have multiple SIOP domains. Finally, the laboratory measured water quality parameter concentrations were used to calculate the accuracy and precision of the MIM approach.

In both validation sets the preferred retrieval weighting scheme (MER_BU_RAN2) had a lower mean error than the conventional exact three band or unweighted over-determined system schemes. In the two latter cases chlorophyll *a* was systematically overestimated when compared to the laboratory measurements whereas the weighted scheme neither underestimated nor overestimated. If the two validation sets are pooled the MER_BU_RAN2 weighting scheme has a mean error of chlorophyll *a* retrieval of 1.0 μgl^{-1}, the three band scheme had a mean error of 4.2 μgl^{-1} and the unweighted scheme had a mean error of 5.5 μgl^{-1}. This is not to say that this is the definitive error for the method as a number caveats should be attached to these results. Firstly, the range of water quality parameter concentrations measured in the two field campaigns was limited. For example, the measured *in situ* chlorophyll *a* values ranged from 1.8-7.7 μgl^{-1}, but 80% of the values within the range of 2.7-5.5 μgl^{-1}. Chapter 4 showed how the minimum detection limits and retrieval accuracy of water quality parameters are dependent on the parameter as well as the concentrations of the other colour producing agents in the water. Likewise, there is no way to evaluate the accuracy of the atmospheric correction on any particular image without some additional *in situ* data. Lastly, it is not possible to be definitive about the accuracy when there is notable uncertainty in the ground truth values. An attempt to quantify this uncertainty was made in §5.3.3 which showed the mean error between the two replicate groups was 0.3 μgl^{-1} with a standard deviation of 0.35 μgl^{-1} and the maximum difference was 1.36 μgl^{-1}.

The assessment of the average error for tripton retrieval suffers from the same caveats as those mentioned from the chlorophyll *a* retrieval: that is, a limited range and uncertainty in the ground truth data. In the latter case, the apparent inconsistencies in the laboratory determination of the tripton concentration demonstrated in Table 5-6 are a fatal flaw. For the August 2009 the TSM concentrations of the samples were measured by the Citiwater, a National Association of Testing Authorities (NATA) accredited laboratory in Townsville. Discussions with the laboratory manager revealed that the volume of water filtered was only 20% of the volume filtered for the October 2008 fieldwork even though a sufficient volume of sample water was available. In light of these uncertainties only the results for the October 2008 image is discussed and their usefulness is limited by the sample size of ten. The best performed MER_BL_REF3 weighting scheme had a mean error of 1.2 mgl^{-1}, the three band scheme had a mean error of 3.4 mgl^{-1} and the unweighted scheme had a mean error of 1.8 mgl^{-1}. In this case the difference between the weighted and unweighted schemes is significant at only the 70% level.

As with tripton, the assessment of the CDOM retrieval accuracy suffers from a small sample size but it was found that the best performed MER_BL_RAN1 weighting scheme had a mean error of 0.12 m^{-1}, the three band scheme had a mean error of 0.25 m^{-1} and the unweighted scheme had a mean error of 0.52 m^{-1}. In this case the difference between the weighted and the three band scheme is significant at only the 85% level and the three band and unweighted scheme difference is significant at only the 90% level.

A rudimentary test showed that the estimation of water quality parameter concentrations was only slightly affected by errors in the atmospheric correction. The simulation in §4.6.1 showed that the error had a linear response to an increase in atmospheric noise and the test in this chapter showed that the gradient of the line was reasonably flat for a practical application. This result is encouraging as it suggests that the risks inherent in the approximations and assumptions in the atmospheric correction may be reasonable.

6. Field Validation of the Particle Swarm Optimisation at Burdekin Falls Dam, Queensland, Australia

Key Points

- *When used with the Particle Swarm Optimisation, the Spectral Information Divergence and Spectral Angle Mapper similarity measures are incapable of retrieving tripton and CDOM concentrations accurately.*
- *The Particle Swarm Optimisation does not offer improvements in accuracy and precision sufficient enough to justify the increased computational overhead in the inversion.*

This chapter describes the work done to validate the findings of the previous chapters with regards to the Particle Swarm Optimisation (PSO) algorithm and the Spectral Angle Mapper (SAM), Spectral Information Divergence (SID), the minimum distance and the Spectral Correlation Mapper (SCM) similarity measures. The algorithm was validated using the same field data, taken at Burdekin Falls Dam in October 2008 and August 2009, that was used in the work described in Chapter 5. The chapter describes how the optical closure was again used to identify the most appropriate SIOP set in Burdekin Falls Dam when the SID, SAM and minimum distance similarity measures were used. This method was found to be ineffective in the case of the SCM similarity measure and the simpler minimum misclose sum used by Phinn et al. (2005) was used instead. After that, the laboratory measured water quality parameter concentrations were used to calculate the accuracy and precision of PSO.

6.1 Burdekin Falls Dam October 2008

6.1.1. Laboratory Measurements

The water quality parameter concentrations for the Burdekin Falls Dam in October 2008 were measured using the methods described in §2.2 at the measurement stations shown in Figure 6-1. The range of the measured chlorophyll *a* values was 2.8 – 7.7 μgl^{-1}, the range of the measured

tripton was 5.6 – 10.3 mgl^{-1}, the measured CDOM range was 0.88 – 1.21 m^{-1} and the Secchi depth range was 0.9 – 1.3 m. A table showing the individual measurements is shown in Appendix A.

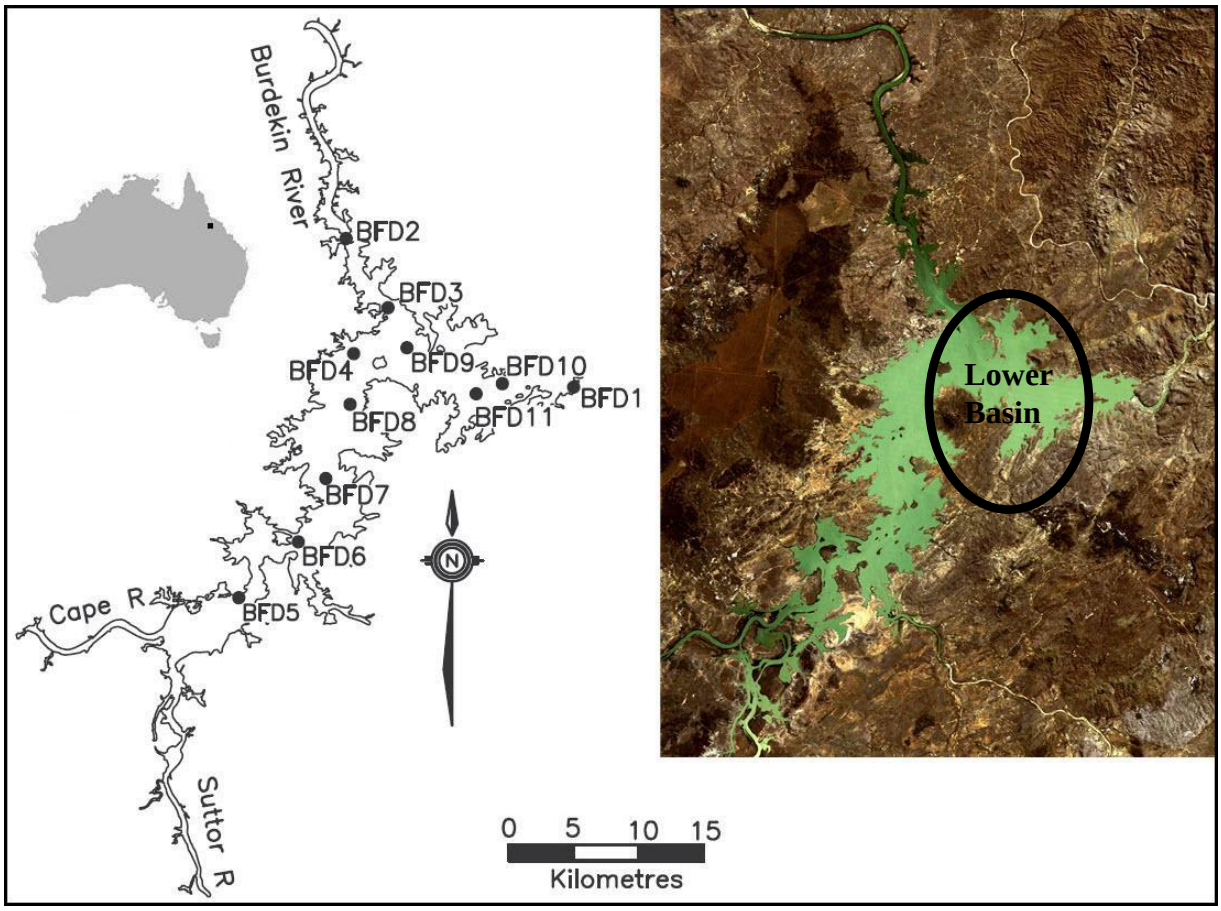

Figure 6-1 Location of the SIOP sample sites for the October 2008 fieldwork activities on Burdekin Falls Dam, Australia. The left hand image shows the calculated full supply level and the right hand image shows a Landsat 5 TM true colour image at the same scale as the map, captured on 22nd August 2008.

6.1.2. Image Processing

The image used was the same image as in Chapter 3. Table 6-1 shows the final parameters used in the atmospheric correction.

Table 6-1 The S6 parameters for the 15th October 2008 image.

Parameter	Value	Source
Atmosphere Model	Tropical†	
Illumination	Thuillier Sun	
CO_2	360ppm	Average Value (No effect in Vis. Region)
H_2O	2.971	Obtained from MODIS 07 Product
O_3	0.289 ATM-cm	Obtained from MODIS 07 Product
Aerosol Model	Maritime	Prevailing wind was from the SW
AOT at 550nm	0.15	Tuned on *in situ* overpass stations
Ground Altitude	0.154km	Burdekin Falls Dam water level RL
Sensor Altitude	799km	MERIS Specifications
Sensor Zenith,	11.07°	MERIS Image
Sensor Azimuth	282.33°	MERIS Image
Solar Zenith Angle	29.88°	MERIS Image
Solar Azimuth	70.41°	MERIS Image
Low pass filter size for Background File	9 x 9	
Radiance to irradiance conversion factor (Q)	4.0	*Hydrolight*® simulations

†Selected Tropical because the main constituent is the water content.

The atmospheric correction was tuned using 0.5% DDV pixels compared to the auxiliary file MER_LAP_AX DDV values.

6.1.3. Algorithm Application

SIOP Sets

The inversions were performed using the upper and lower SIOP set as described in the §2.5.2 and shown in Figure 6-2 overlaid with the MERIS bands.

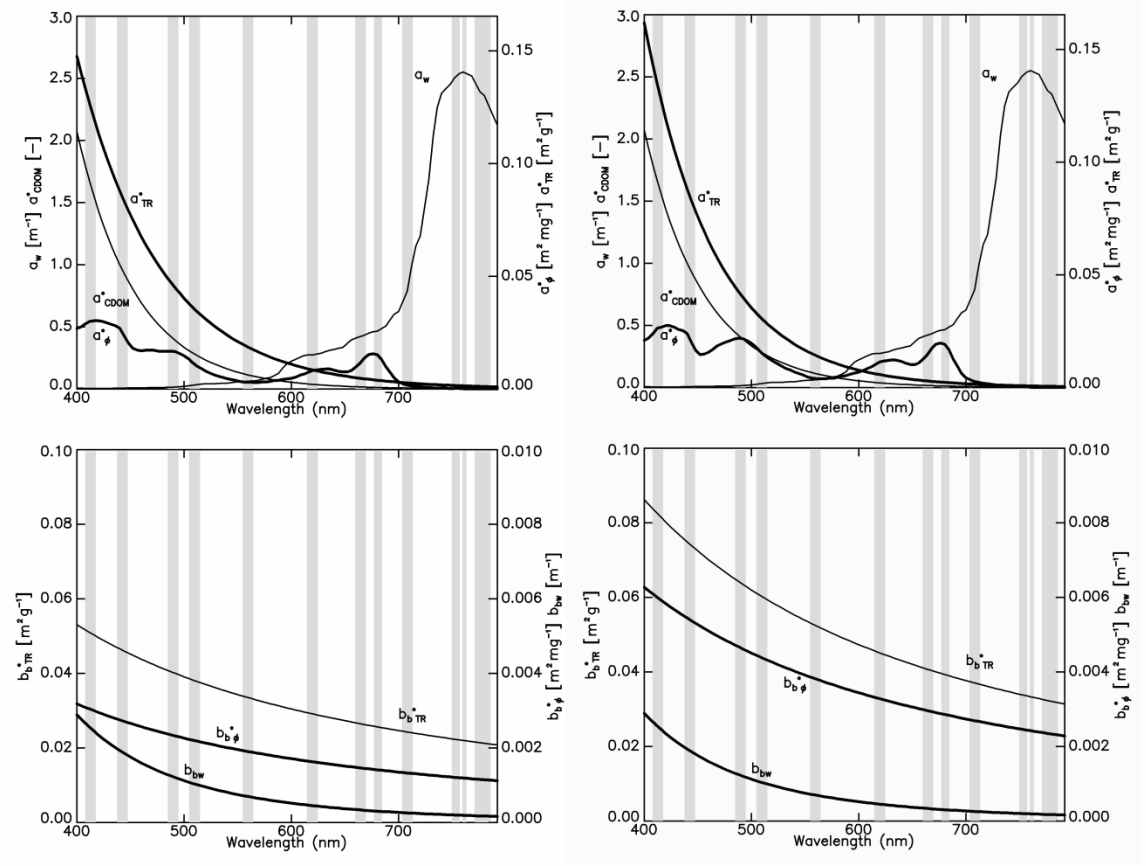

Figure 6-2 SIOP sets upper basin (left) and lower basin (right) for Burdekin Falls Dam measured during the October 2008 field work. The upper graph shows the spectral absorption of water (*w*) and the chlorophyll *a* specific absorption spectra of phytoplankton (ϕ), total suspended material (*TSM*) and coloured dissolved organic matter (*CDOM*). The lower shows the spectral backscattering of water (*w*) and the specific backscattering spectra of chlorophyll *a*(ϕ) and total suspended material (TSM).The shaded areas represent the MERIS bands.

Image Inversion

The PSO algorithm was applied to the 15th October 2008 image and the water quality parameter concentrations were retrieved. The best fit spectra returned by the PSO algorithm for each similarity measure are shown for the lower SIOP set in Figure 6-3 and in Figure 6-4 for the upper SIOP set.

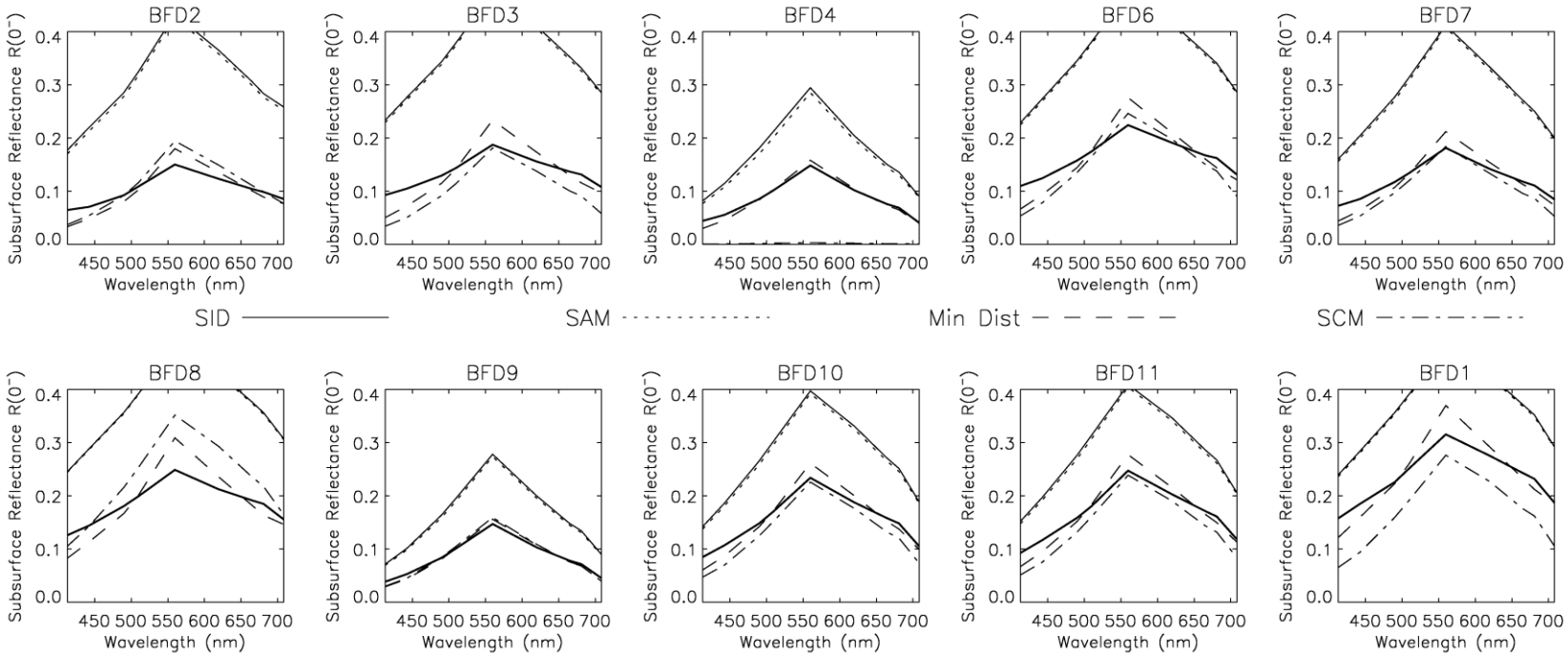

Figure 6-3 The optical closure for the 15th October 2008 image spectra for the lower SIOP set. For each station the plot shows the measured spectra (bold) and the best fit spectra returned by the PSO algorithm for each similarity measure. The spectra for the SID criterion are shown with a solid line, the SAM criterion with a dotted line, the minimum distance criterion with the dashed line and the SCM criterion is shown with a dash dot line.

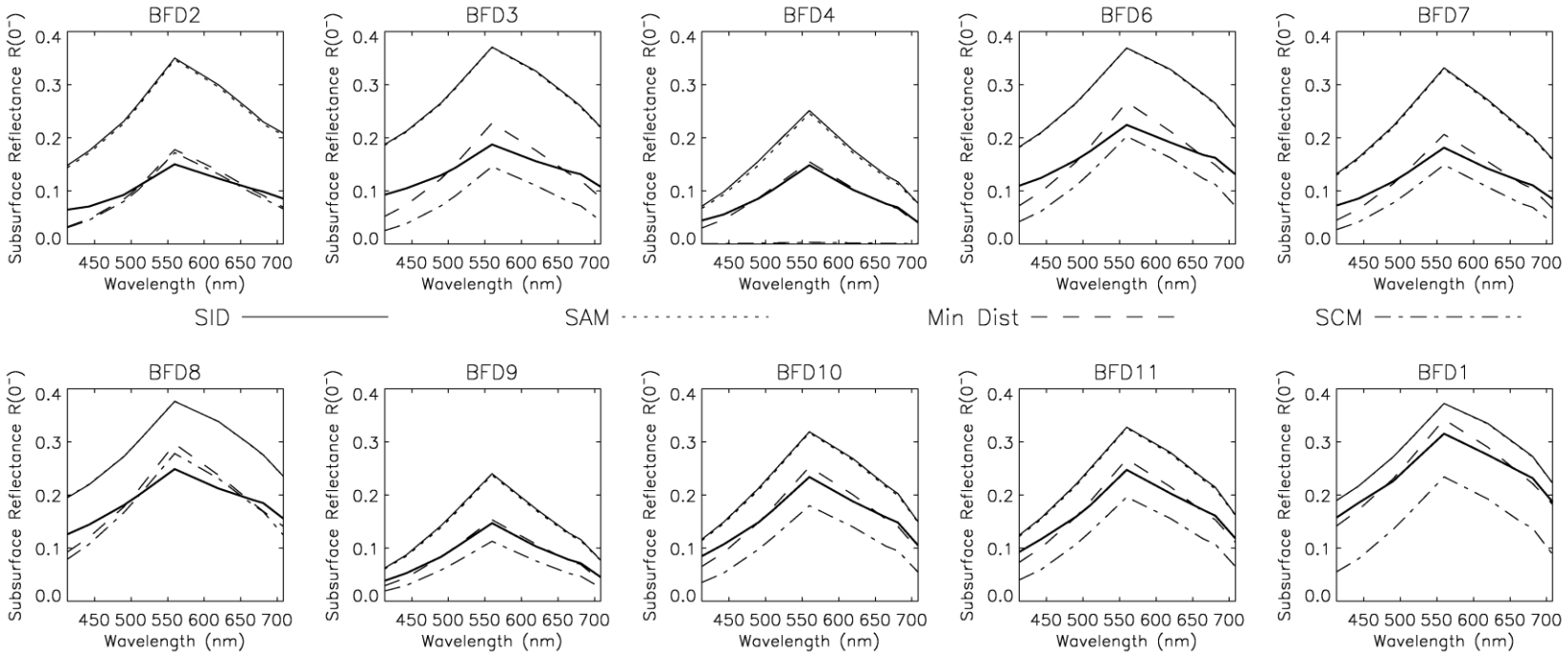

Figure 6-4 The optical closure for the 15th October 2008 image spectra for the upper SIOP set. For each station the plot shows the measured spectra (bold) and the best fit spectra returned by the PSO algorithm for each similarity measure. The spectra for the SID criterion are shown with a solid line, the SAM criterion with a dotted line, the minimum distance criterion with the dashed line and the SCM criterion is shown with a dash dot line.

SIOP Set Selection

As was the case with §5.2.3 the inversions confirmed the assumption made in Chapter 2 that the SIOP variation measured in Burdekin Falls Dam was sufficient to warrant using multiple SIOP sets. To investigate whether the same approach to SIOP set selection that was used in the MIM algorithm was applicable, misclose sums resulting from the two SIOP sets for each similarity measure were compared as before and are shown in Figure 6-5. The SID, SAM and the minimum distance criteria displayed a similar behaviour to that which was observed in the MIM algorithm. Lines of best fit were calculated for the two groups with gradient and R^2 values for each criterion shown in Table 6-2.

Table 6-2 The best fit slopes and R^2 values for the SID, SAM, minimum distance and SCM matching criteria.

	Upper Basin		Lower Basin		Mean
	Slope	R^2	Slope	R^2	
SID	0.401	0.847	0.253	0.644	0.327
SAM	0.406	0.866	0.256	0.677	0.331
Min Dist	0.759	0.940	0.485	0.735	0.622
SCM	0.661	0.265	0.663	0.339	n.d.

The SCM criterion did not show the same behaviour as the other criteria. For this criterion the simpler minimum misclose sum used by Phinn et al. (2005) was retried. This technique looked at the difference of misclose sums resulting from the two SIOP sets rather than the ratio as in the modified case. This was able to discern the most appropriate SIOP set more accurately than using the ratio but not as satisfactorily as with the other three similarity measures. The distributions of the misclose sum differences are shown in Figure 6-6.

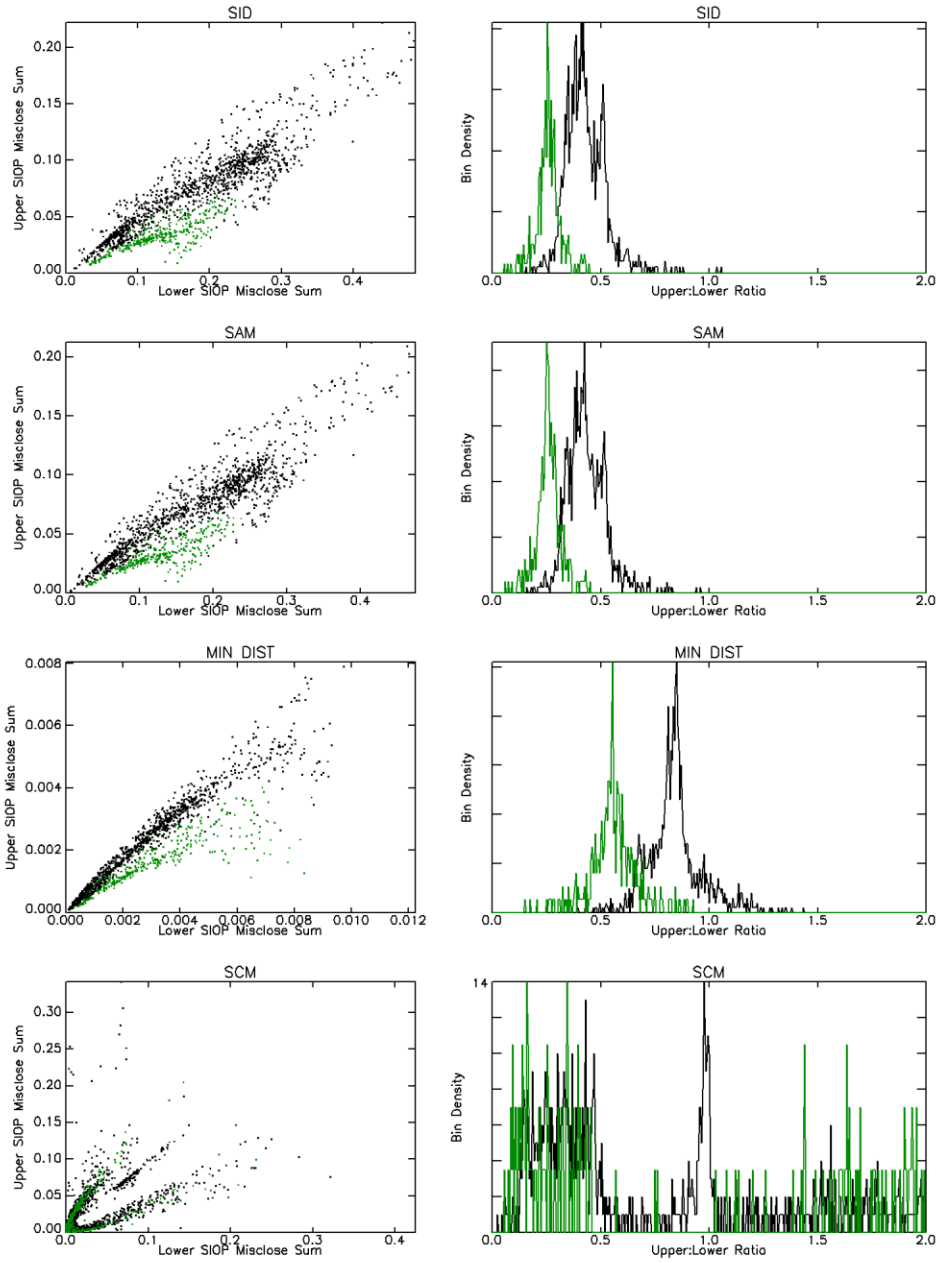

Figure 6-5 The misclose sum that results from the lower basin SIOP set against the misclose sum that results from using the upper basin SIOP set (left) and histograms showing the distribution of the Lower : Upper ratio for the upper basin and lower basin SIOP group of pixels. Those data associated with pixels in the upper basin group are plotted in black and those associated with the lower basin group are plotted in green. The histograms have been normalised to the peaks in their distributions for easier comparison.

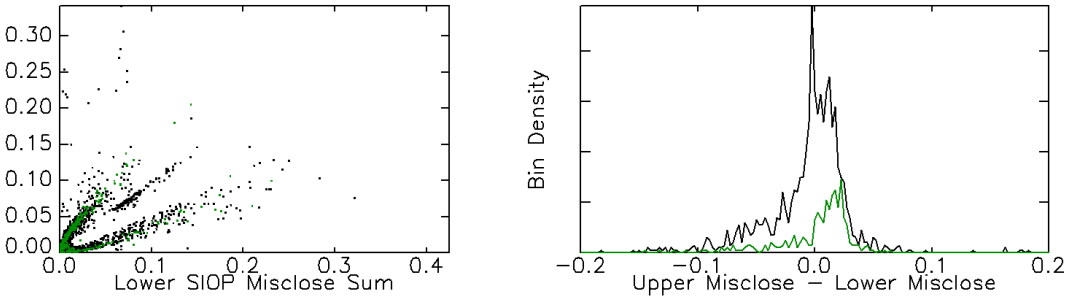

Figure 6-6 The misclose sum that results from the lower basin SIOP set against the misclose sum that results from using the upper basin SIOP set (left) and a histogram showing the distribution of the difference between the lower and upper basin SIOP set misclose sum for the upper basin and lower basin SIOP group of pixels. Those data associated with pixels in the upper basin group are plotted in black and those associated with the lower basin group are plotted in green. The histograms have been normalised to the peak in their distributions for easier comparison.

The inversions were run again using the thresholds to select the SIOP set. The accuracy and precision results are shown in Table 6-3, SIOP selection images are shown in Figure 6-7 and the resultant water quality parameter comparison graphs are shown in Figure 6-8.

Table 6-3 The means of the absolute values of error between the laboratory measured concentrations and those retrieved from the 15th October 2008 image for selected matching criteria.

	Chl (μgl^{-1})		TR (mgl^{-1})		CDOM(m^{-1})	
	Av	SD	Av	SD	Av	SD
SID	3.27	3.32	14.5	9.03	1.31	0.69
SAM	3.72	3.32	14.3	8.98	1.28	0.70
Min Dist	4.07	2.70	3.35	2.29	0.30	0.26
SCM	4.65	1.78	2.45	2.11	0.33	0.21

The SID and SAM criteria performed very poorly with respect to the estimation of tripton and CDOM concentration. Both these criteria mathematically eliminate the magnitude of the reflectance spectra from the calculation and focus on its shape. Considering that the 'flattening' of the measured spectra observed in §5.2.3 this is to be expected but it is surprising that the chlorophyll *a* retrieval is as good as it is.

The best fit measure of the MIM is equivalent to the minimum distance criterion. Comparing the values shown in Table 6-3 to the MIM results from Table 5-3 it may have been expected that it would return similar results to the unweighted MIM inversion. Although the differences are not

significant at the 95% level, the tripton and CDOM differences are nearly so. The difference that is there will be due to the parameterisation of the two algorithms. Although both algorithms were parameterised with the same simulations the process of curve fitting to produce the f as a function of reflectance relationship for the MIM and the f as a function of ω_b for the PSO will produce different outcomes.

The SCM produced statistically significantly better retrievals for the tripton and CDOM water quality parameters. The SCM is a modification of the SAM that takes into account sign of the correlation not just the magnitude (Carvalho & Menezes 2000). It may be that since the optical closure differences were equally distributed either side of the 560 nm peak the ability to 'balance' the misclosure has led to a more reliable result. Notwithstanding the mean error, it should be noted that the SCM returned the greatest number of physically impossible negative concentrations for chlorophyll *a*.

Comparing the values shown in Table 6-3 to the MIM results from Table 5-3 shows that the chlorophyll *a* retrievals using the PSO with the SID and SAM criteria are only outperformed by the MIM when the MER_BU_RAN1 and MER_BU_RAN2 weighting schemes are used, albeit at only the 80% significance level for a two tailed t test. The MIM chlorophyll *a* retrievals using the 3_BANDS weighting scheme was less accurate than all the PSO similarity measures but this difference was only at the 95% significance level for the SCM.

With regards to the tripton concentration retrieval the SID and SAM criteria are clearly the worst performers. The other approaches are not significantly different.

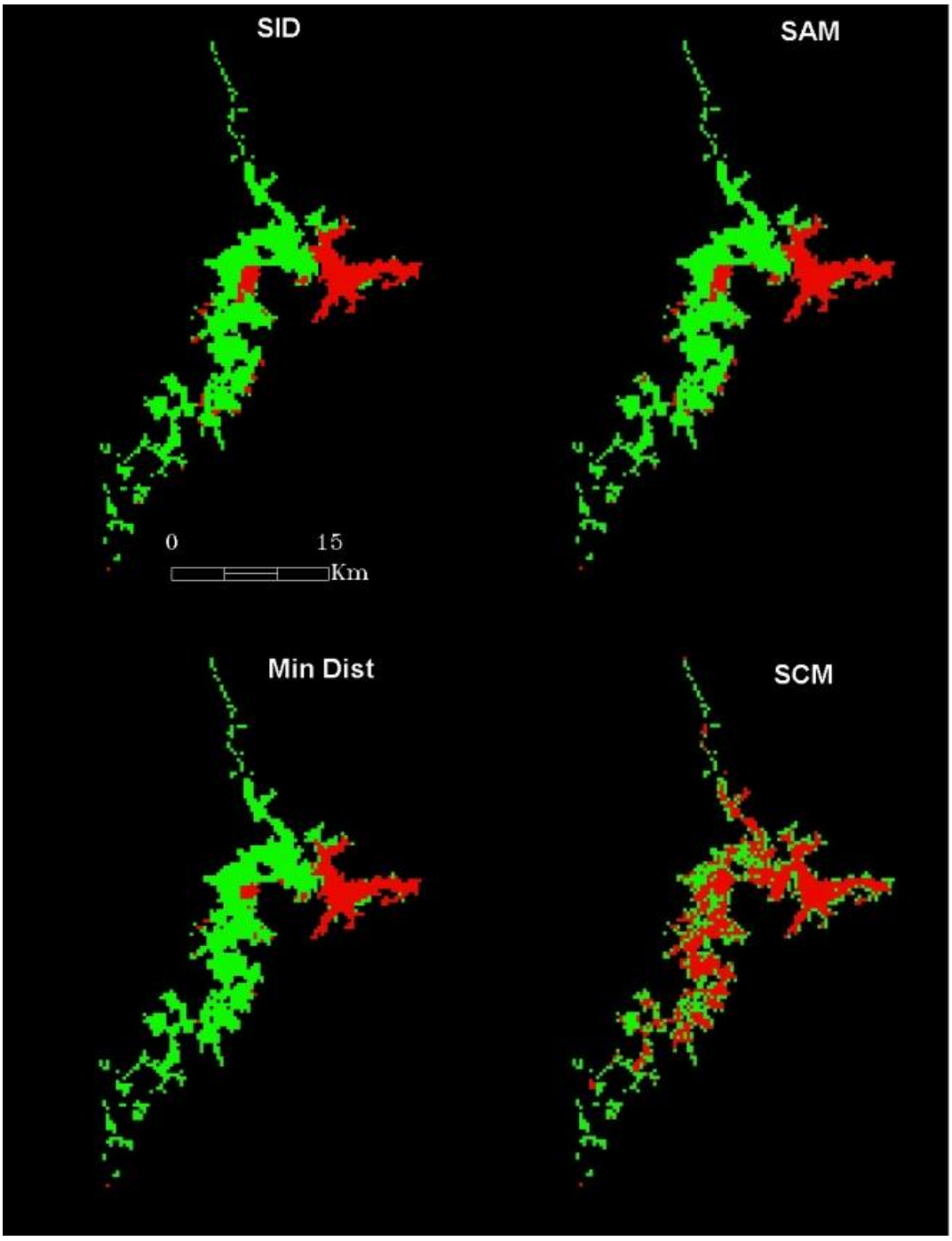

Figure 6-7 The SIOP set selected for the SID (top left), SAM (top right), minimum distance (bottom left) and SCM (bottom right) criteria. The pixels coloured green selected the upper basin SIOP set while the pixels coloured red selected the lower basin SIOP set.

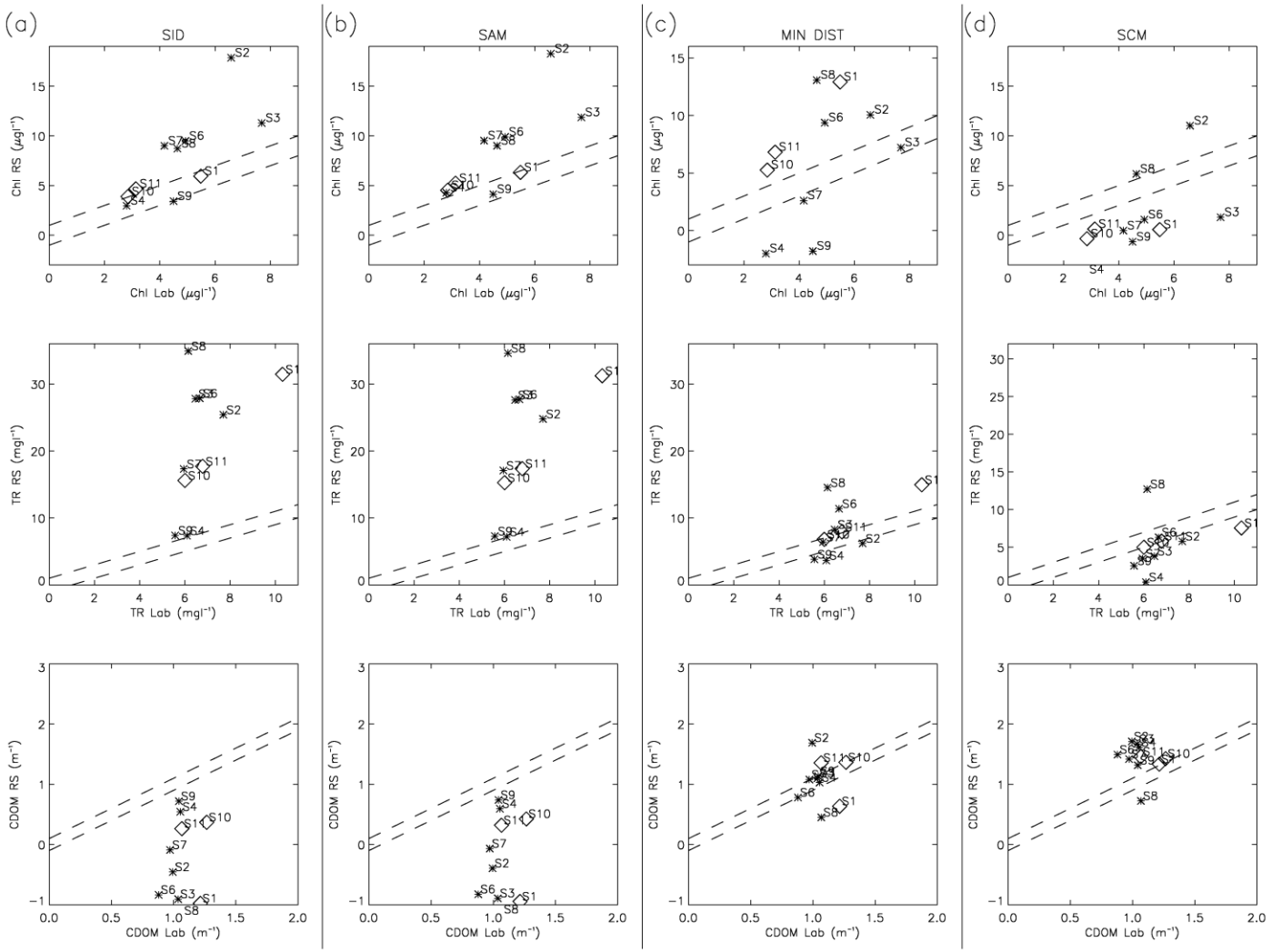

Figure 6-8 The laboratory concentrations vs. image retrieved concentrations for the15th October 2008 images for a) SID, b)SAM, c) Minimum Distance and d) SCM. Each column shows the comparison for chlorophyll *a* (top), tripton (middle) and CDOM (bottom). The diamond symbols show the stations that are geographically in the lower basin. The dotted lines show the bounds of 1μgl^{-1} for chlorophyll *a*, 1mgl^{-1} of tripton and 0.1 m^{-1} for CDOM.

6.2 Burdekin Falls Dam August 2009

6.2.1. Observation Stations

Water samples were taken from the surface water at 25 observations stations on the afternoon of 12th August 2009 between 1:40 pm and 4:10 pm. The locations of those observation stations are shown in Figure 6-9.

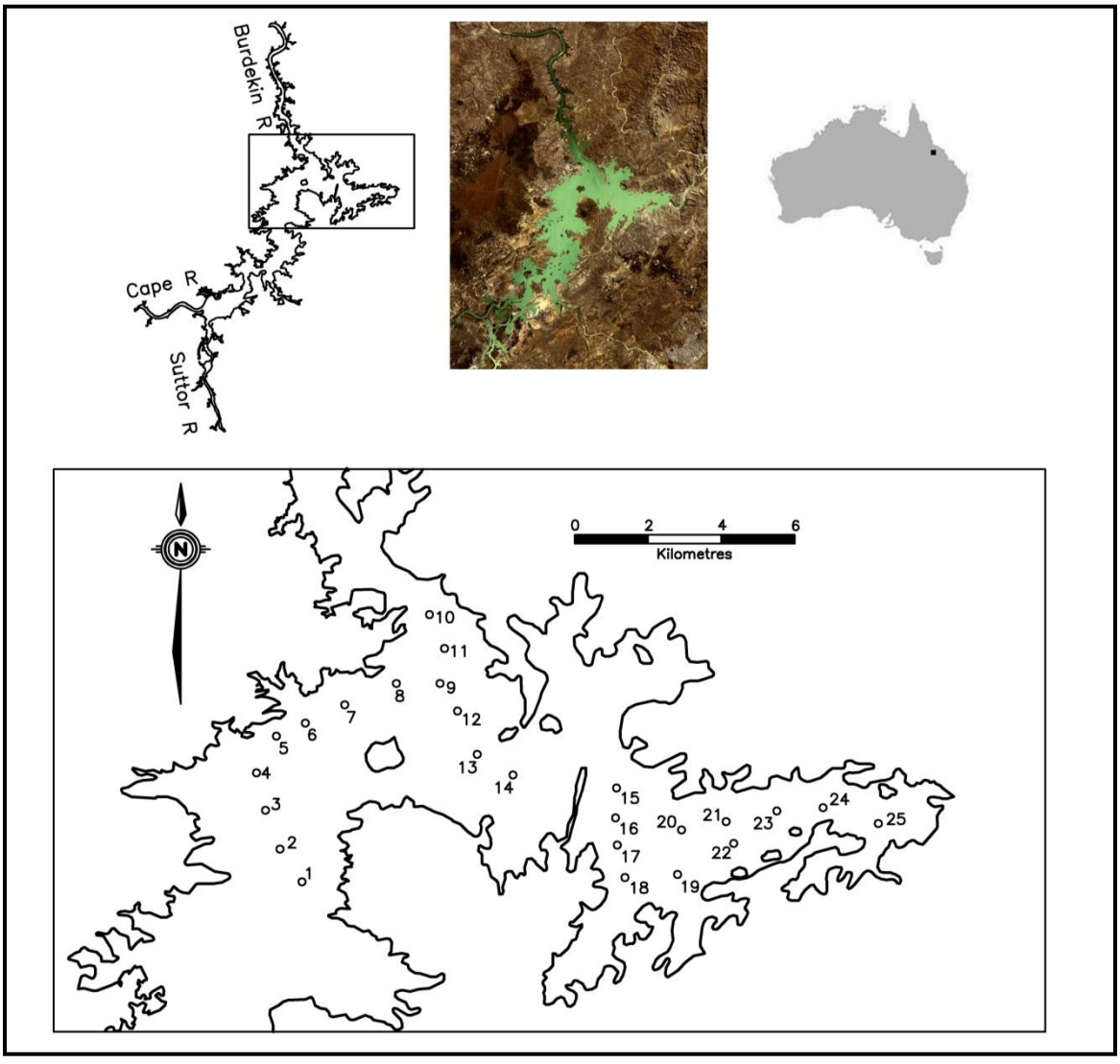

Figure 6-9 Location of the validation sample sites for the August 2009 fieldwork activities on Burdekin Falls Dam, Australia. The upper left hand image shows the calculated full supply level and the upper middle image shows a Landsat 5 TM true colour image captured on 22nd August 2008. The lower image shows the location of the 25 validation sample sites.

6.2.2. Image Processing

A MERIS full resolution level 1b images were obtained for the 13th August 2009. The satellite overpassed the site at approximately 10:00 am on each day. Table 6-4 shows the final parameters used in the atmospheric correction for the MERIS images.

Table 6-4 The S6 parameters for the August 2009 MERIS images.

Parameter	Value	Source
Atmosphere Model	Tropical†	
Illumination	Thuillier Sun	
CO_2	360ppm	Average Value (No effect in Vis. Region)
H_2O	2.322	Obtained from MODIS 07 Product
O_3	0.275 ATM-cm	Obtained from MODIS 07 Product
Aerosol Model	Maritime	Prevailing wind was from the SW
ARVI threshold	0.4	
AOT at 550nm	0.09	Tuned on DDV pixels
Ground Altitude	0.154km	Burdekin Falls Dam water level RL
Sensor Altitude	799km	MERIS Specifications
Sensor Zenith	27.48°	MERIS Image
Sensor Azimuth	281.60°	MERIS Image
Solar Zenith Angle	46.61°	MERIS Image
Solar Azimuth	43.22°	MERIS Image
Low pass filter size for Background File	9 x 9	
Radiance to irradiance conversion factor (Q)	4.0	*Hydrolight*® simulations

†Selected Tropical because the main constituent is the water content.

The atmospheric correction was tuned using 0.5% DDV pixels compared to the auxiliary file MER_LAP_AX DDV values.

6.2.1. Laboratory Measurements

The water quality parameter concentrations for the Burdekin Falls Dam in August 2009 were measured using the methods described in §5.3.2. The range of the measured chlorophyll *a* values was 1.83 – 6.88 μgl^{-1} and the range of the measured tripton was 0.8 – 7.7 mgl^{-1}. A table showing the individual measurements is shown in Appendix F.

6.2.2. Algorithm Application

The PSO algorithm was applied to the 13th August 2009 image and the water quality parameter concentrations were retrieved. The SIOP selection criteria that were described in §6.1.3 were applied and the SIOP selection maps are shown in Figure 6-10. The best fit spectra returned by the PSO algorithm for each similarity measure are shown for the lower SIOP set in Figure 6-11 and in Figure 6-12 for the upper SIOP set. The accuracy and precision results are shown in Table 6-5 and the resultant water quality parameter comparison graphs are shown in Figure 6-13.

Table 6-5 The means of the absolute values of error between the laboratory measured concentrations and those retrieved from the 13th August 2009 image for selected matching criteria.

	Chl (μgl^{-1})		TR (mgl^{-1})	
	Av	SD	Av	SD
SID	1.52	1.11	12.5	3.37
SAM	1.68	1.26	12.0	3.23
Min Dist	2.22	1.07	5.57	2.38
SCM	1.85	1.56	5.16	2.84

The SID, SAM and SCM similarity measures were equally good at retrieving chlorophyll *a* and the SID measure performed statistically significantly better than the minimum distance criterion. In relation to tripton concentration retrieval, the minimum distance and SCM criteria are both better than the other two criteria but neither is superior to the other. On this basis it is clear that the SCM would be the preferred similarity measure but its limited ability to select the most appropriate SIOP set from only the image itself means that it should be treated with caution in complex water bodies like Burdekin Falls Dam.

Comparing the values shown in Table 6-5 to the MIM results from Table 5-5 shows that the SID, SAM and SCM chlorophyll *a* retrievals are only outperformed by the MIM when the MER_BU_RAN1 and MER_BU_RAN2 weighting schemes are used. The chlorophyll *a* retrieval using the minimum distance criterion is better than the MIM using the 3_BANDS and MER_BL_REF3 weighting schemes but not at a statistically significant level.

With regards to the tripton concentration retrieval the SID and SAM criteria are clearly the worst performers. The other approaches are not significantly different with the exception of the MIM using the MER_BL_RAN1 and MER_BU_DER6 which are superior to all others with

MER_BU_DER6 being the best performer. This conclusion should be treated with caution because of the concerns raised in Table 5-6 and discussed on p198.

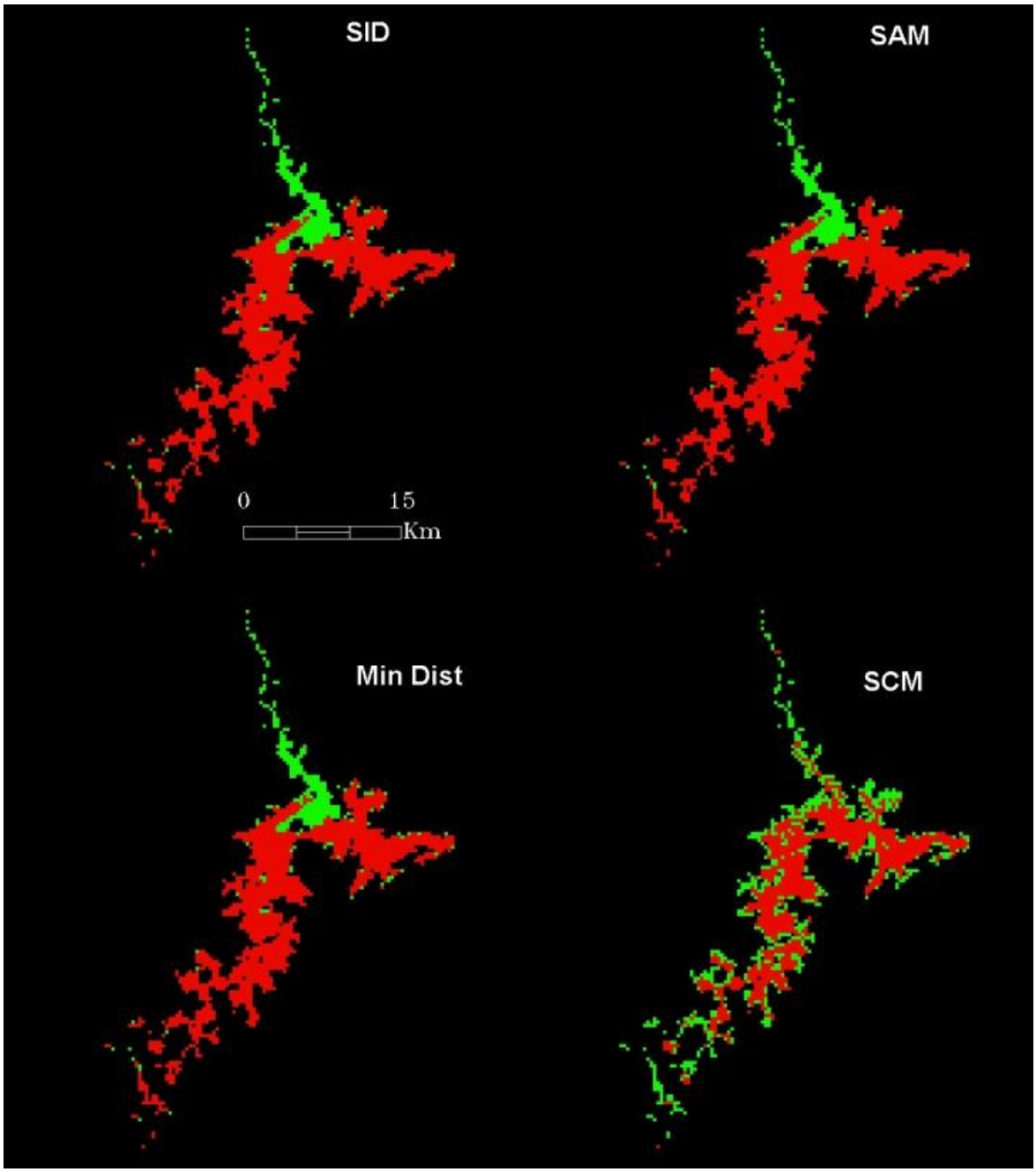

Figure 6-10 The SIOP set selected for the SID (top left), SAM (top right), minimum distance (bottom left) and SCM (bottom right) criteria. The pixels coloured green selected the upper basin SIOP set while the pixels coloured red selected the lower basin SIOP set.

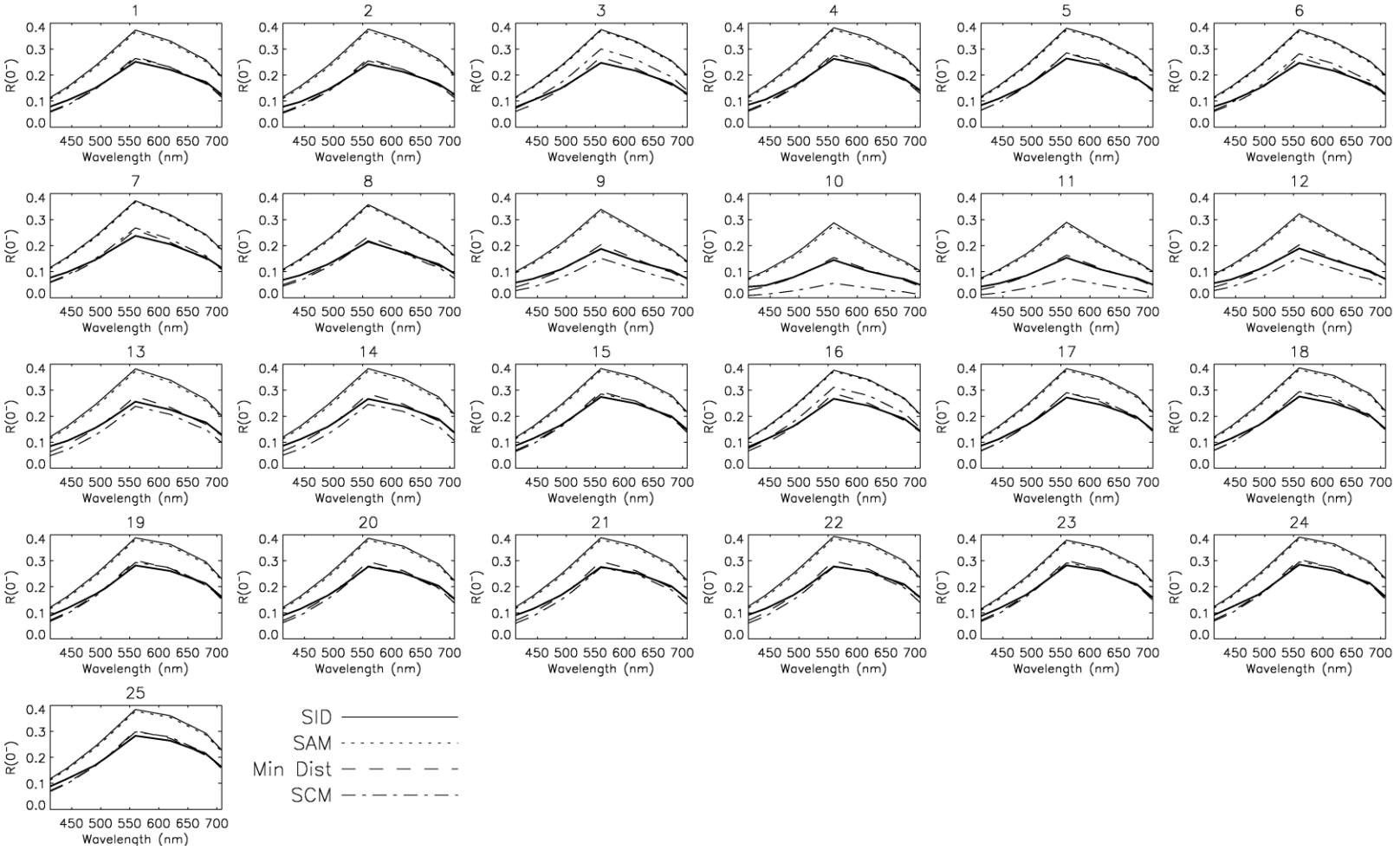

Figure 6-11 The optical closure for the13th August 2009 image spectra for the lower SIOP set. For each station the plot shows the measured spectra (bold) and the best fit spectra returned by the PSO algorithm for each similarity measure. The spectra for the SID criterion are shown with a solid line, the SAM criterion with a dotted line, the minimum distance criterion with the dashed line and the SCM criterion is shown with dash dot line.

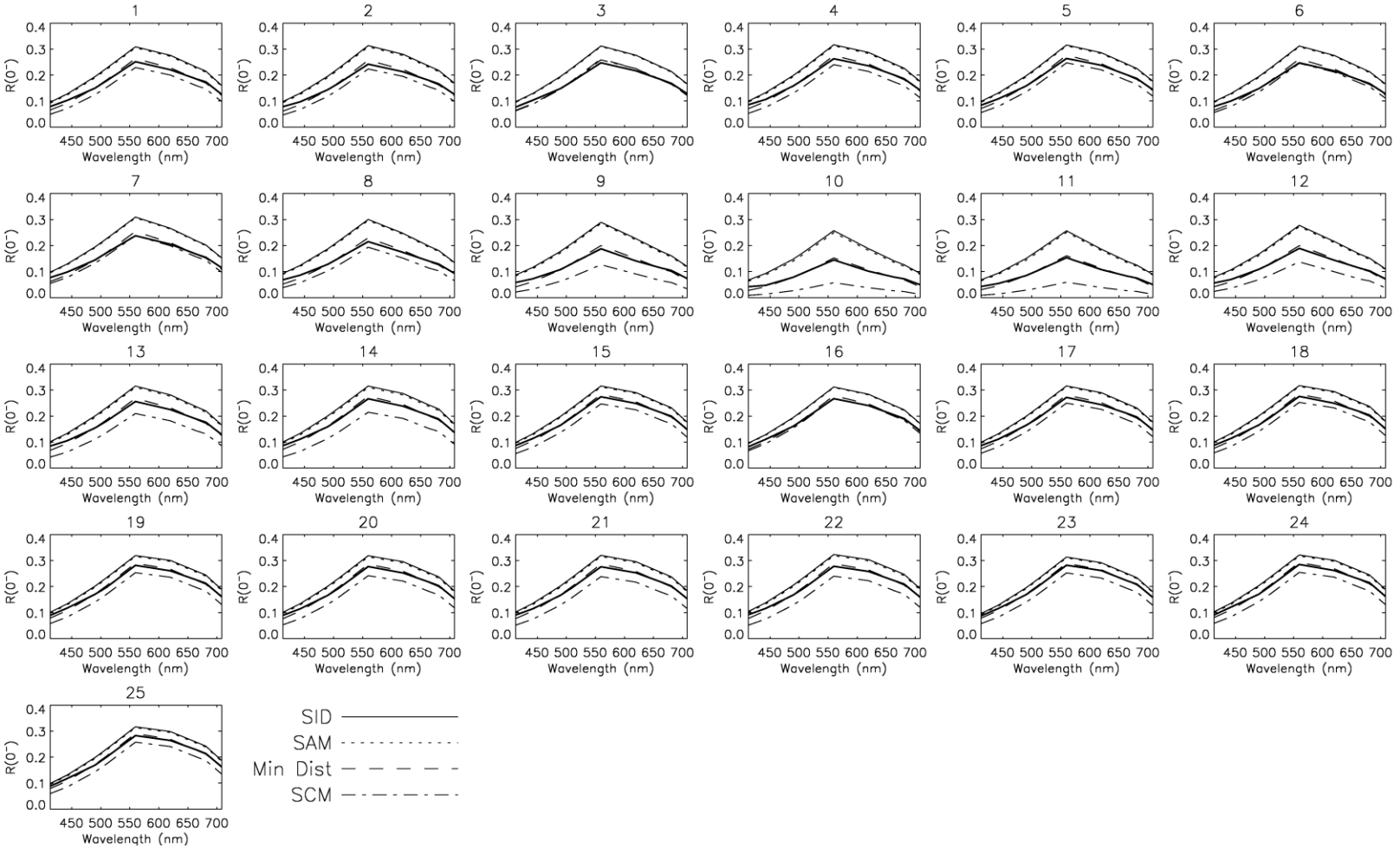

Figure 6-12 The optical closure for the13th August 2009 image spectra for the upper SIOP set. For each station the plot shows the measured spectra (bold) and the best fit spectra returned by the PSO algorithm for each similarity measure. The spectra for the SID criterion are shown with a solid line, the SAM criterion with a dotted line, the minimum distance criterion with the dashed line and the SCM criterion is shown with dash dot line.

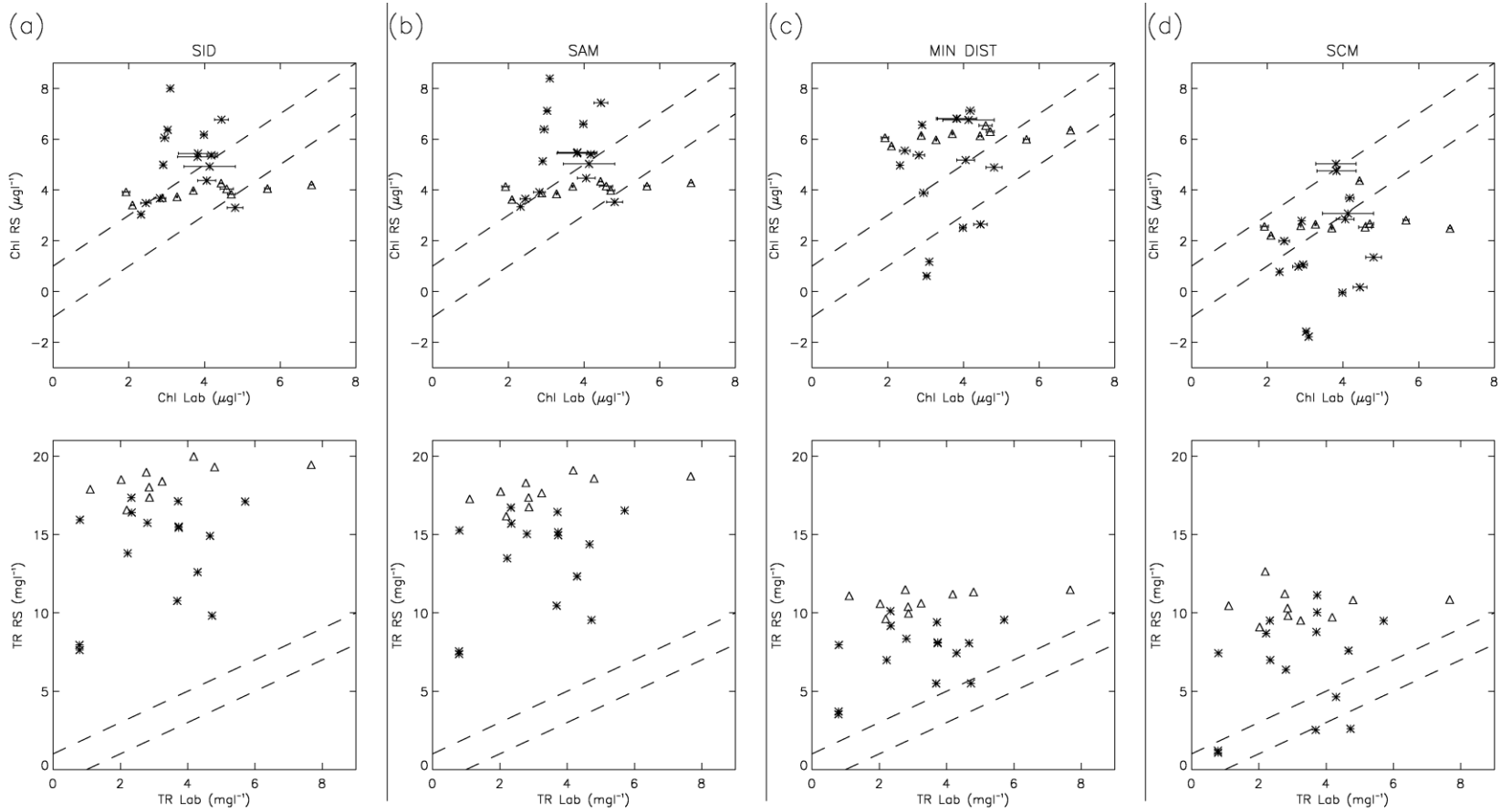

Figure 6-13 The laboratory concentrations vs. image retrieved concentrations for the13th August 2009 image for a) SID, b) SAM, c) Minimum Distance and d) SCM. Each column shows the comparison for chlorophyll *a* (top) and tripton (bottom). The diamond symbols show the stations that are geographically in the lower basin. The dotted lines show the bounds of 1μgl^{-1} for chlorophyll *a* and 1mgl^{-1} of tripton.

6.3 Ambiguity of the Water Spectrum

The PSO determines the water quality parameter values by searching the solution space and returning those values that give the best 'match' between the forward modelled spectrum and the measured pixel spectrum. In this chapter four different similarity measures were used to define the best 'match' for the measured and modelled spectra. The four similarity measures mathematically gave preference to different aspects of similarity, like magnitude or shape. The solution to the inversion problem for inland water remote sensing is ambiguous because multiple combinations of water quality parameter concentrations can lead to the same or very similar reflectance spectra (Defoin-Platel & Chami 2007). The ability to deal with this ambiguity may be related to the aspect of similarity to which the matching criterion gives preference. To investigate the variation in reflectance with the water quality parameter value, each of the simulated spectra were compared to the other 1088 simulated spectra in the set using the four similarity measures. To reduce the dimensionality of the comparison, the mean difference between each of the other spectra was calculated, and then the mean and standard deviation over all CDOM values for each pair of chlorophyll *a* and tripton was calculated. The similarity was considered low if a spectrum was appreciably different from the other spectra. That meant it had a high mean difference, and if a change in CDOM had a large effect on the spectrum then the standard deviation was large as well. Conversely, water quality parameter combinations that produced reflectance spectra that exhibited a high level of similarity were considered to be ambiguous. This was because small errors in these measured reflectance spectra may lead to large errors in the water quality parameter values retrieved by any inversion. The results for the spectra simulated with the Burdekin Falls Dam lower basin SIOP set are plotted in Figure 6-14 where the colour indicates the relative similarity (red – high similarity, purple – low similarity) and the standard deviation is shown by over-plotted contours.

All the similarity measures showed low similarity and hence high separability, at low chlorophyll *a* and tripton concentrations. Change in the similarity varied more strongly with variation in tripton concentration than chlorophyll *a* concentration. The SID criterion showed consistent trend of increased similarity with the increased concentration of tripton until the

tripton value reached approximately 5 mgl^{-1} then it reached a constant value. This would imply that the SID criterion should perform better in waters that are not dominated by tripton.

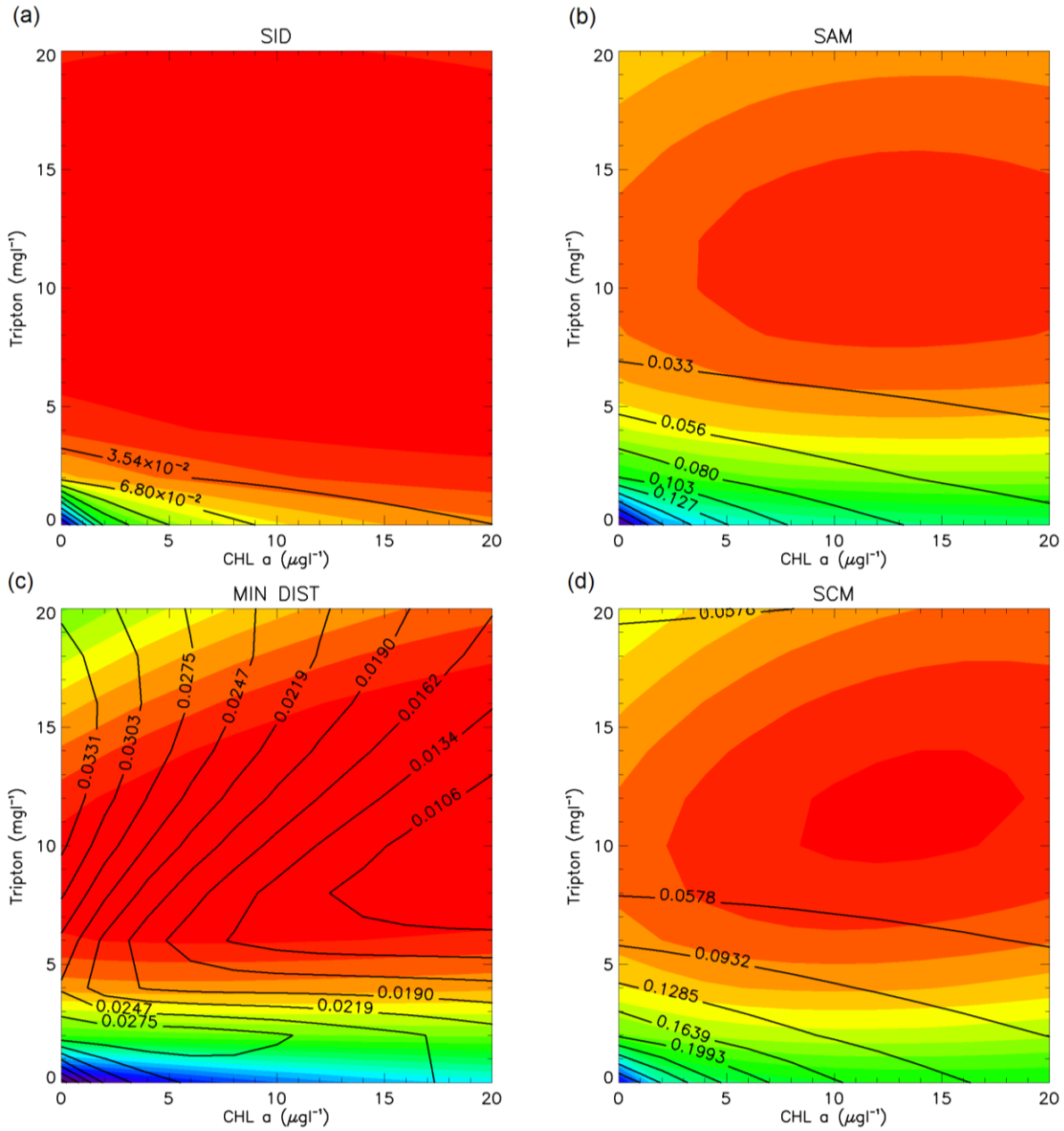

Figure 6-14 The similarity of the simulated spectra for the lower SIOP set at a solar angle of 37°. The colour indicates the relative similarity (red – high similarity, purple – low similarity) and the standard deviation is shown by over-plotted contours.

The other similarity measures showed a more complex interaction between the similarity and the water quality parameter concentrations. In each case the similarity exhibited a minimum at high

chlorophyll *a* concentration and a tripton concentration of approximately 10 mgl^{-1} before increasing again with increased tripton concentration. The diagram suggested that for the Burdekin Falls Dam lower basin SIOP set the level of ambiguity, and hence the water quality parameter retrieval accuracy, was most dependent on the concentration of tripton.

6.4 Conclusions

In the simulations described in §4.6.2 the minimum distance criterion was shown to be the most resistant to the introduction of environmental noise, particularly in the case of tripton and CDOM retrieval. It was found to perform poorly when noise associated with the atmospheric correction or SIOP measurement was introduced. Given that the validation showed that the SID and SAM similarity measures are incapable of retrieving tripton and CDOM concentrations accurately, it would appear that the environmental noise dominates the atmospheric and SIOP noise in both validation data sets.

The SCM criterion showed a limited ability to select the most appropriate SIOP set from only the image itself. The misclose sum ratio method used in the MIM approach was effective, albeit with different thresholds, for the other similarity measures but failed with the SCM. The simpler minimum misclose sum method was able to discern the most appropriate SIOP set better than using the ratio but not as satisfactorily as with the other three similarity measures. On the basis of the mean retrieval error for tripton it is clear that the SCM would be the preferred similarity measure but its limited ability to select the most appropriate SIOP set from only the image itself means that it should be treated with caution in complex water bodies like Burdekin Falls Dam.

If the two validation sets are pooled the SID similarity measure had a mean error of chlorophyll *a* retrieval of 2.0 μgl^{-1}, the SAM criterion 2.3 μgl^{-1} and the minimum distance and SCM criteria both had a mean error of 2.7 μgl^{-1}. As with the MIM, a number of caveats should be attached to these results. Firstly, the range of water quality parameter concentrations measured in the two field campaigns was limited, secondly, there is no way to evaluate the accuracy of the atmospheric correction on any particular image without some additional *in situ* data and lastly, it is not possible to be definitive about the accuracy when there is notable uncertainty in the ground truth values.

The assessment of the average error for tripton retrieval is covered by the same caveats as those mentioned for the chlorophyll *a* retrieval: that is, a limited range and uncertainty in the ground truth data. In light of these uncertainties in the ground truth for the August 2009 field trip, only the results for the October 2008 image is discussed and their usefulness is limited by the sample size of ten. The best performed SCM criterion had a mean error of 2.5 mgl^{-1} and the minimum distance criterion had 3.4 mgl^{-1}. The SID and SAM criteria were incapable of retrieving a credible tripton concentration.

As with tripton, the assessment of the CDOM retrieval accuracy suffers from a small sample size but it was found that the best performed minimum distance similarity measure had a mean error of 0.30 m^{-1} and the SCM criterion had a mean error of 0.33 m^{-1}. Both these measures were superior to the SID and SAM measures with mean errors of 1.31m^{-1} and 1.28m^{-1} respectively.

One of the useful aspects of the PSO is the ability to include more complex reflectance models or matching criteria simply, but comparing the above values to those quoted in §5.5 shows that the PSO, as implemented in this research, is superior to the traditional MIM three band inversion approach for only chlorophyll *a* retrieval and is inferior to other weighting schemes. This chapter has found that the PSO, as implemented with this reflectance model and similarity measures, does not offer improvements in accuracy and precision sufficient enough to justify the increased computational overhead of the inversion. This is not to say that the application of the method to a more accurate and complex reflectance model or a non-linear SIOP to IOP relationship or another similarity measure could not change the balance between the two considerations.

7. Conclusions and Future Research

This research was designed to answer the research problem that was stated in §1.3, that is:

> *The parameterisations developed for the remote sensing of inland waters in temperate northern hemisphere environments must be adapted or improved before they can be applied to tropical and sub-tropical water bodies.*

The problem was addressed by breaking the work into four objectives. In the section below each objective is restated and the key findings and limitations of each objective are discussed.

7.1 Key Findings and Limitations

7.1.1. Objective 1 Atmospheric Correction

Adapt existing atmospheric correction techniques to create an image based correction approach that allows images of inland water bodies to be corrected in the absence of in situ *data.*

Any atmospheric correction procedure must rely on *a priori* knowledge of either the atmospheric properties or the water leaving radiance. For a single 'snapshot' of an environment it would be feasible to collect and use *in situ* measurements taken at the time of the satellite overpass to correct the image. This approach is not feasible if the intention is to use remote sensing for ongoing monitoring or historical change studies. In those circumstances it is necessary to use an image based technique that identifies areas of the image that have known reflectance properties. The work described in Chapter 3 showed that atmospheric correction methods for Northern Australian inland waters cannot rely on site independent *a priori* knowledge of the water leaving radiance that has been developed from other environments.

This thesis showed that MERIS images of inland water bodies in selected Australian environments were successfully and accurately corrected by taking advantage of dense dark vegetation surrounding the impoundment. The atmosphere was modelled using 6S radiative transfer code and its standard atmospheric and aerosol models. It was assumed that the appropriate atmosphere and aerosol model could be chosen based on the prevailing

meteorological conditions at the site. The radiative transfer model makes assumptions about the vertical distribution of water vapour and aerosols that may or may not be an accurate reflection of the site specific vertical profiles. Likewise, the assumption is made that the air mass over the water body is the same as the air mass over the DDV pixels. The air mass has been assumed to be of constant thickness with a base that is co-incident with the level of the water surface. This assumes that the variation in topography of the DDV pixels is not significant in relation to the other assumptions. The area surrounding each of the study sites was gently undulating so this assumption appears reasonable. The expected DDV reflectance spectra vary with biome, vegetation type and its physical state. The MERIS global mean for equatorial Asia was used. There is a direct relationship between the accuracy of the DDV model and the accuracy of the atmospheric correction. A DDV model specific to Queensland tropical savannah vegetation would be required to increase the accuracy of the atmospheric correction. The rudimentary test reported in §5.3.4 does give cause for some optimism as the retrieval was found to be reasonably robust in the presence of error in the AOT estimation.

7.1.2. Objective 2 SIOP Measurement

Measure and model the specific inherent optical properties in a selection of Northern Australian water bodies.

Three large Northern Australian water bodies were selected and the SIOPs of their optical water quality parameters were sampled and parameterised. It was found that there was sufficient intra-impoundment variation in the specific absorption and specific scattering of phytoplankton and tripton to require a well distributed network of measurement stations. The specific absorption of CDOM showed limited variation within and between the sampled water bodies. The limited measurement range may allow the CDOM absorption measurement to be omitted in site investigations in the future. Kirk (1994) who measure CDOM absorption in other Australian waters found a somewhat larger range so for the time being continued measurement of the CDOM absorption is recommended.

The thesis found that some inland water bodies, such as Burdekin Falls Dam, may need more than one SIOP set to characterise the optical domains present. Even though the IDL hierarchical

clustering algorithm was used as a guide, the allocation of continuously varying parameters into representative bins is a task that is best left to professional judgement. Much like fitting a curve to a scatter plot, there are risks associated with under-fitting (too few SIOP sets) or over-fitting (too many SIOP sets). This judgement will need to take into account the purposes of the monitoring and measurement to achieve the correct complexity versus accuracy balance.

The measured backscattering ratio deviated from the conventional Petzold (1972) San Diego Harbour ratio with Burdekin Falls Dam being substantially higher and Wivenhoe Dam being marginally lower. The size of the variation measured shows that there are substantial risks associated with obtaining the backscattering spectra directly from the scattering spectra measured with an instrument like an *ac-9*. This problem is lessened, but not totally avoided by using the *Hydroscat-6* instrument, as it uses an assumed VSF to calculate the total backscattering from the scattering at a single angle (Maffione & Dana 1997). There now exist instruments that can routinely measure the VSF *in situ* (Dana & Maffione 2002) that could be used in further work to clarify the backscattering behaviour of tripton and phytoplankton in Australian waters.

Compared to a solution of the same pigments, pigmented cells tend to absorb radiation less efficiently. The chlorophyll *a* specific absorption of phytoplankton spectrum is lowered and flattened with respect to the spectrum of a solution with the same concentration (Kirk 1994; Morel & Bricaud 1981; Prieur & Sathyendranath 1981). In general terms, a spectrum is lowered if the intra-cellular pigment concentration is increased for a constant cell size or the cell size increases with a constant total pigment and total biomass, but it is raised if the biomass increases for a constant total pigment for the system (Kirk 1975). This is referred to as either the package or packet effect. No allowance was made for the package effect in calculating the chlorophyll *a* specific absorption of phytoplankton. Other systematic errors that might exist in the SIOP measurements were discussed at length on p167 ff.

7.1.3. Objective 3 Algorithm Development and Assessment

Parameterise and modify existing algorithms to retrieve water quality parameter concentrations and map water quality parameters from optically deep inland waters so they can be applied to Northern Australian water bodies and available data.

Hydrolight® simulations were used to investigate whether improvements could be made in the MIM approach to retrieving water quality parameters. The thesis showed that the anisotropy factor (*f*) is not only dependent on the illumination conditions but is affected by the scattering and absorption of the water and the water quality parameters. It showed how sensitive the inversion was to the selected value of the anisotropy factor. The anisotropy factor was allowed to vary with respect to wavelength, IOP set and sun position. It has been shown in other work that *f* also varies with respect to the view zenith angle (Morel & Gentili 1993). No allowance was made for this effect as calculations based on Lee et al. (2004) showed that for a view zenith angle of 20°, the effect was of lower magnitude than the effect of the sun zenith angle.

The MIM in this thesis used a linear model of reflectance to allow for a direct inversion. If an iterative approach is taken then it is possible to extend weighted least squares to cover non-linear problems where it has been shown that the residuals are smaller for the non-linear model than for a comparable linear model (Vos et al. 2003). Work (unreported in this thesis) was performed to see if moving to a non-linear model would improve the accuracy and precision of the inversion. The advantages reported by Vos et al. could not be replicated and so the work was abandoned.

Chapter 4 showed how the concentrations of the other colour producing agents in the water affect the retrieval accuracy of a particular water quality parameter concentration. It was not possible to take this investigation further to show how the accuracy of the inversion of one water quality parameter is correlated to the concentrations of the other water quality parameters.

The *Hydrolight*® simulations were used to show that empirical modelling of the anisotropy factor combined with the over-determined systems of equations improved the water quality parameter retrieval in the presence of image noise, atmospheric correction uncertainty and SIOP measurement errors. The simulations showed that the accuracy and precision of the exact

solution is more susceptible to the $NE\Delta R(0^{-})_E$. The noise effect may be reduced if the assumption that the noise in each band is independent is not valid. With the exception of the three band approach and a few other exceptions there was little difference between the performances of the weighting schemes. No single supposition about the relationship between the band weights and modelled reflectance spectrum was found to be superior.

With regards to the PSO, the minimum distance criterion was shown to be the most resistant to the introduction of environmental noise in general, and the $NE\Delta R(0^{-})_E$ in particular, but to perform poorly when noise associated with the atmospheric correction or SIOP measurement was introduced. The simulations found that there was no discernable difference between performance of the SID and SAM measures which both have equal or sometimes superior performance to the SCM measure. This finding was not supported by the validation study, perhaps because the environmental noise dominated the atmospheric and SIOP noise in both validation data sets.

Simulations were used to negate the unquantifiable errors associated with spatial and temporal patterns in the dynamic nature of the aquatic environment, which make it difficult to establish the retrieval accuracy for the water quality constituent concentrations. Therefore, the necessary caveat to attach to this result is that the calculated values will not necessarily translate directly to real world problems.

7.1.4. Objective 4 Algorithm Validation

Apply and validate the algorithms Northern Australian water bodies and determine the monitoring accuracy and precision that could be expected for each water quality parameter concentration in each scenario.

Chapters 5 and 6 showed that optical closure can be used to identify the most appropriate SIOP set in water bodies that have multiple SIOP domains. The size of the optical closure was consistent with other published works, but the contributing factors discussed on pp163 ff meant that the differences in closure due to the application of different SIOP sets were masked. The threshold value for the ratio of the lower basin SIOP set to the upper basin SIOP set misclose

sums that was used and was effective but remains unsatisfactory for two reasons. The first is the practical reason that it would not be able to be extended to a situation with more than two SIOP sets and the second, perhaps more philosophical reason, is that no physical explanation for why it should be so could be deduced.

The validation chapters confirmed the finding of the simulations that the over-determined weighted MIM algorithm was more accurate and precise than the conventional three band or unweighted approach. Like in Chapter 4 it was found that there is no weighting scheme that is optimal for all water quality parameters. Rather, it would be sensible to apply three weighting schemes to produce the three normal water quality parameter maps.

The PSO, as implemented in this research, does not offer improvements in accuracy and precision sufficient enough to justify the increased computational overhead in the inversion. This is not to say that the application of the method to a more accurate and complex reflectance model or a non-linear SIOP to IOP relationship or another similarity measure could not change the balance between the two considerations.

7.1.5. Summary

The initial hypothesis that remote sensing techniques for inland waters need to be adapted to a regional coverage rather than a global coverage was borne out by the results of the four previously stated objectives. The proven necessity of using regional approaches to water quality monitoring on inland waters invites consideration of the other choices that were made as part of this thesis.

Each remote sensing application is confronted with the seven interrelated choices. These choices are not binary; each one can be represented on a continuum. This work has focussed on a single approach to the remote sensing of inland water quality, one that holds promise for the monitoring of inland water quality in Australia. Figure 7-1 shows a graphical representation of where this work sits on the seven continua. The medium resolution sensor MERIS was employed as it had sufficient spectral and temporal resolution and it accommodated the project's resource limitations. The physics based semi-analytical approach was chosen as it had the advantage of

requiring less field data and allowing greater scope for multi-temporal series to be developed without repeated *in situ* measurements. That these choices were made as they were does not imply that empirical approaches cannot provide a workable solution for the remote sensing of water quality parameters in the tropical and subtropical environments.

Inversion Technique	Analytic	●	Empirical
Data Type	Image Data	●	Field Data
Spectral Resolution	Hyper-spectral	●	Multi-spectral
Spatial Resolution	High	●	Low
Temporal Resolution	High	●	Low
Coverage Size	Global	●	Site Specific
Timeline	Serial	●	Episodic

Figure 7-1 The remote sensing approach used in this project described in relation to seven remote sensing approach options.

7.2 Research Significance

Lakes and reservoirs provide sources of freshwater for urban, agricultural and industrial users as well as providing the means for recreational activities, fisheries and aquaculture. In addition, recent studies have shown that inland water bodies have a disproportionate effect on the on the global carbon cycle with water bodies that are supersaturated with carbon dioxide consequently emitting it to the atmosphere (Cole et al. 2007). Higher carbon dioxide concentrations in warm lakes have been attributed to higher rates of respiration (Kosten et al. 2010). Remote sensing is an essential tool to understand the spatial distribution of the factors involved in the ecology of aquatic systems but its application to tropical and sub-tropical inland impoundments has been limited. Figure 7-2 shows the sites of inland water remote sensing activity described in literature cited in this thesis. Of the studies located in tropical and sub-tropical zones only the work at Lake Taihu, China (Hu et al. 2010; Le et al. 2009; Ma et al. 2009; Ma et al. 2006) is part of a systematic remote sensing program. The other studies (Loiselle et al. 2009a; Loiselle et al. 2009b) are using the IOPs to study chemical processes within the lake or are of limited scope (Okullo et al. 2007). This thesis has extended the remote sensing of optical water quality parameters to tropical and sub-tropical impoundments. While it is not certain that the results of this work are immediately transferable to other water bodies in the tropical and subtropical zones, Australia is one of the few countries in this zone that have the financial resources to support scientific research of this type.

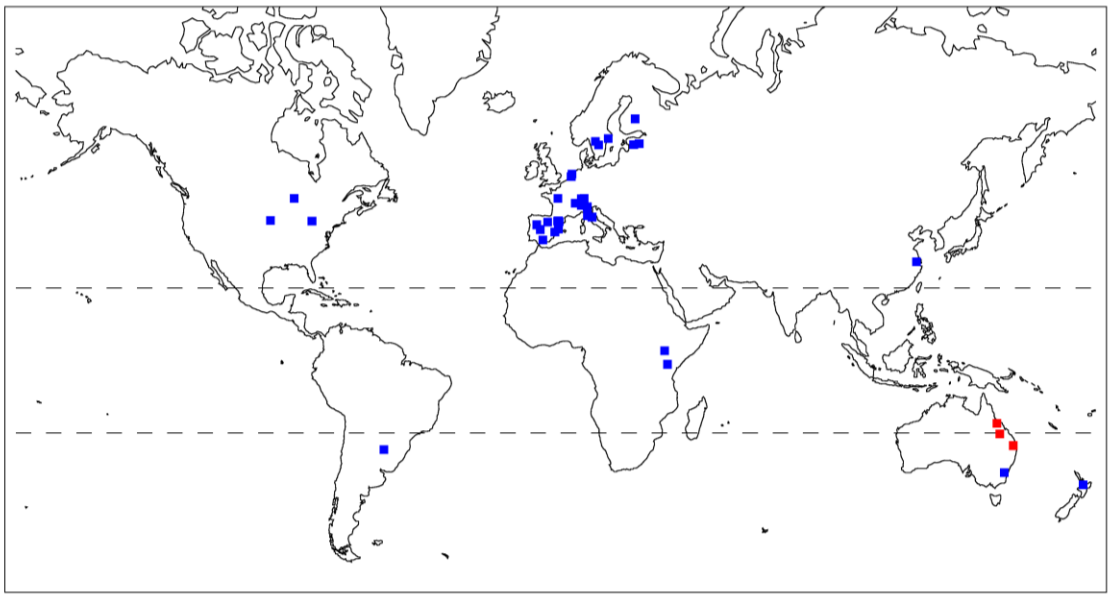

Figure 7-2 The sites of inland water remote sensing activity described in literature cited in this thesis (blue squares). The red squares show the study sites for this thesis.

The SIOP sets presented in this thesis are the first complete sets to be reported for Australian inland waters. Although John Kirk was a pioneer in the field of hydrological optics, investigation into the optical properties of Australian inland waters has been in a protracted hiatus for approximately twenty years while the focus has shifted to case-II coastal waters (Brando & Dekker 2003; Brando et al. 2008; Dekker et al. 2005; Dekker et al. 2004; Oubelkheir et al. 2006; Wettle & Brando 2006). Early work by Jupp, Kirk and Oliver (Jupp et al. 1994; Kirk 1976, 1986; Kirk & Oliver 1995; Oliver 1990) included only incomplete SIOP measurements.

The thesis has established the validity, or otherwise, of the implicit assumptions and approximations usually used in inland water remote sensing with respect to the new environment. It showed that the assumptions relating to the tripton SIOPs that are used in the MERIS standard product and the BEAM Case-2 Regional Processor (Eutrophic Lakes) are not valid in the case of Burdekin Falls and Fairbairn Dams and so the correction methods cannot be used. It showed that it is necessary to consider the sensor calibration when selecting a sun model to perform the radiance to reflectance calculation if some of the anomalies found in other published works (Bagheri et al. 2005; Candiani et al. 2007a; Sterckx & Debruyn 2004) are to be avoided. The simulations showed that there are risks associated with previous approaches like

assuming of a constant anisotropy factor (f) (Hakvoort et al. 2002; Hoogenboom et al. 1998b; Keller 2001a) or relating f to only the sun vertical angle (Hoogenboom et al. 1998a; Kutser et al. 2001; Pasterkamp et al. 1999). The fact that the anisotropy factor is related to the SIOP values of the water quality parameters has been noted before by Vos et al. (2003) but they did not integrate it into their approach as they ascertained that it had a minor effect for the dark water they were dealing with. The water in the Australian water bodies studied here is not dark enough to avoid dealing with the f SIOP dependence.

The work in this thesis has applied mathematical techniques from other fields to the inversion of the water leaving reflectance spectrum. With the increase in the number of bands in more recent instruments there have been moves from using exact (same number of bands as unknowns) systems (Brando & Dekker 2003; Giardino et al. 2007; Hoge & Lyon 1996; Hoge et al. 1999; Hoogenboom et al. 1998b; Lyon & Hoge 2006) to over-determined (more bands than unknowns) systems (Boss & Roesler 2006; Hakvoort et al. 2002; Vos et al. 2003). Aside from a passing reference by Hakvoort et al. (2002), weighted least-squares method has not been applied in the past. This technique has been long used for the adjustment of survey control networks used for mapping and construction purposes where it has been shown to be an efficient method in dealing with systems that have a high degree of redundancy. The increased number of bands in remote sensors has increased the amount of redundancy in the inland water inversion problem and weighting the bands has been shown to be an effective way of utilising the new information. Because the error sources are far more easily quantified and modelled in the case of survey networks, it is possible to both predict the inherent accuracy of the system as well as evaluate its accuracy after the measurements have been made. It is unfortunate that the errors associated with the remote sensing system will not be able to be quantified in the same way and so allow *a posteriori* accuracy estimates of the retrieved water quality parameters.

The Particle Swarm Optimisation is a stochastic optimisation technique that was first applied to ocean colour by Slade et al. (2004) working on a simulated data set. Apart from the published advantages over traditional methods for finding global minima when the search space is non-convex, discontinuous, multimodal, or is not easily differentiable, it allows inversion to utilise matching criteria that eliminate the magnitude of the reflectance spectra from the calculation and

focus on its shape. This thesis describes the first practical implementation of the PSO to the problem of water quality remote sensing. The much larger calculation overhead that is associated with stochastic search techniques should not be a significant impediment to their use for inland waters because of the reduced size of the monitoring targets when compared to coastal or open ocean waters. It would be a mistake to entirely abandon the consideration of stochastic approaches to optimisations on the basis of the results of this thesis. The great advantage these methods have is that they can be more easily adapted to more complicated water reflectance models.

Lastly, the work in this thesis has begun the process of demonstrating the possibilities of remote sensing to water resource managers. There are approximately 500 artificial water bodies in Australia classified as large dams, that is, with a height of greater that 15 m (ANCOLD 2010). The owners of each of these water bodies have responsibilities to maintain and report upon the quality of water in the storage. This work has chosen to use a sensor of medium resolution because of resource limitations and hence has focussed on three of the larger dams. It has however, had to deal with matters that need to be addressed no matter what observing platform or sensor is used. Some of the questions that still need to be resolved to allow these methods to move from demonstration to adoption is discussed in the next section but the results of the thesis show that the technical restrictions are not insurmountable.

7.3 Future Research Directions

Opportunity for future research falls into two broad categories: that work which will facilitate a closer understanding of the science involved and that work which will allow the potential of remote sensing of inland water to be realised through its adoption by water resource managers.

7.3.1. Fundamental Work

The method described in this thesis provides a convenient simplification to allow for the complexity of the photon direction distribution in natural waters, rather than shedding any light onto the physics of the problem. The method described in the thesis lacks elegance. This is not just a philosophical objection: the fact that the anisotropy factor is related to the SIOP values of

the water quality parameters means that a very large computational overhead is imposed every time a new environment is targeted. A more analytical relationship between the SIOP values and the anisotropy factor would reduce this overhead. A comparison of the empirical *f* approximations made for the three complete SIOP sets used in this thesis showed that the backscattering appeared to have the greatest effect.

The inversion problem for inland water remote sensing is ill-posed. The solution is ambiguous because multiple combinations of water quality parameter concentrations can lead to the same or very similar reflectance spectra. When random measurement noise is superimposed on this already ill-posed problem then the retrieval uncertainties are exacerbated. It would be of benefit to be able to predict the areas of greatest uncertainty directly from the SIOP measurements and use the result to flag those inverted pixels as being of uncertain quality.

What is still poorly understood is the range of possible SIOP values that may exist in inland waters throughout the world. The data that does exist is often only selectively published. The field and laboratory work that is required to parameterise the SIOPs is expensive and time consuming and is rarely financed by private institutions. What is lacking is a mechanism for data sharing that minimises the transaction costs associated with copyright and other trade protections. The information technology for this process exists and is being used in other contexts. For example, in the ocean colour realm, the NASA bio-Optical Marine Algorithm Data set (NOMAD), is a global, high quality *in situ* bio-optical data set that has been made publicly available for use in ocean colour algorithm development and satellite data product validation activities (Werdell & Bailey 2005). What is lacking in the inland water realm is the institutional incentive to create such a data repository.

7.3.2. From Science to Engineering

One of the most immediate concerns for water quality managers is the ability to monitor for harmful algal blooms. In the Australian context, it has been asserted that a practical remote sensing system must be able to measure accurately to below 10 $\mu g l^{-1}$ in turbid waters to be useful in pre-bloom conditions (Jupp et al. 1994). This thesis has demonstrated that this goal can be

achieved for one Northern Australian reservoir. The impediments to moving beyond the experimental science stage to the end user product stage are both technical and institutional.

From a technical point of view the methods described in this thesis require too much specialist knowledge to be implemented by an environmental engineer or technician. Research that focuses on developing 'black box' solutions, like the BEAM software add-ons, should be encouraged. For example, this thesis has shown that the existing water leaving radiance image correction methods are not appropriate in the Australian environment, but this is not to say that similar techniques cannot be re-parameterised to take into account the differences in the SIOPs of the target water bodies. The BEAM Case-2 Regional Processor (Eutrophic Lakes) required a large parameterisation overhead before it was ready to be applied to images. A full understanding of the SIOP variability of an environment is necessary before the minimum number of necessary add-ons can be devised.

What is missing from the final water quality parameter maps created for this thesis is some form of simultaneous confidence map. As discussed earlier, it is unfortunate that remote sensing system errors will not be able to be quantified in the same way as survey networks, but preliminary work, not reported in this thesis, shows that there may be a usable link between the misclose sum of an inversion and the error in the tripton and CDOM estimation. There is potential to at least assess the relative accuracy of a retrieval with respect to other pixels in the same image and give the user confidence in the result. This potential should be pursued.

Information can be evaluated by its usefulness as well as its accuracy (Andrus 1976). If its form closely matches the user's requirements its value increases. Information has greater value to the decision maker if it is available when needed. Information that can be obtained without time lags will be preferred to that which will take time to collect (Ference 1975). Lastly, information has greater value if it can be accessed or delivered easily. Information can be said to have form, time and place utility. Providing it is supported with sufficient documentation on how it was achieved, using high temporal resolution sensors like MERIS, remotely sensed water quality information has some advantages over traditional point source *in situ* measurements in terms of time and place utility. However, more work needs to be done in terms of form utility. In Queensland algal

alert levels are linked to cell counts rather than chlorophyll *a* levels (Orr & Schneider 2006). The link between chlorophyll *a* concentration and cell counts is too tenuous to make for scientific purposes but it may still be useful for management purposes. Delivering maps that report broad action levels rather than defined chlorophyll *a* concentrations should be explored. If anything, research that considers the psychological dimensions of information in the context of inland water remote sensing may provide the most useful short term gains.

References

Aas, E, Høkedal, J & Sørensen, K 2005, 'Spectral backscattering coefficient in coastal waters', *International Journal of Remote Sensing*, vol. 26, no. 2, pp. 331 - 43.

Acharya, PK, Berk, A, Anderson, GP, Larsen, NF, Tsay, SC & Stamnes, KH 1999, 'MODTRAN4: Multiple scattering and bi-directional reflectance distribution function (BRDF) upgrades to MODTRAN', in AM Larar (ed.), *Proc. of SPIE, Optical Spectroscopy Techniques and Instrumentation for Atmospheric and Space Research III*, vol. 3756, pp. 354-62.

Ahn, YH, Bricaud, A & Morel, A 1992, 'Light backscattering efficiency and related properties of some phytoplankters', *Deep-Sea Research*, vol. 39, pp. 1835-55.

Albert, A & Mobley, CD 2003, 'An analytical model for subsurface irradiance and remote sensing reflectance in deep and shallow case-2 waters', *Optics Express*, vol. 11, no. 22, pp. 2873-90.

ANCOLD 2010, *Register of large dams in Australia*, viewed 7 July 2010, <http://www.ancold.org.au/images/files/ICOLD_Dam_Register_02.xls>.

Andrus, RR 1976, 'Approaches to information evaluation', in GB Davis & CC Everest (eds), *Readings in Management Information Systems*, McGraw-Hill, New York, pp. 103-8.

Arar, EJ & Collins, GB 1997, *Method 445.0, In Vitro Determination of Chlorophyll a and Pheophytin a in Marine and Freshwater Algae by Fluorescence, Revision 1.2.*, National Exposure Research Laboratory, Office of Research and Development, U.S. Environmental Protection Agency, Cincinnati, OH.

Austin, RW 1974, 'The remote sensing of spectral radiance from below the ocean surface', in NG Jerlov & E Steeman Nielsen (eds), *Optical Aspects of Oceanography*, Academic Press, London and New York, pp. 316-44.

Australian State of the Environment Committee 2001, *Australia, State of the Environment 2001 Inland waters theme report*, CSIRO Publishing, Melbourne.

Bagheri, S, Peters, S & Yu, T 2005, 'Retrieval of marine water constituents from AVIRIS data in the Hudson/Raritan Estuary', *International Journal of Remote Sensing*, vol. 26, no. 18, pp. 4013 - 27.

Bainbridge, Z, Brodie, J, Lewis, S, Duncan, I, Post, D, Faithful, J & Furnas, M 2006a, *Event-based water quality monitoring in the Burdekin Dry Tropics Region: 2004/05 wet season. ACTFR Report No. 06/01 for the Burdekin Dry Tropics NRM.*, Australian Centre for Tropical Freshwater Research, James Cook University, Townsville.

Bainbridge, Z, Lewis, S, Brodie, J, Faithful, J, Maughan, M, Post, D, O'Reagain, P, Bartley, R, Ross, S, Schaffelke, B, McShane, T & Baynes, L 2006b, *Monitoring of sediments and nutrients in the Burdekin Dry Tropics Region: 2005/06 wet season. ACTFR Report No. 06/13 for the Burdekin Dry Tropics NRM.*, Australian Centre for Tropical Freshwater Research, James Cook University, Townsville.

Baruah, PJ, Tamura, M, Oki, K & Nishimura, H 2001, 'Neural network modeling of lake surface chlorophyll and suspended sediment from Landsat TM imagery', in *22nd Asian Conference of Remote Sensing*, Singapore, pp. 911-6.

Belzile, C, Vincent, WF, Howard-Williams, C, Hawes, I, James, MR, Kumagai, M & Roesler, CS 2004, 'Relationships between spectral optical properties and optically active substances in a clear oligotrophic lake', *Water Resources Research*, vol. 40, no. 12, p. W12512.

Berk, A, Anderson, GP, Bernstein, LS, Acharya, PK, Dothe, H, Matthew, MW, Adler-Golden, SM, Chetwynd, JJH, Richtsmeier, SC, Pukall, B, Allred, CL, Jeong, LS & Hoke, ML 1999, 'MODTRAN4 radiative transfer modeling for atmospheric correction', in *Optical Spectroscopic Techniques and Instrumentation for Atmospheric and Space Research III*, Denver, CO, USA, vol. 3756, pp. 348-53.

Binding, CE, Jerome, JH, Bukata, RP & Booty, WG 2008, 'Spectral absorption properties of dissolved and particulate matter in Lake Erie', *Remote Sensing of Environment*, vol. 112, no. 4, pp. 1702-11.

Blondeau-Patissier, D, Brando, VE, Oubelkheir, K, Dekker, AG, Clementson, LA & Daniel, P 2009, 'Bio-optical variability of the absorption and scattering properties of the Queensland inshore and reef waters, Australia', *Journal of Geophysical Research-Oceans*, vol. 114.

Boss, E & Roesler, CS 2006, 'Over Constrained Linear Matrix Inversion with Statistical Selection', in Z Lee (ed.), *Report of the International Ocean-Colour Coordinating Group No. 5: Remote Sensing of Inherent Optical Properties: Fundamentals, Tests of Algorithms, and Applications* International Ocean-Colour Coordinating Group, Dartmouth, Canada.

Bourg, L 2004, *MERIS Spectral Characterisation - Wavelengths and Irradiances*, 19/10/2007, Excel Spreadsheet, <http://earth.esa.int/object/doc.cfm?fobjectid=4522&linkSource=fulltext>.

Brando, VE & Dekker, AG 2003, 'Satellite hyperspectral remote sensing for estimating estuarine and coastal water quality', *IEEE Transactions on Geoscience and Remote Sensing*, vol. 41, no. 6, pp. 1378-87.

Brando, VE, Dekker, AG, Schroeder, T, Park, YJ, Clementson, LA, Steven, A & Blondeau-Patissier, D 2008, 'Satellite retrieval of chlorophyll CDOM and NAP in optically complex waters using a semi-analytical inversion based on specific inherent optical properties. A case study for

Great Barrier Reef coastal waters', paper presented to Ocean Optics XIX, Barga, Italy, 6-10 Oct., 2008.

Bricaud, A, Babin, M, Morel, A & Claustre, H 1995, 'Variability in the chlorophyll-specific absorption-coefficients of natural phytoplankton - analysis and parameterization', *Journal of Geophysical Research-Oceans*, vol. 100, no. C7, pp. 13321-32.

Buiteveld, H 1995, 'A model for calculation of diffuse light attenuation (PAR) and Secchi depth', *Aquatic Ecology*, vol. 29, no. 1, pp. 55-65.

Buiteveld, H, Hakvoort, JHM & Donze, M 1994, 'Optical properties of pure water', in JS Jaffe (ed.), *Proceedings of SPIE Ocean Optics XII*, SPIE, vol. 2258, pp. 174-83.

Bukata, RP 2005, *Satellite monitoring of inland and coastal water quality : retrospection, introspection, future direction*, Taylor&Francis, Boca Raton.

Bukata, RP, Jerome, JH, Borstad, GA, Brown, LN & Gower, JFR 2004, 'Mitigating the impact of trans-spectral processes on multivariate retrieval of water quality parameters from case 2 waters', *Canadian Journal of Remote Sensing*, vol. 30, no. 1, pp. 8-16.

Burford, MA & O'Donohue, MJ 2006, 'A comparison of phytoplankton community assemblages in artificially and naturally mixed subtropical water reservoirs', *Freshwater Biology*, vol. 51, no. 5, pp. 973-82.

Campbell, G & Phinn, SR 2008, 'The efficacy of band weighting schemes for improving the accuracy and precision of water quality parameters estimated from MERIS and MODIS image data', in *14th Australasian Remote Sensing & Photogrammetry Conference*, Darwin, Australia, p. p12.

Candiani, G, Giardino, C & Brando, VE 2007a, 'Adjacency Effects and Bio-Optical Model Regionalisation: MERIS Data to Assess Lake Water Quality in the Subalpine Ecoregion ', in H Lacoste & L Ouwehand (eds), *Envisat Symposium 2007*, Montreux, Switzerland.

Candiani, G, Giardino, C, Brando, VE, Bartoli, M & Reverberi, F 2007b, 'MERIS timeseries data to detect water quality in Subalpine lakes', paper presented to 3rd Workshop Remote Sensing of the Coastal Zone, Bolzano, Italy, 7-9 June 2007.

Carder, KL, Steward, RG, Harvey, GR & Ortner, PB 1989, 'Marine humic and fulvic-acids - their effects on remote-sensing of ocean chlorophyll', *Limnology and Oceanography*, vol. 34, no. 1, pp. 68-81.

Carvalho, OA & Menezes, PR 2000, 'Spectral Correlation Mapper (SCM): an improvement on the Spectral Angle Mapper', in *Ninth JPL Airborne Earth Science Workshop*, Jet Propulsion Laboratory, Pasadena, California, pp. 65-74.

CEOS 2008, *CEOS recommended solar irradiance spectrum for use in Earth Observation applications*, viewed 3 September 2008, <http://eocalibration.wordpress.com/2006/12/15/ceos-recommended-solar-irradiance-spectrum-for-use-in-earth-observation-applications>.

Chavez, FP, Buck, KR, Bidigare, RR, Karl, DM, Hebel, D, Latasa, M & Campbell, L 1995, 'On the chlorophyll *a* retention properties of glass-fiber GF/F filters', *Limnology and Oceanography*, vol. 40, no. 2, pp. 428-33.

Chorus, I, Falconer, IR, Salas, HJ & Bartram, J 2003, 'Health risks caused by freshwater cyanobacteria in recreational waters', *Journal of Toxicology and Environmental Health Part B: Critical Reviews*, vol. 3, no. 4, pp. 323 - 47.

Clementson, LA, Parslow, JS, Turnbull, AR, McKenzie, DC & Rathbone, CE 2001, 'Optical properties of waters in the Australasian sector of the Southern Ocean', *Journal of Geophysical Research-Oceans*, vol. 106, no. C12, pp. 31611-25.

Clerc, M & Kennedy, J 2002, 'The particle swarm - explosion, stability, and convergence in a multidimensional complex space', *IEEE Transactions on Evolutionary Computation*, vol. 6, no. 1, pp. 58-73.

Cole, JJ, Prairie, YT, Caraco, NF, McDowell, WH, Tranvik, LJ, Striegl, RG, Duarte, CM, Kortelainen, P, Downing, JA, Middelburg, JJ & Melack, J 2007, 'Plumbing the global carbon cycle: Integrating inland waters into the terrestrial carbon budget', *Ecosystems*, vol. 10, no. 1, pp. 171-84.

Commonwealth Bureau of Meteorology 2009, *Climate statistics for Australian locations*, viewed 9th October 2009, <http://www.bom.gov.au/climate/averages/tables/cw_040189.shtml>.

Curran, PJ & Steele, CM 2005, 'MERIS: the re-branding of an ocean sensor', *International Journal of Remote Sensing*, vol. 26, no. 9, pp. 1781 - 98.

Dall'Olmo, G & Gitelson, AA 2005, 'Effect of bio-optical parameter variability on the remote estimation of chlorophyll-a concentration in turbid productive waters: experimental results', *Applied Optics*, vol. 44, no. 3, pp. 412-22.

Dana, DR & Maffione, RA 2002, 'Determining the backward scattering coefficient with fixed-angle backscattering sensors—revisited', in *Ocean Optics XVI*, Santa Fe, NM., p. 9.

Davies-Colley, RJ, Pridmore, RD & Hewitt, JE 1986, 'Optical properties of some freshwater phytoplanktonic algae', *Hydrobiologia*, vol. 133, pp. 165-78.

Davies-Colley, RJ & Vant, WN 1987, 'Absorption of light by yellow substance in freshwater lakes', *Limnology and Oceanography*, vol. 32, no. 2, pp. 416-25.

de Haan, JF & Kokke, JMM 1996, *Remote Sensing Algorithm Development TOOLKIT I: Operationalisation of Tools for Atmospheric Correction of Remote Sensing Data of Coastal and Inland Waters*, 96-16, Beleidscommissie Remote Sensing.

de Haan, JF, Kokke, JMM, Dekker, AG & Rijkeboer, M 1999, *Remote sensing algorithm development, TOOLKIT for water quality continued. Operationalisation of tools for the analysis and processing of remote sensing data of coastal and inland waters. National Remote Sensing Program (NRSP) report-98-12*, Beleids Comissie Remote Sensing (Dutch Remote Sensing Board).

Defoin-Platel, M & Chami, M 2007, 'How ambiguous is the inverse problem of ocean color in coastal waters?' *Journal of Geophysical Research-Oceans*, vol. 112, no. C3, p. C03004.

Dekker, AG 1993, 'Detection of optical water quality parameters for eutrophic waters by high resolution remote sensing.' Ph.D. thesis, Vrije Universiteit.

Dekker, AG, Brando, VE & Anstee, JM 2005, 'Retrospective seagrass change detection in a shallow coastal tidal Australian lake', *Remote Sensing of Environment*, vol. 97, no. 4, pp. 415-33.

Dekker, AG, Brando, VE, Oubelkheir, K, Wettle, M, Clementson, LA, Peters, S, Pasterkamp, R & van der Woerd, H 2004, 'When freshwater meets ocean water: How variable siops affect remote sensing products of estuaries, bays and coastal seas.' paper presented to Ocean Optics XVII, Freemantle, Australia, 24-29 Oct. 2004.

Dekker, AG, Vos, RJ & Peters, SWM 2001, 'Comparison of remote sensing data, model results and in situ data for total suspended matter (TSM) in the southern Frisian lakes', *The Science of The Total Environment*, vol. 268, no. 1-3, pp. 197-214.

Devred, E, Sathyendranath, S & Platt, T 2006, 'Inversion Based on a Semi-Analytical Reflectance Model', in Z Lee (ed.), *Report of the International Ocean-Colour Coordinating Group No. 5: Remote Sensing of Inherent Optical Properties: Fundamentals, Tests of Algorithms, and Applications* International Ocean-Colour Coordinating Group, Dartmouth, Canada.

Doerffer, R & Schiller, H 2007, 'The MERIS Case 2 water algorithm', *International Journal of Remote Sensing*, vol. 28, no. 3, pp. 517 - 35.

—— 2008, *Algorithm Theoretical Basis Document (ATBD) MERIS Regional Coastal and Lake Case 2 Water Project Atmospheric Correction ATBD*.

Douglas, G, Palmer, M, Caitcheon, G & Orr, P 2007, 'Identification of sediment sources to Lake Wivenhoe, South-East Queensland, Australia', *Marine and Freshwater Research*, vol. 58, no. 9, pp. 793-810.

Du, Y, Chang, C-I, Ren, H, Chang, C-C, Jensen, JO & D'Amico, FM 2004, 'New hyperspectral discrimination measure for spectral characterization', *Optical Engineering*, vol. 43, no. 8, pp. 1777-86.

Duntley, SQ 1942, 'The optical properties of diffusing materials', *Journal of the Optical Society of America*, vol. 32, pp. 61-70.

Erm, A, Arst, H, Nõges, P, Reinart, A & Sipelgas, L 2002, 'Temporal variations in bio-optical properties of four North Estonian lakes in 1999-2000', *Geophysica*, vol. 38, no. 1-2, pp. 89-111.

ESA 2006, 'MERIS Product Handbook Ver 2.1', viewed 19 April 2009, <http://envisat.esa.int/pub/ESA_DOC/ENVISAT/MERIS/meris.ProductHandbook.2_1.pdf>.

Ference, TP 1975, 'Organizational communications systems and the decision process', in A Rappaport (ed.), *Information for decision making : quantitative and behavioral dimensions*, 2nd edn, Prentice-Hall, Englewood Cliffs, N.J.

Floricioiu, D & Rott, H 2005, 'Atmospheric correction of MERIS data over perialpine regions', in *MERIS (A)ATSR Workshop 2005 (ESA SP-597).* Frascati, Italy.

Garnett, C, Shaw, G, Moore, D, Florian, P & Moore, M 2003, *Impact of climate change on toxic cyanbacterial (blue green algal) blooms and algal toxin production in Queensland,* National Research Centre for Environmental Toxicology.

Giardino, C, Brando, VE, Dekker, AG, Strombeck, N & Candiani, G 2007, 'Assessment of water quality in Lake Garda (Italy) using Hyperion', *Remote Sensing of Environment*, vol. 109, no. 2, pp. 183-95.

Gilerson, A, Zhou, J, Hlaing, S, Ioannou, I, Schalles, J, Gross, B, Moshary, F & Ahmed, S 2007, 'Fluorescence component in the reflectance spectra from coastal waters. Dependence on water composition', *Optics Express*, vol. 15, no. 24, pp. 15702-21.

Gordon, HR 1978, 'Removal of atmospheric effects from satellite imagery of the oceans', *Applied Optics*, vol. 17, no. 10, pp. 1631-6.

—— 1986, 'Ocean color remote sensing: influence of the particle phase function and the solar zenith angle.' *EOS Transactions, American Geophysical Union*, no. 14, p. 1055.

Gordon, HR, Brown, OB, Evans, RH, Brown, JW, Smith, RC, Baker, KS & Clark, DK 1988, 'A Semianalytic radiance model of ocean color', *Journal of Geophysical Research*, vol. 93, no. D9, pp. 10909-24.

Gordon, HR, Brown, OB & Jacobs, MM 1975, 'Computed relationships between the inherent and apparent optical properties of a flat homogeneous ocean', *Applied Optics*, vol. 14, no. 2, pp. 417-27.

Gordon, HR & Wang, M 1994, 'Retrieval of water-leaving radiance and aerosol optical thickness over the oceans with SeaWiFS: a preliminary algorithm', *Applied Optics*, vol. 33, no. 3, pp. 443-52.

Gower, J, King, S, Borstad, G & Brown, L 2005, 'Detection of intense plankton blooms using the 709nm band of the MERIS imaging spectrometer', *International Journal of Remote Sensing*, vol. 26, no. 9, pp. 2005-12.

Griffiths, DJ & Faithful, JW 1996, 'Effects of the sediment load of a tropical North-Australian river on water column characteristics in the receiving impoundment.' *Archive für Hydrobiolie (Supplement 113), Large Rivers*, vol. 10, no. 1-4, pp. 147-57.

Guanter, L, Ruiz-Verdú, A, Odermatt, D, Giardino, C, Simis, S, Estellés, V, Heege, T, Domínguez-Gómez, JA & Moreno, J 2010, 'Atmospheric correction of ENVISAT/MERIS data over inland waters: Validation for European lakes', *Remote Sensing of Environment*, vol. 114, no. 3, pp. 467-80.

Hakvoort, H, de Haan, JF, Jordans, RRW, Vos, RJ, Peters, SWM & Rijkeboer, M 2002, 'Towards airborne remote sensing of water quality in The Netherlands--validation and error analysis', *ISPRS Journal of Photogrammetry and Remote Sensing*, vol. 57, no. 3, pp. 171-83.

Hayase, K & Tsubota, H 1985, 'Sedimentary humic acid and fulvic acid as fluorescent organic materials', *Geochimica et Cosmochimica Acta*, vol. 49, no. 1, pp. 159-63.

Helms, JR, Stubbins, A, Ritchie, JD, Minor, EC, Kieber, DJ & Mopper, K 2008, 'Absorption spectral slopes and slope ratios as indicators of molecular weight, source, and photobleaching of chromophoric dissolved organic matter', *Limnology and Oceanography*, vol. 53, no. 3, pp. 955-69.

Herlevi, A 2002a, 'Inherent and apparent optical properties in relation to water quality in Nordic waters', Ph.D. thesis, University of Helsinki.

—— 2002b, 'A study of scattering, backscattering and a hyperspectral reflectance model for boreal waters', *Geophysica*, vol. 38, no. 1-2, pp. 113-32.

HOBILabs Inc 2008, *HydroScat-6 Spectral Backscattering Sensor User's manual (Revision H)*, Hydro-Optics, Biology, and Instrumentation Laboratories, Inc. (HOBILabs).

Hoepffner, N & Sathyendranath, S 1991, 'Effect of pigment composition on absorption properties of phytoplankton', *Marine Ecology Progress Series*, vol. 73, pp. 11-23.

Hoge, FE & Lyon, PE 1996, 'Satellite retrieval of inherent optical properties by linear matrix inversion of oceanic radiance models: An analysis of model and radiance measurement errors', *Journal of Geophysical Research*, vol. 101, no. C7, pp. 16631-48.

Hoge, FE, Vodacek, A, Swift, RN, Yungel, JK & Blough, NV 1995, 'Inherent optical properties of the ocean: retrieval of the absorption coefficient of chromophoric dissolved organic matter from airborne laser spectral fluorescence measurements', *Applied Optics*, vol. 34, no. 30, pp. 7032-8.

Hoge, FE, Wright, CW, Lyon, PE, Swift, RN & Yungel, JK 1999, 'Satellite retrieval of the absorption coefficient of phytoplankton phycoerythrin pigment: Theory and feasibility status', *Applied Optics*, vol. 38, no. 36, pp. 7431-41.

Hoogenboom, HJ, Dekker, AG & Althuis, IA 1998a, 'Simulation of AVIRIS sensitivity for detecting chlorophyll over coastal and inland waters', *Remote Sensing of Environment*, vol. 65, no. 3, pp. 333-40.

Hoogenboom, HJ, Dekker, AG & de Haan, JF 1998b, 'Retrieval of chlorophyll and suspended matter from imaging spectrometry data by matrix inversion', *Canadian Journal of Remote Sensing*, vol. 24, no. 2, pp. 144-52.

Hotzel, G & Croome, R 1999, *A phytoplankton methods manual for Australian freshwaters*, Land and Water Resources Research and Development Corporation, Canberra.

Hu, C, Lee, Z, Ma, R, Yu, K, Li, D & Shang, S 2010, 'Moderate Resolution Imaging Spectroradiometer (MODIS) observations of cyanobacteria blooms in Taihu Lake, China,' *Journal of Geophysical Research-Oceans*, vol. 115, p. C04002.

Ibelings, BW, Mur, LR & Walsby, AE 1991, 'Diurnal changes in buoyancy and vertical-distribution in populations of Microcystis in 2 shallow lakes', *Journal of Plankton Research*, vol. 13, no. 2, pp. 419-36.

IOCCG 2006, *Remote sensing of inherent optical properties: fundamentals, tests of algorithms, and applications* 5, International Ocean-Colour Coordinating Group, Dartmouth, Canada.

Joo, M, Yu, B, Fentie, B & Caroll, C 2005, 'Estimation of long-term sediment loads in the Fitzroy catchment, Queensland, Australia', in A Zerger & RM Argent (eds), *MODSIM 2005 International Congress on Modelling and Simulation.*, pp. 1161-7.

Jupp, DLB, Kirk, JTO & Harris, GP 1994, 'Detection, identification and mapping of cyanobacteria-using remote sensing to measure the optical quality of turbid inland waters.' *Australian Journal of Marine and Freshwater Research*, vol. 45, no. 5, pp. 801-28.

Kallio, K, Pulliainen, J & Ylöstalo, P 2005, 'MERIS, MODIS and ETM+ channel configurations in the estimation of lake water quality from subsurface reflectance using semianalytical and empirical Algorithms', *Geophysica*, vol. 41, no. 1-2, pp. 31-55.

Kaufman, YJ & Tanre, D 1992, 'Atmospherically resistant vegetation index (ARVI) for EOS-MODIS', *Geoscience and Remote Sensing, IEEE Transactions on*, vol. 30, no. 2, pp. 261-70.

Keller, PA 2001a, 'Comparison of two inversion techniques of a semi-analytical model for the determination of lake water constituents using imaging spectrometry data', *The Science of The Total Environment*, vol. 268, no. 1-3, pp. 189-96.

—— 2001b, 'Imaging spectroscopy of lake water quality parameters.' PhD thesis, Remote Sensing Series 36, Remote Sensing Laboratories, University of Zurich.

Kirk, JTO 1975, 'A theoretical analysis of the contribution of algal cells to the attenuation of light within natural waters. I. General treatment of suspensions of pigmented cells', *New Phytologist*, vol. 75, no. 1, pp. 11-20.

—— 1976, 'Yellow substance (gelbstoff) and its contribution to attenuation of photosynthetically active radiation in some inland and coastal Southeastern Australian waters', *Australian Journal of Marine and Freshwater Research*, vol. 27, no. 1, pp. 61-71.

—— 1981, 'Monte Carlo study of the underwater light field in, and the relationship between optical properties of, turbid yellow waters.' *Australian Journal of Marine and Freshwater Research*, vol. 32, pp. 517-32.

—— 1984, 'Dependence of relationship between inherent and apparent optical properties of water on solar altitude', *Limnology and Oceanography*, vol. 29, no. 2, pp. 350-6.

—— 1986, 'Optical limnology-- a manifesto', in WD Williams & P De Deckker (eds), *Limnology in Australia*, CSIRO ; Dordrecht : Junk, Melbourne.

—— 1992, 'Monte Carlo modeling of the performance of a reflective tube absorption meter', *Applied Optics*, vol. 31, no. 30, pp. 6463-8.

—— 1994, *Light and photosynthesis in aquatic ecosystems*, 2nd edn, Cambridge University Press, Cambridge England ; New York, NY.

Kirk, JTO & Oliver, RL 1995, 'Optical closure of an ultraturbid lake', *Journal of Geophysical Research*, vol. 100, no. C7, pp. 13221-5.

Kishino, M, Takahashi, M, Okami, N & Ichimura, S 1985, 'Estimation of the spectral absorption-coefficients of phytoplankton in the sea', *Bulletin of Marine Science*, vol. 37, no. 2, pp. 634-42.

Kosten, S, Roland, F, Marques, D, Van Nes, EH, Mazzeo, N, Sternberg, LDL, Scheffer, M & Cole, JJ 2010, 'Climate-dependent CO_2 emissions from lakes', *Global Biogeochemical Cycles*, vol. 24.

Kotchenova, SY & Vermote, EF 2007, 'Validation of a vector version of the 6S radiative transfer code for atmospheric correction of satellite data. Part II. Homogeneous Lambertian and anisotropic surfaces', *Applied Optics*, vol. 46, no. 20, pp. 4455-64.

Kotchenova, SY, Vermote, EF, Levy, R & Lyapustin, A 2008, 'Radiative transfer codes for atmospheric correction and aerosol retrieval: intercomparison study', *Applied Optics*, vol. 47, no. 13, pp. 2215-26.

Kotchenova, SY, Vermote, EF, Matarrese, R & Klemm, FJ 2006, 'Validation of a vector version of the 6S radiative transfer code for atmospheric correction of satellite data. Part I: Path radiance', *Applied Optics*, vol. 45, no. 26, pp. 6762-74.

Kutser, T 2004, 'Quantitative detection of chlorophyll in cyanobacterial blooms by satellite remote sensing', *Limnology and Oceanography*, vol. 49, no. 6, pp. 2179-89.

Kutser, T, Herlevi, A, Kallio, K & Arst, H 2001, 'A hyperspectral model for interpretation of passive optical remote sensing data from turbid lakes', *The Science of The Total Environment*, vol. 268, no. 1-3, pp. 47-58.

Kutser, T, Metsamaa, L & Dekker, AG 2008, 'Influence of the vertical distribution of cyanobacteria in the water column on the remote sensing signal', *Estuarine Coastal and Shelf Science*, vol. 78, no. 4, pp. 649-54.

Kutser, T, Metsamaa, L, Strömbeck, N & Vahtmäe, E 2006, 'Monitoring cyanobacterial blooms by satellite remote sensing', *Estuarine, Coastal and Shelf Science*, vol. 67, no. 1-2, pp. 303-12.

Laanen, M 2007, 'Yellow Matters: Remote sensing of Coloured Dissolved Organic Matter in inland freshwaters', PhD thesis, Vrije Universiteit.

Le, C, Li, Y, Zha, Y & Sun, D 2009, 'Specific absorption coefficient and the phytoplankton package effect in Lake Taihu, China', *Hydrobiologia*, vol. 619, pp. 27-37.

Lee, Z & Carder, KL 2002, 'Effect of spectral band numbers on the retrieval of water column and bottom properties from ocean color data', *Applied Optics*, vol. 41, no. 12, pp. 2191-201.

Lee, Z, Carder, KL & Du, K 2004, 'Effects of molecular and particle scatterings on the model parameter for remote-sensing reflectance', *Applied Optics*, vol. 43, no. 25, pp. 4957-64.

Lee, Z, Carder, KL, Hawes, SK, Steward, RG, Peacock, TG & Davis, CO 1994, 'Model for interpretation of hyperspectral remote-sensing reflectance.' *Applied Optics*, vol. 33, no. 24, pp. 5721-32.

Lee, Z, Carder, KL, Mobley, CD, Steward, RG & Patch, JS 1999, 'Hyperspectral remote sensing for shallow waters. 2. Deriving bottom depths and water properties by optimization', *Applied Optics*, vol. 38, no. 18, pp. 3831-43.

Leroy, M, V., B-P, Hautecoeur, O, Bréon, FM & Baret, F 1998, *Corrections atmosphériques des données MERIS/ENVISAT: caractérisations de la BRDF de surfaces "sombres"*, European Space Agency final report.

Levy, RC, Remer, LA & Kaufman, YJ 2004, 'Effects of neglecting polarization on the MODIS aerosol retrieval over land', *IEEE Transactions on Geoscience and Remote Sensing*, vol. 42, no. 11, pp. 2576-83.

Lewis, SE, Bainbridge, ZT, Sherman, BS, Brodie, JE & Cooper, M 2009, *The trapping efficiency of the Burdekin Falls Dam: Estimates from a three-year monitoring program.*, Marine and Tropical Sciences Research Facility. Reef and Rainforest Research Centre Limited and Australian Centre for Tropical Freshwater Research (ACTFR), Townsville.

Lohrenz, SE, Weidemann, AD & Tuel, M 2003, 'Phytoplankton spectral absorption as influenced by community size structure and pigment composition', *Journal of Plankton Research*, vol. 25, no. 1, pp. 35-61.

Loiselle, SA, Bracchini, L, Cozar, A, Dattilo, AM, Tognazzi, A & Rossi, C 2009a, 'Variability in photobleaching yields and their related impacts on optical conditions in subtropical lakes', *Journal of Photochemistry and Photobiology B-Biology*, vol. 95, no. 2, pp. 129-37.

Loiselle, SA, Bracchini, L, Dattilo, AM, Ricci, M, Tognazzi, A, Cozar, A & Rossi, C 2009b, 'Optical characterization of chromophoric dissolved organic matter using wavelength distribution of absorption spectral slopes', *Limnology and Oceanography*, vol. 54, no. 2, pp. 590-7.

Lyon, PE & Hoge, FE 2006, 'The linear matrix inversion algorithm', in Z Lee (ed.), *Report of the International Ocean-Colour Coordinating Group No. 5: Remote Sensing of Inherent Optical Properties: Fundamentals, Tests of Algorithms, and Applications* International Ocean-Colour Coordinating Group, Dartmouth, Canada.

Ma, RH, Pan, DL, Duan, HT & Song, QJ 2009, 'Absorption and scattering properties of water body in Taihu Lake, China: backscattering', *International Journal of Remote Sensing*, vol. 30, no. 9, pp. 2321-35.

Ma, RH, Tang, J, Dai, J, Zhang, Y & Song, Q 2006, 'Absorption and scattering properties of water body in Taihu Lake, China: absorption', *International Journal of Remote Sensing*, vol. 27, no. 19, pp. 4277 - 304.

Maffione, RA & Dana, DR 1997, 'Instruments and methods for measuring the backward-scattering coefficient of ocean waters', *Applied Optics*, vol. 36, no. 24, pp. 6057-67.

Maritorena, S, Siegel, DA & Peterson, AR 2002, 'Optimization of a semianalytical ocean color model for global-scale applications', *Applied Optics*, vol. 41, no. 15, pp. 2705-14.

Matarrese, R, Chiaradia, MT, De Pasquale, V & Pasquariello, G 2004, 'Chlorophyll-a concentration measure in coastal waters using MERIS and MODIS data', in *IGARSS 2004: IEEE International Geoscience and Remote Sensing Symposium Proceedings, Vols 1-7 - Science for Society: Exploring and Managing a Changing Planet*, vol. 6, pp. 3639-41 vol.6.

Metsamaa, L, Kutser, T & Strombeck, N 2006, 'Recognising cyanobacterial blooms based on their optical signature: a modelling study', *Boreal Environment Research*, vol. 11, no. 6, pp. 493-506.

Minor, E & Stephens, B 2008, 'Dissolved organic matter characteristics within the Lake Superior watershed', *Organic Geochemistry*, vol. 39, no. 11, pp. 1489-501.

Mitchell, BG 1990, 'Algorithms for determining the absorption coefficient for aquatic particulates using the quantitative filter technique.' in *Ocean Optics X. 1302*, pp. 137–48.

Mitrovic, SM, Bowling, LC & Buckney, RT 2001, 'Vertical disentrainment of Anabaena circinalis in the turbid, freshwater Darling River, Australia: quantifying potential benefits from buoyancy', *Journal of Plankton Research*, vol. 23, no. 1, pp. 47-55.

Mobley, CD & Sundman, L 2001, *Hydrolight 4.2 Users' Guide.*, Sequoia Scientific, Inc., Redmond, WA.

Mobley, CD, Sundman, L, Davis, CO, Bowles, JH, Downes, TV, Leathers, RA, Montes, MJ, Bissett, WP, Kohler, DDR, Reid, RP, Louchard, EM & Gleason, A 2005, 'Interpretation of hyperspectral remote-sensing imagery by spectrum matching and look-up tables', *Applied Optics*, vol. 44, no. 17, pp. 3576-92.

Moore, GF, Aiken, J & Lavender, SJ 1999, 'The atmospheric correction of water colour and the quantitative retrieval of suspended particulate matter in Case II waters: application to MERIS', *International Journal of Remote Sensing*, vol. 20, no. 9, pp. 1713-33.

Morel, A 1974, 'Optical properties of pure water and pure seawater', in NG Jerlov & E Steeman Nielsen (eds), *Optical Aspects of Oceanography*, Academic, pp. 1-24.

Morel, A & Bricaud, A 1981, 'Theoretical results concerning light absorption in a discrete medium, and application to specific absorption of phytoplankton', *Deep-Sea Research*, vol. 28, pp. 1375-93.

Morel, A & Gentili, B 1993, 'Diffuse reflectance of oceanic waters. 2. Bidirectional aspects', *Applied Optics*, vol. 32, no. 33, pp. 6864-72.

Morel, A & Prieur, L 1977, 'Analysis of variations in ocean color', *Limnology and Oceanography*, vol. 22, no. 4, pp. 709-22.

Morris, DP & Hargreaves, BR 1997, 'The role of photochemical degradation of dissolved organic carbon in regulating the UV transparency of three lakes on the Pocono Plateau', *Limnology and Oceanography*, vol. 42, no. 2, pp. 239-49.

Mueller, JL, Fargion, GS, McClain, CR, Pegau, S, Zaneveld, JRV, Mitchell, BG, Kahru, M, Wieland, J & Stramska, M 2003, *Ocean Optics Protocols For Satellite Ocean Color Sensor Validation, Revision 4, Volume IV: Inherent Optical Properties: Instruments, Characterizations, Field Measurements and Data Analysis Protocols*, NASA, Greenbelt, Maryland.

O'Reagain, PJ, Brodie, J, Fraser, G, Bushell, JJ, Holloway, CH, Faithful, JW & Haynes, D 2005, 'Nutrient loss and water quality under extensive grazing in the upper Burdekin river catchment, North Queensland', *Marine Pollution Bulletin*, vol. 51, pp. 37-50.

O'Reilly, JE, Maritorena, S, Mitchell, BG, Siegel, DA, Carder, KL, Garver, SA, Kahru, M & McClain, C 1998, 'Ocean color chlorophyll algorithms for SeaWiFS', *Journal of Geophysical Research*, vol. 103, no. C11, pp. 24937-53.

Odermatt, D, Giardino, C & Heege, T 2010, 'Chlorophyll retrieval with MERIS Case-2-Regional in perialpine lakes', *Remote Sensing of Environment*, vol. 114, no. 3, pp. 607-17.

Odermatt, D, Heege, T, Nieke, J, Kneubuhler, M & Itten, K 2008a, 'Water quality monitoring for lake constance with a physically based algorithm for MERIS data', *Sensors*, vol. 8, no. 8, pp. 4582-99.

Odermatt, D, Kiselev, V, Heege, T, Kneubühler, M & Itten, KI 2008b, 'Adjacency effect considerations and air/water constituent retrieval for Lake Constance.' in ESA/ESRIN (ed.), *2nd MERIS/AATSR workshop*, Frascati, Italy.

Okullo, W, Ssenyonga, T, Hamre, B, Frette, Ø, Sørensen, K, Stamnes, JJ, Steigen, A & Stamnes, K 2007, 'Parameterization of the inherent optical properties of Murchison Bay, Lake Victoria', *Applied Optics*, vol. 46, no. 36, pp. 8553-61.

Oliver, R 1990, 'Optical properties of waters in the Murray-Darling Basin, South-eastern Australia', *Marine and Freshwater Research*, vol. 41, no. 5, pp. 581-601.

Orr, PT & Schneider, PM 2006, *Toxic cyanobacteria risk assessment: Reservoir vulnerability and water use best practice*, SEQ Water, Brisbane.

Oubelkheir, K, Clementson, LA, Webster, IT, Ford, PW, Dekker, AG, Radke, LC & Daniel, P 2006, 'Using inherent optical properties to investigate biogeochemical dynamics in a tropical macrotidal coastal system', *Journal of Geophysical Research-Oceans*, vol. 111, no. C7, p. C07021.

Paavel, B, Arst, H & Herlevi, A 2007, 'Dependence of spectral distribution of inherent optical properties of lake waters on the concentrations of different water constituents', *Nordic Hydrology*, vol. 38, no. 3, pp. 265-85.

Pasterkamp, R, Dekker, AG, Hoogenboom, HJ, Rijkeboer, M & Hakvoort, JHM 1999, 'The effect of the specific inherent optical properties on assessing water quality in Dutch inland waters using matrix inversion', in *Geoscience and Remote Sensing Symposium, 1999. IGARSS '99 Proceedings. IEEE 1999 International*, vol. 4, pp. 2095-7 vol.4.

Pegau, WS, Gray, D & Zaneveld, JRV 1997, 'Absorption and attenuation of visible and near-infrared light in water: dependence on temperature and salinity', *Applied Optics*, vol. 36, no. 24, pp. 6035-46.

Pegau, WS & Zaneveld, JRV 1993, 'Temperature-Dependent Absorption of Water in the Red and Near-Infrared Portions of the Spectrum', *Limnology and Oceanography*, vol. 38, no. 1, pp. 188-92.

Petzold, TJ 1972, *Volume Scattering Functions for Selected Ocean Waters*, Scripps Institution of Oceanography, San Diego.

Phinn, SR, Roelfsema, C, Scarth, P, Dekker, AG, Brando, VE, Anstee, JM & Marks, A 2005, *An integrated remote sensing approach for adaptive management of complex coastal waters. Final Report - Moreton Bay Remote Sensing Tasks (MR2), CRC for Coastal Zone, Estuary & Waterway Management.*, CRC for Coastal Zone.

Pierson, DC & Strömbeck, N 2001, 'Estimation of radiance reflectance and the concentrations of optically active substances in Lake Mälaren, Sweden, based on direct and inverse solutions of a simple model', *The Science of The Total Environment*, vol. 268, no. 1-3, pp. 171-88.

Pope, RM & Fry, ES 1997, 'Absorption spectrum (380 -700 nm) of pure water. II. Integrating cavity measurements', *Applied Optics*, vol. 36, no. 33, pp. 8710-23.

Pozdnyakov, D, Lyaskovsky, A, Grassl, H & Pettersson, L 2002, 'Numerical modelling of transspectral processes in natural waters: implications for remote sensing.' *International Journal of Remote Sensing*, vol. 23, no. 8, pp. 1581-607.

Preisendorfer, RW 1959, 'Theoretical proof of the existence of characteristic diffuse light in natural waters', *Journal of Marine Research*, vol. 18, no. 1, pp. 1-9.

Prieur, L & Sathyendranath, S 1981, 'An optical classification of coastal and oceanic waters based on the specific spectral absorption curves of phytoplankton pigments, dissolved organic matter, and other particulate materials', *Limnology and Oceanography*, vol. 26, no. 4, pp. 671-89.

Queensland Department of Natural Resources and Mines 2005, *Monitoring standard for freshwater blue-green algae (cyanobacteria)*, Department of Natural Resources, Mines and Water.

Raateoja, M, Seppälä, J & Ylöstalo, P 2004, 'Fast Repetition Rate Fluorometry Is Not Applicable to Studies of Filamentous Cyanobacteria from the Baltic Sea', *Limnology and Oceanography*, vol. 49, no. 4, pp. 1006-12.

Richardson, LL 1996, 'Remote Sensing of Algal Bloom Dynamics', *BioScience*, vol. 46, no. 7, pp. 492-501.

Rijkeboer, M, Dekker, AG & Gons, HJ 1997, 'Subsurface irradiance reflectance spectra of inland waters differing in morphometry and hydrology', *Aquatic Ecology*, vol. 31, no. 3, pp. 313-23.

Risovic, D 1993, 'Two-component model of sea particle size distribution', *Deep Sea Research Part I: Oceanographic Research Papers*, vol. 40, no. 7, pp. 1459-73.

Santer, R, Carrere, V, Dessailly, D, Dubuisson, P & Roger, C 2006, 'Algorithm theoretical basis document (ATBD) 2.15: Atmospheric corrections over land.' vol. 2006, no. 24 November, viewed 1 November 2006, <http://envisat.esa.int/instruments/meris/pdf/atbd_2_15.pdf>.

Santer, R, Carrere, V, Dubuisson, P & Roger, JC 1999, 'Atmospheric correction over land for MERIS', *International Journal of Remote Sensing*, vol. 20, no. 9, pp. 1819-40.

Sathyendranath, S, Lazzara, L & Prieur, L 1987, 'Variations in the spectral values of specific absorption of phytoplankton', *Limnology and Oceanography*, vol. 32, no. 2, pp. 403-15.

Schaale, M, Fischer, J & C. Olbert 1998, 'Quantitative estimation of substances contained in inland water from multispectral airborne measurements by neural networks', in *ASPRS-RTI Annual Conference*, Tampa, USA, pp. 1345-56.

Schagerl, M & Künzl, G 2007, 'Chlorophyll *a* extraction from freshwater algae — a reevaluation', *Biologia*, vol. 62, no. 3, pp. 270-5.

Schuster, A 1905, 'Radiation through a foggy atmosphere', *Astrophysical Journal*, vol. 21, no. 1, pp. 1-22.

Slade, WH, Ressom, HW, Musavi, MT & Miller, RL 2004, 'Inversion of ocean color observations using particle swarm optimization', *IEEE Transactions on Geoscience and Remote Sensing*, vol. 42, no. 9, pp. 1915-23.

Smith, RC & Baker, KS 1981, 'Optical properties of the clearest natural waters (200-800 nm)', *Applied Optics*, vol. 20, no. 2, pp. 177-84.

Sørensen, K, Grung, M & Röttgers, R 2007, 'An intercomparison of *in vitro* chlorophyll *a* determinations for MERIS level 2 data validation', *International Journal of Remote Sensing*, vol. 28, no. 3, pp. 537 - 54.

South East Queensland Water Corporation Ltd 2005, *Key features of dams and storages* viewed 25 May 2006, <http://www.seqwater.com.au/files/pdf/KeyDamStatistics.pdf>.

Sterckx, S & Debruyn, W 2004, 'A hyperspectral view of the North Sea', in *Proceedings of the Airborne Imaging Spectroscopy Workshop* Bruges.

Stewart, AJ & Wetzel, RG 1980, 'Fluorescence : absorbance ratios-a molecular weight tracer of dissolved organic matter', *Limnology and Oceanography*, vol. 25, no. 3, pp. 559-64.

Strömbeck, N & Pierson, DC 2001, 'The effects of variability in the inherent optical properties on estimations of chlorophyll a by remote sensing in Swedish freshwaters', *The Science of the Total Environment*, vol. 268, no. 1-3, pp. 123-37.

Su, FC, Ho, CR, Zheng, Q, Kuo, NJ & Chen, CT 2006, 'Satellite chlorophyll retrievals with a bipartite artificial neural network model', *International Journal of Remote Sensing*, vol. 27, no. 8, pp. 1563-79.

Sunwater 2005, *Sunwater 04-05 annual report*, viewed 25 May 2006, <http://www.sunwater.com.au/pdf/about/SunWater_Annual_Report.pdf>.

Tassan, S & Ferrari, GM 1995, 'An alternative approach to absorption measurements of aquatic particles retained on filters', *Limnology and Oceanography*, vol. 40, no. 8, pp. 1358-68.

Thuillier, G, Hersé, M, Labs, D, Foujols, T, Peetermans, W, Gillotay, D, Simon, PC & Mandel, H 2003, 'The solar spectral irradiance from 200 to 2400 nm as measured by the SOLSPEC spectrometer from the Atlas and Eureca missions', *Solar Physics*, vol. 214, no. 1, pp. 1-22.

Tilstone, GH, Moore, GF, Sorensen, K, Doerffer, R, Rottgers, R, Ruddick, KG, Pasterkamp, R & Jorgensen, PV 2002, *REVAMP protocols document*, European Space Agency.

Trees, CC, Kennicutt, MC & Brooks, JM 1985, 'Errors associated with the standard fluorimetric determination of chlorophylls and phaeopigments', *Marine Chemistry*, vol. 17, no. 1, pp. 1-12.

Twardowski, MS, Boss, E, Macdonald, JB, Pegau, WS, Barnard, AH & Zaneveld, JRV 2001, 'A model for estimating bulk refractive index from the optical backscattering ratio and the implications for understanding particle composition in case I and case II waters', *Journal of Geophysical Research-Oceans*, vol. 106, no. C7, pp. 14129-42.

Ulloa, O, Sathyendranath, S & Platt, T 1994, 'Effect of the particle-size distribution on the backscattering ratio in seawater', *Applied Optics*, vol. 33, no. 30, pp. 7070-7.

Vaillancourt, RD, Brown, CW, Guillard, RRL & Balch, WM 2004, 'Light backscattering properties of marine phytoplankton: relationships to cell size, chemical composition and taxonomy', *Journal of Plankton Research*, vol. 26, no. 2, pp. 191-212.

van der Woerd, HJ & Pasterkamp, R 2008, 'HYDROPT: A fast and flexible method to retrieve chlorophyll-a from multispectral satellite observations of optically complex coastal waters', *Remote Sensing of Environment*, vol. 112, no. 4, pp. 1795-807.

Van Heukelem, L & Thomas, CS 2001, 'Computer-assisted high-performance liquid chromatography method development with applications to the isolation and analysis of phytoplankton pigments', *Journal of Chromatography A*, vol. 910, no. 1, pp. 31-49.

Vermote, EF, Tanré, D, Deuzé, JL, Herman, M, Morcrette, JJ, Kotchenova, SY & Miura, T 2006, 'Second simulation of the satellite signal in the solar spectrum (6S), 6S user guide version 3', viewed 11 August 2008, <http://6s.ltdri.org/>.

Vidot, J & Santer, R 2005, 'Atmospheric correction for inland waters - application to SeaWiFS', *International Journal of Remote Sensing*, vol. 26, no. 17, pp. 3663-82.

Volten, H, de Haan, JF, Hovenier, JW, Schreurs, R, Vassen, W, Dekker, AG, Hoogenboom, HJ, Charlton, F & Wouts, R 1998, 'Laboratory measurements of angular distributions of light scattered by phytoplankton and silt', *Limnology and Oceanography*, vol. 43, no. 6, pp. 1180-97.

Vos, RJ, Hakvoort, JHM, Jordans, RRW & Ibelings, BW 2003, 'Multiplatform optical monitoring of eutrophication in temporally and spatially variable lakes', *The Science of The Total Environment*, vol. 312, no. 1-3, pp. 221-43.

Werdell, PJ & Bailey, SW 2005, 'An improved in-situ bio-optical data set for ocean color algorithm development and satellite data product validation', *Remote Sensing of Environment*, vol. 98, no. 1, pp. 122-40.

WET Labs Inc 2005, *ac-9 Protocol Document (Revision J)*, Western Environmental Technology Laboratories (WETLabs), Philomath, OR.

—— 2006, *Absorption and Attenuation Meter ac-9 User's Guide (Revision O)*, Western Environmental Technology Laboratories (WETLabs), Philomath, OR.

Wettle, M & Brando, VE 2006, *SAMBUCA Semi-Analytical Model for Bathymetry, Un-mixing, and Concentration Assessment*, 22/06, CSIRO Land and Water, Canberra.

Whitlock, CH, Poole, LR, Usry, JW, Houghton, WM, Witte, WG, Morris, WD & Gurganus, EA 1981, 'Comparison of reflectance with backscatter and absorption parameters for turbid waters', *Applied Optics*, vol. 20, no. 3, pp. 517-22.

Whitmire, AL, Boss, E, Cowles, TJ & Pegau, WS 2007, 'Spectral variability of the particulate backscattering ratio', *Opt. Express*, vol. 15, no. 11, pp. 7019-31.

Zaneveld, JRV, Kitchen, JC & Moore, C 1994, 'The scattering error correction of reflecting-tube absorption meters.' in *Ocean Optics XII*, vol. 2258, pp. 44-55.

Zhan, H, Lee, Z, Ping, S, Chuqun, C & Carder, KL 2003, 'Retrieval of water optical properties for optically deep waters using genetic algorithms', *IEEE Transactions on Geoscience and Remote Sensing*, vol. 41, no. 5, pp. 1123-8.

Zhang, YL, Liu, ML, Wang, X, Zhu, GW & Chen, WM 2009, 'Bio-optical properties and estimation of the optically active substances in Lake Tianmuhu in summer', *International Journal of Remote Sensing*, vol. 30, no. 11, pp. 2837-57.

Zhang, YL, Zhang, B, Wang, X, Li, JS, Feng, S, Zhao, QH, Liu, ML & Qin, BQ 2007, 'A study of absorption characteristics of chromophoric dissolved organic matter and particles in Lake Taihu, China', *Hydrobiologia*, vol. 592, pp. 105-20.

Appendix A- Water Quality Parameter Measurements

A.1 Wivenhoe Dam

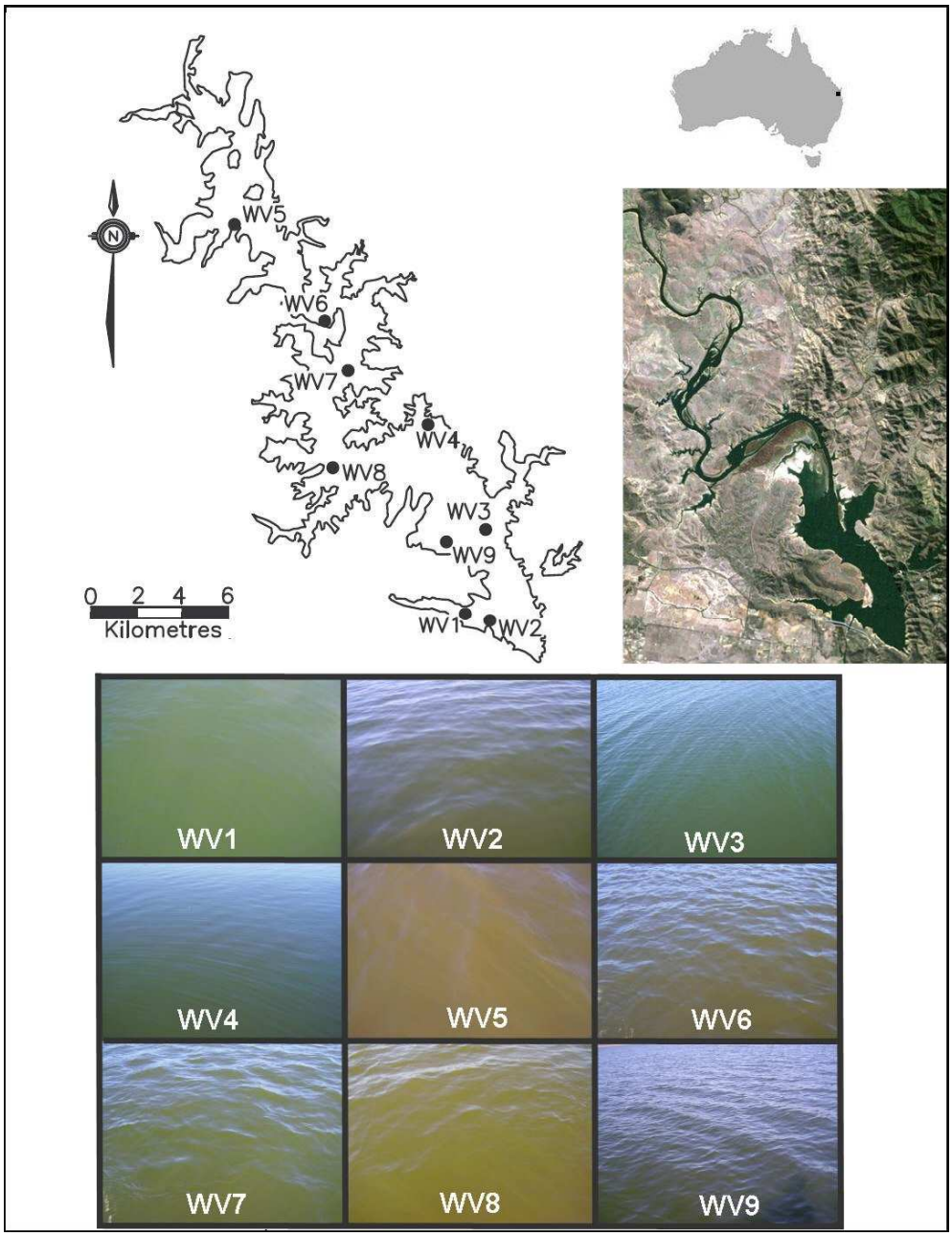

Figure A-1 Location of the SIOP sample sites for the July 2007 fieldwork activities on Wivenhoe Dam, Australia. The upper left hand image shows the calculated full supply level and the upper right hand side shows a true colour Landsat 5 Thematic Mapper (TM) image, at the same scale captured on 16th July 2007. Note the reduced water extent at the time of the fieldwork activities. The lower section of the figure shows photographs of the sample sites taken at the time of sampling.

The water quality parameter concentrations measured for Wivenhoe Dam during the July 2007 fieldwork are shown in Table A-1.

Table A-1 The measured water quality parameter concentrations for Wivenhoe Dam measurement stations.

Station	CSIRO Laboratory			SEQWater		
	Chlorophyll *a* (μgl^{-1})	Tripton (mgl^{-1})	CDOM 440nm (m^{-1})	Chlorophyll *a* (μgl^{-1})	Tripton (mgl^{-1})	Secchi Depth (m)
WV1	5.0	0.9	0.36	5	2	2.5
WV2	7.5	4.3	0.36	8	3	2.2
WV3	7.9	2.6	0.36	5	2	2.0
WV4	7.5	3.4	0.49	9	4	1.75
WV5	42.7	11.2	0.56	60	11	0.9
WV6	40.3	8.2	0.62	41	10	1.15
WV7	34.3	4.8	0.65	32	6	1.3
WV8	12.5	5.1	0.46	13	4	1.7
WV9	11.0	4.4	0.40	8	4	2.0

Phytoplankton Absorption

The laboratory measured absorption spectra for phytoplankton are shown in Figure A-2.

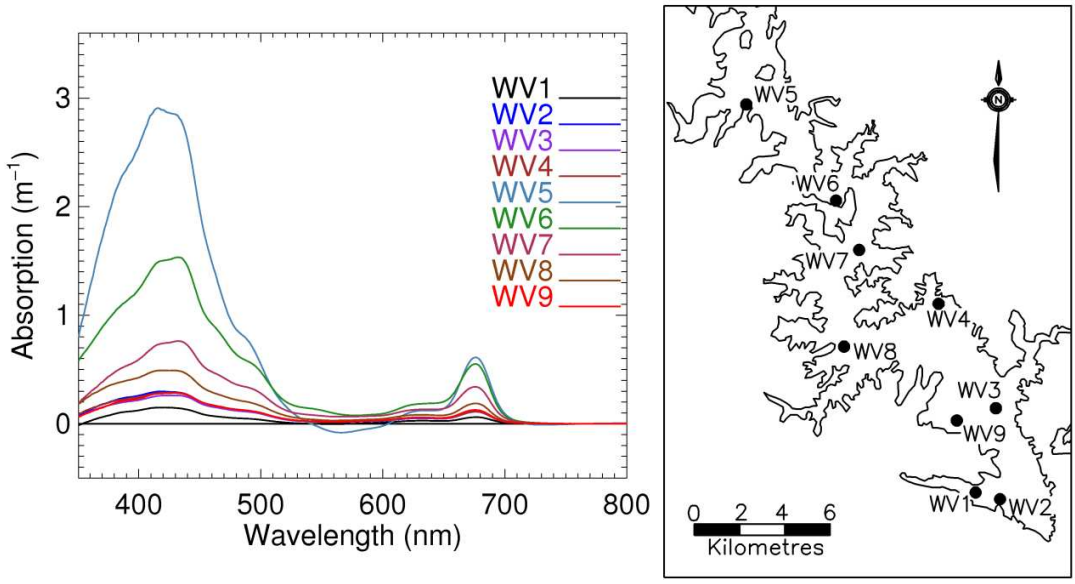

Figure A-2 The laboratory measured absorption for phytoplankton for the Wivenhoe Dam stations.

CDOM Absorption

The laboratory measured absorption spectra for CDOM are shown in Figure A-3.

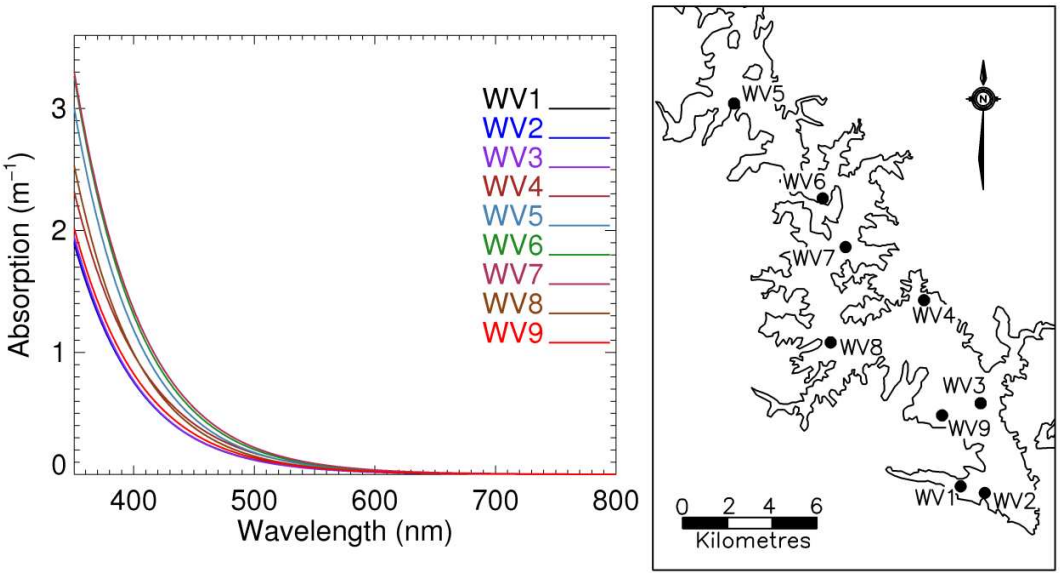

Figure A-3 The laboratory CDOM absorption for phytoplankton for the Wivenhoe Dam stations.

Tripton Absorption

The laboratory measured absorption spectra for tripton are shown in Figure A-4.

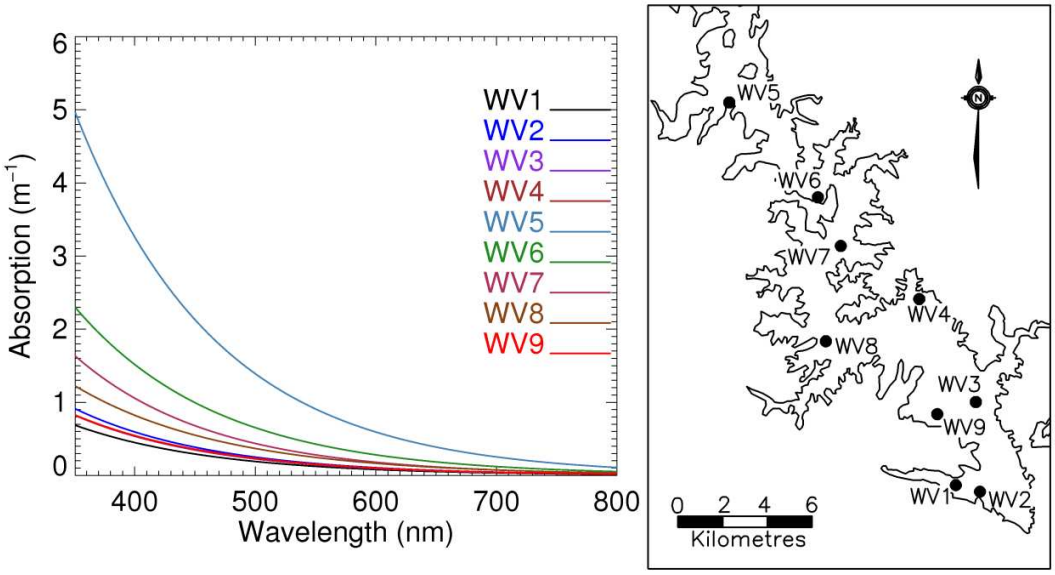

Figure A-4 The laboratory tripton absorption for phytoplankton for the Wivenhoe Dam stations.

A.2 Burdekin Falls Dam

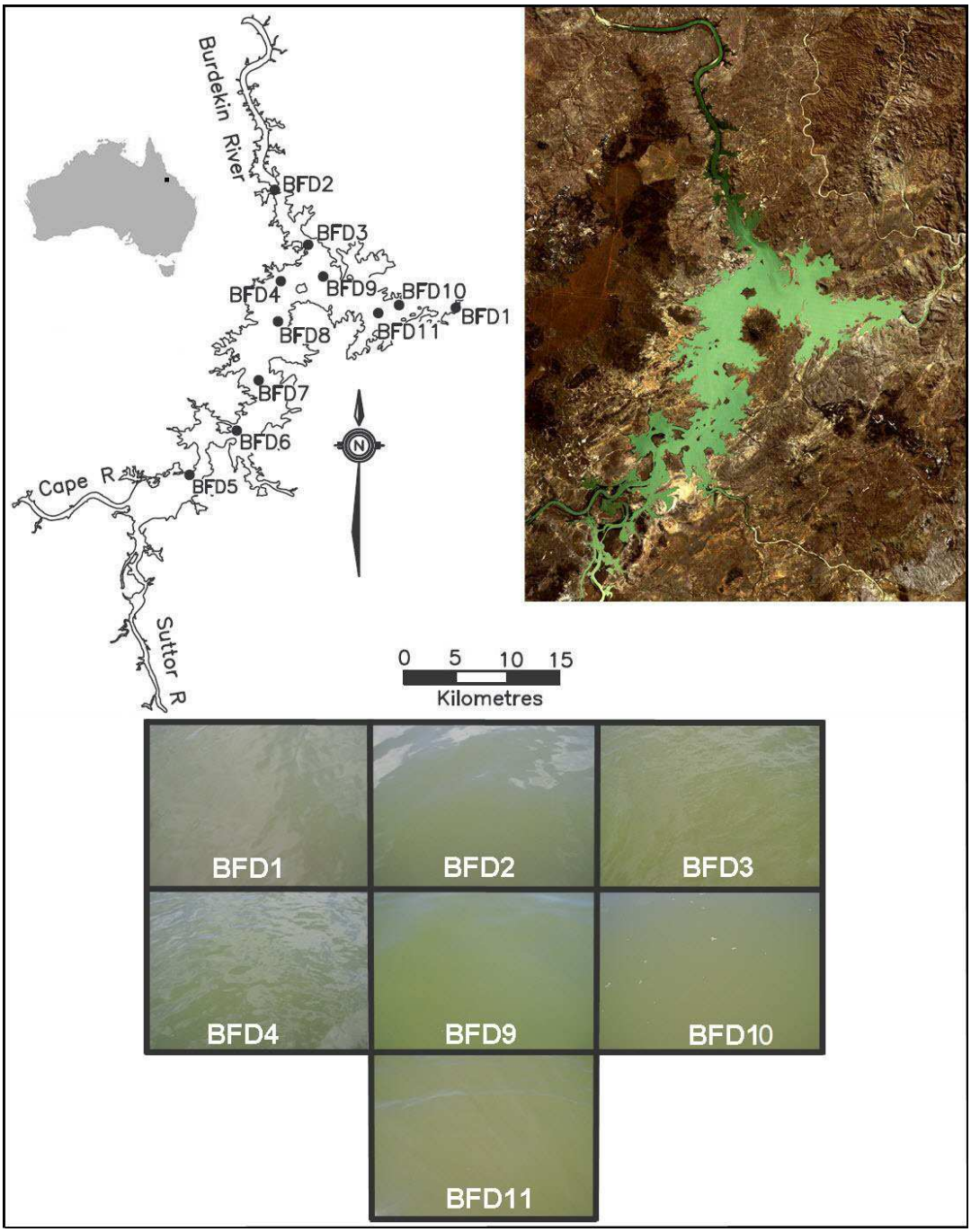

Figure A-5 Location of the SIOP sample sites for the October 2008 fieldwork activities on Burdekin Falls Dam, Australia. The upper left hand image shows the calculated full supply level and the upper right hand image shows a Landsat 5 TM true colour image at the same scale as the map, captured on 22nd August 2008. The lower section of the figure shows photographs of the sample sites taken at the time of sampling. No photographs were taken of Stations 5-8 due to a camera malfunction.

The water quality parameter concentrations measured for the Burdekin Falls Dam stations are shown in Table A-2.

Table A-2 The measured water quality parameter concentrations for Burdekin Falls Dam measurement stations.

Station	Chlorophyll *a* (μgl^{-1})	Tripton (mgl^{-1})	CDOM 440nm (m^{-1})	Tripton Inorganic Fraction (%)	Secchi Depth (m)
BFD1	5.5	10.3	1.21	88	0.9
BFD2	6.6	7.7	0.99	69	1.2
BFD3	7.7	6.5	1.04	73	1.0
BFD4	2.8	6.1	1.05	73	1.0
BFD5	5.4	6.9	1.01	78	0.9
BFD6	4.9	6.7	0.88	82	0.9
BFD7	4.2	5.9	0.97	74	1.1
BFD8	4.6	6.1	1.07	71	1.1
BFD9	4.5	5.6	1.04	74	1.3
BFD10	2.8	6.0	1.27	79	1.0
BFD11	3.1	6.8	1.07	79	1.0

Phytoplankton Absorption

The laboratory measured absorption spectra for phytoplankton in Burdekin Falls Dam are shown in Figure A-6.

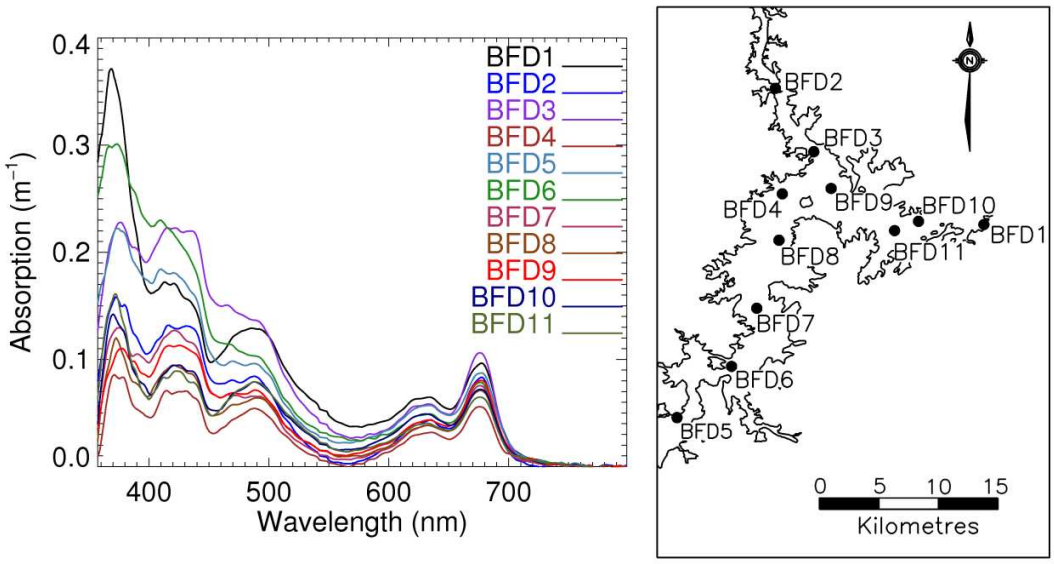

Figure A-6 The laboratory measured absorption for phytoplankton for the Burdekin Falls Dam stations.

CDOM Absorption

The results of the laboratory measurement of the CDOM absorption for the Burdekin Falls Dam stations are shown in Figure A-7.

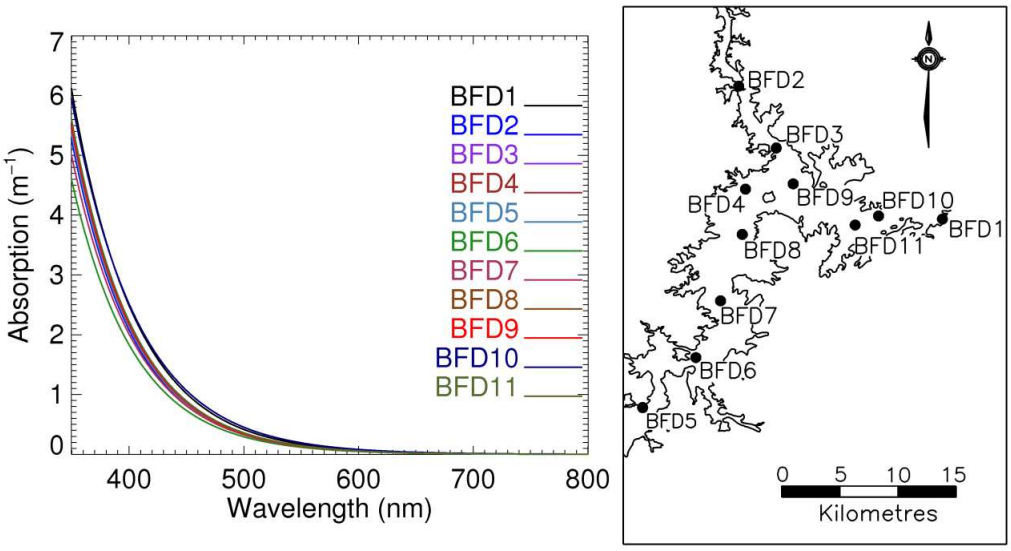

Figure A-7 The laboratory measured absorption for CDOM for the Burdekin Falls Dam stations.

Tripton Absorption

The results of the laboratory measurement of the tripton absorption for the Burdekin Falls Dam stations are shown in Figure A-8.

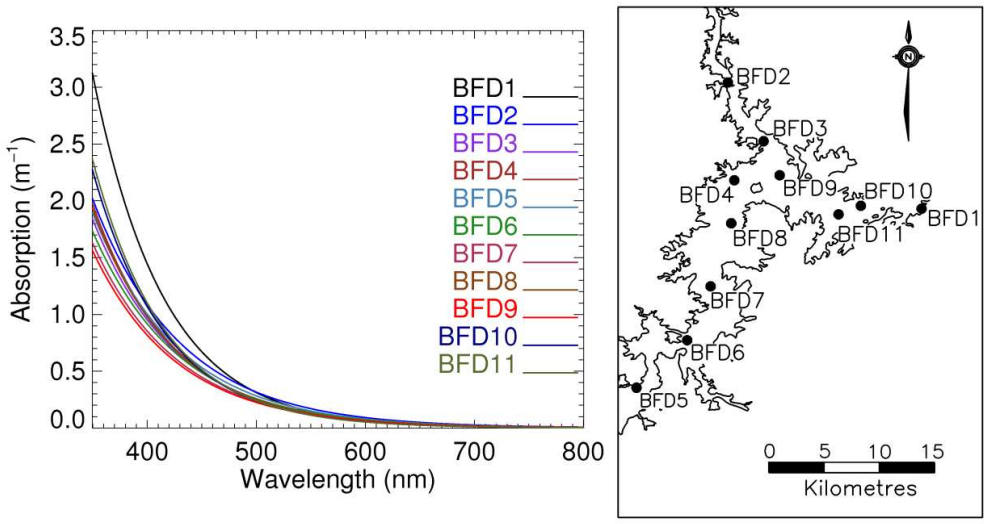

Figure A-8 The laboratory absorption for tripton for the Burdekin Falls Dam stations.

A.3 Fairbairn Dam

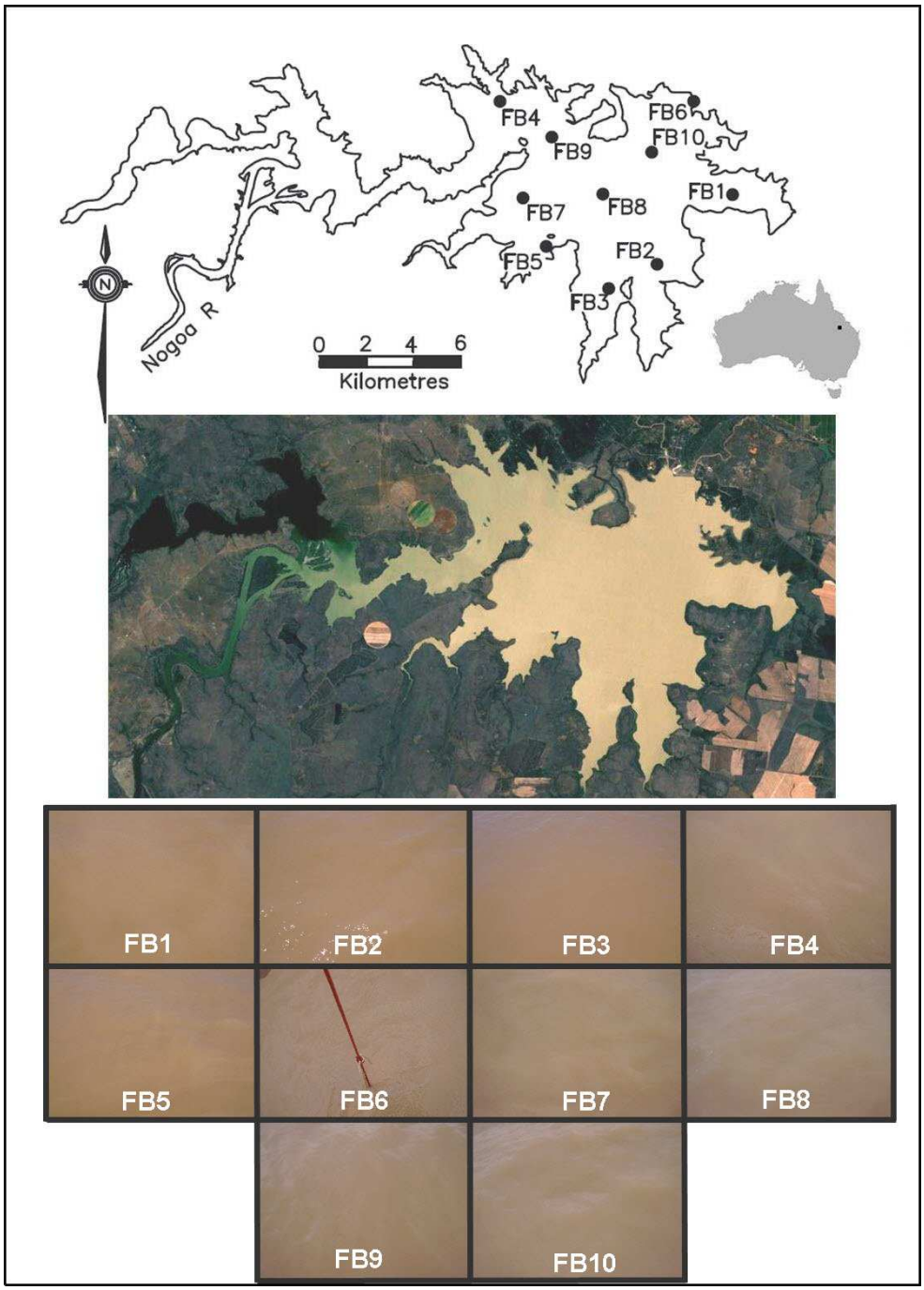

Figure A-9 Location of the SIOP sample sites for the October 2008 fieldwork activities on Fairbairn Dam, Australia. The top image shows the calculated full supply level and the middle image shows a Landsat 5 TM true colour image at the same scale as the map, captured on 3rd November 2008. The lower section of the figure shows photographs of the sample sites taken at the time of sampling.

The water quality parameter concentrations measured for the Fairbairn Dam stations are shown in Table A-3. Due to the very heavy tripton levels a CDOM sample was not filtered at every station.

Table A-3 The measured water quality parameter concentrations for Fairbairn Dam measurement stations.

Station	Chlorophyll *a* (μgl^{-1})	Tripton (mgl^{-1})	CDOM 440nm (m^{-1})	Tripton Inorganic Fraction (%)	Secchi Depth (m)
FB1	0.9	158.9	1.18	92	0.15
FB2	1.1	166.4	-	94	0.15
FB3	2.1	163.8	1.22	94	0.15
FB4	2.8	149.0	1.59	92	0.20
FB5	1.2	170.4	1.16	92	0.15
FB6	2.9	161.8	1.19	93	0.20
FB7	1.5	165.4	-	91	0.20
FB8	1.2	159.5	1.19	91	0.15
FB9	1.8	153.9	1.16	91	0.20
FB10	1.3	159.9	-	90	0.20

CDOM Absorption

The laboratory measured absorption spectra for CDOM were taken at seven of the ten sampling stations and are shown in Figure A-10.

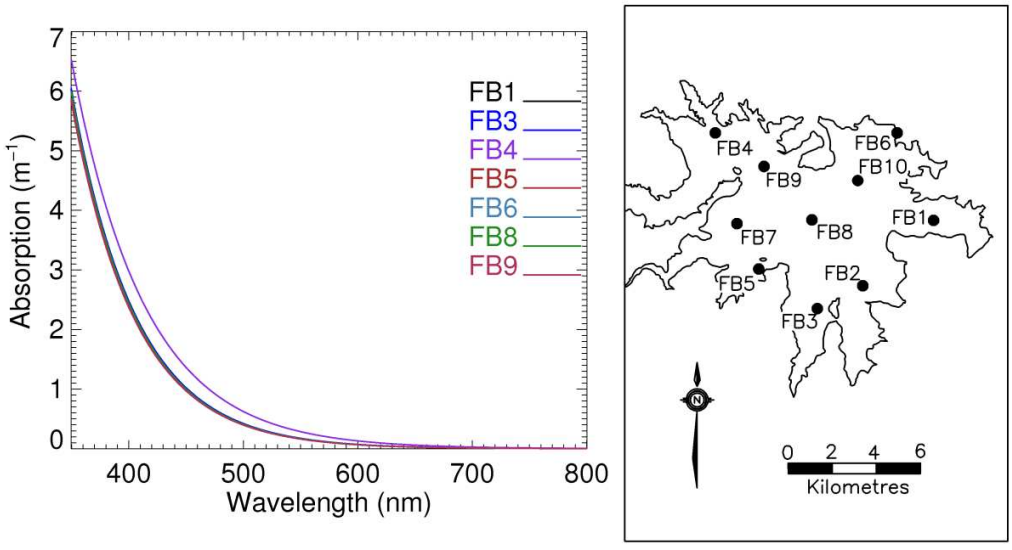

Figure A-10 The laboratory measured absorption for CDOM for the Fairbairn Dam stations.

Appendix B- Image Details

Table B-1 - Table B-3 list details the level 1b full resolution cloud free MERIS images obtained for the study sites

Table B-1 Sun and view geometry for the centre of Wivenhoe Dam for the 2007 and 2008 MERIS cloud free images

UTC Date	UTC Time (hh:mm:ss)	Sun Zenith (Decimal degrees)	Sun Azimuth (Decimal degrees)	View Zenith (Decimal degrees)	View Azimuth (Decimal degrees)
16th June 2007	23:40:33	59.61°	34.81°	16.59°	282.13°
29th June 2007	23:32:03	60.97°	37.37°	0.08°	357.36°
2nd July 2007	23:37:43	60.12°	36.41°	11.18°	282.45°
5th July 2007	23:43:23	59.24°	35.45°	21.65°	281.81°
18th July 2007	23:34:53	59.14°	38.90°	5.66°	282.77°
27th July 2007	23:51:54	55.37°	36.33°	35.31°	280.87°
22nd June 2008	23:48:58	58.80°	33.21°	31.09°	281.18°
8th July 2008	23:46:08	58.62°	35.23°	26.57°	281.50°
2nd Oct. 2008	23:43:15	36.08°	58.85°	21.63°	281.81°

Table B-2 Sun and view geometry for the centre of Fairbairn Dam for the 2008 MERIS cloud free images

UTC Date	UTC Time (hh:mm:ss)	Sun Zenith (Decimal degrees)	Sun Azimuth (Decimal degrees)	View Zenith (Decimal degrees)	View Azimuth (Decimal degrees)
22nd Sept 2008	23:56:40	38.13°	56.27°	7.92°	282.54°
26th Sept 2008	00:02:20	36.09°	55.58°	18.97°	281.98°
29th Sept. 2008	00:08:01	34.06°	55.58°	29.00°	281.43°
15th Oct. 2008	00:05:11	30.02°	64.26°	24.14°	281.70°
18th Oct 2008	00:10:52	28.12°	64.40°	33.51°	281.15°
27th Oct. 2008	23:56:40	29.16°	73.97°	7.92°	282.53°
31st Oct. 2008	00:02:20	27.46°	74.60°	18.97°	281.97°

Table B-3 Sun and view geometry for the centre of Burdekin Falls Dam for the 2008 MERIS cloud free images

UTC Date	UTC Time (hh:mm:ss)	Sun Zenith (Decimal degrees)	Sun Azimuth (Decimal degrees)	View Zenith (Decimal degrees)	View Azimuth (Decimal degrees)
26th Sept. 2008	0:01:34	35.44°	60.87°	5.21°	282.58°
29th Sept. 2008	00:07:15	33.41°	60.86°	16.71°	282.09°
15th Oct. 2008	00:04:25	29.88°	70.41°	11.07°	282.33°

Appendix C – Model Parameterisation

C.1 Matrix Inversion Method

To model the effect of the sun position nine simulation sets were run for clear skies with the sun zenith angle varying from 0° to 61.1°. For each set a quadratic and cubic function were used to model *f* as a function of subsurface reflectance. The results of these simulations are shown in Table C-1 and Table C-2.

Table C-1 The fitting co-efficients for the quadratic function $f = C_2 R(0^-)^2 + C_1 R(0^-) + C_0$, θ_s is the sun zenith angle and μ_w is the cosine of the sun zenith angle after it has passed through the air-water interface.

θ_s	μ_w	Co-efficients		
		C_2	C_1	C0
0	1.000	-8.535	2.330	0.312
9.5	0.992	-8.708	2.367	0.316
19.1	0.969	-9.059	2.438	0.325
28.95	0.931	-9.460	2.518	0.336
36.87	0.892	-9.986	2.655	0.363
43.53	0.855	-10.146	2.675	0.364
49.46	0.821	-10.364	2.750	0.392
54.9	0.788	-10.495	2.767	0.393
61.1	0.753	-10.518	2.821	0.421

Table C-2 The fitting co-efficients for the cubic function $f = C_3 R(0^-)^3 + C_2 R(0^-)^2 + C_1 R(0^-) + C_0$, θs is the sun zenith angle and μ_w is the cosine of the sun zenith angle after it has passed through the air-water interface.

θ_s	μ_w	Co-efficients			
		C_3	C_2	C_1	C0
0	1.000	70.578	-19.980	2.807	0.308
9.5	0.992	71.116	-20.429	2.864	0.312
19.1	0.969	74.510	-21.703	2.989	0.320
28.95	0.931	79.593	-23.420	3.147	0.330
36.87	0.892	80.563	-25.205	3.395	0.356
43.53	0.855	86.133	-26.455	3.470	0.356
49.46	0.821	83.793	-27.250	3.627	0.383
54.9	0.788	88.127	-28.292	3.693	0.383
61.1	0.753	81.339	-27.941	3.784	0.411

The co-efficients detailed in Table C-1 and Table C-2 were then plotted against $1/\cos(\mu_w)$ as shown in Figure C-1 and Figure C-2 to obtain functions to generate co-efficients for any sun position.

Quadratic Fit

$$C_2 = 23.50\left(\frac{1}{\mu_w}\right)^2 - 60.44\left(\frac{1}{\mu_w}\right) + 28.34 \quad \text{(C-1)}$$

$$C_1 = -4.158\left(\frac{1}{\mu_w}\right)^2 + 11.088\left(\frac{1}{\mu_w}\right) - 4.585 \quad \text{(C-2)}$$

$$C_0 = -0.1346\left(\frac{1}{\mu_w}\right)^2 + 0.6322\left(\frac{1}{\mu_w}\right) - 0.1847 \quad \text{(C-3)}$$

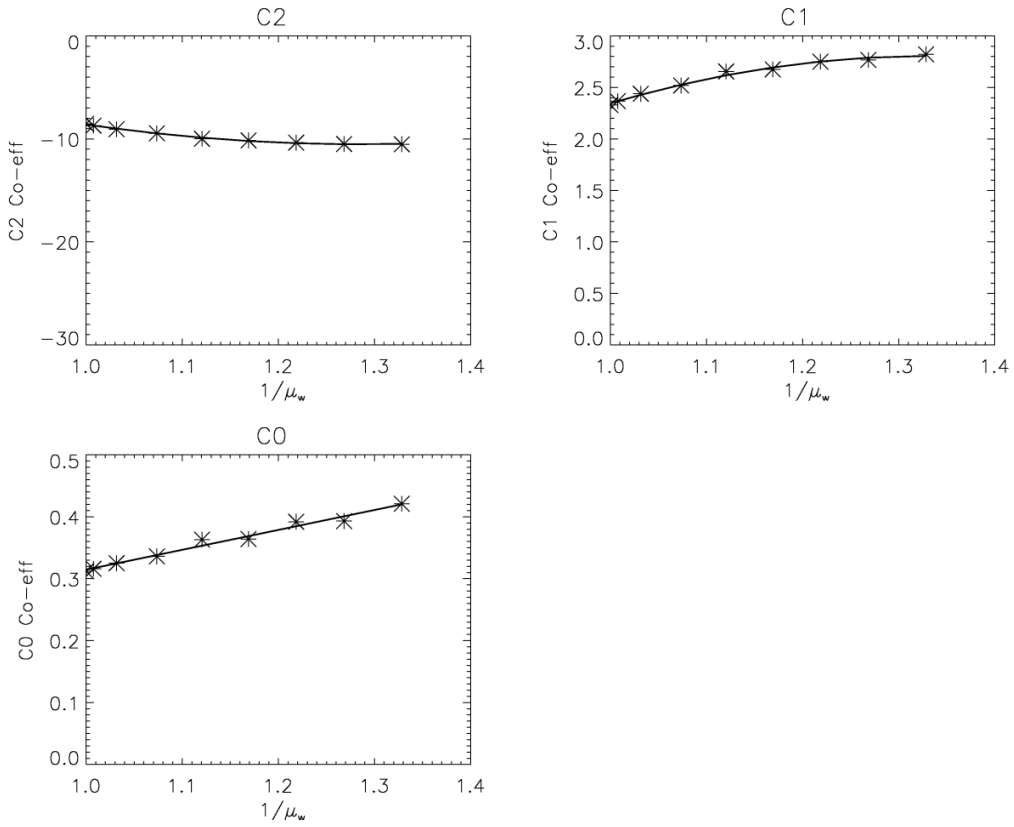

Figure C-1 The co-efficients detailed in Table C-1 plotted against $1/\mu_w$ and the function of best fit for those co-efficients.

Cubic Fit

$$C_3 = -307.1\left(\frac{1}{\mu_w}\right)^2 + 752.3\left(\frac{1}{\mu_w}\right) - 374.8 \quad \text{(C-4)}$$

$$C_2 = 87.32\left(\frac{1}{\mu_w}\right)^2 - 227.8\left(\frac{1}{\mu_w}\right) + 120.4 \quad \text{(C-5)}$$

$$C_1 = -7.062\left(\frac{1}{\mu_w}\right)^2 + 19.34\left(\frac{1}{\mu_w}\right) - 9.458 \quad \text{(C-6)}$$

$$C_0 = -0.1014\left(\frac{1}{\mu_w}\right)^2 + 0.5349\left(\frac{1}{\mu_w}\right) - 0.1244 \quad \text{(C-7)}$$

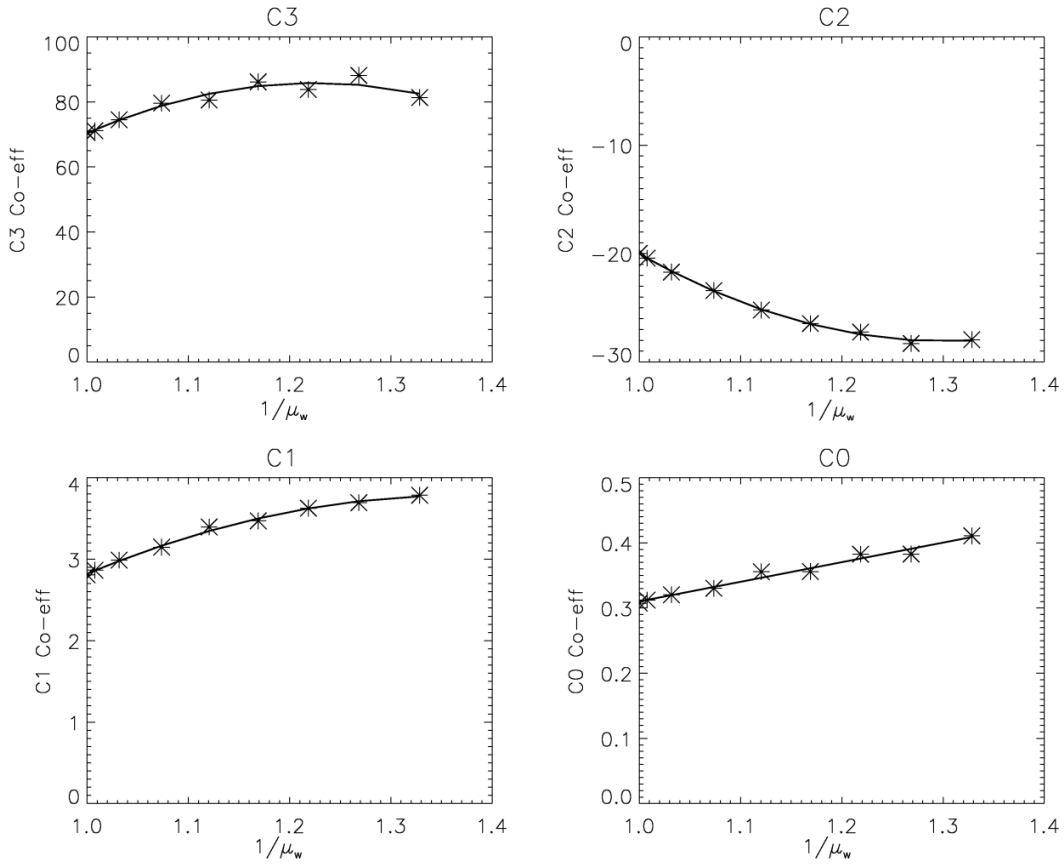

Figure C-2 The co-efficients detailed in Table C-2 plotted against $1/\mu_w$ and the function of best fit for those co-efficients.

C.2 PSO

By using the forward model and a spectrum matching approach the effect of the non-linear nature of the model is easier to deal with. Three approaches were used to model the reflectance from the IOP values. The first used the Lee et al. (2004) approach and the other two used the Gordon et al. (1975) formulation in a quadratic and cubic form.

Lee et al. (2004) Form

As the surface is dependent on the sun angle a surface was generated for each of the nine simulated data sets. The results of the planar fit are shown in Table C-3 and the curved surface in Table C-4.

Not all the co-efficients shown in Table C-4 and Figure C-3 display a particularly regular variation with the change in the sun angle. However each term contributes a different proportion of the final reflectance value and a sensitivity analysis showed those co-efficents that show the least consistent pattern make the smallest contributions to the reflectance value. Over the typical water quality parameter concentrations for Wivenhoe Dam the sensitivity analysis showed that contribution from the C_0 (1.5%), C_1(22%), C_2 (0.5%) parameters was relatively stable with the change in sun position. This is to be expected as the phase function of the water is uniform so the change in the sun elevation will not change that proportion of the photons that are scattered upwards. Furthermore the trend in C_2 is negligible for practical purposes and its contribution is consistently small so it can safely be replaced by a constant value. For the other co-efficients the increase in sun zenith angle means the influence of the C_3 (57-66%) increases significantly, C_4 (7-0.5%) co-efficient decreases rapidly and C_5 (11-8%) decreases slightly until 50° when the former two reverse the direction of their trend.

Table C-3 The fitting co-efficients for the plane surface $R(0^-)= C2\ \omega_p + C1\ \omega_w + C0$, θs is the sun zenith angle and μ_w is the cosine of the sun zenith angle after it has passed through the air-water interface.

θ_s	μ_w	Co-efficients		
		C_2	C_1	C_0
0	1.0	0.4678	0.3797	-0.0051
9.5	0.9923	0.4760	0.3796	-0.0052
19.1	0.9694	0.4909	0.3813	-0.0053
28.95	0.9314	0.5083	0.3852	-0.0054
36.87	0.8925	0.5497	0.3838	-0.0056
43.53	0.8555	0.5509	0.3922	-0.0056
49.46	0.8207	0.5881	0.3857	-0.0057
54.9	0.7884	0.5893	0.3939	-0.0056
61.1	0.7541	0.6269	0.3820	-0.0057

Table C-4 The fitting co-efficients for polynomial surface $R(0^-)= C5\ \omega_p^2 + C4\ \omega_w\ \omega_p + C3\ \omega_p + C2\ \omega_w^2 + C1\ \omega_w + C0$, θs is sun zenith angle and μ_w is the cosine of the sun zenith angle after it has passed through the air-water interface.

θ_s	μ_w	Co-efficients					
		C_5	C_4	C_3	C_2	C_1	C_0
0	1.0	0.5559	1.4475	0.3421	-0.1534	0.3539	-0.0007
9.5	0.9923	0.5583	1.3132	0.3498	-0.1529	0.3574	-0.0007
19.1	0.9694	0.5597	1.1562	0.3645	-0.1594	0.3636	-0.0009
28.95	0.9314	0.5583	1.0681	0.3823	-0.1741	0.3708	-0.0010
36.87	0.8925	0.5491	0.373	0.4263	-0.1594	0.3867	-0.0013
43.53	0.8555	0.5446	0.7029	0.4283	-0.1987	0.3885	-0.0013
49.46	0.8207	0.5189	-0.0952	0.4719	-0.1432	0.4000	-0.0016
54.9	0.7884	0.5141	0.2103	0.4739	-0.1874	0.4023	-0.0016
61.1	0.7541	0.4877	-0.9201	0.5185	-0.1166	0.4148	-0.0019

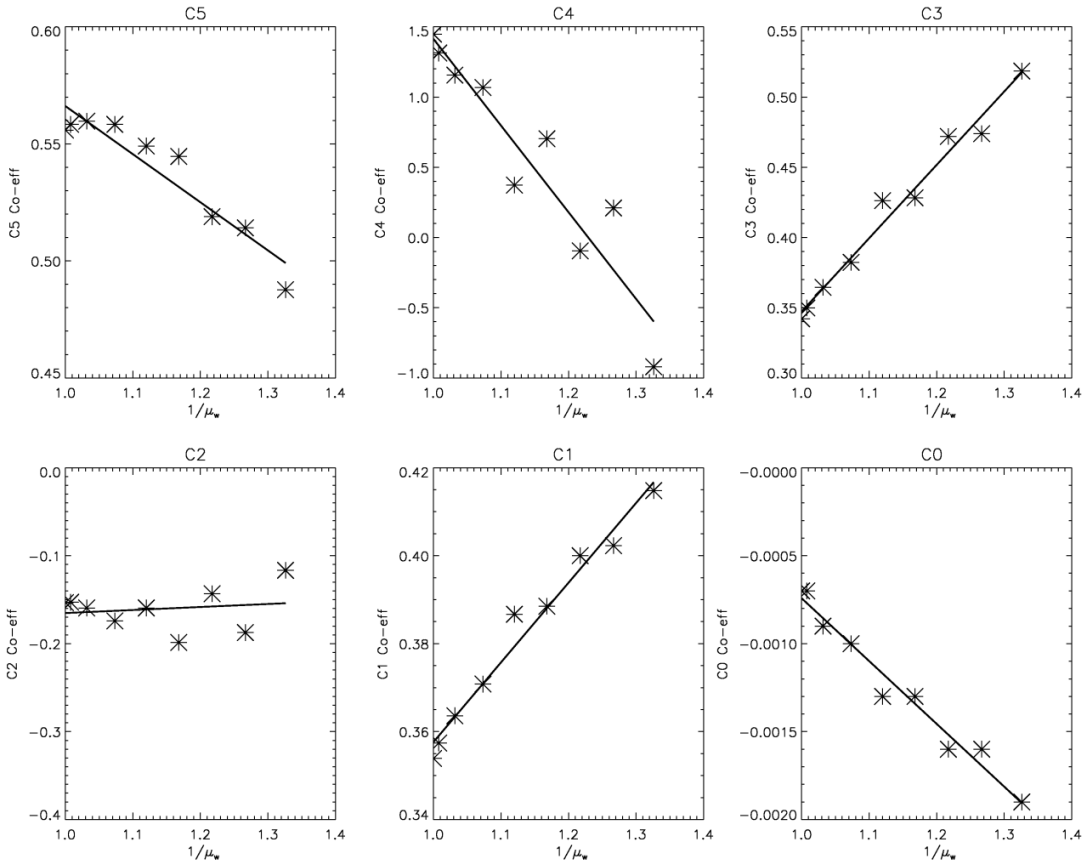

Figure C-3 The co-efficients detailed in Table 4 plotted against 1/cos(μ_w) and the function of best fit for those co-efficients.

$$C_5 = -0.2055\left(\frac{1}{\mu_w}\right) + 0.7716 \quad \text{(C-8)}$$

$$C_4 = -6.169\left(\frac{1}{\mu_w}\right) + 7.582 \quad \text{(C-9)}$$

$$C_3 = 0.5221\left(\frac{1}{\mu_w}\right) - 0.1748 \quad \text{(C-10)}$$

$$C_2 = -0.1610 \quad \text{(C-11)}$$

$$C_1 = 0.1812\left(\frac{1}{\mu_w}\right) + 0.1765 \quad \text{(C-12)}$$

$$C_0 = -0.0028\left(\frac{1}{\mu_w}\right) + 0.0036 \quad \text{(C-13)}$$

Gordon et al.(1975) Form

To see whether the added complexity of the Lee et al (2004) approach increased the accuracy of the ensuing data retrieval the co-efficients of the traditional Gordon et al. (1975) approach were calculated by fitting $R(0^-) = \sum_{n=0}^{n=3} f_n(0)\left(\frac{b_b}{a+b_b}\right)^n$ for n= 2 and n=3.

Table C-5 The fitting co-efficients for the quadratic formulation $R(0^-) = C2\ \omega^2 + C1\ \omega + C0$, θs is the sun zenith angle and μ_w is the cosine of the sun zenith angle after it has passed through the air-water interface.

θ_s	μ_w	Co-efficients		
		C_2	C_1	C_0
0	1	0.5556	0.3424	-0.0007
9.5	0.9923	0.5582	0.3500	-0.0007
19.1	0.9694	0.5600	0.3644	-0.0009
28.95	0.9314	0.5589	0.3821	-0.0010
36.87	0.8925	0.5510	0.4252	-0.0013
43.53	0.8555	0.5462	0.4276	-0.0013
49.46	0.8207	0.5218	0.4702	-0.0016
54.9	0.7884	0.5168	0.4725	-0.0016
61.1	0.7541	0.4920	0.5158	-0.0019

Table C-6 The fitting co-efficients for cubic formulation $R(0^-) = C3\ \omega^3 + C2\ \omega^2 + C1\ \omega + C0$, θs is the sun zenith angle and μ_w is the cosine of the sun zenith angle after it has passed through the air-water interface.

θ_s	μ_w	Co-efficients			
		C_3	C_2	C_1	C_0
0	1	-0.8315	0.8471	0.3155	-0.0002
9.5	0.9923	-0.9267	0.8831	0.3200	-0.0002
19.1	0.9694	-1.0880	0.9415	0.3293	-0.0002
28.95	0.9314	-1.2615	1.0012	0.3414	-0.0002
36.87	0.8925	-1.7367	1.1600	0.3691	-0.0002
43.53	0.8555	-1.6951	1.1405	0.3728	-0.0002
49.46	0.8207	-2.1209	1.2655	0.4017	-0.0003
54.9	0.7884	-2.0794	1.2459	0.4053	-0.0003
61.1	0.7541	-2.5518	1.3861	0.4334	-0.0003

Quadratic Fit

$$C_2 = -0.7097\left(\frac{1}{\mu_w}\right)^2 + 1.444\left(\frac{1}{\mu_w}\right) - 0.1764 \quad \text{(C-14)}$$

$$C_1 = -0.2703\left(\frac{1}{\mu_w}\right)^2 + 1.137\left(\frac{1}{\mu_w}\right) - 0.5225 \quad \text{(C-15)}$$

$$C_0 = 0.0035\left(\frac{1}{\mu_w}\right)^2 - 0.0116\left(\frac{1}{\mu_w}\right) + 0.0074 \quad \text{(C-16)}$$

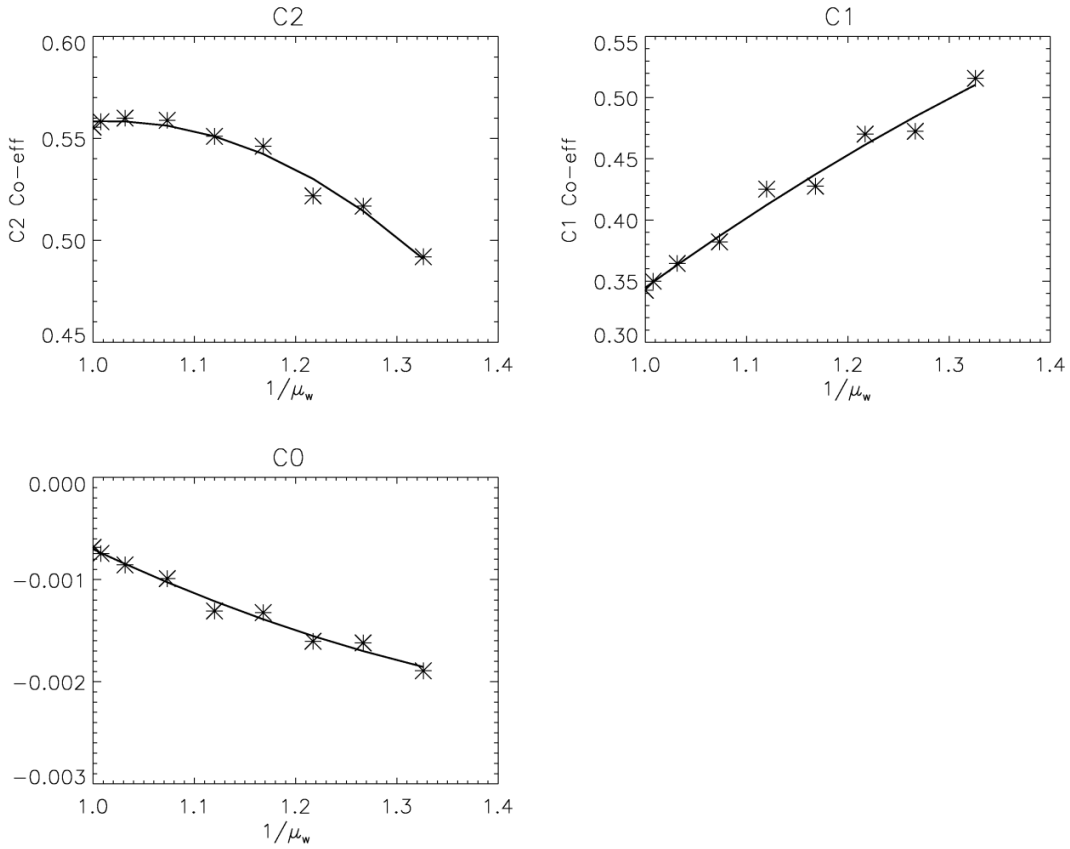

Figure C-4 The co-efficients detailed in Table C-5 plotted against $1/\mu_w$ and the function of best fit for those co-efficients.

Cubic Fit

$$C_3 = 4.213\left(\frac{1}{\mu_w}\right)^2 - 14.70\left(\frac{1}{\mu_w}\right) + 9.613 \quad \text{(C-17)}$$

$$C_2 = -2.197\left(\frac{1}{\mu_w}\right)^2 + 6.621\left(\frac{1}{\mu_w}\right) - 3.559 \quad \text{(C-18)}$$

$$C_1 = -0.1322\left(\frac{1}{\mu_w}\right)^2 + 0.6579\left(\frac{1}{\mu_w}\right) - 0.2093 \quad \text{(C-19)}$$

$$C_0 \approx 0 \quad \text{(C-20)}$$

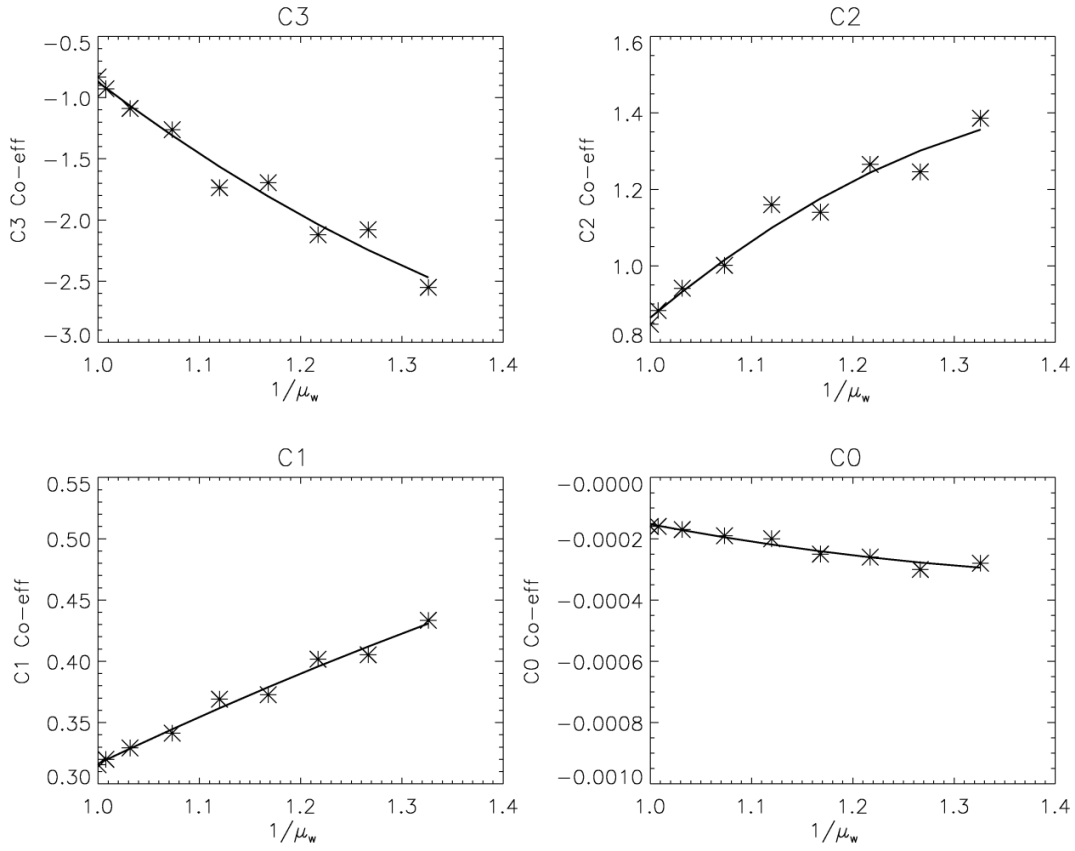

Figure C-5 The co-efficients detailed in Table C-6 plotted against $1/\mu_w$ and the function of best fit for those co-efficients.

Appendix D Minimum Detection Limits

D.1 Wivenhoe Dam SIOP Set

Figure D-1- Figure D-3 show the signal sensitivity for water quality for the Wivenhoe Dam SIOP set ($c_0 = 0.5159$, $c_1 = 0.4916$). There is one volume for each MERIS band.

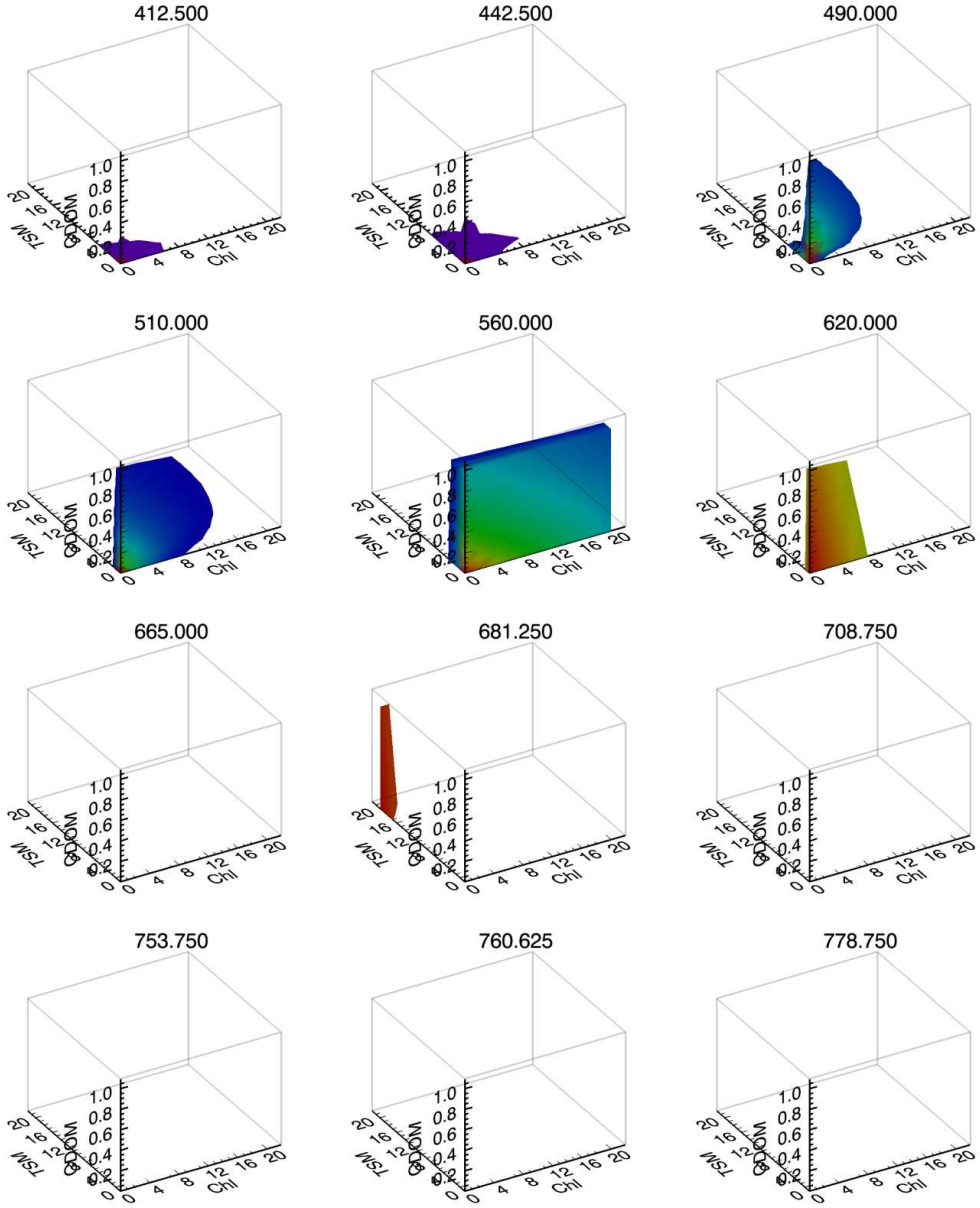

Figure D-1 Acceptable water quality parameter combinations that allow the change in the reflectance spectra for that wavelength to be distinguished from environmental noise with a change in concentration of chlorophyll *a* by 1µgl^{-1}. The volumes were calculated with the quadratic model for reflectance that was derived from the θ_s =61.1° simulation calculated with the Wivenhoe Dam SIOP set.

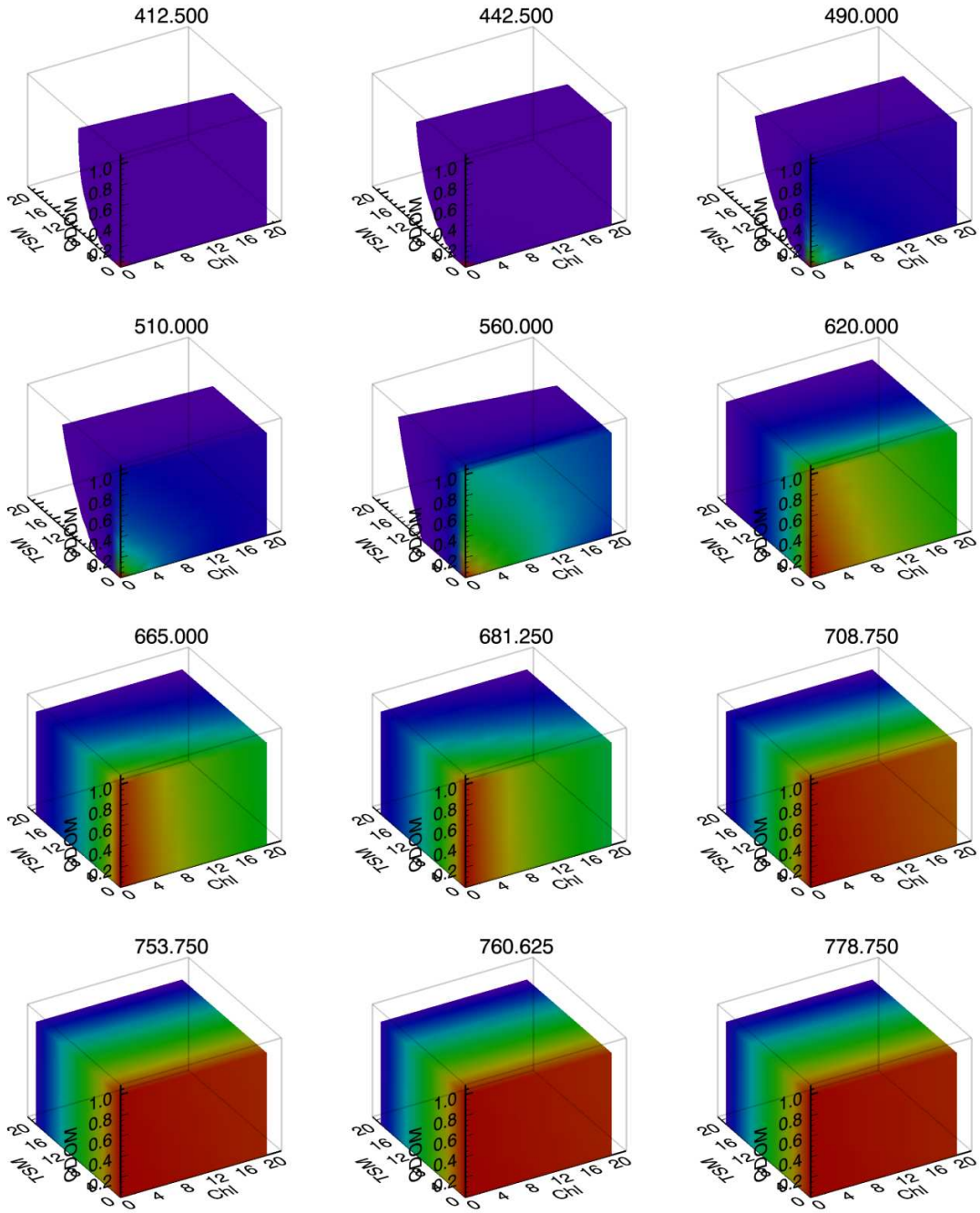

Figure D-2 Acceptable water quality parameter combinations that allow the change in the reflectance spectra for that wavelength to be distinguished from environmental noise with a change in concentration of TSM by 1mgl^{-1}. The volumes were calculated with the quadratic model for reflectance that was derived from the θ_s =61.1° simulation calculated with the Wivenhoe Dam SIOP set.

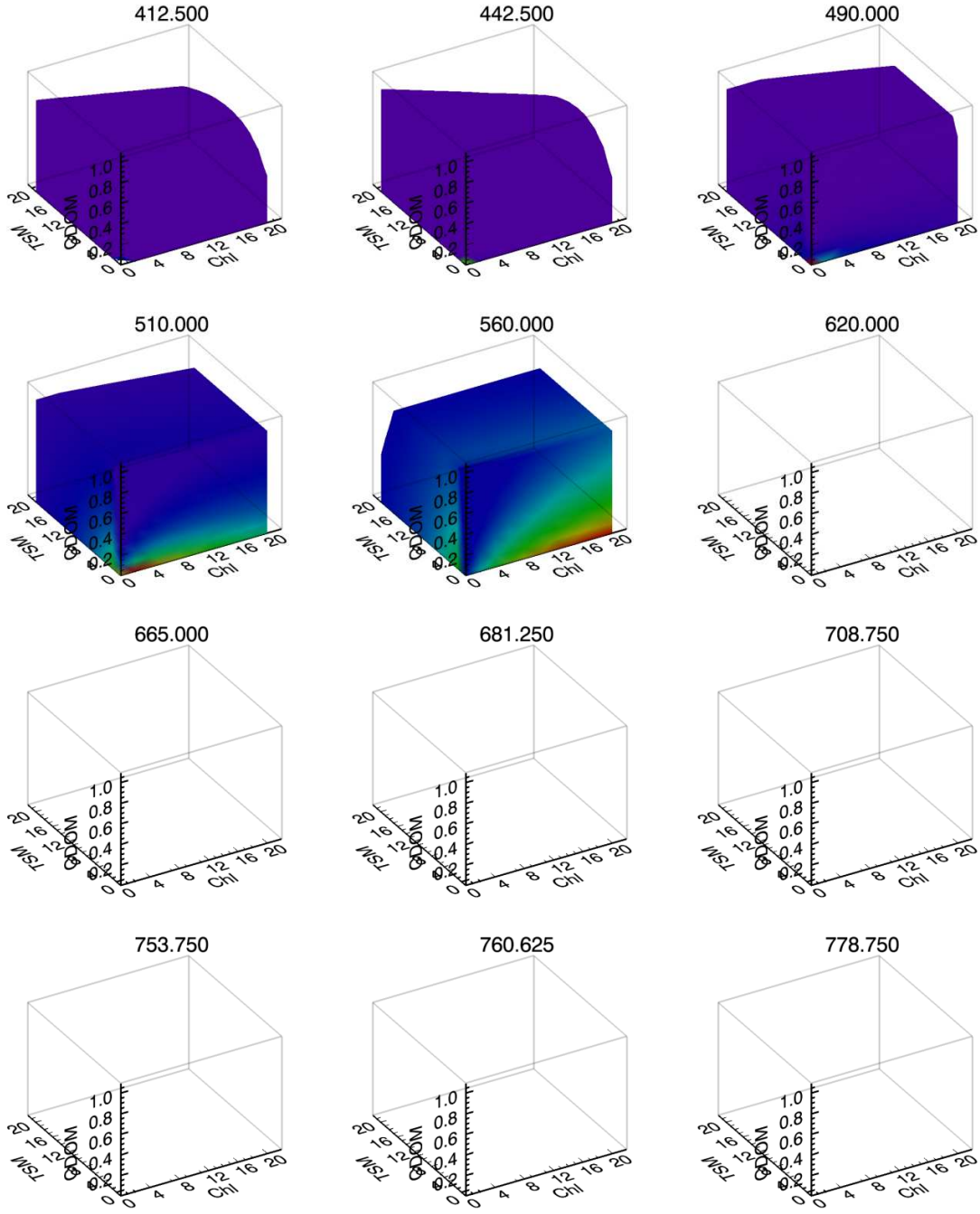

Figure D-3 Acceptable water quality parameter combinations that allow the change in the reflectance spectra t for that wavelength to be distinguished from environmental noise with a change in concentration of CDOM by 0.1 m^{-1}. The volumes were calculated with the quadratic model for reflectance that was derived from the θ_s =61.1° simulation calculated with the Wivenhoe Dam SIOP set.

D.2 Burdekin Falls Dam Lower Basin SIOP Set

Figure D-4 - Figure D-6 show the signal sensitivity for water quality for the Burdekin Falls Dam lower SIOP set (Lower: $c_0 = 0.4102$, $c_1 = 0.2578$). There is one volume for each MERIS band.

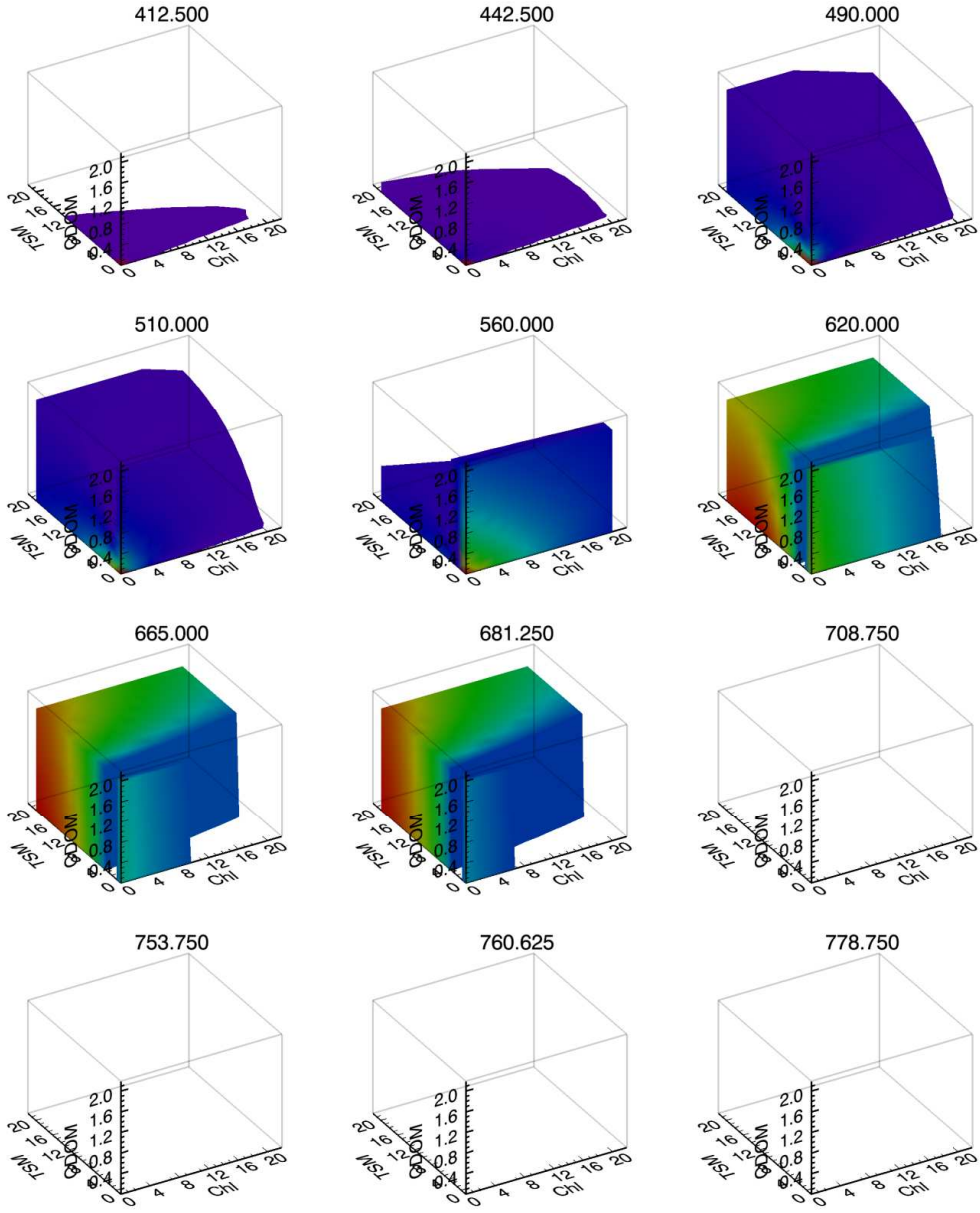

Figure D-4 Acceptable water quality parameter combinations that allow the change in the reflectance spectra for that wavelength to be distinguished from environmental noise with a change in concentration of chlorophyll *a* by 1µgl^{-1}. The volumes were calculated with the quadratic model for reflectance that was derived from the θ_s =61.1° simulation calculated with the Burdekin Falls Dam lower SIOP set.

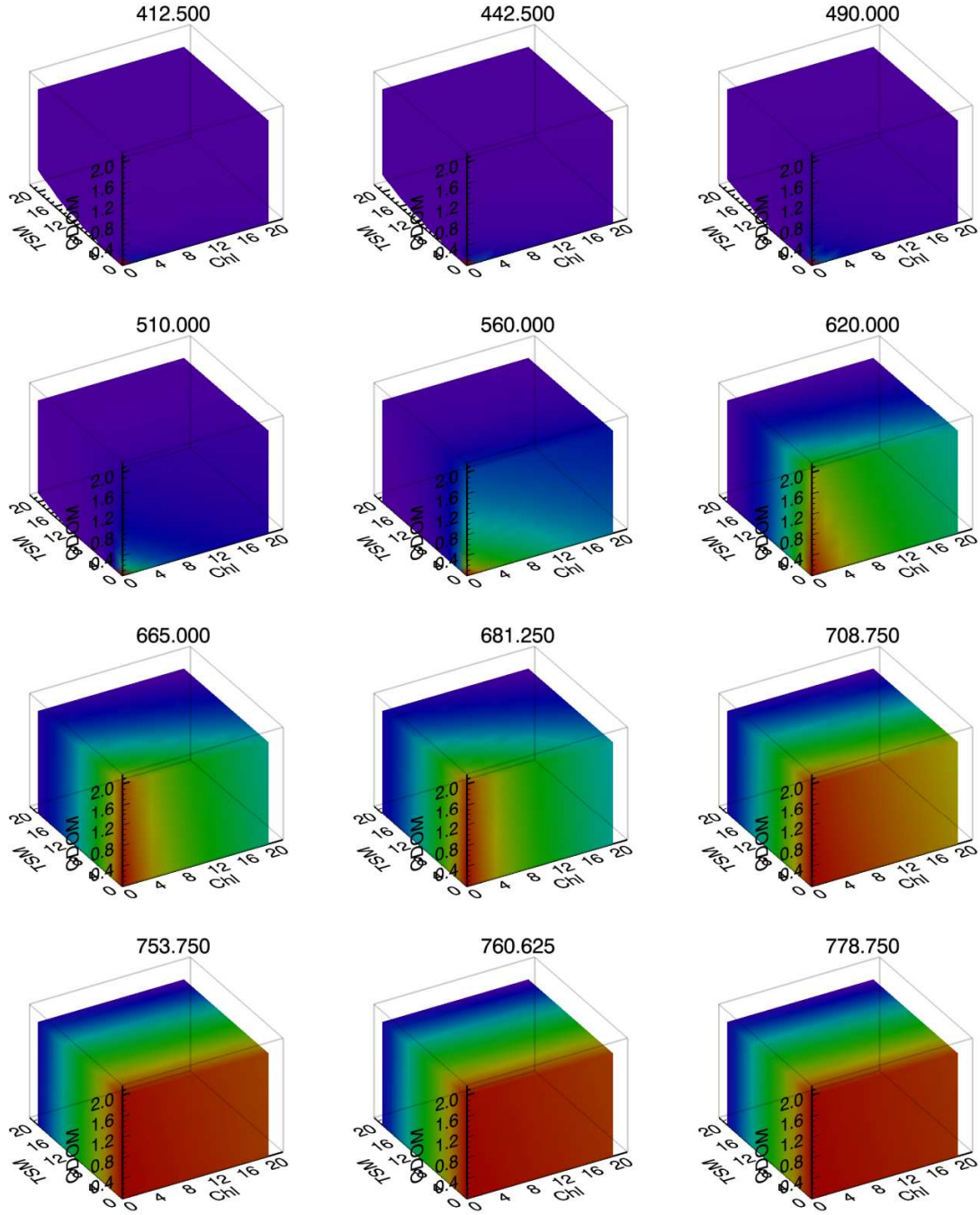

Figure D-5 Acceptable water quality parameter combinations that allow the change in the reflectance spectra for that wavelength to be distinguished from environmental noise with a change in concentration of TSM by 1mgl^{-1}. The volumes were calculated with the quadratic model for reflectance that was derived from the θ_s =61.1° simulation calculated with the Burdekin Falls Dam lower SIOP set.

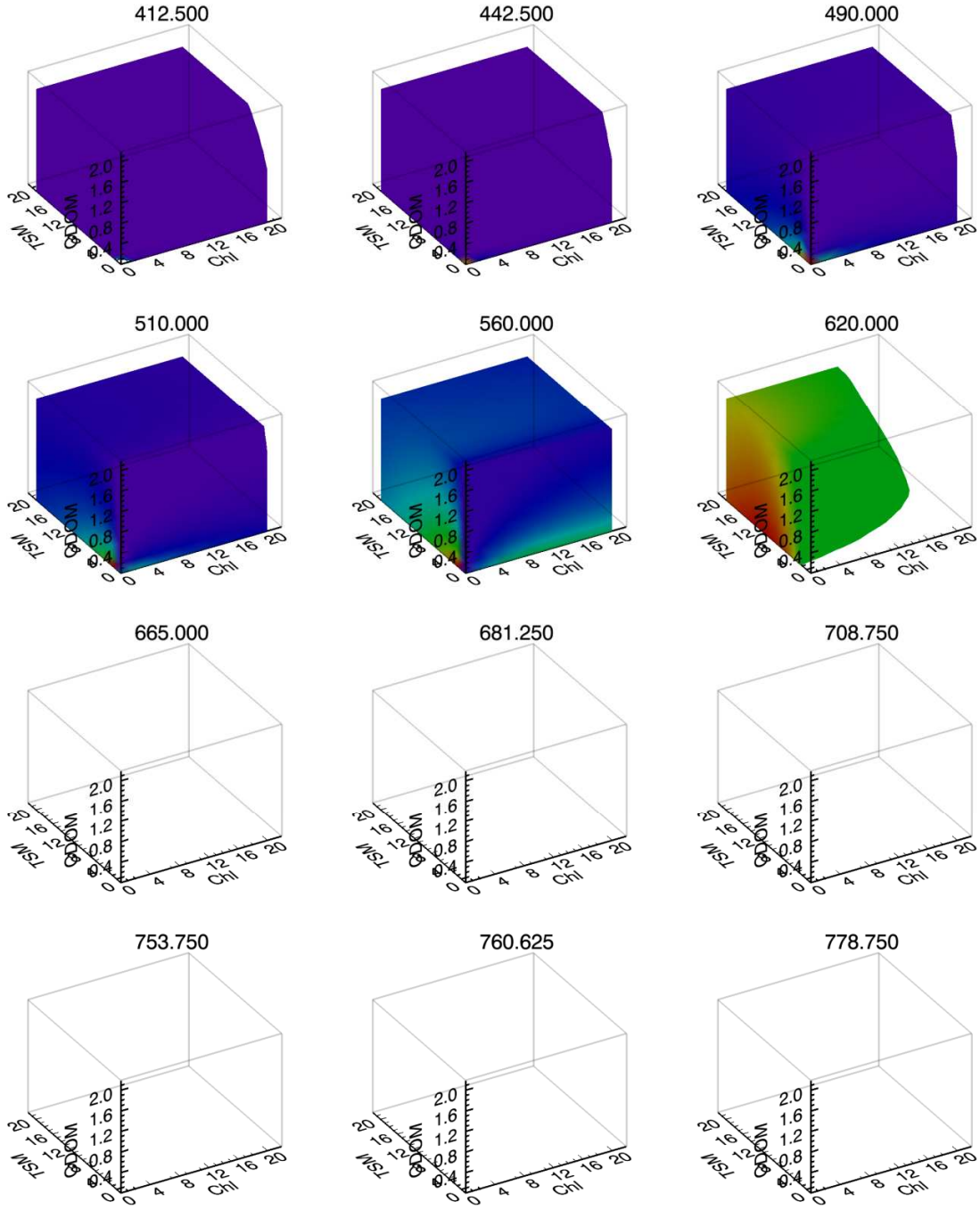

Figure D-6 Acceptable water quality parameter combinations that allow the change in the reflectance spectra for that wavelength to be distinguished from environmental noise with a change in concentration of CDOM by0.1 m^{-1}. The volumes were calculated with the quadratic model for reflectance that was derived from the θ_s =61.1° simulation calculated with the Burdekin Falls Dam lower SIOP set.

Appendix E October 2008 MIM Inversion Results

Table E-1 shows the means of the absolute values of error calculated for the each weighting schemes shown in Figure E-1. Figure E-2 - Figure E-5 show plots of the laboratory concentrations vs image retrieved concentrations for some selected weighting schemes.

Table E-1 The means of the absolute values of error between the laboratory measured concentrations and those retrieved from the 15th October 2008 image for all the trialled weighting schemes.

	Chl (μgl^{-1})		TR (mgl^{-1})		CDOM(m^{-1})	
	Av	SD	Av	SD	Av	SD
NO_WEIGHTS	4.31	2.82	1.79	1.23	0.52	0.26
3_BANDS	7.72	5.53	3.39	3.04	0.25	0.25
MER_BL_DER1	9.53	7.34	2.63	1.32	0.51	0.31
MER_BL_DER2	12.3	10.6	2.31	1.15	0.41	0.23
MER_BL_DER3	3.19	1.91	2.57	2.18	0.46	0.31
MER_BL_DER4	2.43	1.04	2.60	2.13	0.28	0.31
MER_BL_DER5	3.03	1.86	2.20	1.93	0.47	0.30
MER_BL_DER6	3.28	2.16	4.22	1.12	0.87	0.18
MER_BL_DER7	3.79	2.84	3.84	1.11	0.79	0.19
MER_BL_RAN1	13.8	5.35	1.74	0.84	0.12	0.11
MER_BL_RAN2	3.53	2.57	1.30	1.12	0.47	0.25
MER_BL_RAN3	26.6	15.3	3.11	1.87	0.58	0.24
MER_BL_RAN4	5.40	2.81	1.81	1.26	0.53	0.26
MER_BL_RAN5	5.04	2.71	2.20	2.00	0.21	0.22
MER_BL_RAN6	2.41	0.68	2.56	2.21	0.21	0.22
MER_BL_RAN7	7.84	7.18	2.21	1.27	0.48	0.22
MER_BL_RAN8	5.40	2.81	1.81	1.26	0.53	0.26
MER_BL_REF1	5.80	5.23	1.50	1.21	0.44	0.23
MER_BL_REF2	4.44	3.91	1.28	1.18	0.44	0.24
MER_BL_REF3	3.88	3.31	1.24	1.07	0.39	0.24
MER_BU_DER1	9.25	5.54	2.68	1.58	0.58	0.29
MER_BU_DER2	8.28	7.27	2.73	1.29	0.48	0.27
MER_BU_DER3	3.19	1.91	2.57	2.18	0.46	0.31
MER_BU_DER4	2.43	1.04	2.60	2.13	0.28	0.31
MER_BU_DER5	3.03	1.86	2.20	1.93	0.47	0.30
MER_BU_DER6	3.28	2.16	4.22	1.12	0.87	0.18
MER_BU_DER7	3.79	2.84	3.84	1.11	0.79	0.19
MER_BU_RAN1	1.44	1.68	2.71	2.36	0.28	0.17
MER_BU_RAN2	1.66	1.62	2.69	2.35	0.25	0.18
MER_BU_RAN3	15.4	11.6	2.99	1.55	0.61	0.20
MER_BU_RAN4	17.7	11.4	2.72	1.79	0.52	0.35
MER_BU_RAN5	8.98	1.68	2.83	1.39	0.84	0.22
MER_BU_RAN6	26.4	9.15	3.06	1.63	0.96	0.31
MER_BU_RAN7	5.38	5.71	2.86	1.63	0.30	0.20
MER_BU_RAN8	13.0	5.55	2.31	1.37	0.54	0.21
MER_BU_REF1	5.80	5.23	1.50	1.21	0.44	0.23
MER_BU_REF2	4.74	4.15	1.29	1.18	0.43	0.24
MER_BU_REF3	4.41	4.27	1.39	1.27	0.49	0.24

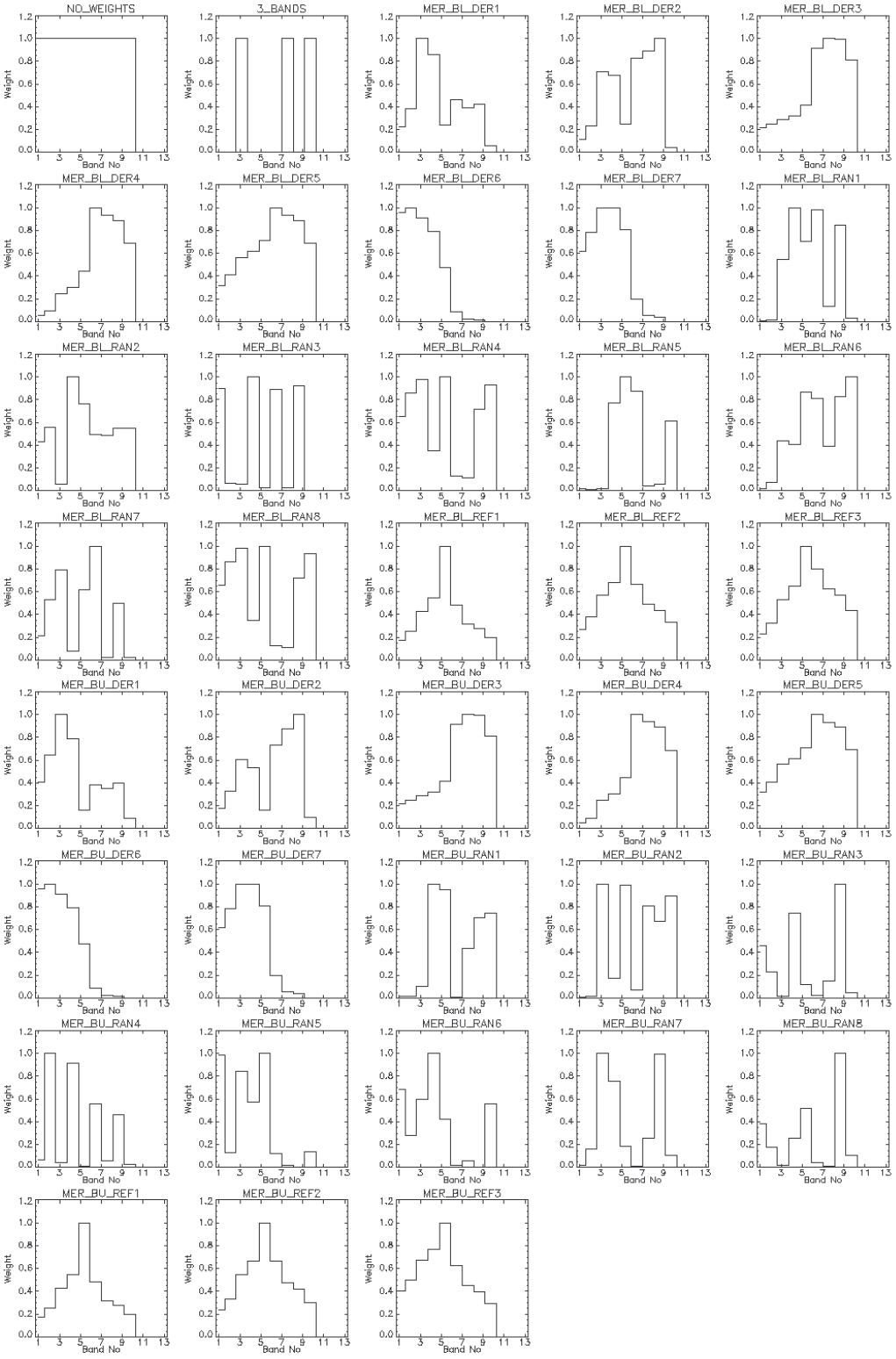

Figure E-1 The weighting schemes applied to the Burdekin Falls Dam images.

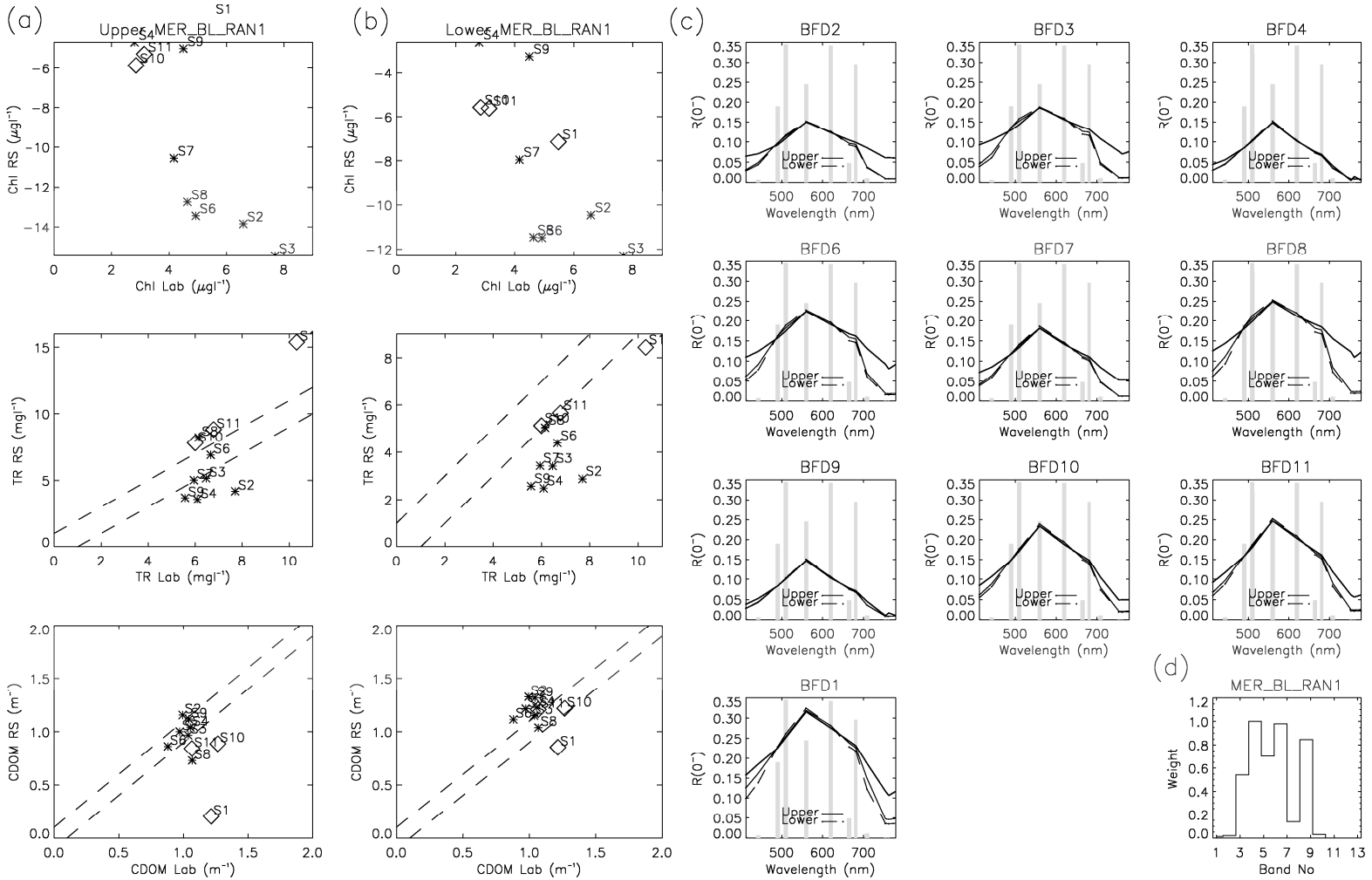

Figure E-2 The laboratory concentrations vs image retrieved concentrations using the MER_BL_RAN1 weighting scheme. (a) Using the Upper basin SIOP set. (b) Using the Lower basin SIOP set. The diamond symbols show the stations that are geographically in the lower basin. The dotted lines show the bounds of 1μgl^{-1} for chlorophyll *a*, 1mgl^{-1} of tripton and 0.1 m^{-1} for CDOM. (c) The optical closure for each station (d) The weighting scheme.

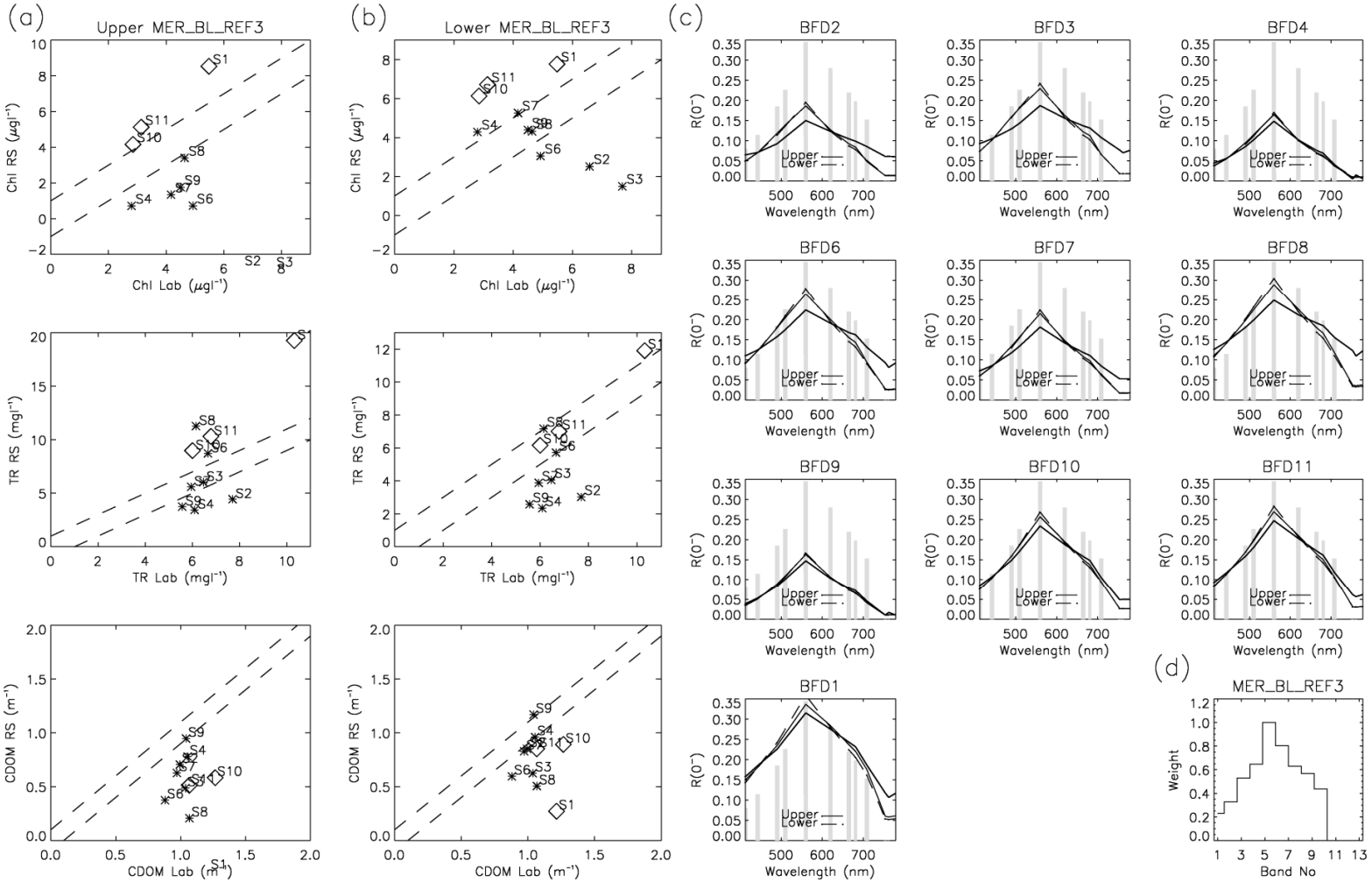

Figure E-3 The laboratory concentrations vs image retrieved concentrations using the MER_BL_REF3 weighting scheme. (a) Using the Upper basin SIOP set. (b) Using the Lower basin SIOP set. The diamond symbols show the stations that are geographically in the lower basin. The dotted lines show the bounds of 1μgl^{-1} for chlorophyll *a*, 1mgl^{-1} of tripton and 0.1 m^{-1} for CDOM. (c) The optical closure for each station (d) The weighting scheme.

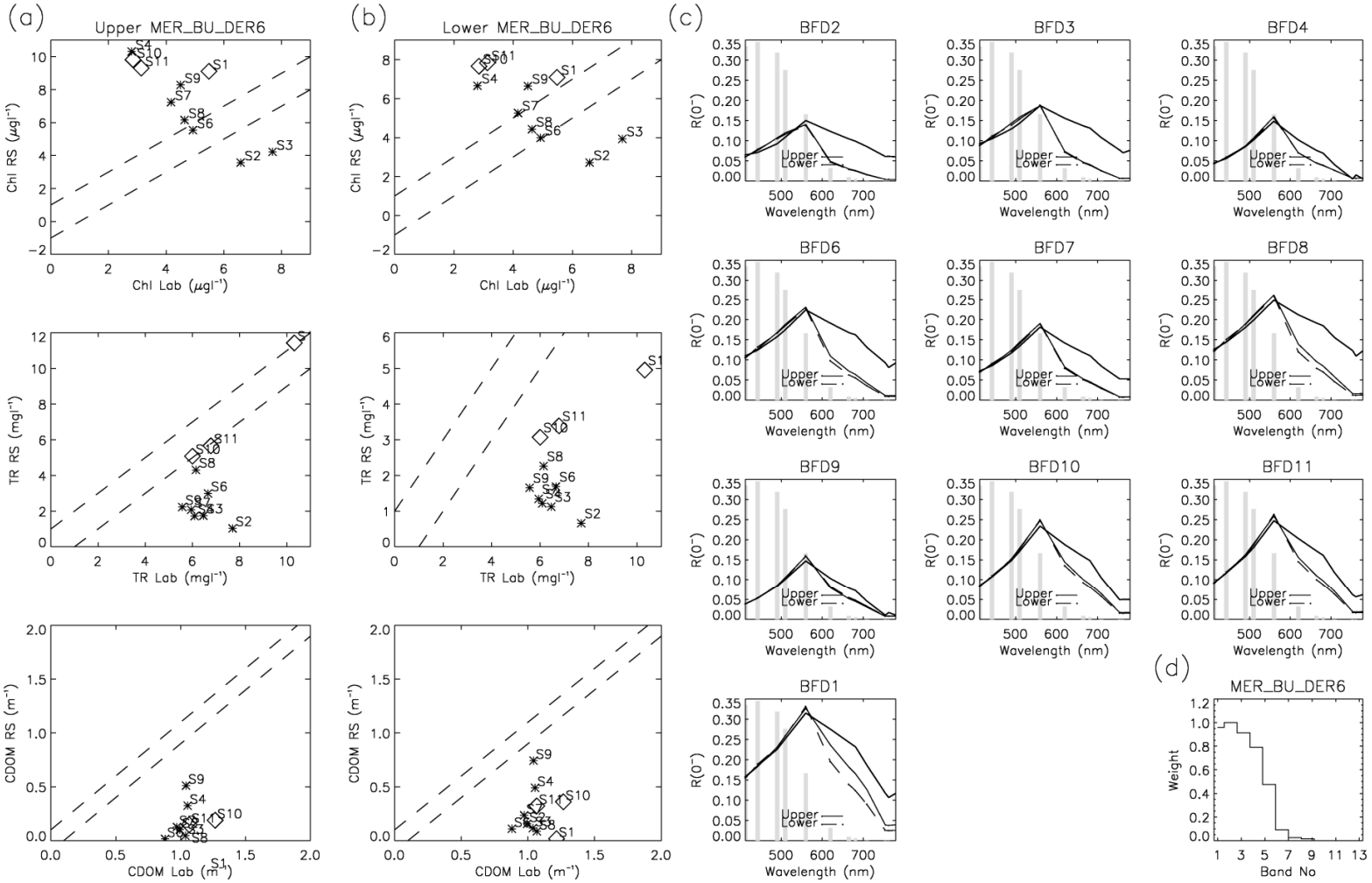

Figure E-4 The laboratory concentrations vs image retrieved concentrations using the MER_BU_DER6 weighting scheme. (a) Using the Upper basin SIOP set. (b) Using the Lower basin SIOP set. The diamond symbols show the stations that are geographically in the lower basin. The dotted lines show the bounds of 1μgl^{-1} for chlorophyll *a*, 1mgl^{-1} of tripton and 0.1 m^{-1} for CDOM. (c) The optical closure for each station (d) The weighting scheme.

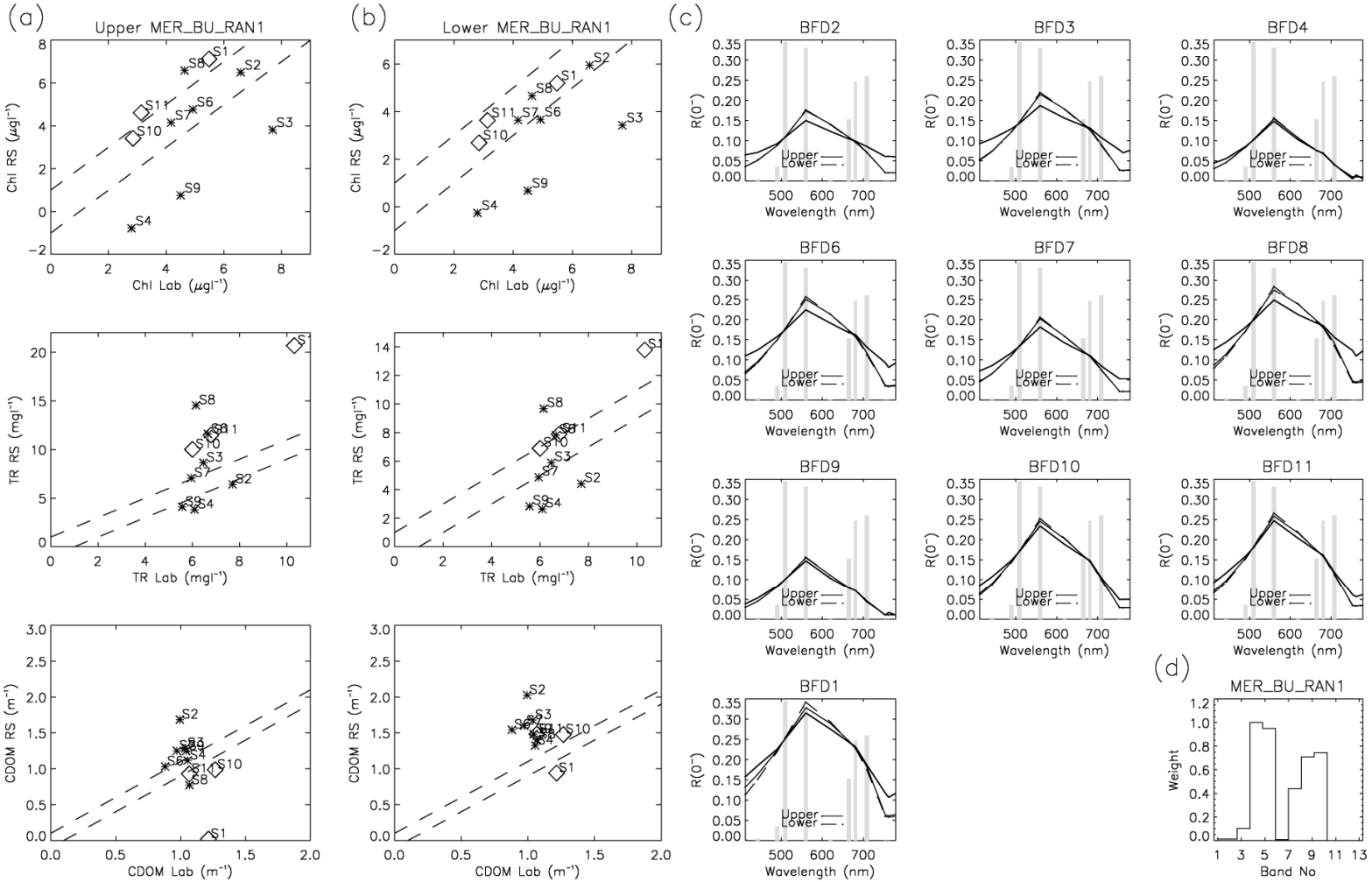

Figure E-5 The laboratory concentrations vs image retrieved concentrations using the MER_BU_RAN1 weighting scheme. (a) Using the Upper basin SIOP set. (b) Using the Lower basin SIOP set. The diamond symbols show the stations that are geographically in the lower basin. The dotted lines show the bounds of 1μgl^{-1} for chlorophyll *a*, 1mgl^{-1} of tripton and 0.1 m^{-1} for CDOM. (c) The optical closure for each station (d) The weighting scheme.

Appendix F – Validation Water Quality Parameter Measurements

F.1 Observation Stations

Water samples were taken from the surface water at 25 observations stations on the afternoon of 12th August 2009 between 1:40 pm and 4:10 pm. The locations of those observation stations are shown in Figure F-1.

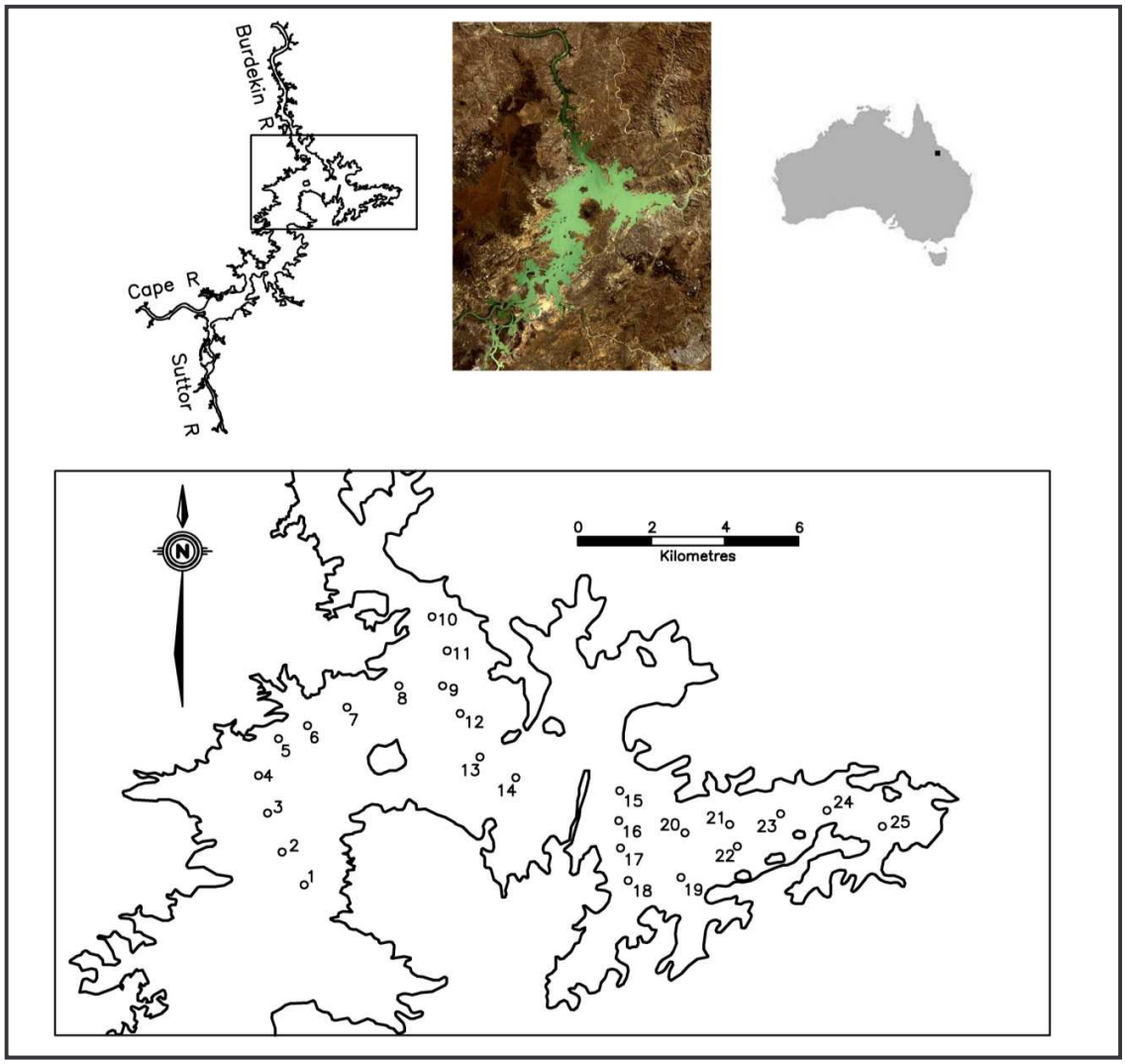

Figure F-1 Location of the validation sample sites for the August 2009 fieldwork activities on Burdekin Falls Dam, Australia. The upper left hand image shows the calculated full supply level and the upper middle image shows a Landsat 5 TM true colour image captured on 22nd August 2008. The lower image shows the location of the 25 validation sample sites.

F.2 Laboratory Measurements Results

The water quality parameter concentrations measured using the methods described in §5.3.3 for the Burdekin Falls Dam in August 2009 stations are shown in Table F-1.

Table F-1 The measured water quality parameter concentrations for the August 2009 Burdekin Falls Dam measurement stations.

Station	Chlorophyll *a* Replicate 1 (μgl^{-1})	Chlorophyll *a* Replicate 2 (μgl^{-1})	Tripton (mgl^{-1})
1	4.60	5.02	4.7
2	2.94	2.88	0.8
3	4.34	3.28	3.7
4	4.81	3.45	3.7
5	4.07	4.29	5.7
6	4.34	3.31	3.7
7	3.82	4.29	2.2
8	2.83	3.06	4.3
9	4.27	4.63	3.7
10	3.11	3.08	0.8
11	3.08	2.97	0.8
12	4.07	3.90	4.7
13	2.67	2.97	2.8
14	2.36	2.97	2.3
15	2.31	2.59	2.3
16	4.40	4.47	2.2
17	2.03	1.83	2.9
18	2.14	2.06	2.9
19	2.88	2.89	4.8
20	3.69	3.72	3.2
21	6.78	6.88	2.0
22	4.76	4.41	4.2
23	5.74	5.59	1.1
24	4.81	4.60	7.7
25	3.29	3.26	2.8

Appendix G August 2009 MIM Inversion Results

Table G-1shows the means of the absolute values of error calculated for the each weighting schemes shown in Figure E-1. Figure G-1- Figure G-4 show plots of the laboratory concentrations vs image retrieved concentrations for some selected weighting schemes.

Table G-1 The means of the absolute values of error between the laboratory measured concentrations and those retrieved from the 13th August 2009 image for all the trialled weighting schemes.

	Chl (μgl^{-1})		TR (mgl^{-1})	
	Av	SD	Av	SD
NO_WEIGHTS	5.96	1.26	5.20	2.46
3_BANDS	2.81	1.16	5.74	2.46
MER_BL_DER1	9.34	2.63	5.84	2.79
MER_BL_DER2	3.97	1.83	5.71	2.61
MER_BL_DER3	3.46	1.20	5.39	2.44
MER_BL_DER4	2.45	1.12	5.37	2.42
MER_BL_DER5	3.98	1.34	5.23	2.43
MER_BL_DER6	4.64	2.14	1.69	1.25
MER_BL_DER7	3.98	1.46	1.93	1.48
MER_BL_RAN1	7.08	1.14	3.61	1.98
MER_BL_RAN2	4.15	1.60	4.93	2.39
MER_BL_RAN3	12.2	6.65	6.63	3.66
MER_BL_RAN4	6.56	1.17	5.03	2.44
MER_BL_RAN5	3.68	1.27	5.10	2.40
MER_BL_RAN6	1.85	0.95	5.36	2.40
MER_BL_RAN7	1.58	1.45	3.85	2.19
MER_BL_RAN8	6.56	1.17	5.03	2.44
MER_BL_REF1	1.99	0.91	4.19	2.23
MER_BL_REF2	3.06	1.56	4.63	2.34
MER_BL_REF3	2.73	1.48	4.82	2.36
MER_BU_DER1	11.9	1.99	6.06	2.85
MER_BU_DER2	5.76	2.24	5.84	2.67
MER_BU_DER3	3.46	1.20	5.39	2.44
MER_BU_DER4	2.45	1.12	5.37	2.42
MER_BU_DER5	3.98	1.34	5.23	2.43
MER_BU_DER6	4.64	2.14	1.69	1.25
MER_BU_DER7	3.98	1.46	1.93	1.48
MER_BU_RAN1	0.88	0.61	5.44	2.38
MER_BU_RAN2	0.78	0.70	5.41	2.37
MER_BU_RAN3	4.81	2.87	5.48	2.65
MER_BU_RAN4	8.67	5.50	6.69	3.14
MER_BU_RAN5	11.3	1.39	2.92	1.90
MER_BU_RAN6	19.6	3.10	5.02	2.62
MER_BU_RAN7	3.26	1.61	5.74	2.54
MER_BU_RAN8	5.28	1.94	3.75	2.05
MER_BU_REF1	1.99	0.91	4.19	2.23
MER_BU_REF2	2.75	1.44	4.58	2.32
MER_BU_REF3	3.96	1.79	4.54	2.35

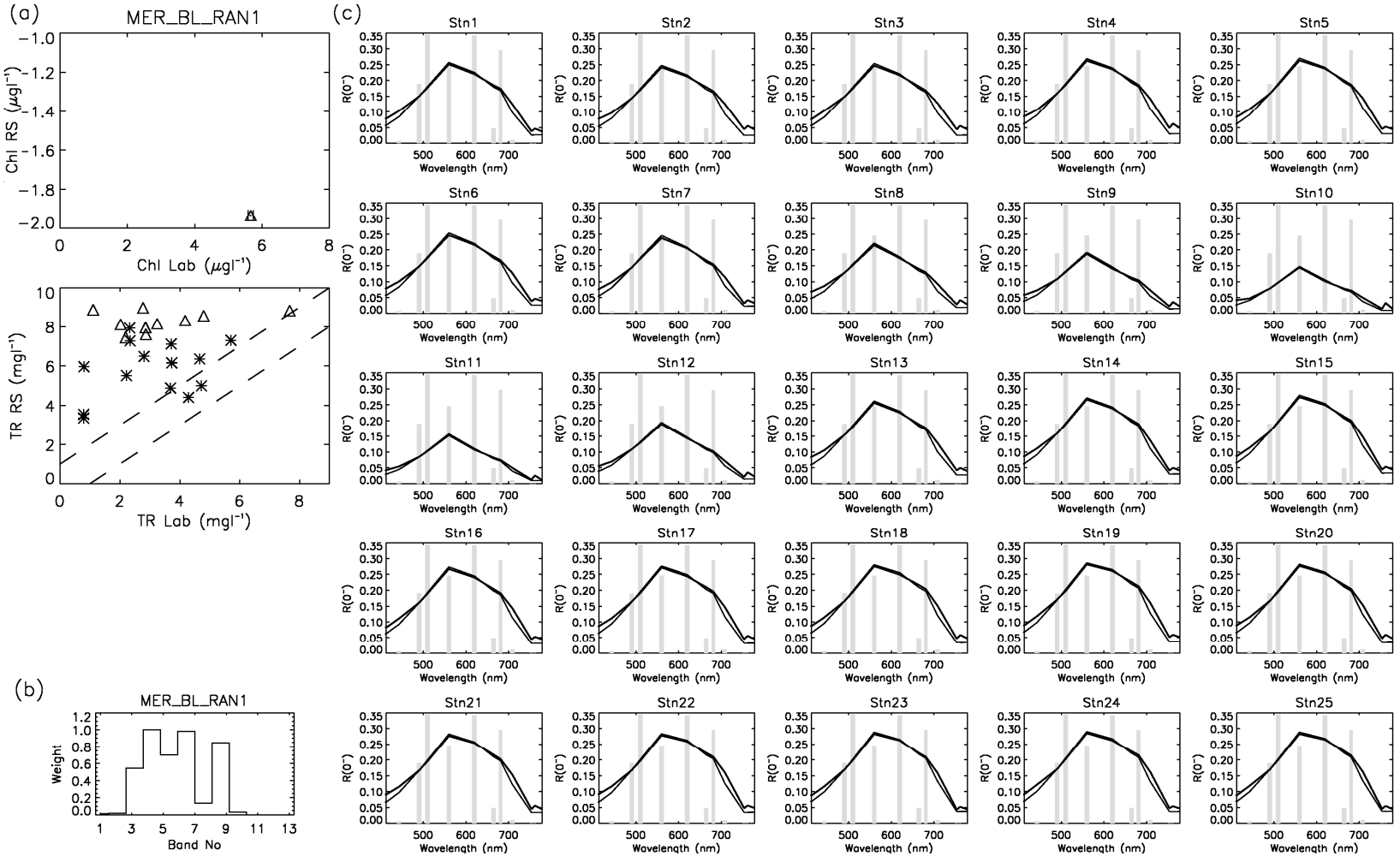

Figure G-1 (a) The laboratory concentrations vs image retrieved concentrations using the MER_BL_RAN1 weighting scheme. The diamond symbols show the stations that are geographically in the lower basin. The dotted lines show the bounds of 1μgl^{-1} for chlorophyll *a* and 1mgl^{-1} of tripton. (b) The weighting scheme. (c) The optical closure for each station.

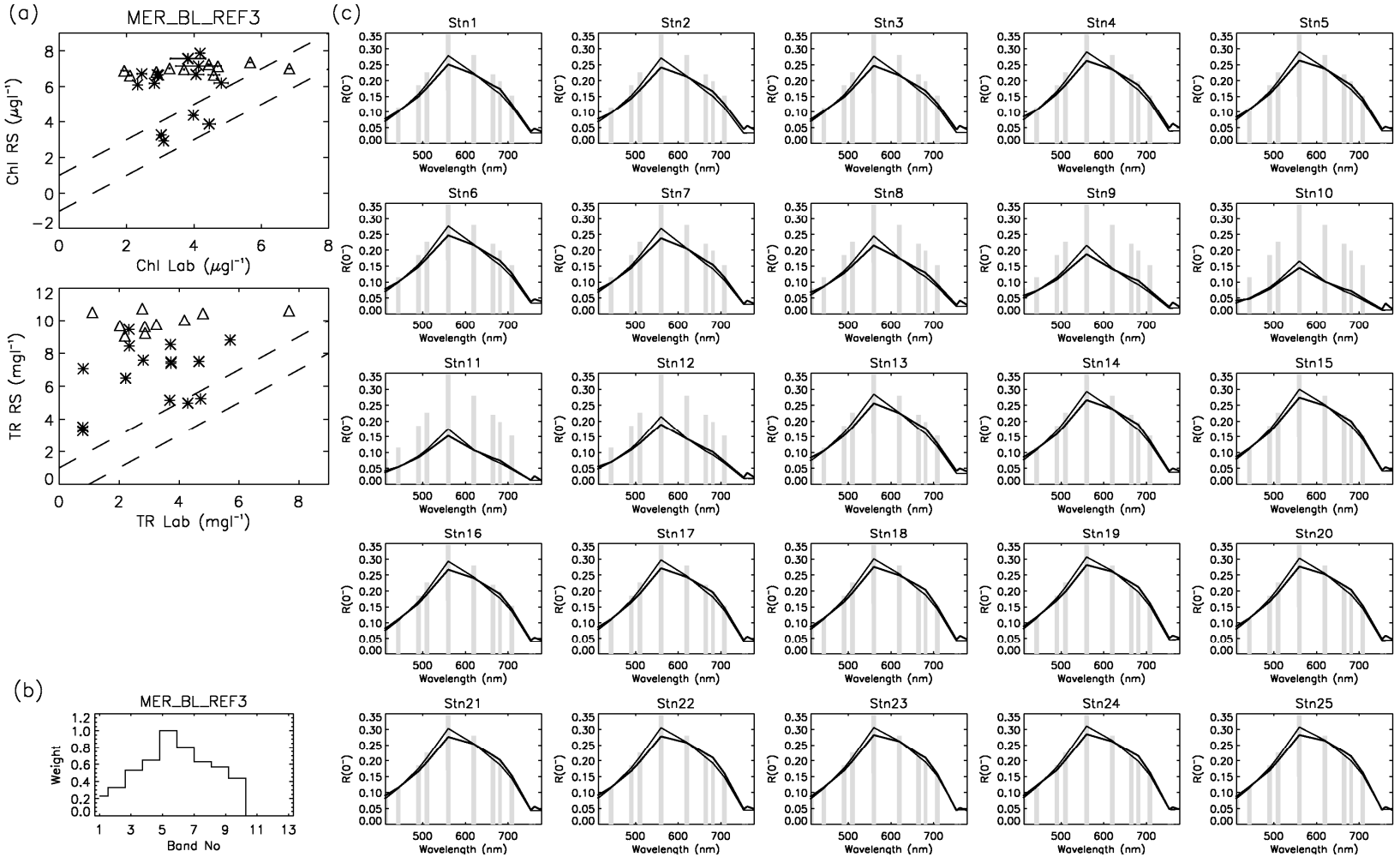

Figure G-2 (a) The laboratory concentrations vs image retrieved concentrations using the MER_BL_REF3 weighting scheme. The diamond symbols show the stations that are geographically in the lower basin. The dotted lines show the bounds of 1µgl^{-1} for chlorophyll *a* and 1mgl^{-1} of tripton. (b) The weighting scheme. (c) The optical closure for each station.

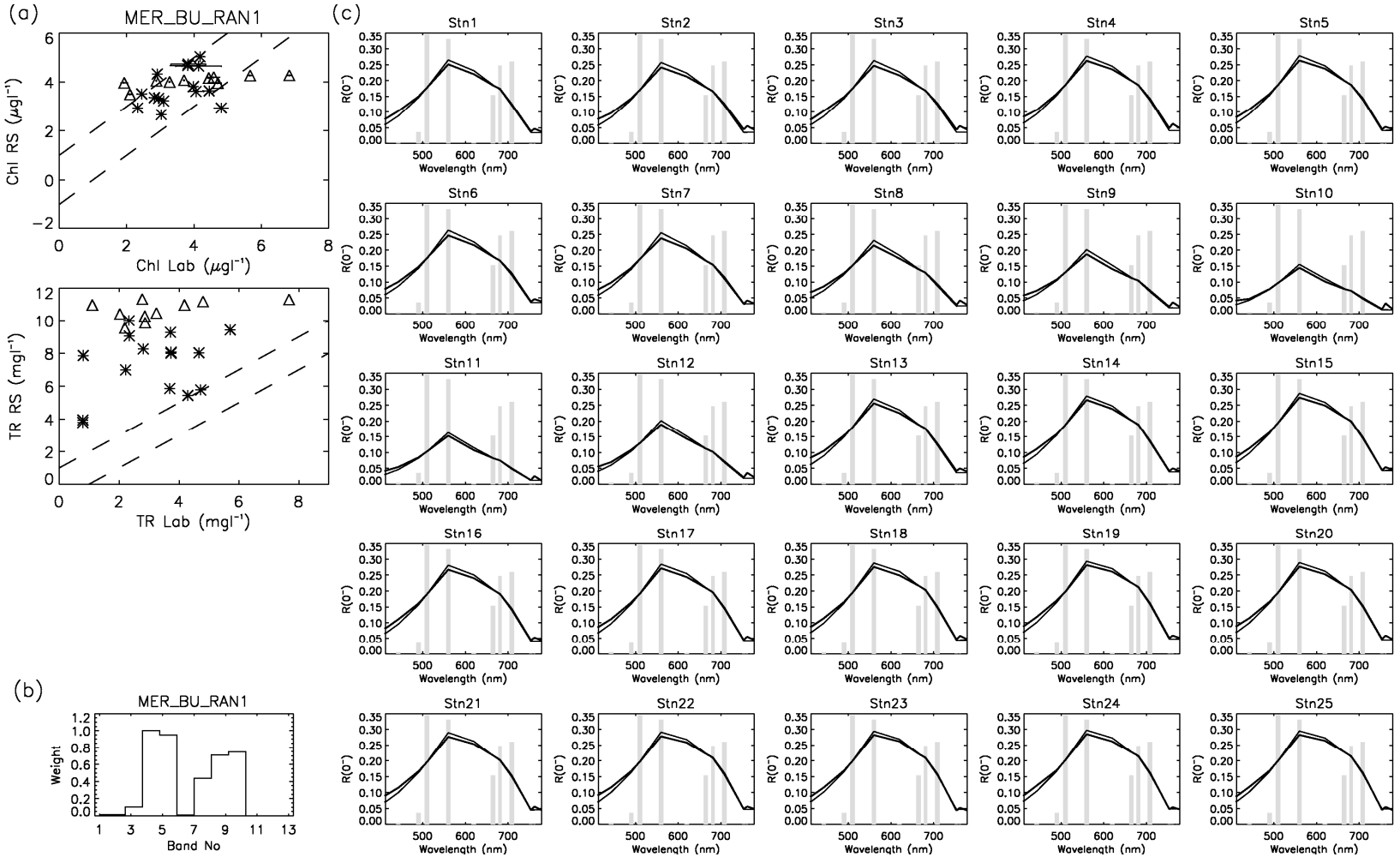

Figure G-3 (a) The laboratory concentrations vs image retrieved concentrations using the MER_BU_RAN1 weighting scheme. The diamond symbols show the stations that are geographically in the lower basin. The dotted lines show the bounds of 1μgl^{-1} for chlorophyll *a* and 1mgl^{-1} of tripton. (b) The weighting scheme. (c) The optical closure for each station.

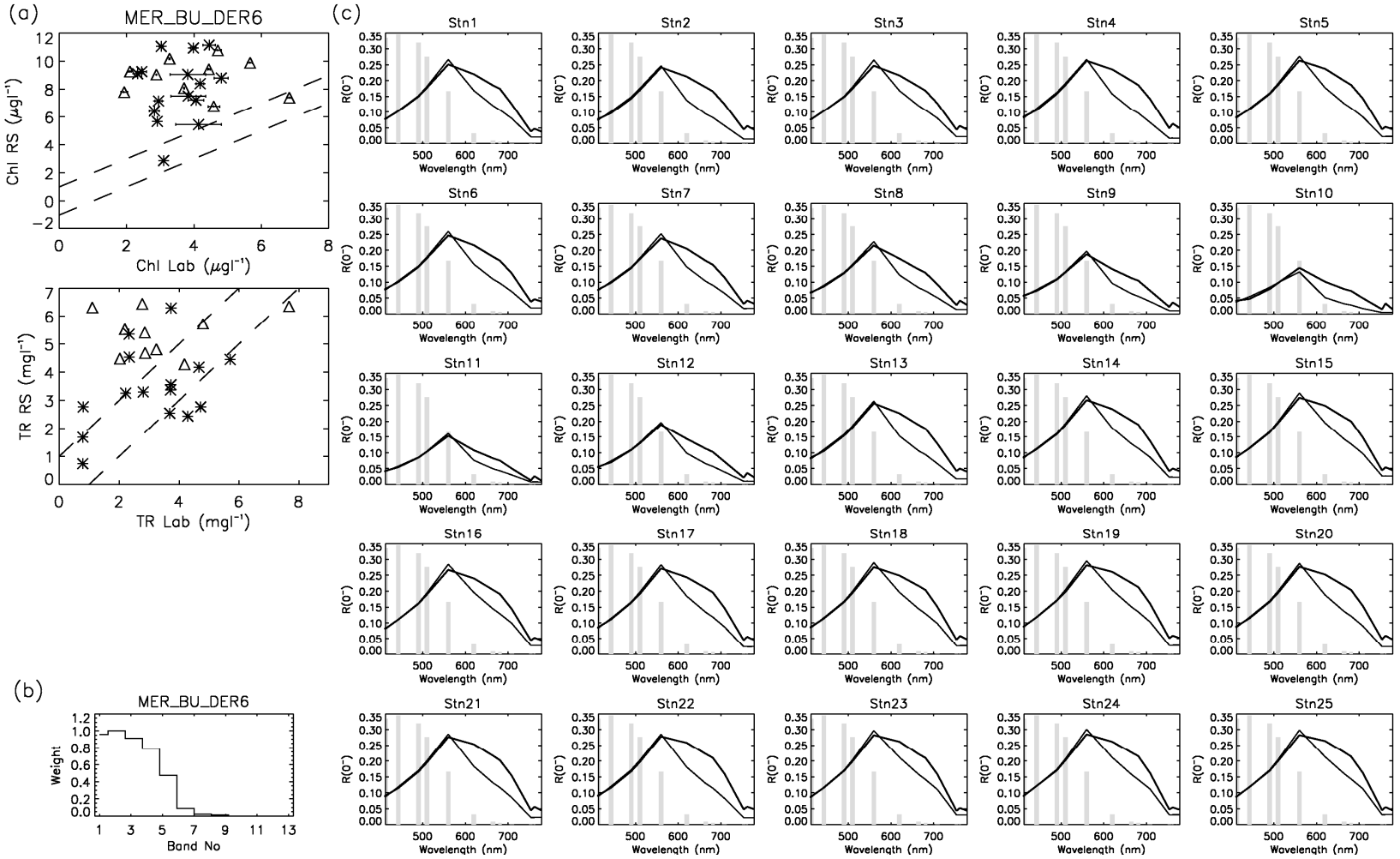

Figure G-4 (a) The laboratory concentrations vs image retrieved concentrations using the Upper the MER_BU_DER6 weighting scheme. The diamond symbols show the stations that are geographically in the lower basin. The dotted lines show the bounds of 1μgl^{-1} for chlorophyll *a* and 1mgl^{-1} of tripton. (b) The weighting scheme. (c) The optical closure for each station